UNIVERSITÀ DI PARMA

UNIVERSITÀ DI PARMA

UNIVERSITA' DEGLI STUDI DI PARMA

DOTTORATO DI RICERCA IN SCIENZA E TECNOLOGIA DEI MATERIALI

CICLO XXXVIII

Correlated Electrons in Organic Media: Spin-Optical Interfaces, CISS, and Crystallochromism for Quantum Technologies

Coordinatore:
Prof. Riccò Mauro

Supervisori:
Prof. Painelli Anna
Prof. Di Maiolo Francesco
Prof. Phan Huu Dang Khoa Andrea

Dottorando: Savi Lorenzo

Anni Accademici 2022/2023 – 2024/2025

Funding Acknowledgments
This thesis work was supported by the National Recovery and Resilience Plan (NRRP), Mission 4 Component 2 Investment 1.3 - Call for tender No. 341 of 15/03/2022 of the Italian Ministry of University and Research funded by the European Union – NextGenerationEU.

Project Details
Award Number: Project code PE0000023, Concession Decree No. 1564 of 11/10/2022 adopted by the Italian Ministry of University and Research, CUP D93C22000940001.

Project Title: "National Quantum Science and Technology Institute" (NQSTI).

Publisher
First printed in December 2025 by UNIPR

Contents

1 Introduction

1.1 Quantum technologies

When we talk about "Quantum technologies" we refer to a broad spectrum of instruments, techniques, and theoretical concepts that use the principles of quantum mechanics to create new applications. Among them, *quantum information science* (QIS)[1] studies the information carried by quantum systems, exploiting fundamental quantum phenomena, such as quantum entanglement, evolution of coherences, and the creation of quantum phases for applications in communication, computation, and sensing [2], while, at the same time, deepening our understanding of reality [3].

The concept of quantum information was born in the early days of information theory and quantum mechanics. Only a couple of decades after the description of classical information theory by Shannon[4], it was recognized that quantum mechanics cannot be described by classical statistics, as demonstrated by Bell's inequalities [5, 6]. The mathematical description of QIS is due to Ingarden [1]. The resulting background is very solid, but its extremely counterintuitive nature hindered its exploitation. In this Chapter, the basic unit of information in QIS, the quantum bit, will be presented, as well as some molecular systems and fundamental phenomena that could be exploited in the fabrication of qubits.

1.2 Qubits

A quantum bit (qubit) is the quantum analog of the classical two-state bit. A qubit can be prepared in two states, $|0\rangle$ and $|1\rangle$, the analogs of the 0 and 1 states of a classical bit.However, in contrast to classical bit, any (normalized) linear combination of the two basis states is a valid state for the qubit:

$$\left|\psi\right\rangle = \alpha\left|0\right\rangle + \beta\left|1\right\rangle \tag{1.1}$$

where α and β are complex numbers. The outcome of a measurement on the qubit will be either 0 with probability $|\alpha|^2$ or 1 with probability $\left|\beta\right|^2$. Accordingly, after the measurement, the qubit will collapse into either $|0\rangle$ or $|1\rangle$. The state of a qubit can be pictorially represented using the Bloch sphere, as illustrated in Figure 1.1. Any single-qubit useful operation can be defined as a unitary rotation, and so the Bloch sphere is a useful tool to intuitively understand the basics of QIS.

The operators $\hat{S}$ that manipulate the quantum states of a single qubit are 2X2 unitary matrices with trace equal to zero. These operators are called *quantum gates*. The most important single qubit gates are the three Pauli Matrices:

$$X \equiv \begin{bmatrix} 0 & 1 \\ 1 & 0 \end{bmatrix}; \quad Y \equiv \begin{bmatrix} 0 & -i \\ i & 0 \end{bmatrix}; \quad Z \equiv \begin{bmatrix} 1 & 0 \\ 0 & -1 \end{bmatrix}$$

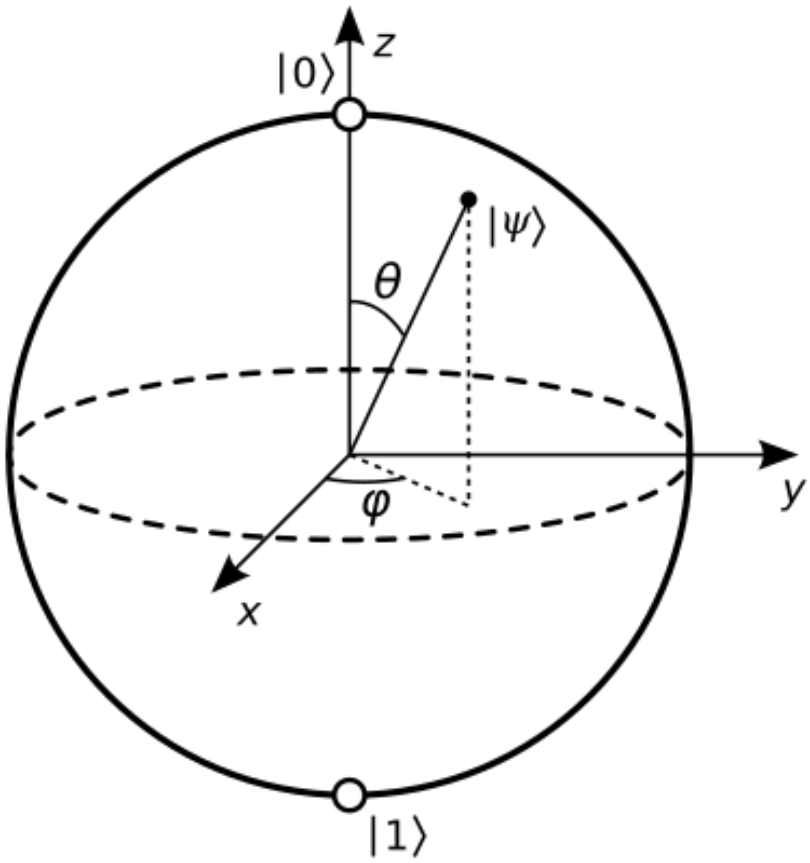

Figure 1.1: Bloch sphere representation of a qubit state. The computational basis correspond to the position $|0\rangle = (0, 0, 1)$ and $|1\rangle = (0, 0, -1)$. Each valid state can be represented using $\left|\psi\right\rangle = cos\frac{\theta}{2}|0\rangle + e^{i\phi}sin\frac{\theta}{2}|1\rangle$

The Hadamard gate, which is the simplest gate capable of creating superposition states:

$$H = \frac{1}{\sqrt{2}}\begin{bmatrix}1 & 1\\ 1 & -1\end{bmatrix}$$

and the arbitrary phase gate:

$$R(\phi) = \begin{bmatrix}1 & 0\\ 0 & \exp(i\phi)\end{bmatrix}$$

A final important gate is the rotation around an arbitrary axis $\vec{n}$ in the Bloch sphere representation, which is:

$$R_{\vec{n}}(\theta) = cos(\theta/2)I - isin(\theta/2)(x_x\hat{X} + n_y\hat{Y} + n_z\hat{Z})$$

The most intuitive (even if theoretical) realization of a qubit is an electron in a magnetic field, whose spin can be controlled by magnetic pulses, as done in EPR measurements. Any rotation around an axis $\vec{n}$ can be achieved by arbitrary duration EPR pulses along the three directions $\vec{x}, \vec{y}, \vec{z}$.

Computation cannot be done with a single bit, and so to make use of useful QM algorithms, we need to build a processor made of multiple qubits. The Hilbert space resulting from the coupling of n qubits is the tensor product of the Hilbert spaces of each individual qubit. For example, a system made of two qubits can be described as a linear combination of

four basis states:

$$\left|\psi\right\rangle = \alpha\left|0_A 0_B\right\rangle + \beta\left|0_A 1_B\right\rangle + \gamma\left|1_A 0_B\right\rangle + \delta\left|1_A 1_B\right\rangle \tag{1.2}$$

The possibilities of creating superposition states in quantum systems become interesting when we take entanglement into consideration. For example, consider the famous Bell states.

$$\left|\Psi_{\pm}\right\rangle = \frac{\left|00\right\rangle \pm \left|11\right\rangle}{\sqrt{2}} \tag{1.3}$$

$$\left|\Phi_{\pm}\right\rangle = \frac{\left|01\right\rangle \pm \left|10\right\rangle}{\sqrt{2}} \tag{1.4}$$

If we measure one of the bits of $\left|\Psi_{+}\right\rangle$, we can obtain 0 or 1 with equal probability. However, if we measure 0 on the first bit, we know with 100% certainty that the second bit is in the 0 state.

To execute operations on two (multiple) qubit systems, we need two-qubit (multiple-qubit) gates. Of course, each qubit responds to its own single-qubit gate, but a way to execute different operations while checking the overall state of the ensemble is needed. The two most important two-qubit gates are the *controlled* gates, where a specific operation on a qubit is executed depending on the state of the other qubit.

In general, any multiple-qubit gate can be composed by combinations of single- and double-qubit quantum gates [7]. A set of gates that allows the construction of any possible quantum algorithm is called *universal*.

Quantum computers are not trivial substitutes for classical computers, they are qualitatively different systems. Indeed, some operations that are trivially executed by classical computers cannot be done by quantum algorithms. For example, qubit states cannot be copied [8]. But quantum computers can be exploited in several ways, for example, to devise algorithms that are polynomially faster than classical algorithms [9], spy-proof communication [10], search algorithms employing the diffusion of coherence [11], superdense coding[12] or the development of exotic phenomena like quantum teleportation [13].

1.3 Physical realization of qubits

Theoretically, any two-state quantum system can be used as a qubit. However, from a practical perspective, to make use of quantum computing, any experimental setup on which the quantum computer is built must meet at least five conditions, called the *DiVincenzo criteria* [14]:

- It must be a scalable physical system with two well-characterized states
- It must be possible to initialize its state to a simple fiducial state, a state with a well-defined nature
- The qubit states must have long coherence times
- A "universal" set of quantum gates.
- A qubit-specific measurement capability.

In addition, to allow for quantum communication (and hence for the transmission of information), we must also have:

- The ability to interconvert stationary and flying qubits
- The ability to faithfully transmit flying qubits between specified locations.

These requirements are highly non-trivial. For example, if we consider molecular systems, it is difficult to obtain long coherence times while maintaining the possibility to address the qubit with external stimuli when required. Moreover, these criteria hide other complications: as for quantum gates, they must be reliable and should not produce noise, but operations mediated by a classical system cannot be error-proof. To mitigate the noise created by specific sources, effort is spent in the development of quantum-error correction algorithms [15] that can protect logical qubits from being corrupted by transferring the noise to ancilla qubits. Error correction is far from being an accessory procedure to be applied in naive cases; rather, it represents the only practicable way to exploit quantum computing. Several quantum error correction algorithms are known, developed to solve specific sources of noise [15], all of them relying on aggregating several qubits into virtual *logical* qubits that are more resistant to noise.

Nowadays the most studied qubits are based on Josephson junctions on superconductive devices [16–19], Rydberg atoms[20–22], trapped ions [23, 24], photons[19, 25–27], and magnetically active molecules [28–31] among others[32–35].

While QCs based on superconducting qubits are the most studied and at present represent the only commercially available qubits, molecular qubits, the focus of this thesis, offer a very interesting alternative. As chemical objects, they can be carefully designed to obtain the desired properties. Molecules are inherently small, few nanometers at most, and so chips of thousands of qubits can in principle be packed in few micrometers. The coherence time of molecular qubits can reach milliseconds, and the interaction time is usually in the order of nanoseconds, allowing millions of operations in one go. Finally, molecular systems may possess more than two addressable states. An example of this type of molecule is reported in Figure 1.2. Systems with more than 2 addressable states are called *qudits* and offer interesting characteristics, such as the possibility to embed quantum-error correction algorithms without the need to collapse the information on multi-qubits structures [30, 36, 37].

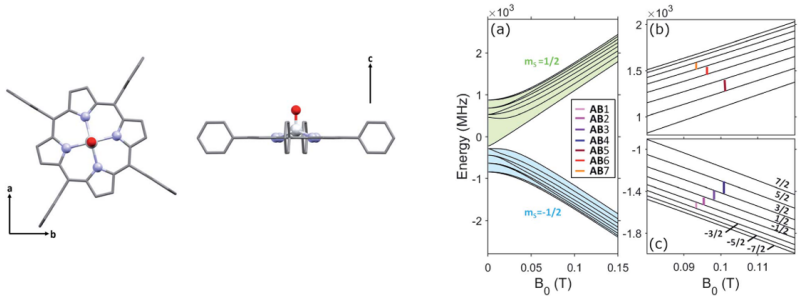

Figure 1.2: Left: the VOTPP metal complex. Right: the energy level of the system under the Zeeman splitting imposed by a magnetic field. The unpaired electron of the molecule is coupled with the 8 energy level of the spin $\frac{7}{2}$ vanadium.Reproduced from [36]. Published by the Royal Society of Chemistry. Licensed under CC BY-NC 4.0.

Nowadays, organic radicals and diradicals are among the most studied molecules for QIS applications [38–44]. Organic open-shell systems can be engineered to have long spin coherence times. Their electronic structure can be tailored via molecular design to achieve well-isolated

spin states, controllable exchange interactions, and predictable coupling to the environment. Moreover, organic frameworks are synthetically versatile and compatible with scalable, lightweight, and potentially low-cost materials, making them promising complements or alternatives to the extensively studied metallorganic qubits.

1.4 Summary of the work

Inspired by the growing interest in the field, after Chapter 2 that presents a brief introduction to the models and computational approaches adopted in this work, Chapter 3 is dedicated to the study of a class of promising radicals, triangulenes, and diradicals bridged by triangulene inverted singlet–triplet energy-gap systems. These systems are promising for QIS applications in terms of the tunability of their photophysical properties, favorable energy gaps for population selectivity at room temperature, and applications in the Optically-Detected Magnetic Resonance (ODMR) mechanism. In the same chapter, preliminary results on the tetrathiafulvalene–perchlorotriphenylmethyl (TTF-PTM) donor–acceptor radical dimer are shown. Previous experimental studies demonstrated that the molecule is a switchable unit[45–48]. Accordingly, it is an interesting molecular unit to be used as a coupling switch between two molecular qubits. We tried to extrapolate the TTF-PTM behavior in an isolated environment.

Along with innovative qubit designs, the phenomenon of Chirality-Induced Spin Selectivity (CISS) is very promising for a wide range of new applications in QIS [49–52]. CISS is an umbrella term indicating that the passage of an electron through a chiral medium is influenced by its spin state. Opposite enantiomers cause opposite effects on electrons with opposite spins. One of the most intriguing possibilities is to use chirality-driven spin selection to polarize the spin of an electron that undergoes charge transfer between two linked molecular moieties. The induced polarization could also inhibit electron recombination, thus increasing the lifetime of the excitation. Experimental evidences for CISS has emerged in a variety of different measurements [2, 53, 54]. However, despite the large number of experiments, modeling CISS is far from trivial. Specifically, the large CISS responses observed experimentally are difficult to simulate in organic systems characterized by weak spin-orbit coupling. In Chapter 4, a novel approach to simulate CISS in transport experiments is proposed.

Finally, Chapter 5 is devoted to the study of a molecular crystal using a multiscale modeling approach that, starting from ab initio calculations on crystal fragments, leads to a reliable parametrization of a Frenkel-Holstein excitonic model. Along this line, a good understanding of absorption and fluorescence spectra of two polymorphs of quinacridone is obtained, highlighting the role of intermolecular interactions in the definition of the photophysics of crystalline materials. Molecular materials are increasingly explored as platforms where excitons—delocalized electronic excitations—play a central role in energy transport, quantum sensing, and photophysical mechanisms relevant for qubit initialization or readout [55–59]. Moreover, understanding the effect of the environment on

the photophysical properties of molecules can help to design functional devices.

Methods 2

This chapter briefly summarizes the techniques adopted in this work. The first part addresses ab initio computational approaches, focusing mainly on post-Hartree–Fock approaches. I was introduced to these techniques during my research stay in the group of Prof. Yoann Olivier, with significant guidance from Dr. Danillo Valverde and Dr. Gaetano Ricci. This collaboration was crucial to the development of this work. DFT and TD-DFT are also briefly summarized, as they offer computationally efficient approaches, either to add correlation to a multiconfigurational wavefunction or as stand-alone methods.

In the second part of the chapter, the semi-empirical models adopted to simulate specific systems are presented. Although ab initio methods are powerful and general, the use of models to understand the specific physics of paradigmatic systems remains relevant. The focus of the chapter will be on the Hubbard model, the Pariser–Parr–Pople (PPP) model, and the exciton model.

2.1 Post Hartree-Fock methods

In the Hartree-Fock (HF) approximation, the ground state of a closed-shell molecule is obtained as a Slater determinant of one-electron orbitals. This solution is the result of a mean-field approximation, implying that each electron does not interact instantaneously with the complex many-body system but rather experiences the average electronic density generated by the other electrons. The energy difference between the "true" energy of the many-body system and the mean-field Hartree-Fock solution is defined as the correlation energy E_{corr}. To recover E_{corr}, various methods are available. Here, we address the CAS, RAS, and Multi-Configurational PT2 approaches, which are widely employed to study strongly correlated molecular systems.

In the following, where relevant, we make use of Configuration State Functions (CSF), defined as eigenfunctions of the total spin operator. CSFs can be obtained by diagonalizing the $\hat{S}^2$ operator written in the Slater Determinant (SD) basis, but they are most often obtained by exploiting the Graphical Unitary Group Approach (GUGA) [60, 61]. Since CSFs are eigenvectors of $\hat{S}^2$ and the Hamiltonian (provided spin-orbit coupling is neglected) is spin-independent, it is convenient to define spin-averaged excitation operators:

$$\hat{E}_{pq} = \sum_{\sigma} \hat{a}^{\dagger}_{p\sigma} \hat{a}_{q\sigma} \tag{2.1}$$

with $\hat{a}^{\dagger}_{p\sigma}$ and $\hat{a}_{p\sigma}$ being the fermionic operators that create/destroy an electron with spin σ on orbital p. Consequently, the relation $[\hat{E}_{pq}, \hat{E}_{rs}] = \delta_{qr}\hat{E}_{ps} - \delta_{ps}\hat{E}_{qr}$ holds true. As a recurrent combination of two-electron operators, we define:

$$\hat{e}_{abcd} = \hat{E}_{ab}\hat{E}_{cd} - \delta_{bc}\hat{E}_{ad} \tag{2.2}$$

Finally, we adopt the chemistry notation for monoelectronic and bielectronic integrals, with:

$$h_{pq} = \left\langle \phi_p(\boldsymbol{r}) \right| \hat{h} \left| \phi_q(\boldsymbol{r}) \right\rangle = \int \nabla \phi_p^*(\boldsymbol{r}) \nabla \phi_q(\boldsymbol{r}) d\boldsymbol{r} + \sum_A \int \frac{Z_A \phi_p^*(\boldsymbol{r}_1) \phi_q(\boldsymbol{r}_1)}{|\boldsymbol{r}_1 - \boldsymbol{R}_A|} d\boldsymbol{r} \tag{2.3}$$

$$(pq|rs) = \left\langle \phi_p(r_1)\phi_r(r_2) \right| \frac{1}{|\boldsymbol{r}_1 - \boldsymbol{r}_2|} \left| \phi_q(r_1)\phi_s(r_2) \right\rangle = \int \frac{\phi_p^*(\boldsymbol{r}_1)\phi_q(\boldsymbol{r}_1)\phi_r^*(\boldsymbol{r}_2)\phi_s(\boldsymbol{r}_2)}{|\boldsymbol{r}_1 - \boldsymbol{r}_2|} d\boldsymbol{r}_1 d\boldsymbol{r}_2 \tag{2.4}$$

where $\boldsymbol{R}_A$ is the position of nucleus A with charge Z_A.

With this notation, the non-relativistic many-body electronic Hamiltonian in the Born-Oppenheimer approximation reads:

$$\hat{H} = \sum_{pq} h_{pq} \hat{E}_{pq} + \frac{1}{2} \sum_{pqrs} (pq|rs) \hat{e}_{pqrs} \tag{2.5}$$

Starting from the Hartree-Fock solution, CAS and RAS approaches diagonalize the Hamiltonian in the Hilbert space defined by locating the electrons within a selected subset of molecular orbitals. PT techniques, instead, add perturbative corrections to the energies and wavefunctions.

To ensure computational feasibility, an efficient method is required to calculate Hamiltonian matrix elements between different CSFs. The Slater-Condon rules provide this framework. Specifically, the Hamiltonian matrix elements $H_{D_iD_j}$ between two CSF (D_i and D_j) vanish except in three cases:

- $\left|D_j\right\rangle = |D_i\rangle$. In this case:

  $$H_{D_iD_i} = \sum_k h_{kk} \langle D_i| \hat{n}_k |D_i\rangle + \sum_{kl} [(kk|ll) - (kl|lk)] \langle D_i| \hat{n}_k \hat{n}_l |D_i\rangle$$

  where $\hat{n}_k = \hat{E}_{kk} = \hat{a}_k^\dagger \hat{a}_k$ counts the number of electrons in the k-th MO.
- $\left|D_j\right\rangle = \hat{E}_{pq} |D_i\rangle$, i.e. the two SDs differ by the occupation of a single pair of orbitals. In this case:

  $$H_{D_iD_j} = h_{pq} + \sum_k [(pq|kk) - (pk|kq)] \langle D_i| \hat{n}_k \left|D_j\right\rangle$$

- $\left|D_j\right\rangle = \hat{E}_{rs}\hat{E}_{pq} |D_i\rangle$, i.e. the two SDs differ by the occupation of two pairs of orbitals. In this case:

  $$H_{D_iD_j} = (pq|rs) - (ps|qr)$$

2.1.1 Complete Active Space

The Complete Active Space (CAS) is a family of post-HF techniques relying on a configuration interaction (CI) expansion [62], and is one of the most widely used approaches to address metal-organic clusters, organic molecules, dimers, and aggregates. In CI methods, the correlation energy is recovered by expanding the wavefunctions as a sum of CSFs, writing the wavefunction as a linear combination of CSFs:

$$|\Psi\rangle = \sum_I C_I |D_i\rangle \tag{2.6}$$

with $|D_i\rangle$ being the CSFs and C_I their coefficients. The vector $\boldsymbol{C}_\Psi$, containing the C_i coefficients, is called the *configuration interaction (CI) vector* for the state Ψ.

In the CAS-CI approach, an active space of orbitals is defined, and a full-CI calculation is performed within this space while maintaining the occupation of all the remaining orbitals fixed (equal to 2 for occupied orbitals and equal to 0 for virtual orbitals). See Figure 2.1 panel a) for a schematic view. The idea is that the properties of a specific state

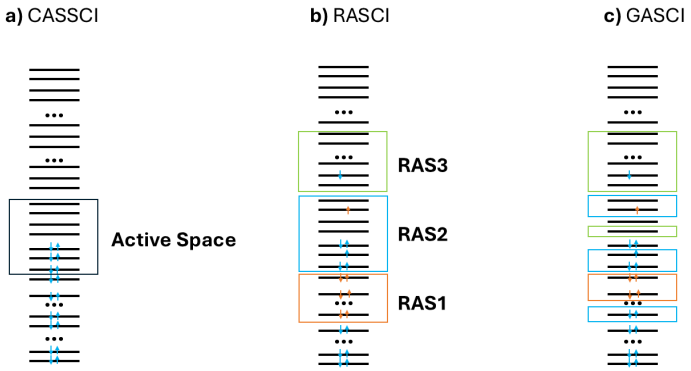

Figure 2.1: Scheme of the different flavors of CI MR methods. a) Complete active space CI (CASSCI). An active space is selected in which a full-CI calculation is done. All the other occupations remain fixed. b) Restricted Active Space CI (RASCI). Three spaces are selected: RAS2 is used for an internal full-CI. RAS1 is allowed to create n holes in RAS2. RAS3 is allowed to create m particles from RAS2. c) Generalized Active Space CI (GASCI). Custom spaces with different excitation rules are allowed.

can be reasonably well understood by accounting for the CI obtained by distributing the electrons in a subset of most relevant orbitals. The dimension of the active space is typically represented by writing the number of electrons and orbitals entering the active space in parentheses. For example, a CASCI calculation with 8 electrons in an active space of 10 orbitals is indicated as "CASCI(8,10)" or "CASCI(8e,10o)".

The selection of relevant MOs is critical: while it is often stated that the choice of the active space relies on "chemical intuition", identifying the orbitals that best describe a state without prior knowledge is non-trivial. Usually, several calculations with different active spaces must be tested to reach a satisfying result. A good rule of thumb is to perform MP2 calculations, analyze the occupation numbers of the resulting Natural Orbitals (NO), and include all NOs with occupation numbers between 0.05 and 1.95 [63]. However, 1) the number of these orbitals is usually much larger than what is computationally feasible; 2) MP2 fails for radicals or open-shell singlets where the single-reference HF solution poorly describes the ground state; and 3) MP2 is poorly applicable to excited states.

Several variants of the original CAS-CI are available. In the Restricted Active Space CI (RASCI) [64], three different spaces are selected: (a) RAS2, a space in which a complete active space calculation is executed; (b) RAS1, a space from which single electron excitations are considered towards RAS2; and (c) RAS3, a space to which single electron excitations are considered from RAS2 (see Figure 2.1b). This method is useful when active spaces must be considered that are beyond the capability of CAS-CI. Several variants of RASCI are also available: single hole/excitations between different spaces in the RASCI(h,p) approach; the creation of multiple holes and particles, up to n holes and m particles, in the RASCI(nh,mp) method; mixing different types of excitations such as RASCI(h,p,2h,2p,3h,5p...); and finally, the creation of hole-particle pairs

from RAS1 to RAS3 in the RASCI(hp) flavor. Other Generalized Active Space (GAS) methods have also been developed [65], in which custom spaces with custom rules can be created.

To further improve the quality of the result, in CASSCF and RASSCF, not only are the coefficients of the CI expansion optimized, but the orbitals are also self-consistently optimized. Specifically, the molecular orbitals $\psi_i(\boldsymbol{r})$ entering each CSF are expressed as linear combinations of basis functions $|\chi_\nu\rangle$:

$$\left|\psi_i\right\rangle = \sum_\nu k_\nu \left|\chi_\nu\right\rangle \tag{2.7}$$

In CASSCF and RASSCF, the CI coefficients are optimized simultaneously with the k_ν coefficients. This optimization is achieved by exploiting carefully designed algorithms, such as the Super CI [66] or Newton-Raphson [62]. This optimization is computationally expensive, and it is possible to selectively optimize a subset of orbitals. Typically, the MO space is divided into 5 different subspaces: frozen orbitals, which are always doubly occupied and are not optimized; inactive orbitals, which are always doubly occupied and are optimized; active orbitals, which constitute the active space and are optimized; virtual orbitals, which are always unoccupied and are optimized; and deleted orbitals, which are removed from the Hilbert space. Although frozen/deleted orbitals are very low/high in energy and usually play a marginal role, the selection of the orbitals pertaining to each space is delicate and can affect the quality of the result.

Orbital relaxation recovers some correlation energy and may alleviate some of the issues related to the choice of the active space. At the same time, several convergence issues may arise. An additional problem is the need to predefine the quantity of interest for the optimization. One can choose to optimize the energy of a specific state, as in State-Specific CASSCF (SS-CASSCF). However, this may result in a poor description of other states. Furthermore, two SS-CASSCF calculations on different states can only be compared by looking at the optimized energies, as they are solutions of different Hamiltonians. To overcome some of these problems, State-Averaged CASSCF calculations (SA-CASSCF) were introduced, where the optimization parameter is an average quantity over a set of states. Naturally, this introduces the number (and nature) of the states to be averaged as an additional degree of freedom, as well as the weights employed in the averaging procedure. Generally, including more states allows faster convergence but lower accuracy, while accounting for a small number of states leads to more accurate results, though convergence may become difficult, especially if states of different nature are averaged together.

To sum up, CASSCF is not a "black box" technique, and several issues must be carefully considered to obtain meaningful results. Several tutorials with suggestions and best practices can be found [63]. A good procedure to follow is summarized below.

- **Read the literature.** Every system has its own challenges. For example, for PES scans, CASCI calculations are usually suggested, and if charge transfer states are present, a careful selection of the active space to include a balanced set of orbitals from the donor and the acceptor fragments is required. Before planning a general calculation, study previous work.

- **Prepare the orbitals.** Start from orbitals that already contain some correlation energy. For singlet states, MP2 Natural Orbitals are suggested. In the case of radicals and correlated molecules, Quasi-Restricted DFT orbitals (QRO) [67] from unrestricted DFT calculations generally lead to better results. For diradicals, Restricted-Open Kohn-Sham (ROKS) orbitals or MOs obtained by a CASSCF calculation on a minimal active space are suggested.
- **Analyze the states.** It is important to have an initial guess regarding the nature of the states of interest. Analyze experimental spectra and/or rely on TD-DFT with benchmark functionals.
- **Start from simple calculations.** Perform calculations on minimal active spaces, averaging over a large number of states. Analyze transition properties to verify if the states of interest are present. Aim for a good qualitative result before seeking quantitative accuracy.
- **Optimize the parameters.** Begin to increase the size of the active space and decrease the number of states to be averaged. Track changes in transition energies, total energy, and transition properties until convergence is reached.

CAS- or RAS-based approaches work with a limited set of orbitals and do not lead to exact solutions. Some missing correlation energy can be retrieved by exploiting Perturbation Theory approaches, which are briefly addressed in the next section.

2.1.2 Perturbation theory

Perturbation Theory (PT) corrects the energies and wavefunctions by adding small corrections. The correlation energy introduced thereby is called "dynamic correlation", and it can be recovered by considering the correction to the wavefunction due to the CSFs not introduced into the Active Space.

PT starts with a reference Hamiltonian $\hat{H}_0$ and its eigenfunctions. The complete problem involves the solution of a Hamiltonian $\hat{H}$ that is the reference Hamiltonian plus a small perturbation $\hat{V}$:

$$\hat{H} = \hat{H}_0 + \hat{V} \tag{2.8}$$

The first- and second-order corrections to the energy of a state are then:

$$E_\Psi^{(1)} = \langle \Psi | \hat{V} | \Psi \rangle \tag{2.9}$$

$$E_\Psi^{(2)} = \sum_{l \neq k} \frac{\left| \langle l | \hat{V} | \Psi \rangle \right|^2}{E_l^{(0)} - E_\Psi^{(0)}} \tag{2.10}$$

The corrections to the wavefunction read:

$$\left| \Psi^{(1)} \right\rangle = \sum_{l \neq k} |l\rangle \frac{\langle l | \hat{V} | \Psi \rangle}{E_l^{(0)} - E_\Psi^{(0)}} \tag{2.11}$$

$$\left| \Psi^{(2)} \right\rangle = \sum_{l \neq \Psi} \sum_{m \neq \Psi} |l\rangle \frac{\langle l | \hat{V} | m \rangle \langle m | \hat{V} | \Psi \rangle}{(E_l^{(0)} - E_\Psi^{(0)})(E_m^{(0)} - E_\Psi^{(0)})} \tag{2.12}$$

$$- \sum_{l \neq \Psi} |l\rangle \frac{\langle l | \hat{V} | \Psi \rangle \langle \Psi | \hat{V} | \Psi \rangle}{(E_l^{(0)} - E_\Psi^{(0)})^2} \tag{2.13}$$

Being interested in specific states $|\Psi\rangle$, we do not need to build the entire Hilbert space; rather, only the states reached upon the application of single and double excitation operators on the reference state are needed. This smaller Hilbert space is called the *First-Order interacting space*.

The different variants of PT approaches differ in the choice of the reference Hamiltonian and in the approximations adopted to speed up the calculation. We used two PT models: the standard Multi-Configurational PT2 applied to CAS wavefunctions (CASPT2) and the n-electron valence PT2 (NEVPT2). CASPT2 starts from CAS wavefunctions and applies Eq. 2.10 directly. The reference Hamiltonian is the generalized Fock Hamiltonian:

$$\hat{F}(\Psi) = \sum_{pq} \left\{ h_{pq} + \sum_{rs} [(pq|rs) - \frac{1}{2}(pr|qs)] \langle \Psi | \hat{E}_{rs} | \Psi \rangle \right\} \hat{E}_{pq} \tag{2.14}$$

Note that the generalized Fock operator is state-specific, as the reduced one-particle density matrix of the state Ψ enters into the definition of the operator. The generalized Fock operator is diagonal in the MO space, but not in the CAS space. To solve this problem, the Hamiltonian is projected into the reference and perturbation spaces, as discussed in more detail in Appendix 2.A.

In CASPT2, the perturbative Hamiltonian reads:

$$\hat{V} = \sum_{pqrs} \hat{e}_{pqrs}(pq|rs) - \hat{E}_{pq} \sum_{rs} \langle \Psi | \hat{E}_{rs} | \Psi \rangle \left[(pq|rs) - \frac{1}{2}(pr|rs) \right] \tag{2.15}$$

This perturbation term is constructed to cancel the mean-field term in the generalized Fock operator (the second term in Equation 2.14) while adding real electron-electron correlation back, ensuring that the energy calculated as the sum of the Fock energy plus the second-order correction due to $\hat{V}$ is equal to the energy calculated by the CASSCF calculation. More details are reported in Appendix 2.B.

The most common artifact in CASPT2 is due to *intruder states*, i.e., states that are quasi-degenerate with the reference state and cause diverging perturbative corrections. To solve these issues, several techniques were developed [68–70]. The most widely adopted strategy relies on an imaginary shift [71, 72], a value that is added to the denominator $E_i^{(0)} - E_j^{(0)} \rightarrow E_i^{(0)} - E_j^{(0)} + i\epsilon$. The denominators assume the following convergence properties (with $\Delta = E_i^{(0)} - E_j^{(0)}$)[72]:

$$\frac{1}{\Delta} \rightarrow \frac{\Delta \left(\Delta^2 + 2\epsilon^2\right)}{\left(\Delta^2 + \epsilon^2\right)^2} \approx \begin{cases} \frac{\Delta}{\epsilon^2} - \frac{3\Delta^3}{\epsilon^4} & \Delta \ll 1 \\ \frac{1}{\Delta} - \frac{\epsilon^4}{\Delta^5} & \Delta \gg 1 \end{cases} \tag{2.16}$$

This ensures that the denominator does not vanish in cases of degeneracy and is weakly dependent on the parameter otherwise. Generally, a shift of ≈ 0.3 Hartree is considered acceptable.

CASPT2 is expensive, shift-dependent, and suffers from the intruder state problem. To address these issues, the n-electron valence state perturbation theory at second order (NEVPT2) was developed. The main difference from CASPT2 is the selection of the reference Hamiltonian, which is not the generalized Fock Hamiltonian but the Dyall Hamiltonian[69], which

is diagonal in the CAS space. The Dyall Hamiltonian is:

$$\hat{D}^{Dyall} = \hat{H}_{iv} + \hat{H}_{act} \tag{2.17}$$

with

$$\hat{H}_{iv} = \sum_{ij} f_{ij}\hat{E}_{ij} + \sum_{ab} f_{ab}\hat{E}_{ab} + C \tag{2.18}$$

$$f_{ij} = -\langle\Psi|\,\hat{a}_i^\dagger \hat{H}\hat{a}_j\,|\Psi\rangle + \delta_{ij}E_\Psi \tag{2.19}$$

$$f_{ab} = \langle\Psi|\,\hat{a}_a^\dagger \hat{H}\hat{a}_b\,|\Psi\rangle - \delta_{ab}E_\Psi \tag{2.20}$$

$$C = 2\sum_i h_{ii} + \sum_{ij}[2(ii|jj) - (ij|ji)] - 2\sum_k^{frozen} \epsilon_k \tag{2.21}$$

where $\hat{H}$ is the Hamiltonian of Eq. 2.5. $\hat{f}_{ij}$ are elements of a generalized Fock operator, as in CASPT2. $\hat{H}_{iv}$ is a diagonal one-electron Hamiltonian containing the energies of inactive and virtual orbitals. The active part is defined as:

$$\hat{H}_{act} = \sum_{tu}[h_{tu} + \sum_i 2(tu|ii) - (ti|ui)]\hat{E}_{tu} + \frac{1}{2}\sum_{tuvx}\hat{e}_{tuvx} \tag{2.22}$$

The first two terms introduce the field of the inactive electrons into the active part of the Hamiltonian, and with the definition of the constant C, the Dyall Hamiltonian is equivalent to the CAS Hamiltonian of Eq. 2.5 in the CAS space, thus ensuring that NEVPT2 is size-consistent. The perturbation operator $\hat{V}$ is simply defined as the difference between the total Hamiltonian of 2.5 and $\hat{H}^D$, i.e., $\hat{V} = \hat{H} - \hat{H}^D$.

Another key point in NEVPT2 is the generation of the perturbation contribution, which, instead of adopting a projector technique as in CASPT2, exploits the so-called *perturbers*, states generated by solving the equations:

$$\hat{P}_L^{\{k\}}\hat{H}^D\hat{P}_L^{\{k\}}\left|\Psi_{L\mu}^{\{k\}}\right\rangle = E_{L\mu}^{\{k\}}\left|\Psi_{L\mu}^{\{k\}}\right\rangle \tag{2.23}$$

where $\hat{P}_L^{\{k\}}$ are the projectors to one of the 8 spaces of 2.B, and μ labels the different states obtained after diagonalization of the Hamiltonian in the projected space. Different classes of perturbers are generated and diagonalized separately, neglecting the coupling between elements of different classes. This procedure is called Partially-Contracted NEVPT2 (PC-NEVPT2) and significantly speeds up the calculation.The calculation can be further simplified by considering a single perturber for each class:

$$\left|\Psi_L^{\{k\}}\right\rangle = \hat{P}_L^{\{k\}}\hat{H}^D\,|\Psi\rangle \tag{2.24}$$

$$E_L^{\{k\}} = \left\langle\Psi_L^{\{k\}}\right|\hat{H}^D\left|\Psi_L^{\{k\}}\right\rangle \tag{2.25}$$

This approach is called Strongly-Contracted NEVPT2 (SC-NEVPT2), and while extremely approximated, it yields similar results to PC-NEVPT2, being orders of magnitude cheaper [73]. NEVPT2 is useful not only because it is size-consistent and faster than CASPT2, but also because it is immune to the intruder state issue.However, the Dyall Hamiltonian contains double excitations (while the generalized Fock operator does not), and is therefore more expensive to diagonalize. Moreover, NEVPT2 leads

to less accurate results compared with the (non-level shifted) CASPT2. Yet, the effectiveness of the method is impressive, and SC-NEVPT2 may allow for calculations that are too expensive for CASPT2.

In situations in which degenerate states are present at the CAS level, artifacts in the zero-order description of the energy can appear. A Quasi-Degenerate formulation of NEVPT2 is available [74], applying perturbation theory for degenerate states. This formulation is much more reliable than classic NEVPT2 for problematic systems and only marginally increases the computational cost. We adopted this method for diradicals, where degeneracies in the reference Hamiltonian are found between ground state singlets and triplets.

2.2 DFT, TD-DFT and related approaches

The molecular Hamiltonian is the sum of the kinetic energy term $\hat{T}$ (a one-electron term), a one-electron potential collecting the nuclei-electron interaction $\hat{V}$, and the electron-electron interaction term $\hat{W}$:

$$\hat{H} = \hat{T} + \hat{V} + \hat{W} = \sum_i -\frac{\nabla_i^2}{2} + \sum_i v(\boldsymbol{r_i}) + \frac{1}{2}\sum_{i\neq j} w(|\boldsymbol{r_i} - \boldsymbol{r_j}|)$$

DFT, based on the Hohenberg-Kohn theorem, is formulated in terms of the ground-state one-electron density matrix $n_0(\boldsymbol{r})$:

$$n_0(\boldsymbol{r}) = N \sum_\sigma \int d\boldsymbol{r_2} \sum_{\sigma_2} d\boldsymbol{r_3} \sum_{\sigma_3} \cdots d\boldsymbol{r_N} \sum_{\sigma_N} |\Psi_0(\boldsymbol{r}\sigma\boldsymbol{r_2}\sigma_2\boldsymbol{r_3}\sigma_3 ... \boldsymbol{r_N}\sigma_N)|^2$$

The theorem states that for a finite system with N interacting electrons, a one-to-one correspondence exists between the potential $v(\boldsymbol{r})$ and the density of the ground-state $n_0(\boldsymbol{r})$. In other words, the potential is a unique functional of the ground-state density, $v[n_0]$, up to an arbitrary additive constant. Since $\hat{T}$ and $\hat{W}$ only depend on the number of electrons in the system, the Hamiltonian is a direct functional of the ground-state electron density, and similarly, its eigenstates (not only the ground state) are functionals of the ground-state electron density. As a consequence, the energy associated with a specific external potential $E_{v_0}[n] = \langle \Psi[n] | \hat{T} + \hat{W} + \hat{V}_0 | \Psi[n] \rangle$ has a minimum E_0 at the true ground-state electron density $n(\boldsymbol{r}) = n_0(\boldsymbol{r})$.

The energy minimization can be conceptually carried out in two different steps. Instead of directly searching for the density that minimizes the energy, one searches for a wavefunction that leads to a specific density n. Then the energy is minimized with respect to the density:

$$E_0 = \min_n \left\{ \min_{\Psi \longrightarrow n} \langle \Psi | \hat{T} + \hat{W} + \hat{V}_0 | \Psi \rangle \right\} \tag{2.26}$$

Finally, the energy functional is identified as the term in parentheses.

$$E_{v_0}[n] = \min_{\Psi \longrightarrow n} \langle \Psi | \hat{T} + \hat{W} + \hat{V}_0 | \Psi \rangle$$

The energy functional can be written as:

$$E_{v_0}[n] = T[n] + W[n] + \int d\boldsymbol{r} n(\boldsymbol{r}) v_0(\boldsymbol{r}) = F[n] + \int d\boldsymbol{r} n(\boldsymbol{r}) v_0(\boldsymbol{r})$$

where T and W are grouped together as they constitute a universal functional $F[n]$, i.e., a functional that does not depend on the external potential but only on the electron density. Indeed, the explicit form of $F[n]$ is unknown; therefore, it must be approximated.

To overcome the difficulty of approximating the kinetic energy $T[n]$ directly, Kohn and Sham proposed introducing an auxiliary system of non-interacting electrons that yields the same ground-state density as the real interacting system [75]. The kinetic energy of this non-interacting system, $T_s[n]$, is known exactly in terms of the single-particle orbitals. Consequently, one can rearrange the total energy functional $E_{v_0}[n]$ of the interacting system by partitioning it as follows:

$$E_{v_0}[n] = T_s[n] + \int d\boldsymbol{r} n(\boldsymbol{r}) v_0(\boldsymbol{r}) + E_H[n] + E_{xc}[n]$$

Here, $E_H[n]$ is the classical Hartree Coulomb energy:

$$E_H[n] = \frac{1}{2} \int d\boldsymbol{r} \int d\boldsymbol{r'} \frac{n(\boldsymbol{r}) n(\boldsymbol{r'})}{|\boldsymbol{r} - \boldsymbol{r'}|}$$

and $E_{xc}[n]$ is the exchange-correlation functional. This term is formally defined to contain all many-body effects not included in the previous terms, namely the difference between the true and the non-interacting kinetic energy ($T[n] - T_s[n]$), and the non-classical electron-electron interaction.

By applying the variational principle and minimizing the energy with respect to the density one obtains the Euler-Lagrange equation for the interacting system. Comparing this with the Euler-Lagrange equation of the non-interacting system reveals that the two systems yield the exact same density if the non-interacting electrons move in an effective potential $v_s(\boldsymbol{r})$ defined as:

$$v_s[n](\boldsymbol{r}) = v_0(\boldsymbol{r}) + \int d\boldsymbol{r'} \frac{n(\boldsymbol{r'})}{|\boldsymbol{r} - \boldsymbol{r'}|} + v_{xc}[n](\boldsymbol{r})$$

where the exchange-correlation potential is given by the functional derivative $v_{xc}(\boldsymbol{r}) = \frac{\delta E_{xc}[n]}{\delta n(\boldsymbol{r})}$. Finally, the orbitals that minimize the energy of this non-interacting system are obtained by solving the single-particle Schrödinger equation (the Kohn-Sham equation):

$$\left(-\frac{\nabla^2}{2} + v_s(\boldsymbol{r}) \right) \psi_i(\boldsymbol{r}) = \varepsilon_i \psi_i(\boldsymbol{r}) \tag{2.27}$$

The ground state density is then constructed as the sum of the squared moduli of the lowest N occupied Kohn-Sham orbitals:

$$n(\boldsymbol{r}) = \sum_{i=1}^{N} \left| \psi_i(\boldsymbol{r}) \right|^2 \tag{2.28}$$

The Kohn-Sham orbitals are not true molecular orbitals, as the manipula-

tions were used specifically to obtain the electron density. On the other hand, it has been shown that in most cases they behave similarly to the true orbitals of the system. Finding a suitable form for the functional is a fundamental (and open) problem in DFT. Extensive work has been done in the development of functionals, exploring different parameterizations to reproduce experimental data or to satisfy the mathematical properties of the true DFT functionals. A wide range of functionals is available, and their success in reproducing relevant properties depends on the specific molecular system.

DFT was extensively used in this work, mostly to optimize molecular geometries or to obtain KS orbitals with some correlation embedded to speed up CASSCF calculations. Moreover, techniques are available that are variants of DFT. Here, Constrained DFT (cDFT), Multi-Configuration Pair-Density Functional Theory (MC-PDFT), and RAS-short range DFT (RAS-sr-DFT) will be briefly addressed.

cDFT is a conceptually simple technique where specific constraints are introduced by means of Lagrange multipliers, such that the functional of the density behaves as desired. If, for example, we want to constrain N' electrons in a volume Ω inside a molecular system, we can add a Lagrange multiplier V to the energy functional so that the equation becomes:

$$E[n]_{N'|\Omega} = \max_{V} \left[E[n] + V\left(\int_{\Omega} d\boldsymbol{r} n(\boldsymbol{r}) - N' \right) \right]$$

Other constraints can be implemented on the spin state, on the charges on molecular fragments, on magnetic properties, etc. [76].

A follow-up to this approach consists of calculating related DFT ground states, for example, by constraining electrons on different parts of the molecule to obtain a totally neutral and a zwitterionic ground state, and diabatizing the unconstrained DFT ground state on the chosen basis to obtain an effective Hamiltonian with diabatic interactions between the constrained diabatic states. This approach is called cDFT configuration interaction (cDFT-CI) [77].

MC-PDFT [61] belongs to a family of techniques devoted to the application of DFT to multiconfiguration wavefunctions. There are situations where correcting a MC post-HF wavefunction with DFT could help to regain some correlation energy at a computational cost much lower than PT2. MC-PDFT is conceptually simple and avoids by construction some problems that can arise when applying DFT to MC wavefunctions, such as the double counting of electron correlation. The key quantity used in PDFT is not only the electron density but also the on-top pair density Π, defined as:

$$\Pi(\boldsymbol{r}) = \binom{N}{2} \sum_{\sigma} \sum_{\sigma_2} \int d\boldsymbol{r_3} \sum_{\sigma_3} \cdots d\boldsymbol{r_N} \sum_{\sigma_N} |\Psi(\boldsymbol{r}\sigma\boldsymbol{r_2}\sigma_2 \ldots \boldsymbol{r_N}\sigma_N)|_{\boldsymbol{r}=\boldsymbol{r}_2} \tag{2.29}$$

Essentially, Π is the diagonal part of the two-electron density. The energy of a multiconfigurational state Ψ is modified so that another term, which is a functional of both the density and the on-top electron density, is added, and at the same time, the electron-electron correlation is not

double counted by both the wavefunction energy and the DFT energy:

$$E_\Psi = \langle\Psi|\,\hat{T} + \hat{V}_{ne}\,|\Psi\rangle + V_C[n(\boldsymbol{r})] + E_{ot}[\rho, \Pi]$$

where V_C is the Coulomb energy and E_{ot} is the on-top electronic density functional. Again, this functional is unknown. As a first approximation, a standard DFT exchange-correlation functional is adopted. Because it is transformed such that it acquires an explicit dependence on the on-top pair density, that functional is usually labeled as *translated* (with a 't' as prefix). To summarize the procedure, a standard DFT exchange-correlation functional depends only on the total electron density $n(\boldsymbol{r})$, the magnetization $m(\boldsymbol{r}) = n_\uparrow(\boldsymbol{r}) - n_\downarrow(\boldsymbol{r})$, and the absolute value of their gradients $n'(\boldsymbol{r}) = |\nabla n(\boldsymbol{r})|, m'(\boldsymbol{r}) = |\nabla m(\boldsymbol{r})|$. For a single-determinant wavefunction, the following relation holds:

$$m(\boldsymbol{r}) = n(\boldsymbol{r})\sqrt{1 - R(\boldsymbol{r})}$$

with $R = \frac{4\Pi(\boldsymbol{r})}{n(\boldsymbol{r})}$. R must be strictly lower than 1, a requirement not ensured for a multiconfigurational wavefunction. A minor adaptation must be done, and so the translated E_{ot} functional starting from the DFT exchange-correlation functional E_{xc} is defined as:

$$E_{\mathrm{ot}}[n(\mathbf{r}), \Pi(\mathbf{r})] = E_{\mathrm{xc}}\left(n(\mathbf{r}), \begin{cases} n(\mathbf{r})(1-R)^{1/2}, & \text{if } R \le 1 \\ 0, & \text{if } R > 1 \end{cases}, n'(\mathbf{r}), \begin{cases} n'(\mathbf{r})(1-R)^{1/2}, & \text{if } R \le 1 \\ 0, & \text{if } R > 1 \end{cases}\right)$$

By performing this mathematical manipulation, we can recover most of the correlation using DFT, which is cheaper than PT2 techniques.

Finally, RAS-sr-DFT adopts a strategy analogous to MC-PDFT. A parameter μ is introduced to define the length scale at which RAS and DFT contribute most effectively. The idea is that the short-range part of the electron–electron interaction is handled entirely by the DFT component, while the long-range part is described by the RAS method. In practice, the expression for the energy becomes:

$$E^{RAS-srDFT} = \min_{\Psi^\mu} \left\{ \langle\Psi^\mu|\,\hat{T} + \hat{V}_{ne} + \hat{V}_{ee}^{lr,\mu}\,|\Psi^\mu\rangle + E_H^{sr,\mu}[\rho] + E_{xc}^{lr,\mu}[\rho] \right\}$$

The μ-dependence is chosen so that for $\mu = 0$ the energy converges to the DFT energy, while in the limit $\mu \to \infty$ the energy corresponds to the RASCI theory. The transition between the two limits is smooth. Note that, because of the dependence on the electron density, the energy is state-specific. To efficiently implement the method, a state-averaged generalization was derived [78].

Up to now only ground state properties have been addressed; to address excited states, Time-Dependent Density Functional Theory (TD-DFT) was developed [79–81]. TD-DFT relies on the Runge-Gross theorem [82] which, in analogy with the Hohenberg-Kohn theorem, ensures the existence of a one-to-one mapping between the time-dependent ground-state electron density $n_0(\boldsymbol{r}, t)$ and the external potential in which an

N-interacting electron system evolves in time, or:

$$\begin{aligned} n_0(\boldsymbol{r},t) &= n_0[v](\boldsymbol{r},t) \\ v(\boldsymbol{r},t) &= v[n_0](\boldsymbol{r},t) \end{aligned} \tag{2.30}$$

The Runge-Gross theorem does not provide a mapping between an interacting and a non-interacting N-electron system as in the Kohn-Sham cases. The mapping relies on the Van Leeuwen theorem [83], which proves that given an N-electron interacting system with electron density $n(\boldsymbol{r},t)$, it is possible to define a non-interacting system s with electron density $n_s(\boldsymbol{r},t) = n(\boldsymbol{r},t)$ so that:

$$n_s(\boldsymbol{r},t) = \sum_j \left|\psi_j(\boldsymbol{r},t)\right|^2 \tag{2.31}$$

where $\psi_j(\boldsymbol{r},t)$ are the single-particle spin orbitals, solutions of the time-dependent Kohn-Sham equation:

$$i\frac{\partial \psi_j}{\partial t}(\boldsymbol{r},t) = \left(-\frac{\nabla^2}{2} + v_{ext}(\boldsymbol{r},t) + v_H[n](\boldsymbol{r},t) + v_{xc}[n](\boldsymbol{r},t)\right)\psi_j(\boldsymbol{r},t) \tag{2.32}$$

where $v_{ext}(\boldsymbol{r},t)$, $v_H[n](\boldsymbol{r},t) = \int d^3r' \frac{n(\boldsymbol{r}',t)}{|\boldsymbol{r}-\boldsymbol{r}'|}$, and $v_{xc} = \frac{\delta A_{xc}[n]}{\delta n(\boldsymbol{r},t)}$ are the time-dependent external, Hartree, and exchange-correlation potentials, in analogy with the static DFT case. The $A_{xc}[n]$ term is the unknown exchange-correlation action functional, often referred to as the *xc kernel*, and must be approximated. One of the most common TD-DFT approaches is the *Adiabatic Local Density Approximation* (ALDA), based on the assumption that the density varies slowly with time, so that the same exchange-correlation functionals can be used as in time-independent DFT. In Equation 2.32, only the external potential terms explicitly depend on time, while the xc kernel is treated as static in the ALDA approximation, and the Hartree term depends on the time-dependent electron density (and thus depends on time only in an implicit way). The Hamiltonian can be seen as a static term plus a time-dependent perturbative term. If the perturbation is weak, it is possible to apply standard linear response theory. Suppose that the perturbation Hamiltonian $\hat{V}(t)$ can be written as an external scalar potential coupled to the electron density switched on at time t_0:

$$\hat{V}(t) = \int d\boldsymbol{r} v_{ext}(\boldsymbol{r},t) n_0(\boldsymbol{r}) \tag{2.33}$$

The linear response of the density is given by:

$$n_1(\boldsymbol{r},t) = \int_{-\infty}^{\infty} dt' \int d\boldsymbol{r}' \chi_{nn}(\boldsymbol{r},\boldsymbol{r}') v_{ext}(\boldsymbol{r}',t') \tag{2.34}$$

where $\chi_{nn}(\boldsymbol{r},\boldsymbol{r}',t)$ is the density-density response function that does not depend on the external potential. By defining its Fourier Transform and after some algebra [81], it is possible to obtain the excitation energies and transition densities as eigenvalues and eigenvectors of the following equation, first derived by Casida [84]:

$$\begin{bmatrix} \boldsymbol{A} & \boldsymbol{B} \\ \boldsymbol{B}^\dagger & \boldsymbol{A} \end{bmatrix} \begin{bmatrix} \boldsymbol{X} \\ \boldsymbol{Y} \end{bmatrix} = \omega \begin{bmatrix} \boldsymbol{1} & 0 \\ 0 & -\boldsymbol{1} \end{bmatrix} \begin{bmatrix} \boldsymbol{X} \\ \boldsymbol{Y} \end{bmatrix} \tag{2.35}$$

with:

$$\begin{aligned} A_{ia,bj} &= \delta_{ij}\delta_{ab}(\epsilon_a - \epsilon_i) + (ia|jb) + (ia|f_{xc}|jb) \\ B_{ia,bj} &= (ia|bj) + (ia|f_{xc}|bj) \end{aligned} \tag{2.36}$$

and where the indices i, j refer to occupied KS spin-orbitals, and a, b refer to KS virtual orbitals. The first term $\boldsymbol{A}$ is the energy difference of orbitals a and i, the second and the first terms of $\boldsymbol{A}$ and $\boldsymbol{B}$ are the two-electron integrals deriving from the Coulomb and the exchange operator, and the last term of both equations corresponds to the linear response of the xc potential to the perturbation. To simplify Equation 2.35, the Tamm-Dancoff approximation (TDA) is introduced, which neglects the $\boldsymbol{B}$ matrix, leading to the Hermitian eigenvalue equation:

$$\boldsymbol{AX} = \Omega \boldsymbol{X} \tag{2.37}$$

analogous to the Configuration Interaction Singles (CIS) method in the Hartree-Fock approach. Equation 2.37 is also called the TDA-Casida equation [84], and the vector Ω is the vector of the CIS excitation energies from the Ground-State wavefunction $\Psi_0(\boldsymbol{r}_1, ..., \boldsymbol{r}_N)$ to each CIS excited Kohn-Sham state $\Psi_{E_i}(\boldsymbol{r}_1, ..., \boldsymbol{r}_N)$.

2.3 Models

Despite the increasing popularity of ab initio approaches, research in QIS still relies on semi-empirical models. Models are simple, highly tunable, and allow for the simulation of physical phenomena still not encoded in computational software, especially when the focus is on the simulation of novel or exotic physics. Below, the two models adopted in this work will be shortly introduced: the Hubbard model (and the related Pariser–Parr–Pople (PPP) model) and the exciton model.

2.3.1 Hubbard and Pariser-Parr-Pople (PPP) models

The Hubbard model is widely adopted in the physics community to investigate strongly correlated electron systems[85]. In the original and simplest version, the Hubbard model only accounts for nearest neighbor electron hopping, t, and for the repulsion between two electrons residing on the same site, U. The model was extended to account for intersite electron-electron interactions V_{ij}, in the so-called extended Hubbard model[85]. Indeed, the extended Hubbard model is essentially the same as the PPP model developed (much earlier) in the chemistry community and carefully parametrized to simulate the properties of π-conjugated molecules and polymers[86–88].

In the Hubbard model, electrons can occupy site-orbitals, with each site-orbital representing an effective orbital residing on an atom, a portion of a molecule, or even a molecule. The overlap between orbitals residing on different sites is neglected, and only the repulsion between electrons residing on the same site is accounted for. The Hubbard Hamiltonian reads:

$$\hat{H}_{Hubbard} = \sum_{\mu} \varepsilon_{\mu} \hat{n}_{\mu} - \sum_{\mu\nu,\nu>\mu} \sum_{\sigma} t_{\mu\nu} \left(\hat{a}^{\dagger}_{\mu\sigma} \hat{a}_{\nu\sigma} + \hat{a}^{\dagger}_{\nu\sigma} \hat{a}_{\mu\sigma} \right) + \sum_{\mu} U_{\mu} \hat{n}_{\mu\alpha} \hat{n}_{\mu\beta}$$

where $\hat{a}_{\mu,\sigma}$ and $\hat{a}^{\dagger}_{\mu,\sigma}$ destroy and create, respectively, an electron with spin $\sigma = \alpha, \beta$ on site μ; $\hat{n}_{\mu} = \sum_{\sigma} \hat{a}^{\dagger}_{\mu\sigma} \hat{a}_{\mu\sigma}$ counts the total number of electrons on site μ; ε_{μ} is the on-site energy; $t_{\mu\nu}$ is the hopping integral between atomic sites μ and ν; and U_{μ} is the repulsion between two electrons on the same site. If all U_{μ} are set to 0, the Hubbard model reduces to the tight-binding (Hückel) model.

In the extended Hubbard model, repulsion between electrons on different sites is included, in the so-called zero differential overlap (ZDO) approximation. In this approximation, the bielectronic terms where mixed charge distribution appears are neglected, so that the Hamiltonian reads:

$$\hat{H}_{PPP} = \hat{H}_{Hubbard} + \sum_{\mu\nu,\nu>\mu} V_{\mu\nu} \left(Z_{\mu} - \hat{n}_{\mu} \right) \left(Z_{\nu} - \hat{n}_{\nu} \right) \tag{2.38}$$

$V_{\mu\nu}$ denotes the repulsion between electrons on different atoms, while Z_{μ} is the core charge on site μ. As stated above, the extended Hubbard model is equivalent to the PPP model, but the PPP has been parametrized for and successfully applied to π-conjugated molecules and polymers[87].

The Hubbard and PPP models describe correlated electrons, and their Hamiltonian can be diagonalized adopting the same techniques discussed

above. However, the dimension of the relevant basis is often small enough to allow for numerically exact solutions (Full-CI). In this case, rather than proceeding through the HF diagonalization followed by the CI expansion, it is convenient to work on the so-called real-space (RS) basis, which leads to very sparse matrices. The RS basis is constructed by locating relevant electrons in the site-orbitals. To easily account for the fermionic nature of the electrons, it is convenient to work in second quantization.

The real-space vectors are eigenvectors of the $\hat{S}_z = \sum_\nu (\hat{n}_{\nu\uparrow} - \hat{n}_{\nu\downarrow})$ operator, but not of $\hat{S}^2$. For spin-independent Hamiltonians, it is then convenient to work in the subspaces with fixed $\langle \hat{S}_z \rangle$. States with different $\langle \hat{S}^2 \rangle$ can be identified by searching for degeneracies among wavefunctions in different spin subspaces. For example, doublet states can be identified by diagonalizing the PPP Hamiltonian in both $S_z = 0.5$ and $S_z = 1.5$ subspaces, then looking for states that do not have a counterpart in the $S_z = 0.5$ subspace. Conversely, quartet states correspond to eigenstates that are present in both spin subspaces. This procedure grants a reduction of the computational cost compared with the diagonalization of the full RS basis. As N grows, the size of the RS basis expands exponentially, leading to Hamiltonian matrices that are very large yet sparse. The sparse nature of the matrices in the RS basis allows for "full-CI" diagonalization in cases where the dense matrices obtained in the HF-CI approach would be prohibitive. Specifically, when the Hamiltonian becomes too large to be fully diagonalized, the first few eigenstates and eigenvalues are obtained using the implicitly restarted Lanczos algorithm as implemented in the ARPACK package [89].

To facilitate a direct comparison with current quantum chemical techniques, when needed, we will solve the PPP Hamiltonian in the HF approach. Specifically, in the Hartree-Fock (HF) approximation, the PPP Hamiltonian in Eq. 2.38 reduces to the one-electron Fock operator:

$$\hat{\mathcal{F}}_{PPP} = \sum_\mu \left(\varepsilon_\mu + J_{\mu\mu} - K_{\mu\mu}\right) \hat{n}_\mu + \sum_{\mu\nu, \mu\neq\nu} (-t_{\mu\nu} - K_{\mu\nu}) \sum_\sigma \left(\hat{a}^\dagger_{\mu\sigma}\hat{a}_{\nu\sigma} + \hat{a}^\dagger_{\nu\sigma}\hat{a}_{\mu\sigma}\right) \tag{2.39}$$

The ZDO approximation leads to a diagonal form of the Coulomb operator:

$$J_{\mu\mu} = \sum_{\lambda=1}^{N} (P_{\lambda\lambda} - Z_\lambda) V_{\lambda\mu} \tag{2.40}$$

while the exchange operator reads:

$$K_{\mu\nu} = \left(P_{\mu\nu}/2 - Z_\nu \delta_{\mu\nu}\right) V_{\mu\nu} \tag{2.41}$$

In Eqs.2.40 and 2.41 the density matrix elements are defined as:

$$P_{\mu\nu} = \sum_{k=1}^{occ} n_k c_{k\mu} c_{k\nu} \tag{2.42}$$

where k runs over the doubly occupied MOs in the ground state configuration, $c_{k\mu}$ are the expansion coefficients of the k-th MO on the AOs, and n_k is the occupation of the orbital; thus, $n_k = 2$ for doubly occupied MOs and $n_k = 1$ for SOMOs. The Fock operator above is addressed self-consistently through the variational principle.

2.3.2 Exciton Model

The exciton model is widely adopted to study molecular aggregates and crystals [90–92]. An exciton is an excitation with a collective nature, which can be described as a delocalized bound state of an interacting electron and hole pair. Among the different types of excitons, the so-called Frenkel excitons are relevant to molecular materials. In these systems, the distance between the electron and the hole is not larger than the dimension of the molecule (or more generally, the site). A Frenkel exciton can be seen as a molecular excited state, i.e., a strongly bound intramolecular electron-hole pair that is, however, delocalized over different molecular units. Models based on Frenkel excitons are widely employed in physics and chemistry to understand the optical properties of solids and aggregates [92–94], but also in the field of quantum computers made by trapped ions or Rydberg atoms [21], as the relevant physics can also be described using a similar Hamiltonian.

In the exciton model, electrons are localized on each molecular unit, and intermolecular charge-transfer interactions are not accounted for, the only intermolecular interactions being represented by electrostatic terms. The ground state of the system is described as the product of the ground states of the different basic units (chromophores). Excited states are obtained by exciting one (or more) chromophores in the aggregate. The Heitler-London approximation [95, 96] applies when the energy required to excite a chromophore is larger than the interchromophore interaction energy, so that the interactions among states bearing a different number of excitations can be neglected. In this approximation, the problem can be diagonalized in different subspaces, each relevant to a fixed number of excitons. We are typically interested in states bearing a single exciton state, as they are the only ones relevant to (linear) optical spectroscopy.

With these approximations, the relevant states can be described by adopting a basis of states where a single excitation is located on different molecular sites. Considering a one-dimensional array of identical molecules, the exciton Hamiltonian is:

$$\hat{H}_{exc} = \sum_i E\hat{c}_i^\dagger \hat{c}_i + \frac{1}{2}\sum_{i\neq j} J_{ij}(c_i^\dagger \hat{c}_j + c_j^\dagger \hat{c}_i) \tag{2.43}$$

where E is the energy of the excited state and J_{ij} are the excitonic coupling interactions between different sites that measure the electrostatic interaction between the transition dipole moments located on molecules i and j.

If we take the simplest possible system as reference, a monodimensional chain of equivalent sites with nearest neighbor interaction $J_{ij} = J\delta_{i,j\pm1}$, periodic boundary conditions, and N sites, we can diagonalize the Hamiltonian analytically, obtaining as eigenvalues and eigenvectors:

$$E_k = E + 2Jcos(kr)$$
$$|k\rangle = \frac{1}{\sqrt{N}}\sum_j e^{ikrj}\left|j\right\rangle$$

where $k = \pm\frac{n\pi}{2Nr}$ is the wavevector with $n = 0, 1, 2..., N$, r is the intersite distance, and $\left|j\right\rangle$ is the state with an excited molecule on site j, so that

$|j\rangle = \hat{c}_j^\dagger |\rangle$. If the interactions are attractive ($J < 0$), the band has a minimum at $k = 0$, in the center of the Brillouin zone, while it has a minimum at $k = \pi r$ if the interaction between states is repulsive ($J > 0$). The dispersion of the band depends on the magnitude of J and not on its sign. The position of the minimum impacts the photophysics of the aggregate, since both emission and absorption take place from the center of the Brillouin zone. Emission is constrained by the Kasha rule [95] to occur at the minimum of the excited state band. This creates two different types of aggregates: J-aggregates, with $J < 0$, where both the absorption and emission spectra are redshifted with respect to the monomer and emission is bright; and H-aggregates, with $J > 0$, which instead have a blue-shifted absorption and a strongly suppressed emission. Indeed, a weak fluorescence can be seen in H-aggregates as a result of vibronic coupling. This residual fluorescence is, however, very weak and is located much to the red with respect to absorption, so that very large Stokes shifts are observed. A schematic view of these properties is depicted in Figure 2.2.

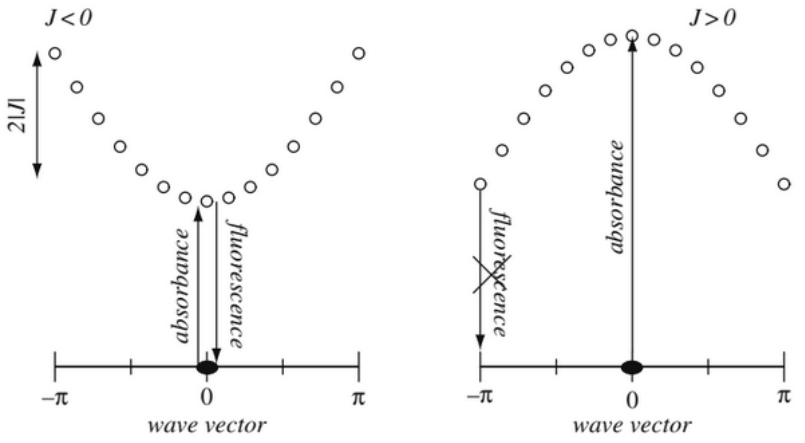

Figure 2.2: The excitonic band in two different monodimensional molecular crystals, characterized by 15 total molecules, a nearest neighbor J interaction, periodic boundary conditions, and intermolecular spacing r [97]. On the left, a J-aggregate is shown, with both the absorption and the emission optically allowed. On the right, an H-aggregate is shown, with the absorption allowed and the emission optically forbidden.

Before closing, we mention that a very similar model is extensively applied to describe Rydberg atom qubits [21, 22].

Appendix

2.A Creation of the reference Hamiltonian by projection

In PT calculations, wave functions are typically not eigenfunctions of the reference Hamiltonian $\hat{H}_0$. Just as an example, in CASPT2 the generalized Fock operator is not diagonal in the CAS space. Moreover, typically the complementary space needed to apply perturbative correction to the reference space is not known. To solve these issues, a projection operator approach is developed. The identity can be expressed as a sum of projection operators:

$$\mathbf{1} = |\Psi\rangle\langle\Psi| + \hat{P}_K + \hat{P}_{SD} + \hat{P}_{TQ}... \tag{2.A.1}$$

with $|\Psi\rangle$ the reference state to be corrected, and the various $\hat{P}_X = \sum_{i\in X} |\Psi_i\rangle\langle\Psi_i|$ projectors on the space X. We consider all states orthonormal in their space. In this notation, K projects on all the other wavefunctions of the CAS space not considered in the reference space, SD is the space of single and double replacements obtained by $\hat{E}_{pq}\hat{E}_{rs}|\Psi\rangle$. The reference Hamiltonian $\hat{H}_0$ generated from the Hamiltonian $\hat{H}$ is created as:

$$\hat{H}_0 = |\Psi\rangle\langle\Psi|\hat{H}|\Psi\rangle\langle\Psi| + \hat{P}_K\hat{H}\hat{P}_K + \hat{P}_{SD}\hat{H}\hat{P}_{SD} + ...$$

In this way, the reference Hamiltonian is block-diagonal. In the process, it is possible that the produced states that span the auxiliary spaces are not orthogonal, nor linearly independent (in the case of the SD subspace, for example); it is then necessary to orthonormalize and eliminate redundant states in each space independently. While the procedure is feasible for $\hat{P}_K$, even the SD space is too big to be stored explicitly. So, the equations are solved iteratively, with all elements generated on the fly [98].

2.B NEVPT2: mathematical details

The states that span the first interaction space of the reference state are obtained by operating with the excitation operators on the reference state:

$$\hat{E}_{ab}\hat{E}_{cd}|\Psi\rangle$$

The resulting CSF states can be distributed in 8 different subspaces. They are labeled by counting the number of electrons that are added/removed from the active space with the letter k (so that $k > 0$ means that electrons are excited from the space of occupied orbitals to the AS, and $k < 0$ indicates that electrons are removed from the AS and excited to the space of virtual orbitals). To discriminate the space in which the electrons move:

- i, j indicate inactive orbitals;
- a, b indicate virtual orbitals;
- t, u, v indicate active orbital

The eight spaces are:

$$\text{internal} \begin{cases} V_A, & k = 1 : \hat{E}_{ti}\hat{E}_{uv} \\ V_B, & k = 2 : \hat{E}_{ti}\hat{E}_{uj} \end{cases}$$

$$\text{semi-internal} \begin{cases} V_C, & k = -1 : \hat{E}_{at}\hat{E}_{uv} \\ V_D, & k = 0 : \hat{E}_{ai}\hat{E}_{tu}, \hat{E}_{ti}\hat{E}_{au} \\ V_E, & k = 1 : \hat{E}_{ti}\hat{E}_{aj} \end{cases}$$

$$\text{external} \begin{cases} V_F, & k = -2 : \hat{E}_{at}\hat{E}_{bu} \\ V_G, & k = -1 : \hat{E}_{ai}\hat{E}_{bt} \\ V_H, & k = 0 : \hat{E}_{ai}\hat{E}_{bj}, \end{cases}$$

Internal, semi-internal, and external simply indicate that the number of virtual orbitals implied in the excitation is 0, 1, or 2. For example, consider the space V_A. It collects all the states created by exciting one electron from the inactive space to the AS ($\hat{E}_{ti}$) and an electron from a different MO in the AS ($\hat{E}_{uv}$). The space V_E, despite having the same k label, indicates the very different situation in which two electrons are excited from the inactive space, one to the AS ($\hat{E}_{ti}$) and the other to the virtual orbital space ($\hat{E}_{aj}$). These spaces are generally used both in CASPT2 and in NEVPT2, although the huge advantage in using these spaces is gained when one employs contracted-NEVPT2 methods.

The functions generated by each of these operators span a different subspace. However, neither the Dyall nor the total Hamiltonian are block-diagonal in these subspaces. In particular, each reference CSF can be written as the antisymmetrized product between the c inactive orbitals and the v active orbitals:

$$|\Psi\rangle = |\Phi_c \Psi^v\rangle$$

And the application of an excitation operator causes the perturbers to have the form $\left|\Phi_{c-k}\Psi_\mu^{v+k}\right\rangle$. This CSF can be written as a linear combination of all the CSFs with the same core electron part and all the possible distributions of the $v + k$ electrons in the CASCI space. The CSFs so built are required not to interact via $\hat{H}_{Dyall}$, and so in the UNEVPT2 it is necessary to orthogonalize them via the set of linear equations:

$$\sum_{\Psi_J^{+k}} \left\langle \Phi_I^{-k}\Psi_I^{+k}\right| \hat{H}^D \left|\Phi_I^{-k}\Psi_J^{+k}\right\rangle C_j + \left\langle \Phi_I^{-k}\Psi_I^{+k}\right| \hat{V} \left|\Psi\right\rangle = E_\Psi C_I$$

While a smaller space than the CASPT2, the number of equations that need to be solved is huge, and the Dyall Hamiltonian is considerably more expensive to calculate than the generalized Fock operator. For this reason, PC-NEVPT2 and SC-NEVPT2 were developed.

Typically, the density matrix elements required to calculate the Dyall Hamiltonian (we are referring to the $\langle\Psi|\,\hat{E}_{ab}\hat{E}_{cd}\ldots|\Psi'\rangle$ terms) are not calculated exactly but approximated up to some order, usually using cumulant expansion [99, 100]. While this approach is generally employed any time the explicit electron-electron correlation is calculated, it causes the CAS wavefunction to not be an eigenvector of the Dyall Hamiltonian anymore. In rare cases, this causes the results to suffer from the *false*

intruder state problem, where a reference state is overstabilized by a perturbative correction that diverges due to quasi-degenerate energies calculated by error. If NEVPT2 results present such a problem, an analysis of all the approximations in play must be done.

Radicals 3

In this chapter, several molecules with possible applications in Quantum Information Science (QIS) are presented. The electronic structure of the molecules of interest was investigated by applying a combination of semi-empirical models, for which we developed in-house codes, and ab initio approaches, exploiting commercial software. In the first part of the chapter, organic radicals based on triangulene organic molecules are presented. In the second part, we design diradical organic molecules using an Inverted Singlet-Triplet (INVEST) energy gap organic molecule as a bridge. In the final part, a discussion concerning a Charge-Transfer radical molecule is presented, and the possibility of exploiting such molecules in quantum gates on a nanometric scale is analyzed. *

3.1 Triangulene-based radicals

Triangulene molecules are small conjugated organic molecules consisting of a core of three condensed benzene rings sharing a central carbon atom (see Figure 1). Formed by an odd number of carbon atoms, these radicalic species are studied as possible emitters for application in organic light-emitting diodes (OLEDs). To date, OLEDs have mainly used closed-shell luminescent molecules, exploiting either fluorescence or phosphorescence[101]. In fluorescent OLEDs, electrogenerated excitons are statistically distributed in 25% singlets and 75% triplets and, since triplet are non-emissive, the maximum internal efficiency of fluorescent OLEDs is fairly poor. Phosphorescent OLEDs introduce heavy atoms (typically Pt or Ir) in the molecular structure, to allow for efficient intersystem crossing (ISC) and phosphorescence, bringing the theoretical maximum internal efficiency to 100%. [102, 103]. However phosphorescent OLEDs have a few limitations, related to the use of heavy metals and to the lack of blue phosphorescent emitters. Another strategy involves emitters that exhibit thermally activated delayed fluorescence (TADF) [38, 101, 104–110], as well as a combination of TADF and fluorescent systems used in hyperfluorescence OLEDs [111–123].

* This Chapter summarizes results obtained in different experiments. Dubbini, M.; Bonvini, F.; Savi, L.; Di Maiolo, F. Turning on Organic Radical Emitters. *J. Phys. Chem. C* **2024**, *128* (43), 18158–18169. I performed all ab-initio calculations in support of the model, and so only those mentioned here are reported with the minimum context to understand the reason of the work. Savi, L.; Barreca, M. T.; Bedogni, M.; Di Maiolo, F. Organic Diradicals Bridged by Inverted Singlet–Triplet Units for Optical–Spin Interfaces. *J. Chem. Theory Comput.* **2025** DOI:10.1021/acs.jctc.5c01571. I executed some of the ab-initio calculations and contributed to introduce SOC in the PPP model. The last part of the Chapter consists of a preliminary study on a molecule I carried on under the supervision of Prof. Yoann Olivier, Dr. Gaetano Ricci, and Dr. Danillo Valverde. The work is still ongoing and unpublished.

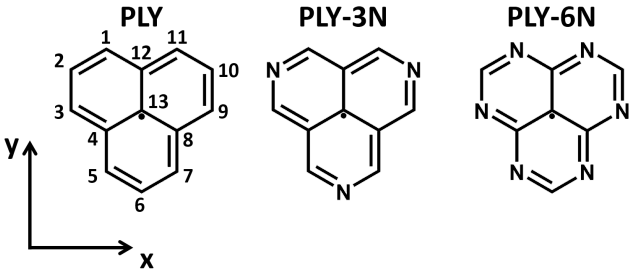

Figure 1: Molecular structures of three prototypical triangular organic radicals, namely phenalenyl (PLY), triazaphenalenyl (PLY-3N), and hexaazaphenalenyl (PLY-6N).

More recently, organic radicals were proposed as innovative emitters for OLED applications [124–133]. Organic radicals, characterized by an open-shell nature with one unpaired electron, open the door to a new mechanism for light emission in OLEDs. Notably, organic radicals bypass the issue of non-emissive triplet states, emitting light through transitions from a low-energy spin-doublet excited state to a doublet ground state. This spin-allowed process potentially results in higher quantum efficiencies, since all recombination processes can contribute to light emission without substantial non-radiative losses. Furthermore, as magnetically active molecules, they can be explored as organic quantum qubits and, in this respect, diradicals are also very important.

The strong electron correlation in organic radicals makes the calculation of their excited state properties complex,and quantum chemistry approaches that can effectively handle the multiconfigurational nature of these electronic states are needed. Among them, we mention the multiconfigurational self-consistent field (MCSCF) [134], complete active space self-consistent field (CASSCF) [127, 135, 136] together with second-order perturbation theory (either CASPT2 [137] or NEVPT2 [133]), state-specific multireference perturbation theory (SSMRPT) [138], configuration interaction singles and doubles (CISD) [134], coupled cluster [139, 140], spin-flip restricted active space configuration interaction (SF-RASCI) [141–151], and complete active space configuration interaction density functional theory (CASCI-DFT) [152]. However, these computationally expensive methods can only be applied to fairly small molecular systems. Conventional ground-state DFT and excited-state time-dependent DFT (TDDFT) methods therefore remain attractive for studying organic radicals [124–130, 132, 153–159]. Due to possible spin-contamination issues in the unrestricted version of TDDFT for open-shell molecules, spin-adapted TDDFT (X-TDDFT) is typically employed. Spin-polarized DFT calculations that incorporate many-body perturbative corrections at the G_0W_0 level have also been proposed [160].

We adopt an alternative approach relying on a comprehensive study of various phenalenyl radicals using the Pariser-Parr-Pople (PPP) model Hamiltonian to account for electron correlation in π-conjugated molecules. Developed in the 1950s [86, 161, 162], this model has proven successful in describing the properties of the ground and excited states of various small organic molecules [87, 88, 161, 163–170]. The PPP model has recently been exploited to address singlet-triplet (ST) inversion in some OLED emitters [116, 118, 171], and doublet emission in planar and non-planar organic radicals [172, 173]. Although the PPP model was originally designed for π-conjugated hydrocarbons, it can be adapted to accommodate non-planar systems by incorporating additional terms that account for deviations

from planarity [170, 173–177]. Moreover, the model can be extended to systems containing heteroatoms by adjusting the relevant parameters [116, 178–182]. These adaptations significantly broaden the applicability of the PPP model [124–133].

An important symmetry inherent to the PPP model, but only approximately followed by more advanced (all-electron) Hamiltonians, is the so-called particle-hole (ph) or alternancy symmetry. Alternant hydrocarbons provide a real molecular framework in which this symmetry is closely approximated [172, 183–195]. In these systems, carbon atoms can be divided into two distinct sets that contain every other carbon atom, ensuring that no two carbons belonging to the same set share a covalent bond. Rings composed of an even number of atoms satisfy this condition, while rings with an odd number of atoms do not. The PPP particle-hole symmetry in alternant hydrocarbons is reflected in the unique arrangement of the orbital energy levels and the specific structure of the MOs. In alternant systems, MOs come in pairs with equal and opposite energies. If the alternant system has an even number of atoms, the negative energy levels are fully occupied in the ground state, while the positive levels remain empty; thus, bonding and antibonding MOs appear as occupied-virtual pairs. Alternant hydrocarbons with an odd number of atoms have an additional feature, namely a singly occupied non-bonding orbital at zero energy. The particle-hole symmetry holds only in the absence of heteroatoms.

In this section, we validate the use of the PPP model to investigate particle-hole symmetry breaking and its effect on doublet emission in several phenalenyl radicals variously decorated with nitrogen atoms. The PPP results are compared against results from state-of-the-art CASSCF results.

PPP does not provide quantitatively accurate results for individual molecules [118, 196], but is serves as a robust and simple method that, when applied to various molecular structures, reveals qualitative trends regarding the effects of electron correlation in π-conjugated molecules. The new insights obtained from this approach will help to establish general and reliable guidelines for the rational design of novel organic radicals with potentially emissive doublet states.

3.1.1 Methods

The PPP model is used, employing the Hamiltonian in Eq. 2.38 of Chapter 2. We investigate the first few excited states. The real-space basis states are eigenstates of the z-component of the total spin operator $\hat{S}_z$. Accordingly, doublet states can be identified by diagonalizing the PPP Hamiltonian in the $S_z = 0.5$ and $S_z = 1.5$ subspaces, searching for states that appear exclusively in the $S_z = 0.5$ subspace. Conversely, quartet states correspond to eigenstates present in both spin subspaces. As N grows, the size of the real space basis expands exponentially, reaching 2,944,656 states in the $S_z = 0.5$ subspace for the phenalenyl radicals in Figure 1, leading to very large but sparse Hamiltonian matrices. The first few eigenstates and eigenvalues are derived using the implicitly restarted Lanczos algorithm as implemented in the ARPACK package [89]. The diagonalization yields full-CI results.

To address optical spectra, an explicit expression of the electric dipole moment operator is needed. For planar molecules it reads:

$$\hat{\vec{\mu}} = \hat{\mu}_x \vec{i} + \hat{\mu}_y \vec{j} = \sum_{\mu} (Z_\mu - \hat{n}_\mu)(x_\mu \vec{i} + y_\mu \vec{j}) \tag{1}$$

where x_μ, y_μ are the Cartesian coordinates of site μ.

Transition energies and transition dipole moments enter the oscillator strength of the $|f\rangle \leftarrow |g\rangle$ transition:[197]

$$f_{fg} = \frac{2}{3} \frac{m_e}{\hbar e^2} \omega_{fg} |\mu_{fg}|^2 \tag{2}$$

where m_e is the electron mass and e the electron charge. Results presented in this study were obtained using an in-house PPP code in Fortran. This code extends the capabilities of the version introduced in Ref.[116] to handle open-shell systems.

3.1.2 Results & Discussion

We begin by focusing on the three phenalenyl radicals depicted in Figure 1. Phenalenyl (PLY), an odd-alternant hydrocarbon with D_{3h} symmetry, has been extensively studied in its ground state using magnetic resonance techniques [198–202]. In contrast, optical spectroscopy data are scarce. In Refs. [203, 204], a weak absorption maximum at ~2 eV is reported for PLY in a MeTHF-ethanol mixture (7:1 v/v). Azaphenalenyls must be stabilized by bulky groups [205–209], and experimental data are even scarcer. In Ref. [207], an absorption peak slightly below 2 eV is reported for the perchloro-2,5,8-triazaphenalenyl radical.

PPP parameters for carbon atoms are well-defined and transferable across various π-conjugated molecules [161, 164, 167, 210, 211]. Specifically, we set the carbon on-site energy to zero, use a standard on-site electron-electron interaction value of $U_C = 11.26$ eV, and a nearest-neighbor C-C hopping value of $t = -2.4$ eV. The situation is different for nitrogen atoms, as there is no universally accepted set of PPP parameters for them [163–167, 210, 212–218]. In this section, unless otherwise stated , we use the aza nitrogen PPP parameters identified by Bedogni et al. [116] for 2T triangulenes, setting the on-site electron-electron repulsion to $U_N = 15.5$ eV and the site energy ε_N to -5 eV. The hopping integrals for C-N bonds were set equal as for C-C bonds, a choice that has minimal impact on the results [219]. For molecular geometry, we set all bond angles to 120° and all bond lengths to 1.4 Å. Results obtained using DFT-optimized geometries show marginal differences. The onsite charges were set to one for either carbon or aza nitrogen atoms. The intersite potential is defined following Ohno [164, 167, 220]:

$$V_{\mu\nu} = \frac{e^2}{4\pi\varepsilon_0} \Bigg/ \sqrt{r_{\mu\nu}^2 + \left(\frac{\varepsilon_r e^2}{4\pi\varepsilon_0 (U_\mu + U_\nu)} \right)^2} \tag{3}$$

where the relative dielectric constant ε_r is set to 2, a typical value for organic media.[167].

As discussed above, PPP allows for full-CI calculations in not too large molecules and is therefore particularly well-suited to examine the accuracy of traditional post-HF approaches to correlated molecular systems. Towards this aim, we undertook post-HF analysis of the radicals. When extending pure spin excited state theories from closed-shell systems to radicals, the definition of excitation levels needs to be re-evaluated. Specifically, besides single excitations, double excitations must be included, which involve the simultaneous promotion of an α electron from the SOMO to virtual MOs and the promotion of a β electron from occupied MOs to the SOMO [221]. This leads to the spin-pure extended CIS (XCIS) theory for the excited states of radicals [173, 221]. The extension to higher order excitations leads to XCISD, XCISDT, etc. In the following, we will always use the extended version of the corresponding CIs to preserve spin purity. After several scans on model parameters and convergence studies, we decided to adopt the PPP-XCISDT calculation, as the inclusion of triplet excitations accounts for most of the correlation energy, as already found for 2T triangulenes [116]. Results are shown in Figure 2. The transition energies shown in Figure 2a, b, and c demonstrate

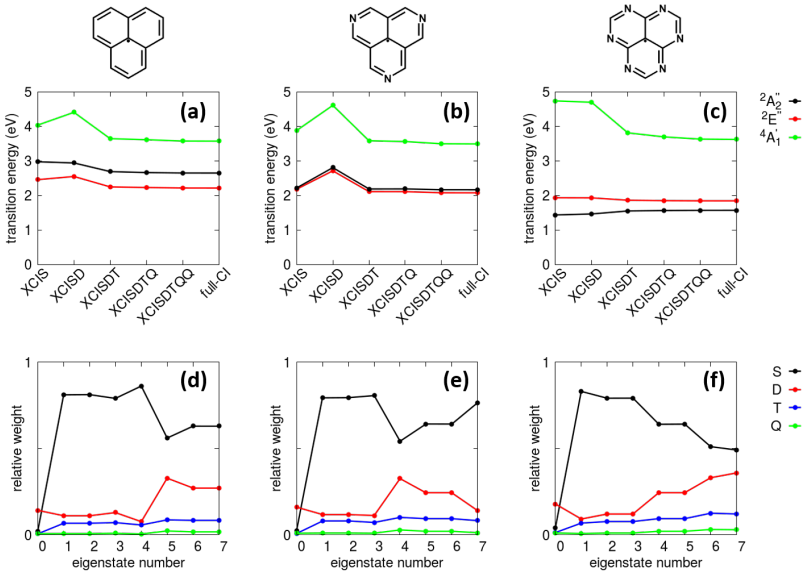

Figure 2: Excitation energies of the first few electronic states of PLY (panel a), PLY-3N (panel b), and PLY-6N (panel c) at various theoretical levels, together with the relative contributions of singly (S), doubly (D), triply (T), and quadruply (Q) excited configurations for the first eight doublet and quadruplet eigenstates of PLY (panel d), PLY-3N (panel e), and PLY-6N (panel f) calculated at the PPP-XCISDT level. Model parameters are specified in the main text.

that truncating the expansion at the XCISD level stabilizes the ground state, but the stabilization of the excited states due to triple excitations is lacking. Consequently, XCISD overestimates transition energies, an error that is corrected when triply excited configurations are included [116].

Panels d, e, and f reveal the relative contributions of single (S), double (D), triple (T), and quadruple (Q) excitations in the lowest eight eigenstates of PLY, PLY-3N, and PLY-6N. Singly and triply excited configurations have a negligible impact on the ground state of the three molecules. In line with the Brillouin's theorem, single and triple CIs do not directly mix with the ground state configuration, and their contribution is limited to indirect interactions with doubly excited configurations. In the first few excited states, the three molecules show double and triple excitations contributing similarly, around 10%. This finding aligns with our results for 2T triangulenes in Ref. [116] and indicates that a reliable approach to the excited states of these molecules should include not only doubly, but also triply excited configurations.

To validate the model, ab initio SA-CASSCF calculations are performed on PLY, PLY-3N, and PLY-6N, using two sets of molecular geometries. The first set adopts the idealized geometry, with all angles fixed at 120° and all bond lengths set to 1.4 Å, while the second set adopts the DFT-optimized geometries (B3LYP/def2-SVP). Results are reported in Table 1.

The CASSCF calculations employed two active spaces, (7,7) and (11,11), using the def2-SVP basis set. The Resolution of Identity (RI) approximation was adopted with the auxiliary basis set def2/JK. The first five doublet roots were calculated, with results for the first three doublet excited states shown in Table 1. The (7,7) active space used 7 frontier molecular orbitals and 7 electrons, while the (11,11) active space used 11 MOs and 11 electrons. For the (7,7) active space, additional calculations were performed using the def2-TZVP basis set. The resulting CASSCF(7,7)/def2-TZVP optimized MOs, shown in Figure 3a, do not significantly differ from those obtained with CASSCF(7,7)/def2-SVP and CASSCF(11,11)/def2-SVP calculations, which are not shown. Instead, they are compared with the PPP-HF MOs in Figure 3b. Second-order perturbation theory, specifically the Full Internal Contracted PT2 correction (FIC_PT2), was applied to the CASSCF energies, obtaining vertical excitation energies and relevant oscillator strengths in Table 2. Large PT2 corrections were observed for the (7,7) active space, reaching 1.61 eV for the $^2A_2''$ state in PLY^{opt}. Smaller corrections were found for the (11,11) active space. DFT geometry optimizations, CASSCF, and CASPT2 calculations were performed using the Orca package (version 4.2.1) [222]. For PLY-6N, we used the improved memory management in Orca version 5.0.3 to perform the SC-NEVPT2 calculations with an expanded active space of (13,13). Relevant results are reported in Table 3. For comparison, Table 1 and Table 2 also include PPP-XCISDT transition energies and oscillator strengths for both the idealized and DFT-optimized geometries.

The agreement between PPP and CASPT2 results for PLY^{ideal} and PLY^{opt}, albeit not perfect, is acceptable for a semiempirical approach. For PLY-3N in the idealized geometry, ab initio results deviate from PPP, with the $^2A_2''$ state consistently below the $^2E''$ state. We ascribe this discrepancy to the idealized geometry that is too constrained for the ab initio treatment of PLY-3N. Better agreement with the PPP model is achieved using the DFT-optimized PLY-3N geometry, where the $^2E''$ state is consistently lower in energy than the $^2A_2''$ state. The comparison between PPP and CASPT2 becomes less favorable for PLY-6N, with $^2E''$ lower than $^2A_2''$ for either the ideal or the DFT-optimized geometry. However, it is important to note that uncertainties as large as 0.27 eV have been estimated for CASPT2 without IPEA shift[223], as used here. Consequently, the order of $^2E''$ and $^2A_2''$ states obtained with CASPT2/def2-SVP and CASPT2/def2-TZVP remains uncertain.

The calculated oscillator strengths show good agreement between PPP and CASPT2 results. Both methods indicate that the intensity of the $^2E'' \leftarrow ^2 A_1''$ transition increases when progressing from PLY to PLY-3N to PLY-6N.

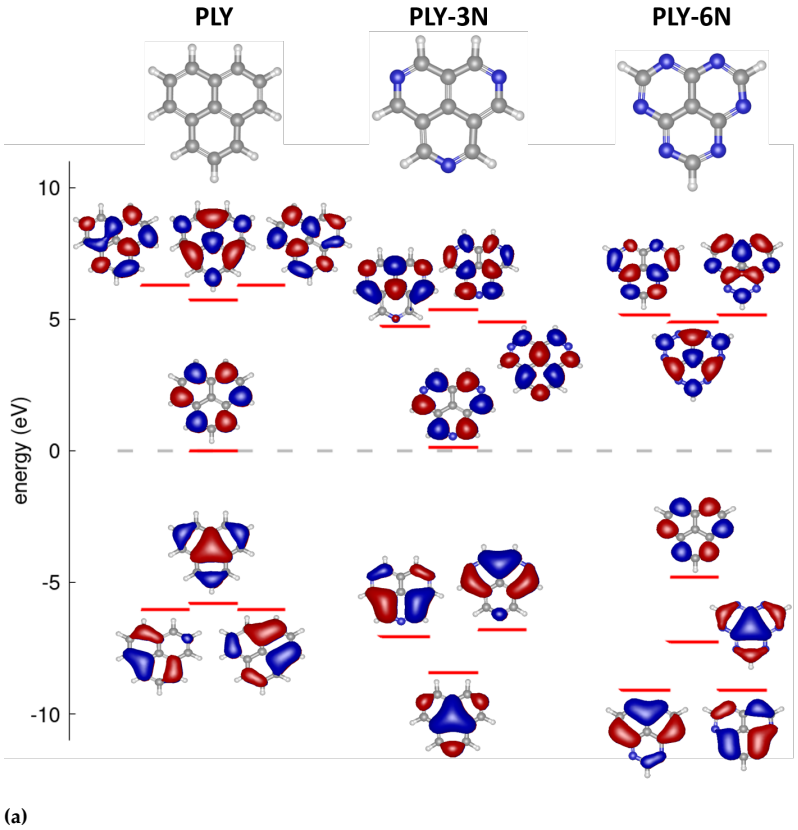

(a)

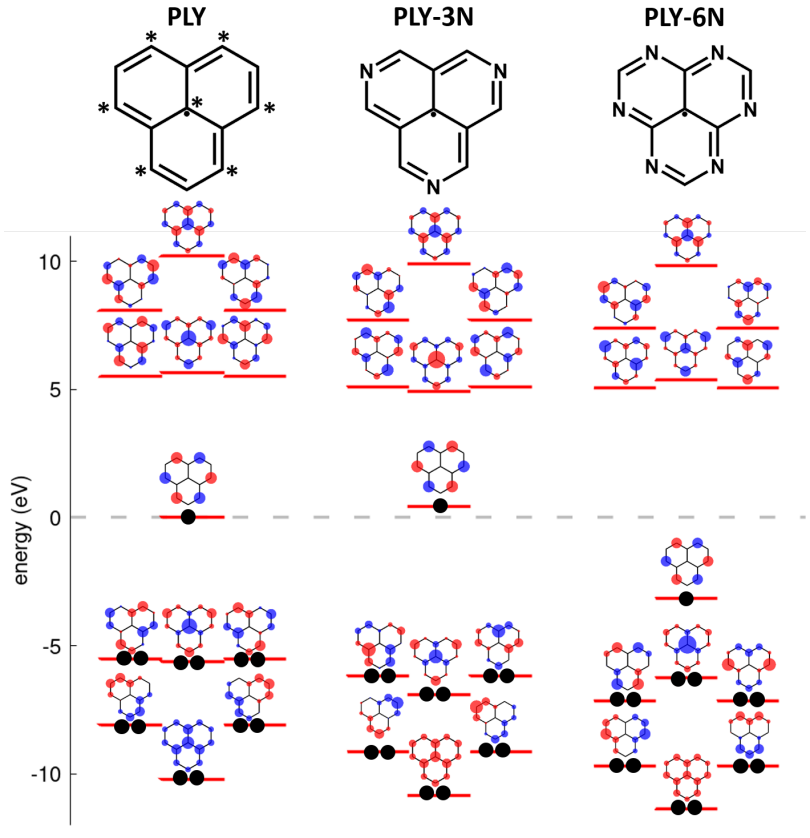

(b)

Figure 3: Comparison between PPP-HF and CASSCF(7,7) orbitals. (a)Frontier molecular orbitals of PLY, PLY-3N, and PLY-6N optimized at the CASSCF(7,7) level with the def2-TZVP basis set. Calculations performed on the DFT-optimized geometries (B3LYP/def2-SVP theory level) shown at the top of the figure. (b)Energy levels calculated at the PPP-HF theory level for PLY, PLY-3N, and PLY-6N, respectively, together with the relevant HF-MOs. Doubly (singly) occupied MOs are marked by two (one) black dots.

Table 1: Vertical excitation energies (in eV) and corresponding oscillator strengths (in parentheses) of the first three doublet excited states of PLY, PLY-3N, and PLY-6N calculated using CASSCF theory level. Results are shown for different active spaces and basis sets. Entries labeled PLY^{ideal}, PLY-3N^{ideal}, and PLY-6N^{ideal} were computed using idealized molecular geometries as described in the main text (all angles set to 120° and all bond lengths to 1.4Å). Entries labeled PLY^{opt}, PLY-3N^{opt}, and PLY-6N^{opt} were computed using DFT-optimized geometries (B3LYP/def2-SVP theory level).

	CASSCF(7,7) def2-SVP	CASSCF(11,11) def2-SVP	CASSCF(7,7) def2-TZVP	PPP-XCISDT
		PLY^{ideal}		
D_1	3.59 (3.6×10^{-4})	2.80 (2.7×10^{-4})	3.55 (5.0×10^{-4})	2.25 (0.0)
D_2	3.59 (3.6×10^{-4})	2.81 (3.5×10^{-4})	3.55 (5.1×10^{-4})	2.25 (0.0)
D_3	3.75 (0.0)	3.45 (10^{-5})	3.60 (0.0)	2.69 (0.0)
		PLY^{opt}		
D_1	3.21 (3.4×10^{-4})	2.74 (2.8×10^{-4})	3.19 (5.2×10^{-4})	2.24 (0.0)
D_2	3.21 (3.4×10^{-4})	2.77 (2.7×10^{-4})	3.19 (5.2×10^{-4})	2.24 (0.0)
D_3	4.08 (0.0)	3.47 (3.4×10^{-4})	3.99 (0.0)	2.69 (0.0)
		PLY-3N^{ideal}		
D_1	3.28 (0.0)	2.67 (2.7×10^{-3})	3.13 (0.0)	2.11 (2.7×10^{-2})
D_2	3.47 (1.1×10^{-2})	2.69 (2.4×10^{-3})	3.44 (1.3×10^{-2})	2.11 (2.7×10^{-2})
D_3	3.47 (1.1×10^{-2})	3.25 (0.0)	3.44 (1.3×10^{-2})	2.19 (0.0)
		PLY-3N^{opt}		
D_1	3.55 (0.0)	2.71 (2.5×10^{-3})	3.02 (1.7×10^{-2})	2.11 (2.9×10^{-2})
D_2	3.64 (3.1×10^{-2})	2.76 (3.9×10^{-3})	3.15 (1.1×10^{-2})	2.11 (2.9×10^{-2})
D_3	3.64 (3.1×10^{-2})	3.95 (10^{-5})	3.45 (3.5×10^{-4})	2.16 (0.0)
		PLY-6N^{ideal}		
D_1	3.12 (0.0)	2.53 (1.6×10^{-2})	2.89 (0.0)	1.55 (0.0)
D_2	3.43 (6.6×10^{-2})	2.54 (1.6×10^{-2})	3.35 (7.4×10^{-2})	1.86 (5.7×10^{-2})
D_3	3.43 (6.6×10^{-2})	3.29 (2×10^{-5})	3.35 (7.4×10^{-2})	1.86 (5.7×10^{-2})
		PLY-6N^{opt}		
D_1	2.73 (0.0)	2.82 (3.5×10^{-2})	2.35 (0.0)	1.46 (0.0)
D_2	3.30 (6.6×10^{-2})	2.84 (3.6×10^{-2})	3.20 (7.9×10^{-2})	1.85 (5.9×10^{-2})
D_3	3.31 (6.6×10^{-2})	3.27 (3×10^{-5})	3.20 (7.9×10^{-2})	1.85 (5.9×10^{-2})

Table 3: Vertical excitation energies (in eV) and corresponding oscillator strengths (in parentheses) of the first three doublet excited states of PLY-6N calculated using NEVPT2 theory level. Results obtained using DFT-optimized geometry (B3LYP/def2-SVP theory level).

	NEVPT2(13,13) def2-SVP
D_1	2.10 (0.0)
D_2	2.69 (2.5×10^{-2})
D_3	2.69 (2.5×10^{-2})

Overall, we demonstrated that triply excited configurations are important to accurately address excited states of three prototypical phenalenyl radicals, namely PLY, PLY-3N, and PLY-6N. In PLY, the lowest optical transition is allowed by point group symmetry, but it is forbidden by particle-hole symmetry, thus making this molecule non-fluorescent and of little interest for OLED applications. Upon decorating the rim with nitrogen atoms, the particle-hole symmetry is broken, and the $^2E'' \leftarrow ^2 A_1''$ transition becomes bright as in PLY-3N and PLY-6N. However, the aza nitrogens on the molecular edge also stabilize the $^2A_2''$ dark state. In the case of PLY-6N, the dark state energy stabilization is so strong that it ends up below the doubly degenerate state, making the molecule non-fluorescent. The results were validated against state-of-the-art CASPT2 calculations, showing agreement between the model and ab initio calculations.

Figure 2 reveals additional details. In panel a, the lowest excited state of

Table 2: Vertical excitation energies (in eV) and corresponding oscillator strengths (in parentheses) of the first three doublet excited states of PLY, PLY-3N, and PLY-6N calculated using CASPT2 theory level. Results are shown for different active spaces and basis sets. Entries labeled PLY^{ideal}, PLY-3N^{ideal}, and PLY-6N^{ideal} were computed using idealized molecular geometries as described in the main text (all angles set to 120° and all bond lengths to 1.4Å). Entries labeled PLY^{opt}, PLY-3N^{opt}, and PLY-6N^{opt} were computed using DFT-optimized geometries (B3LYP/def2-SVP theory level).

	CASPT2(7,7) def2-SVP	CASPT2(11,11) def2-SVP	CASPT2(7,7) def2-TZVP	PPP-XCISDT
		PLY^{ideal}		
D_1	2.18 (2.2×10^{-4})	2.35 (2.9×10^{-4})	2.05 (2.9×10^{-4})	2.25 (0.0)
D_2	2.18 (2.2×10^{-4})	2.37 (2.3×10^{-4})	2.06 (3.0×10^{-4})	2.25 (0.0)
D_3	2.51 (0.0)	3.77 (10^{-5})	2.31 (0.0)	2.69 (0.0)
		PLY^{opt}		
D_1	2.27 (3.4×10^{-4})	2.31 (2.4×10^{-4})	2.15 (3.5×10^{-4})	2.24 (0.0)
D_2	2.28 (3.4×10^{-4})	2.32 (2.3×10^{-4})	2.15 (3.5×10^{-4})	2.24 (0.0)
D_3	2.61 (0.0)	3.11 (3×10^{-4})	2.38 (0.0)	2.69 (0.0)
		PLY-3N^{ideal}		
D_1	2.14 (0.0)	1.40 (0.0)	1.88 (0.0)	2.11 (2.7×10^{-2})
D_2	2.76 (8.5×10^{-3})	2.27 (2.1×10^{-3})	2.31 (8.5×10^{-3})	2.11 (2.7×10^{-2})
D_3	2.81 (8.7×10^{-3})	2.28 (2.3×10^{-3})	2.31 (8.6×10^{-3})	2.19 (0.0)
		PLY-3N^{opt}		
D_1	2.27 (1.9×10^{-2})	2.31 (2.1×10^{-3})	2.18 (1.2×10^{-2})	2.11 (2.9×10^{-2})
D_2	2.28 (1.9×10^{-2})	2.34 (3.3×10^{-3})	2.18 (0.8×10^{-3})	2.11 (2.9×10^{-2})
D_3	2.75 (0.0)	4.13 (1.9×10^{-2})	2.72 (2.7×10^{-4})	2.16 (0.0)
		PLY-6N^{ideal}		
D_1	2.08 (4.0×10^{-2})	2.14 (1.4×10^{-2})	1.95 (4.3×10^{-2})	1.55 (0.0)
D_2	2.08 (4.0×10^{-2})	2.15 (1.3×10^{-2})	1.95 (4.3×10^{-2})	1.86 (5.7×10^{-2})
D_3	2.61 (0.0)	2.94 (2×10^{-5})	2.38 (0.0)	1.86 (5.7×10^{-2})
		PLY-6N^{opt}		
D_1	2.35 (4.7×10^{-2})	2.36 (3×10^{-2})	2.22 (5.5×10^{-2})	1.46 (0.0)
D_2	2.35 (4.7×10^{-2})	2.36 (2.9×10^{-2})	2.22 (5.5×10^{-2})	1.85 (5.9×10^{-2})
D_3	2.43 (0.0)	3.62 (3×10^{-5})	2.32 (0.0)	1.85 (5.9×10^{-2})

PLY is $^2E''$, and since its ground state transforms as $^2A_1''$, the $^2E'' \leftarrow {}^2A_1''$ transition is allowed by spatial symmetry. However, it is forbidden by particle-hole symmetry, so that the calculated transition dipole moment vanishes (see below). The weak absorption observed experimentally for PLY at approximately 2 eV [203, 204] can be reproduced by incorporating inductive effects in the PPP model. Indeed, the PPP particle-hole symmetry can be relaxed by inductive effects [224]. The second excited doublet state of PLY is dark by point group symmetry, transforming as $^2A_2''$, and no effect of particle-hole symmetry breaking is expected. In panel b, the three aza nitrogens on the molecular rim stabilize the $^2A_2''$ dark state by ~0.5 eV with respect to PLY. This effect is not observed for the $^2E''$ doublet, which, however, gains oscillator strength due to partial particle-hole symmetry breaking induced by doping with three nitrogen atoms on the molecular rim (as discussed below). In panel c, the six nitrogens stabilize the $^2A_2''$ dark state so significantly that it ends up below the doubly degenerate state, which remains at nearly the same energy as in PLY and PLY-3N. In both PLY-3N and PLY-6N, the nitrogen atoms located on the rim play a more significant role in breaking particle-hole symmetry compared to the minor PPP on-site energy variations induced by inductive effects. Finally, in all three cases, the first excited quartet state $^4A_1'$ is always well above both $^2E''$ and $^2A_2''$ doublet excited states, being not appreciably affected by the increasing number of aza nitrogen atoms on the molecular rim.

To better quantify particle-hole symmetry breaking, a differential operator D[219] was introduced measuring the difference between the original PPP Hamiltonian in Eq. 2.38 and the PPP Hamiltonian transformed by particle-hole symmetry:

$$\hat{D} = \sum_{\mu} \left[U_{\mu} + 2\varepsilon_{\mu} \right] \left(\hat{n}_{\mu} - 1 \right) \tag{4}$$

where the term in the square bracket is constant if there are no heteroatoms in the system. The absolute value of the ground state expectation value $|\langle \hat{D} \rangle| = |\langle g|\hat{D}|g\rangle|$ is a direct measure of how much the particle-hole symmetry is broken, which in turn impacts the intensity of optical transition. In the following, we will see how $|\langle \hat{D} \rangle|$ changes as a function of the aza nitrogen PPP on-site energy in both PLY-3N and PLY-6N. The behavior observed for $|\langle \hat{D} \rangle|$ will be compared with the oscillator strength of the ${}^2E'' \leftarrow {}^2A_1''$ transition, as it is the lowest energy transition allowed by point group symmetry but forbidden by particle-hole symmetry.

3.1.3 Breaking the Symmetry: The Effect of Nitrogen Doping

The molecules discussed so far belong to the D_{3h} point group and have a low-energy dark doublet (${}^2A_2''$) state that gets stabilized by an increasing number of aza nitrogens on the molecular rim. In order to further investigate the role of the rim in phenalenyl radicals, we decorated the external edge of PLY with an increasing number of aza nitrogen atoms, as shown in Figure 4. All spectral features shift to the red as the number of N atoms on the external rim increases (see Figure 4 panel a). The first dark (${}^2A_2''$) doublet state shifts from ~2.2 eV in PLY-3N to ~1.5 eV in PLY-6N. When the molecular symmetry deviates from D_{3h}, the doublet dark state gains oscillator strength. A second, weaker absorption peak appears at ~2.6 eV in PLY-1N and gradually red-shifts when increasing the number of aza N atoms on the rim. Accordingly, in PLY-2N, PLY-4N, and PLY-5N, the two absorption peaks observed in PLY-1N collapse into a single peak that moves to lower energies with increasing the number of aza N atoms. Quite interestingly, in PLY-1N, a single aza nitrogen is already able to break the particle-hole symmetry, as also shown by a $|\langle \hat{D} \rangle|$ value of ~1.4 eV (panel c). By adding a second nitrogen atom as in PLY-2N, $|\langle \hat{D} \rangle|$ increases to ~2.8 eV. By inspection of panel c, we see that each nitrogen atom contributes ~1.4 eV to the $|\langle \hat{D} \rangle|$ value. Similar behavior is shown by the oscillator strength, with each aza N atom contributing ~0.02 (panel b).

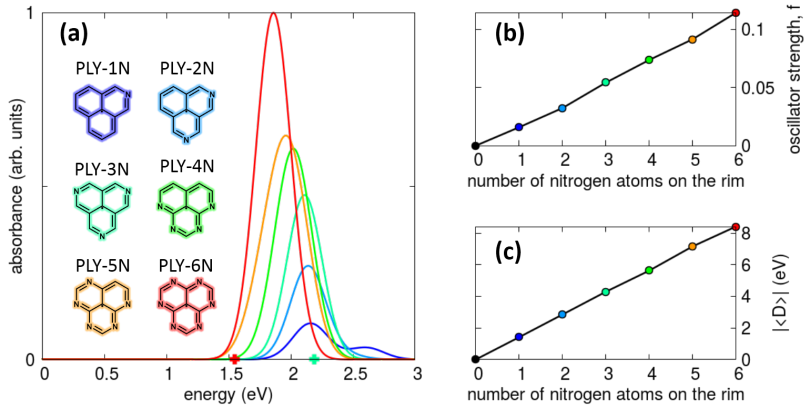

Figure 4: Decorating the rim of the phenalenyl radical with an increasing number of aza nitrogens. Calculated absorption spectra (panel a), oscillator strength integrated over the 0 eV - 3 eV spectral range (panel b), and absolute value of the ground state expectation value of the difference operator (panel c) for six different phenalenyls decorated with an increasing number of aza nitrogen atoms on the rim. In panel a, colored crosses mark the position of PLY-3N and PLY-6N first dark doublet state. In panel a, spectra are normalized to the maximum absorbance of the most intense spectrum. In panels b and c, a black dot is used for PLY results. Other parameters are defined in the main text. Calculations performed at the PPP-XCISDT theory level.

The results discussed so far demonstrate the utility of the PPP model and $|\langle\hat{D}\rangle|$ in investigating the physics of radicals with significantly broken particle-hole symmetry.All-electron Hamiltonians do not strictly obey particle-hole symmetry that is instead built-in in PPP models for alternant hydrocarbons.The degree to which this symmetry is preserved in all-electron Hamiltonians depends on how closely the assumptions of the PPP model align with the specific system being studied.

Looking back at the difference operator expression in Eq. 4, it relies on the on-site electron density, weighted by the repulsion between two electrons on the same atom (U_μ), plus twice the on-site energy (ε_μ). This calculation is then summed over the entire molecule. Therefore, we can consider whether $|\langle\hat{D}\rangle|$ can be determined using the total molecular energies obtained from quantum chemistry methods. Indeed, an effective molecular electron-electron repulsion energy U_{eff} can be estimated as the difference between the ionization potential and the electron affinity of the PLY radical [225, 226], $U_{eff} = E(PLY^-) + E(PLY^+) - 2E(PLY)$, where E is the DFT ground state radical total energy in the different oxidation states. Similarly, the effective on-site energy ε_{eff} can be obtained from the radical ionization potential as $\varepsilon_{eff} = E(PLY) - E(PLY^+)$, thus leading to the effective $|D|_{eff} = U_{eff} + 2\varepsilon_{eff}$. Of course, similar reasoning applies to other radicals as well. In Figure 5, we compare $|\langle\hat{D}\rangle|$ calculated with respect to the PPP-XCISDT ground state and the DFT ground state. While the quantitative agreement is far from perfect, the qualitative trend is well reproduced, with $|\langle\hat{D}\rangle|$ increasing as the number of aza nitrogen atoms on the edge grows.

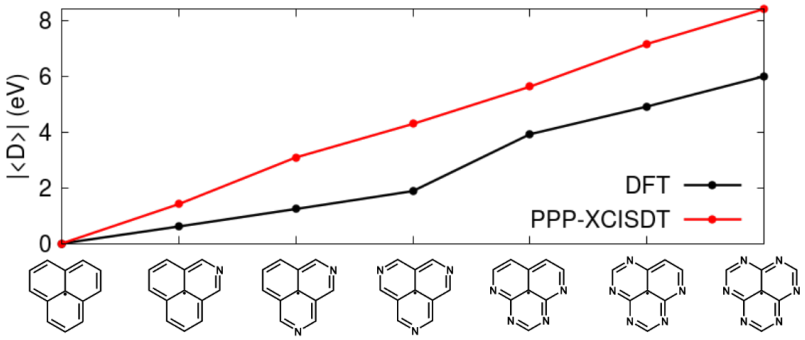

Figure 5: Particle-hole symmetry breaking in DFT and PPP. Ground state $|\langle\hat{D}\rangle|$ calculated for several phenalenyl radicals at DFT and PPP-XCISDT theory levels. PPP model parameters specified in the main text. ROKS DFT calculations performed using B3LYP functional with 6-31G(d,p) basis set as implemented in the Gaussian16 package,[227] and same regular geometry used for PPP calculations. DFT results were rescaled with respect to the value of $|\langle\hat{D}\rangle|$ relative to PLY, 6.77 eV.

3.2 INVEST, radicals and diradicals

Having understood the importance of radical triangulene molecules, we asked ourselves if it is possible to exploit the photophysics of triangulenes to realize molecules of more direct application in Quantum Information Science (QIS). Efforts to realize optically addressable electron spins have driven major advances in QIS, where the ability to initialize and read out spin states through optical transitions underpins optically detected magnetic resonance (ODMR) techniques. Current ODMR frameworks mainly rely on optically active spin defects in diamond, particularly nitrogen-vacancy (NV) centers, which offer exceptional spin coherence and robust photon–spin interfaces [228–231]. However, these defect-based color centers face inherent limitations: they require post-synthetic incorporation with limited spatial control, constraining their scalability, reproducibility, and chemical tunability. Molecular spin systems offer a compelling alternative, with advantages such as atomic-scale precision, modularity, and design-driven functionality that are difficult to achieve in solid-state platforms.

Among these, organic diradicals have emerged as promising candidates for spin-active units [170, 232–239]. Their magnetic properties arise from the interplay of spin–spin interactions, frontier orbital topology, and excited-state dynamics, all of which can be systematically tailored through molecular design. We propose an innovative molecular design strategy for a novel optical-spin interface that enables light-induced switching of spin-spin interactions in diradicals, where the two radical units are connected by a triangulene-based dye with an inverted singlet–triplet (InveST) energy gap (see Figure 6a).

In InveST systems, the highest occupied molecular orbital (HOMO) and lowest unoccupied molecular orbital (LUMO) are localized on complementary atomic sites with minimal spatial overlap [240, 241]. As a result, the lowest excited state predominantly exhibits a multi-resonant charge-transfer (MRCT) character, with the electron density shifting from the HOMO to the LUMO. Under these conditions, the exchange integral, which governs the singlet-triplet (ST) splitting, is very small, and the typically minor spin polarization correction can become large enough to invert the ST energy gap [242–246]. This ST inversion has been experimentally observed in heptazine derivatives [112, 113] and in 1,3,4,6,9b-pentaazaphenalene (5AP) [123], both featuring HOMO and LUMO localized on distinct and complementary atomic sites (see Figure 6b). Moreover, some of us have recently shown [116, 171] that this HOMO-LUMO complementarity is a general feature of polyenes with alternating electron-donor (D) and electron-acceptor (A) groups, with 1,3-diazete representing the smallest molecular motif that exhibits this behavior (see Figure 6b), as already noted in Section 3.1. A hallmark feature of alternant radicals is that their singly occupied molecular orbital (SOMO) is non-bonding and localized exclusively on one of the two sublattices, specifically the one containing more atoms (see Figure 6c).

By covalently linking the non-SOMO-bearing sites of each alternant hydrocarbon radical to the LUMO-localized positions of the InveST dye, spin-spin interactions can be systematically suppressed in the ground state, resulting in diradicals with an intrinsic disjoint character (see Figure 6d). Upon photoexcitation of the InveST bridge via a HOMO→LUMO

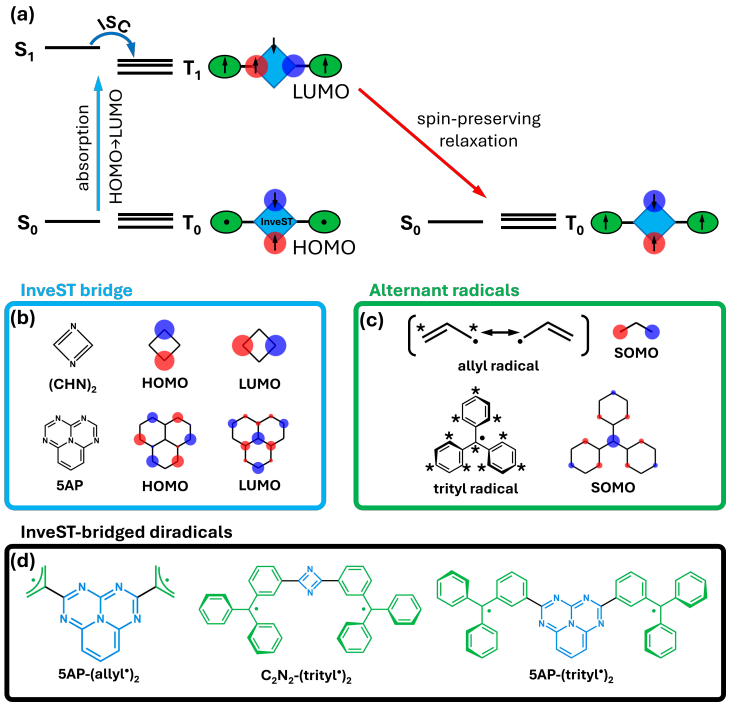

Figure 6: (a) Schematic representation of the InveST-bridged diradical design. The simplified Jablonski diagram shows the InveST-localized HOMO→LUMO transition that induces spin–spin locking in the excited state, and its subsequent spin-preserving relaxation to the triplet ground state. (b) Molecular structures of two prototypical InveST bridges, namely 1,3,4,6,9b-pentaazaphenalene (5AP) and 1,3-diazete, together with their frontier PPP Hartree-Fock MOs. (c) Molecular structures of two prototypical alternant radicals, namely allyl and trityl radicals, together with their SOMO. (d) Molecular structures of the three prototypical InveST-bridged diradicals discussed in this work.

transition, the LUMO becomes occupied and mediates interaction between the radicals, effectively switching on exchange interactions in the excited state. Using a combined theoretical approach based on the PPP model [86, 116, 118, 161, 162, 167–170, 247] and high-level multireference ab initio calculations, we show that InveST-bridged diradicals are promising molecular alternatives to NV centers for quantum information applications.

3.2.1 Electronic Structure Characterization

We used the PPP model, following the same procedure as in Section 3.1 but relying on a PPP-RASCI approach, rather than the PPP-XCISDT approach. Moreover, the PPP model was extended to account for the torsional flexibility around the bonds connecting the InveST core to the radical units that plays a key role in modulating electronic communication between the molecular fragments.

While the PPP model was originally developed for planar π-conjugated hydrocarbons, it can be extended to describe non-planar geometries by incorporating torsional effects into the electronic hopping term [170, 173–177]. In particular, the hopping integral $t_{\mu\nu}$ between the InveST bridge and the radical moieties is modeled to vary as a cosine function of the torsional angle θ, where both dihedral angles (on either side of the bridge) are rotated by the same amount, regardless of whether they rotate in the same or opposite directions. The hopping reaches its maximum value when the molecule adopts a fully planar conformation, i.e., at $\theta = 0°$ or $180°$. Torsional strain is introduced through a steric potential modeled as a squared sine function, $V_{\text{steric}}(\theta) = \sin^2\theta$, assumed to be identical in both the ground and excited electronic states. Finally, the PPP Hamiltonian is solved by exact diagonalization using the RASCI framework introduced in Ref. [171], as it allows for the inclusion of

more configurations compared to the CI framework used in the previous section. The torsional angles for each molecule are highlighted in Figure 7.

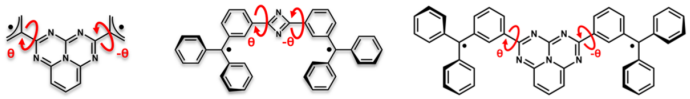

Figure 7: 5AP-(allyl$^\bullet$)$_2$, C_2N_2-(trityl$^\bullet$)$_2$, and 5AP-(trityl$^\bullet$)$_2$ with the torsional angle that modulates the spin-orbit couplings in the model.

In our case, we used a RAS2 space containing 4 electrons in 6 MOs for 5AP-(allyl$^\bullet$)$_2$, 5 MOs for C_2N_2-(trityl$^\bullet$)$_2$, and 4 MOs for 5AP-(trityl$^\bullet$)$_2$. The specific PPP-HF MOs included in RAS2 are shown in Figure 8..

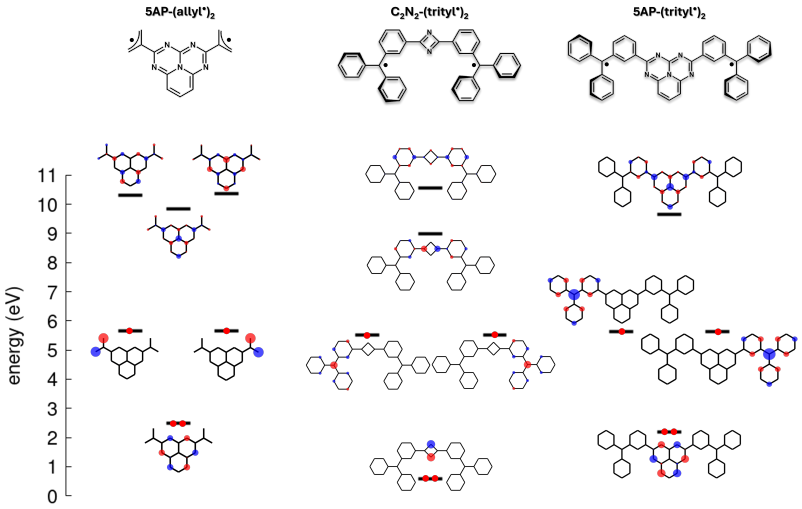

Figure 8: Frontier MOs calculated at the PPP-HF level and included in the RAS2 subspace for 5AP-(allyl$^\bullet$)$_2$, C_2N_2-(trityl$^\bullet$)$_2$, and 5AP-(trityl$^\bullet$)$_2$, shown alongside their corresponding energy levels. Orbitals are marked with one or two red dots to indicate single or double occupancy, respectively.

We adopted a parametrization similar to that of the previous section, with a carbon on-site energy set to zero, a Hubbard U_C of 11.26 eV, and a nearest-neighbor C-C hopping integral of $t = -2.4$ eV. The best agreement with QD-NEVPT2 results (see later) for 5AP-(allyl$^\bullet$)$_2$ diradicals is achieved setting $U = 15$ eV for the pyrrolic nitrogen and 15.5 eV for the aza nitrogen, as proposed in Ref. [116]. The on-site energy for pyrrole nitrogen is set to –13 eV, while aza nitrogen site energies are taken as –3.5 eV in 5AP-(allyl$^\bullet$)$_2$ and –4 eV in 5AP-(trityl$^\bullet$)$_2$. For the C_2N_2-bridged diradical, which features two aza nitrogens and no pyrrolic nitrogen atoms, the parametrization was based on the PPP values for aza nitrogens in porphines reported in Ref. [166]. Specifically, the Hubbard U was taken directly from that work (12.34 eV), while the site energy was slightly adjusted to –3.5 eV. Hopping integrals for C–N bonds were set equal to the C–C values. For computational simplicity, the molecular geometry was simplified by setting all bond angles to 120° and all bond lengths to 1.4 Å. For the trityl radical units, DFT-optimized geometries showed a propeller-like structure, with dihedral angles of approximately 32° between the central carbon and each of the three phenyl rings. As a result, the hopping integrals between the central carbon and its phenyl substituents were scaled by cos (32°). The torsional degrees of freedom around the InveST–radical connecting bonds modulate the electronic coupling between fragments. The hopping integral $t_{\mu\nu}$ connecting the

radical sites to the InveST core was modeled with a cosine dependence on the torsional angle θ, with the two dihedrals rotated by the same amount, regardless of whether the twisting occurs in the same or opposite directions.

The ODMR mechanism requires intersystem crossing (ISC), which in turn depends on the coupling between the singlet and triplet excited state manifolds. This mixing is governed by Spin-Orbit Coupling (SOC). SOC in InveST-bridged diradicals is enabled by thermal torsional fluctuations around the bonds linking the InveST core to the radical units. These out-of-plane distortions disrupt the planarity of the conjugated π system, triggering SOC. Notably, SOC is highly localized at the connection points between the bridge and radicals due to the sharp $1/r^3$ dependence of SOC on interatomic separation. As a result, the primary SOC contributions arise from the immediate vicinity of the InveST–radical linkages, where structural flexibility is most significant. Within the PPP framework, the SOC operator takes the form [170, 248–251]:

$$\hat{H}_{SOC} = A \sum_{\mu\nu} \left(\hat{a}^{\dagger}_{\mu\uparrow} \hat{a}_{\nu\downarrow} - \hat{a}^{\dagger}_{\nu\uparrow} \hat{a}_{\mu\downarrow} \right) \tag{5}$$

where $A = -i(3.94 \times 10^{-4}) \sin\theta$ is the purely imaginary SOC matrix element in eV between neighboring carbon atom $2p_z$ orbitals. Accordingly, in the PPP model, SOC is introduced as an additional spin-flipping hopping term with a purely imaginary amplitude A between atomic sites μ and ν, where these sites correspond to the junctions between the InveST bridge and the two radical units. The effect of this SOC operator is to generate couplings between singlets and triplets with $M_S = \pm 1$. The magnitude of A depends on the local torsional angle, capturing the conformational sensitivity of SOC activation. SOC is introduced in the calculation perturbatively, a good approximation since SOC matrix elements are four orders of magnitude smaller than the typical hopping terms in the PPP Hamiltonian. Thus, the Hamiltonian is solved without the SOC contribution, and then SOC corrections are evaluated at first order by considering the overlap between the spin-pure states and the SOC Hamiltonian.

3.2.2 Calculation set-up and ab-initio results

Geometry optimizations for the InveST-bridged diradicals depicted in Figure 6d were carried out at the DFT level using the UBHandHLYP functional and the 6-31++G(d,p) basis set in the gas phase. All structures were optimized in their triplet ground states. To explore the conformational landscape, potential energy surface scans were performed by rigidly rotating the torsional angle θ around the two bonds linking the InveST core to the radical units, using 2° increments. The resulting energy profiles were then fitted to the steric potential function $V_{\text{steric}}(\theta)$. For all investigated systems, the equilibrium torsional angle was found to be $\theta_{\text{eq}} = 0°$ for all the states taken into consideration. This result was confirmed by excited-state geometry optimizations performed at the TD-DFT level (CAM-B3LYP/def2-SVP) for both S_1 and T_1, although the optimized geometries are not shown here. All geometry optimizations were carried out using the Gaussian16 software package [227].

CASSCF calculations were carried out on the UBHandHLYP-optimized triplet ground-state geometries. To incorporate dynamic electron correlation, the CASSCF state energies were further refined using the van Vleck quasi-degenerate (QD) extension to SC-NEVPT2 [170, 252]. All the CASSCF/QD-NEVPT2 calculations were done with the Orca package (version 5.0.3) [222].

CASSCF calculations were performed using two different active spaces, (4,4) and (6,6), and for two representative θ values, 0° and 30°. All calculations employed the def2-SVP basis set, along with the Resolution of Identity (RI) approximation using the def2/JK auxiliary basis set. The first two triplet and the first two singlet roots were computed in each case. The (4,4) active space included four electrons in four frontier MOs, while the (6,6) space comprised six electrons in six MOs. Upon enlarging the active space, the key frontier orbitals (HOMO, SOMO, and LUMO) remain largely unchanged for the 5AP-(allyl$^\bullet$)$_2$, C_2N_2-(trityl$^\bullet$)$_2$, and 5AP-(trityl$^\bullet$)$_2$ systems (see Figure 9, Figure 10, and Figure 11).

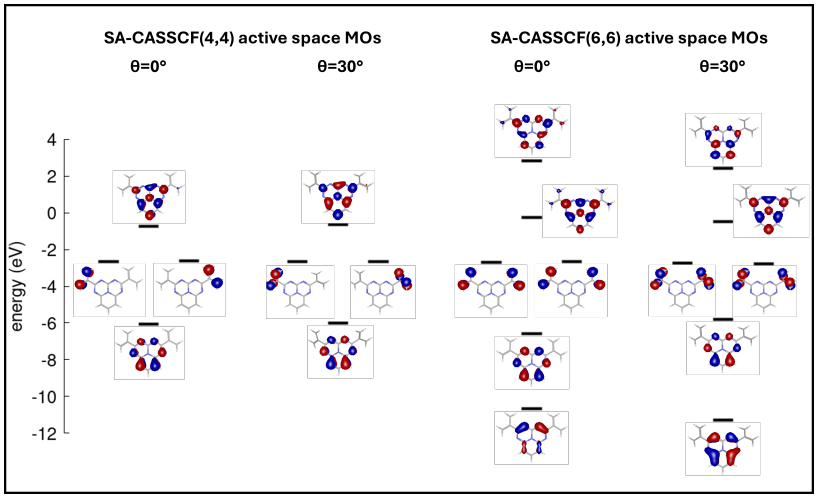

Figure 9: CASSCF frontier molecular orbitals of 5AP-(allyl$^\bullet$)$_2$ calculated with (4,4) and (6,6) active spaces using the def2-SVP basis set at θ = 0° and θ = 30° torsional angles.

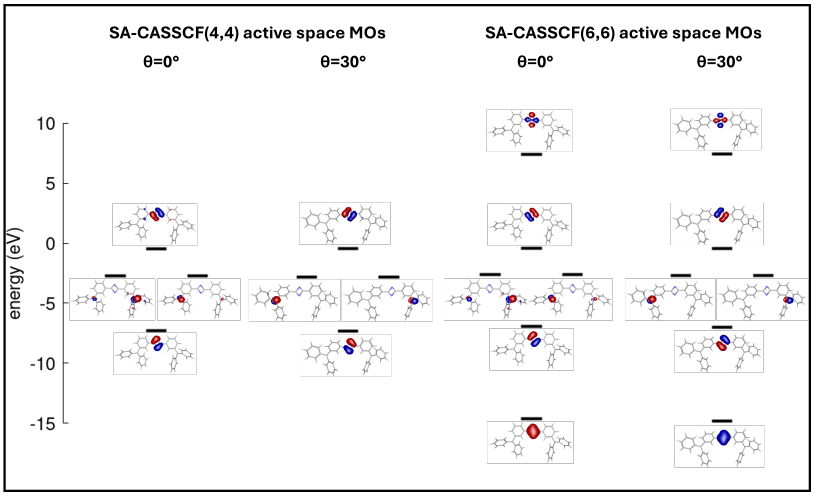

Figure 10: CASSCF frontier molecular orbitals of C_2N_2-(trityl$^\bullet$)$_2$ calculated with (4,4) and (6,6) active spaces using the def2-SVP basis set at θ = 0° and θ = 30° torsional angles.

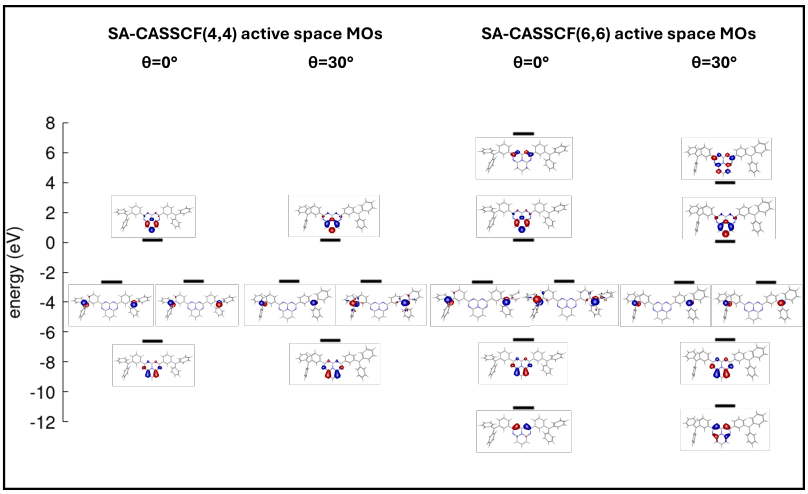

Figure 11: CASSCF frontier molecular orbitals of 5AP-(trityl$^\bullet$)$_2$ calculated with (4,4) and (6,6) active spaces using the def2-SVP basis set at $\theta = 0°$ and $\theta = 30°$ torsional angles.

Second-order perturbative corrections were generally modest across all systems for both (4,4) and (6,6) active spaces. For 5AP-(allyl$^\bullet$)$_2$, corrections ranged from approximately 0.6 eV for T_1 to 0.8 eV for S_1. In contrast, significantly smaller corrections were observed for C_2N_2-(trityl$^\bullet$)$_2$ ($\sim$ 0.1 eV for both S_1 and T_1) and 5AP-(trityl$^\bullet$)$_2$ ($\sim$ 0.07 eV for both states). S_0 and T_0 remain degenerate, and T_1 consistently lies below S_1. For the 5AP-(allyl$^\bullet$)$_2$ system at $\theta = 0°$, the S_1-T_1 energy gap slightly increases from 25 meV with (4,4) to 42 meV with (6,6). At $\theta = 30°$, however, both active spaces yield nearly identical results. For 5AP-(trityl$^\bullet$)$_2$, the gap is still present, but it decreases to a small value of 5 meV at 30°. These results show that the smaller (4,4) active space provides an adequate description of the electronic structure for both systems, with the larger (6,6) active space confirming the reliability of our main findings. All energies can be seen in Table 4, Table 5, and Table 6.

Table 4: Total energies in atomic units of the S_0, T_0, T_1, and S_1 states of 5AP-(allyl$^\bullet$)$_2$ for planar ($\theta = 0°$) and twisted ($\theta = 30°$) geometries at the QD-NEVPT2 theory level.

	QD-NEVPT2(4,4)	QD-NEVPT2(6,6)	QD-NEVPT2(4,4)	QD-NEVPT2(6,6)
	$\boldsymbol{\theta = 0°}$		$\boldsymbol{\theta = 30°}$	
$E(S_0)$	-810.675922	-810.678782	-810.673568	-810.677085
$E(T_0)$	-810.675935	-810.678649	-810.673605	-810.676885
$E(T_1)$	-810.612415	-810.613130	-810.608965	-810.605813
$E(S_1)$	-810.611506	-810.611599	-810.608621	-810.605831

Table 5: Total energies in atomic units of the S_0, T_0, T_1, and S_1 states of C_2N_2-(trityl$^\bullet$)$_2$ for planar ($\theta = 0°$) and twisted ($\theta = 30°$) geometries at the QD-NEVPT2 theory level. Results are shown for two different active spaces.

	QD-NEVPT2(4,4)	QD-NEVPT2(6,6)	QD-NEVPT2(4,4)	QD-NEVPT2(6,6)
	$\boldsymbol{\theta = 0°}$		$\boldsymbol{\theta = 30°}$	
$E(S_0)$	-1644.065430	-1644.045811	-1644.059929	-1644.040222
$E(T_0)$	-1644.065446	-1644.045783	-1644.059936	-1644.040206
$E(T_1)$	-1643.995663	-1643.978743	-1643.988494	-1643.972841
$E(S_1)$	-1643.993669	-1643.976775	-1643.986834	-1643.971281

Table 6: Total energies in atomic units of the S_0, T_0, T_1, and S_1 states of 5AP-(trityl$^\bullet$)$_2$ for planar ($\theta = 0°$) and twisted ($\theta = 30°$) geometries at the QD-NEVPT2 theory level. Results are shown for two different active spaces.

	QD-NEVPT2(4,4)	QD-NEVPT2(6,6)	QD-NEVPT2(4,4)	QD-NEVPT2(6,6)
	$\boldsymbol{\theta = 0°}$		$\boldsymbol{\theta = 30°}$	
$E(S_0)$	-2037.414432	-2037.412602	-2037.411533	-2037.417212
$E(T_0)$	-2037.414443	-2037.412421	-2037.411546	-2037.417112
$E(T_1)$	-2037.308775	-2037.312054	-2037.306158	-2037.321103
$E(S_1)$	-2037.308582	-2037.311809	-2037.305967	-2037.320838

3.2.3 PPP results and comparison with ab initio calculations

We start our discussion with the electronic structure of the 5AP-bridged diradical system (see Figure 12a) at the PPP level, comparing it with high-level multireference CASSCF(4,4)/QD-NEVPT2 calculations. The resulting CASSCF molecular orbitals (MOs) are also reported in panel b, and show a doubly degenerate SOMO, each localized on one of the two radical units and labeled $SOMO_1$ and $SOMO_2$ throughout the text. The HOMO and LUMO are centered on the InveST bridge. This orbital pattern is preserved over the range of torsional angles θ explored in this work.

The potential energy curves as a function of the torsional angle θ computed at the PPP level (panel c) show that both ground and excited state manifolds adopt a planar equilibrium geometry ($\theta_{eq} = 0°$). However, they exhibit markedly different spin behavior. The singlet and triplet ground states (S_0 and T_0) remain degenerate across the entire torsional range, consistent with the expected absence of spin-spin interactions in the ground state. In contrast, the excited state manifold exhibits distinctly different behavior. Upon photoexcitation, population of the InveST LUMO enables interaction between the radicals, effectively switching on an exchange interaction in the excited state. This activation of inter-radical communication opens an energy gap between the first excited triplet (T_1) and singlet (S_1) states, with T_1 stabilized below S_1 over the range of θ values thermally accessible at room temperature (see the Boltzmann distribution calculated for the ground state in panel c). The magnitude of this ST splitting serves as a direct indicator of the light-induced radical-radical interaction, reaching a maximum at $\theta = 0°$ (panel d, black curve). Scanning through the torsional angle θ, the S_1 and T_1 states retain their diradical character, with the two unpaired electrons remaining spatially separated on distinct radical units, rather than forming an intramolecular SOMO-to-SOMO charge-transfer (CT) state.

These PPP predictions are in good agreement with high-level CASSCF/QD-NEVPT2 calculations (panel f), which reproduce the same qualitative behavior, namely degenerate singlet and triplet ground states and a positive, albeit slightly smaller, ST energy gap in the excited state (panel g, black curve).

Figure 12d (red curve) shows the absolute value of the SOC matrix element between the S_1 state and the $M_S = \pm 1$ sublevels of the T_1 state, as calculated at the PPP level. No coupling is found between S_1 and the $M_S = 0$ component of T_1, in agreement with spin selection rules [250]. As expected, the SOC vanishes exactly at $\theta = 0°$, where the system is fully

planar. However, even slight deviations from planarity lead to nonzero SOC values, confirming that minimal torsional distortions are sufficient to activate ISC. The SOC magnitude increases steadily with the torsional angle, reaching approximately 0.01 cm^{-1} at $\theta = \pm 30°$. These values are in line with SOC strengths observed in other organic molecules known to undergo efficient ISC [101, 253], indicating that thermally accessible twisting at the InveST–radical bonds provides a possible pathway for spin-state transitions in this system. Calculations at the CASSCF/QD-NEVPT2 level (panel g, red curve) show good agreement with the PPP results, supporting the reliability of the model in capturing SOC behavior in this diradical architecture. Notably, a similar dependence of the SOC matrix element on the torsional angle was previously reported by Casanova et al. for the tetramethyleneethane molecule using the ab initio RAS-Spin Flip theory level [254].

The oscillator strengths for the $S_0 \rightarrow S_1$ and $T_0 \rightarrow T_1$ transitions, presented in panel e, show only minor variation as a function of the torsional angle θ. While the PPP model systematically underestimates these values by two orders of magnitude compared to CASSCF/QD-NEVPT2 results (panel h), it reproduces the general trend of weak angular dependence. This limited sensitivity to torsion arises from the dominant localization of the S_1 and T_1 excited states on the InveST core, where the main optical transition occurs, with minor involvement of the radical units. As a result, torsional fluctuations at the bridge–radical connections exert little influence on the transition probabilities.

The electronic structure of the 5AP-(allyl$^\bullet$)$_2$ system supports a clear ODMR mechanism. Upon optical excitation, both S_1 and T_1 excited states are populated, with T_1 lying energetically below S_1. Thermal torsional fluctuations activate SOC between these states, enabling ISC from S_1 to specific sublevels of T_1 (sublevels $M_S = \pm 1$). This process leads to a non-uniform population of triplet sublevels. As the excited states relax back to the degenerate S_0/T_0 ground state manifold via radiative or non-radiative pathways, the sublevel-selective population is retained, resulting in ground state triplet spin polarization.

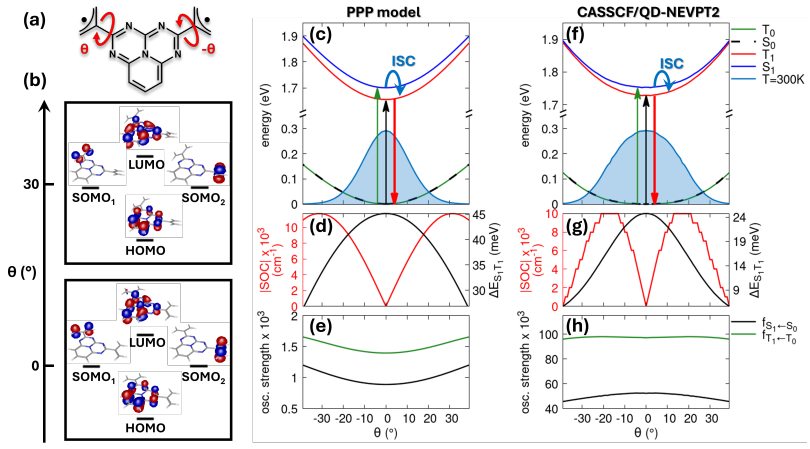

Figure 12: Electronic structure and photophysical properties of the 5AP-(allyl$^\bullet$)$_2$. (a) Molecular structure with torsional coordinate θ around the bridge-radical connecting bonds. (b) CASSCF(4,4) frontier MOs at $\theta = 0°$ and 30°. (c) PPP potential energy curves for S_0, T_0, S_1, T_1 states and ground state Boltzmann distribution at room temperature. (d) Singlet-triplet energy gap (black) and spin-orbit coupling magnitude (red) vs θ. (e) Oscillator strengths for $S_0 \rightarrow S_1$ (black) and $T_0 \rightarrow T_1$ (green) transitions. (f-h) CASSCF(4,4)/QD-NEVPT2 results corresponding to panels (c-e). PPP calculations used the RASCI(h,p,hp) approach. PPP model parameters: $t = -2.4$ eV, $\varepsilon_C = 0$, $U_C = 11.26$ eV, $\varepsilon_N^{aza} = -3.5$ eV, $U_N^{aza} = 15.5$ eV, $\varepsilon_N^{py} = -13$ eV, $U_N^{py} = 15$ eV.

The C_2N_2-bridged diradical system shown in Figure 13a presents electronic and photophysical properties closely resembling those of 5AP-

(allyl$^{\bullet}$)$_2$. As shown in panel b, the CASSCF(4,4) frontier MOs retain the same characteristic pattern: the HOMO and LUMO are localized on the InveST bridge, while the doubly degenerate SOMO remains confined on the radical units. PPP calculations again predict degenerate S_0 and T_0 states throughout the full range of torsional angles, along with a finite ST gap between S_1 and T_1, with T_1 stabilized below S_1 (panel c). These PPP potential energy curves show good overall agreement with the ab initio CASSCF(4,4)/QD-NEVPT2 results (panel f). The torsional dependence and magnitude of the ST energy gap are well reproduced (see black curve in panels d and g), although the vertical excitation energies are slightly underestimated at the PPP level by ~ 0.45 eV compared to QD-NEVPT2.

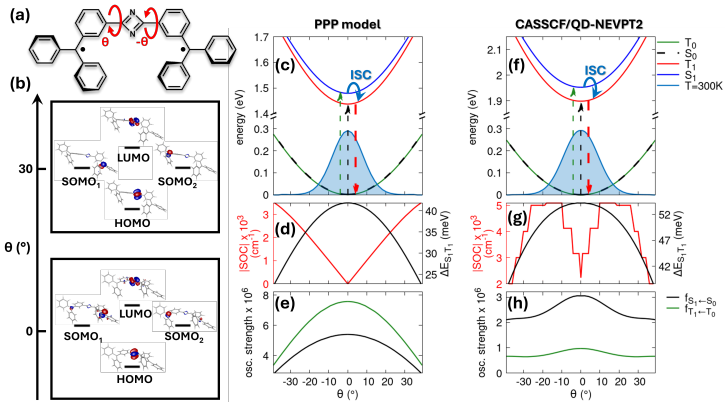

Figure 13: Electronic structure and photophysical properties of C_2N_2-(trityl$^{\bullet}$)$_2$. (a) Molecular structure showing the trityl-based C_2N_2-diradical system with torsional angle θ around the bridge-radical bonds. (b) CASSCF(4,4) frontier molecular orbitals at planar (θ = 0°) and twisted (θ = 30°) geometries. (c) PPP potential energy surfaces and ground state thermal distribution at room temperature. (d) Torsional dependence of the S_1-T_1 energy gap (black) and spin-orbit coupling strength (red). (e) Oscillator strengths for $S_0 \rightarrow S_1$ (black) and $T_0 \rightarrow T_1$ (green). (f-h) CASSCF(4,4)/QD-NEVPT2 relevant results. PPP calculations used the RASCI(h,p,hp) approach (see SI Section S1.2). PPP model parameters: t = −2.4 eV, ε_C = 0, U_C = 11.26 eV, ε_N^{aza} = −3.5 eV, U_N^{aza} = 12.34 eV, ε_N^{py} = −13 eV, U_N^{py} = 15 eV.

Differences arise in the SOC behavior. The absolute value of the SOC between S_1 and T_1 is smaller in this system compared to 5AP-(allyl$^{\bullet}$)$_2$. While the PPP model predicts vanishing SOC at the planar geometry (θ = 0°, red curve in panel d), CASSCF(4,4)/QD-NEVPT2 calculations show a small but finite SOC at equilibrium (red curve in panel g). This residual coupling results from a slight deviation from perfect planarity in the DFT-optimized geometry, specifically a dihedral angle of ~ 0.5° between the InveST bridge and each trityl unit. The ab initio SOC reaches its maximum around θ =10°-20° and shows a minimum near θ = ±39°, in contrast to the PPP SOC which places the maximum at θ = ±39°. Despite these differences in angular dependence, both methods yield SOC values of comparable magnitude.

A key feature of the C_2N_2-(trityl$^{\bullet}$)$_2$ system lies in its optical behavior: the lowest excited states (S_1 and T_1) are optically dark due to the symmetric character of the C_2N_2 bridge (panels e and h). As a result, photoexcitation must proceed through higher-lying excited states, which subsequently relax via internal conversion to the S_1 and T_1 manifolds. SOC between S_1 and T_1 then enables ISC from S_1 to specific T_1 sublevels (M_S = ±1), followed by non-radiative internal conversion (dashed red arrow in panels c and f) that can lead to triplet spin polarization in the ground state.

Turning to the 5AP-(trityl$^{\bullet}$)$_2$ diradical in Figure 14, the system retains the characteristic degeneracy of S_0 and T_0 observed in the previously

discussed cases. However, although an energy gap still opens between S_1 and T_1, with T_1 lying below S_1, the magnitude of this gap is substantially reduced compared to the two smaller diradical analogs. At $\theta = 0°$, the S_1-T_1 splitting reaches only 17 meV at the PPP level and 5 meV in CASSCF(4,4)/QD-NEVPT2 calculations. This already small gap decreases further at non-zero torsional angles. The SOC properties are similarly weakened: the maximum absolute value of the SOC matrix element between S_1 and the $M_S = \pm 1$ sublevels of T_1 is 4.5×10^{-4} cm^{-1} at the PPP level and 10^{-3} cm^{-1} at the CASSCF(4,4)/QD-NEVPT2 level. This represents a reduction of nearly two orders of magnitude compared to the 5AP-(allyl$^\bullet$)$_2$ system (Figure 12d and g). The combination of a minimal S_1-T_1 energy gap and extremely weak SOC makes 5AP-(trityl$^\bullet$)$_2$ unsuitable for efficient ODMR operation.

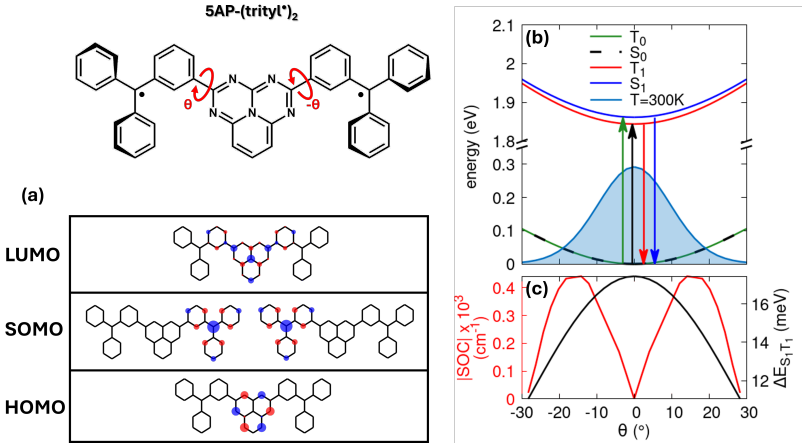

Figure 14: Electronic structure of the trityl-based 5AP-diradical system at the PPP-RASCI(h,p,hp) theory level. (a) PPP frontier molecular orbitals entering RAS2 subspace at planar ($\theta = 0°$) geometry. (b) PPP potential energy curves and ground state thermal distribution. (c) Torsional dependence of the S_1-T_1 energy gap (black) and spin-orbit coupling strength (red).

3.2.4 The ODMR mechanism for InveST-bridged diradicals

The ODMR mechanism in InveST-bridged diradicals emerges from a sequence of spin-dependent photophysical processes that originate in the thermally populated conformational ensemble of the ground state. At room temperature, the degenerate S_0-T_0 ground state spans a distribution of torsional geometries, with appreciable population of twisted conformations around the bonds connecting the InveST core to the radical units. This conformational flexibility plays a key role in activating the SOC pathways that drive the subsequent photophysical dynamics. Upon photoexcitation, the behavior of the system depends on the specific diradical structure and the oscillator strengths of its low-lying electronic transitions. In the case of 5AP-(allyl$^\bullet$)$_2$, direct excitation can populate the S_1 and T_1 states. By contrast, C_2N_2-(trityl$^\bullet$)$_2$ exhibits vanishing oscillator strengths for both $S_0 \rightarrow S_1$ and $T_0 \rightarrow T_1$ transitions, necessitating excitation to higher-lying states. Nonetheless, Kasha's rule ensures rapid, spin-preserving internal conversion from these higher excited states down to S_1 and T_1, effectively funneling excitation into the same manifold regardless of the initial excitation pathway.

Once the S_1 and T_1 states are populated, they serve as the key players in the ODMR mechanism. Thermal fluctuations in the torsional angles dynamically modulate the SOC strength, creating pathways for ISC between S_1 and the $M_S = \pm 1$ sublevels of T_1. The efficiency of ISC

depends on two key factors: (i) the magnitude of SOC, which depends on the instantaneous molecular conformation, and (ii) the S_1-T_1 energy gap, with ISC rates decaying exponentially as this gap widens. This mechanism is most effective when S_1 and T_1 are nearly degenerate, as small energy gaps enhance the probability of ISC. However, this same condition also increases the likelihood of reverse intersystem crossing (RISC), especially at room temperature. The interplay between ISC and RISC determines the distribution of excited state population. When ISC dominates over RISC, the singlet population is preferentially shelved in the triplet state, leading to spin polarization within the excited state manifold.

The final step in achieving ground-state spin polarization relies on preserving the spin-selective character of the decay pathways from the excited states. Whether relaxation occurs via radiative emission or internal conversion, the transition back to the S_0/T_0 manifold must preserve the spin polarization established in the excited state. Critically, the absence of SOC between S_0 and T_0, a consequence of the nodal structure of the HOMO and SOMO in InveST-bridged diradicals, prevents spin mixing during de-excitation. As a result, the spin polarization generated in the excited state can be efficiently transferred and maintained in the ground state population.

To validate this mechanism, we calculate the rates for ISC, RISC, and emission as functions of molecular conformation, following a strategy proposed in ref. [255]. This begins with constructing a diabatic model by diabatizing the potential energy curves associated with S_0, T_0, S_1, and T_1. The model includes four diabatic states: two singlets, corresponding to a neutral state $|^1N\rangle$ and a multi-resonant charge-transfer state $|^1MRCT\rangle$, and two corresponding triplets, $|^3N\rangle$ and $|^3MRCT\rangle$. The neutral states $|^1N\rangle$ and $|^3N\rangle$ define the reference energy (set to zero). The diabatic energy of $|^1MRCT\rangle$ is set to $2z$ and that of $|^3MRCT\rangle$ is set to $2s$. The singlet states are coupled by a torsion-dependent matrix element $-\tau(\theta)$, while the triplet coupling is given by $-\beta(\theta)$. Following the El-Sayed rule, we set SOC between $|^1N\rangle$ and $|^3MRCT\rangle$, and between $|^3N\rangle$ and $|^1MRCT\rangle$, both through a constant matrix element denoted as V_{SOC}. The diabatic Hamiltonian reads:

$$H = \begin{pmatrix} 0 & 0 & -\tau(\theta) & V_{SOC} \\ 0 & 0 & V_{SOC} & -\beta(\theta) \\ -\tau(\theta) & V_{SOC} & 2z & 0 \\ V_{SOC} & -\beta(\theta) & 0 & 2s \end{pmatrix} + \frac{\hbar\omega_t}{2}(\theta^2 + p_\theta^2) + a\theta^4 \quad (6)$$

where the basis states are ordered as $\{|^1N\rangle, |^3N\rangle, |^1MRCT\rangle, |^3MRCT\rangle\}$, ω_t is the frequency associated with the conformational coordinate, and p_θ is the conjugate momentum. The torsional dependence of the off-diagonal couplings is modeled as $-\tau(\theta) = -\tau_0 \cos(2\theta)\sin(2\theta)$ for the singlet manifold and $-\beta(\theta) = -\beta_0 \cos(2\theta)\sin(2\theta)$ for the triplet manifold. A quartic (anharmonic) restoring potential is employed to mimic the potential energy curves of the ground and excited states vs θ.

To obtain the parameters of the model, a fitting procedure was carried out. The model parameters—τ_0, β_0, ω_t, a, $2z$, and $2s$—were optimized to reproduce the adiabatic potential energy curves as a function of θ obtained from either PPP-RASCI or QD-NEVPT2 calculations. Since these two

methods yield slightly different potential energy curves, independent diabatization procedures were performed for each dataset. During this fitting process, the SOC term V_{SOC} was set to zero. This approximation is justified by the small magnitude of SOC in these systems, which has a negligible effect on the shape of the adiabatic curves. Consequently, the diabatization was carried out independently for the singlet (S_0/S_1) and triplet (T_0/T_1) manifolds. For each manifold, the diabatic parameters were tuned so that the eigenvalues of the model closely matched the corresponding adiabatic curves across the entire range of θ. After completing the parameter fitting, the spin–orbit coupling term V_{SOC}—initially omitted—was reintroduced into the model. In the diabatic picture, V_{SOC} is assumed to be independent of θ and is treated as a constant. Its value was chosen so that the matrix element $|\langle S_1|V_{SOC}|T_1\rangle|$, computed using the eigenstates of the diabatic Hamiltonian, matches the θ-dependent SOC profile obtained from either the PPP-RASCI or QD-NEVPT2 calculations, depending on which dataset was used in the original fit.

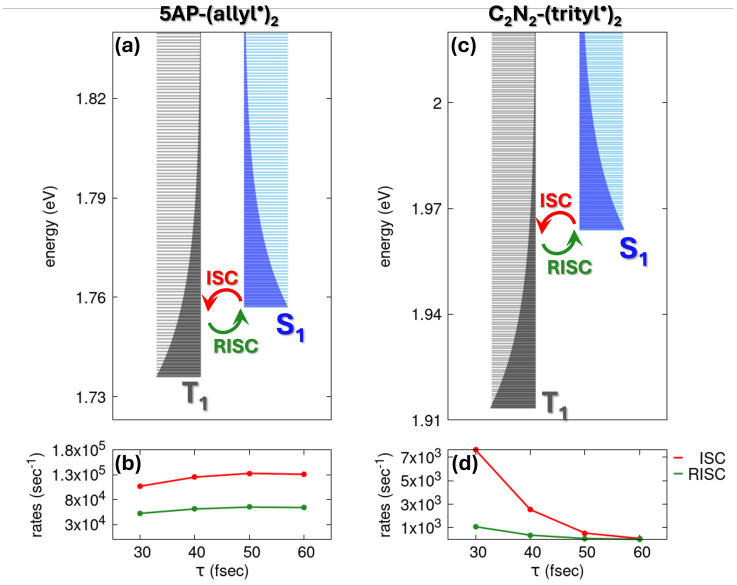

Figure 15: A schematic representation of the vibronic calculation of ISC rates and RISC rates for 5AP-(allyl•)$_2$ (panel a) and C_2N_2-(trityl•)$_2$ (panel c) starting from the CASSCF(4,4)/QD-NEVPT2 results shown in Figure 12 and Figure 13. In both panels, gray and blue lines show the energy of the vibronic triplet and singlet eigenstates, respectively. The global ISC rate is calculated summing all the rates of the S_1 to T_1 processes, averaging on the thermal population of singlet states (graphically represented by the blue shaded area). RISC rates are evaluated from the ISC rate by imposing the microscopic reversibility condition. ISC and RISC rates calculated for different values of the relaxation time τ are reported in panels b and d. Parameters for 5AP-(allyl•)$_2$: $\tau_0 = 0.17$ eV, $\beta_0 = 0.24$ eV, $2z = 1.76$ eV, $2s = 1.74$ eV, $\hbar\omega_t = 8.7 \times 10^{-4}$ eV, $a = -0.15$ eV, $V_{SOC} = -0.09$ eV. Parameters for C_2N_2-(trityl•)$_2$: $\tau_0 = 0.21$ eV, $\beta_0 = 0.22$ eV, $2z = 1.96$ eV, $2s = 1.91$ eV, $\hbar\omega_t = 6.2 \times 10^{-4}$ eV, $a = -0.08$ eV, $V_{SOC} = -0.05$ eV.

ISC and RISC processes are driven by tiny SOC interactions that can be treated perturbatively [256]. To compute the relevant transition rates, we first diagonalize the Hamiltonian in Eq. 6 with V_{SOC} set to zero. Under this approximation, the singlet and triplet manifolds become decoupled, allowing them to be treated separately. The resulting vibronic energy levels in the T_1 and S_1 manifolds are shown as gray and blue lines, respectively, in Figure 15a and c. Since internal conversion is extremely rapid (typically on the order of tens of femtoseconds), we assume that ISC occurs from a thermally equilibrated population of S_1 vibronic states. This thermal distribution is shown by the blue shaded area in Figure 15a and c. Transition rates between singlet and triplet states are calculated using the Fermi Golden Rule $k_{ISC}^{i\to j} = |\langle i|V_{SOC}|j\rangle|^2 S_{ij} 2\pi/\hbar$, where S_{ij} measures the overlap between states $|i\rangle$ and $|j\rangle$[255]. Each state is modeled with a Gaussian lineshape, with width σ related to the inverse of the relaxation time τ as $\sigma = (2\pi\tau\sqrt{2\log 2})^{-1}$. RISC rates are obtained from the corresponding ISC rates using detailed balance.

Panels b and d report ISC and RISC rates for different values of τ. For the 5AP-(allyl$^\bullet$)$_2$ system, ISC rates are on the order of 10^5 s^{-1}, while RISC rates reach 10^4 s^{-1}, with minimal dependence on the τ value because of the small S_1-T_1 gap. In contrast, the C_2N_2-(trityl$^\bullet$)$_2$ system exhibits lower rates, down to 10^3 s^{-1} for both ISC and RISC, due to its smaller SOC and the larger S_1–T_1 energy gap with respect to the 5AP-(allyl$^\bullet$)$_2$. For the C_2N_2-(trityl$^\bullet$)$_2$ system, the calculated ISC and RISC rates tend to converge as the relaxation time τ increases. In particular, at τ = 60 fs, the two processes exhibit nearly identical rate constants. This behavior arises from the combined effect of the narrower Gaussian lineshape (i.e., smaller σ) associated with each vibronic state at longer τ and the larger energy gap between the S_1 and T_1 states compared to 5AP-(allyl$^\bullet$)$_2$, thus reducing overlapping vibronic levels and leading to comparable ISC and RISC efficiencies.

The radiative rate is calculated as $k_{fi} = (\omega_{fi}^3 \mu_{fi}^2)/(3\pi\varepsilon_0\hbar c^3)$, where ω_{fi} is the transition frequency and μ_{fi} is the transition dipole moment between the initial and final states [257]. This rate is calculated as a function of the conformational coordinate θ, yielding a θ-dependent emission rate. We then perform a thermal average over this distribution, weighting each contribution by the energy of the corresponding fluorescent state at that θ value. For 5AP-(allyl$^\bullet$)$_2$, the resulting thermally averaged radiative rate is 3.5×10^7 s^{-1}, whereas for C_2N_2-(trityl$^\bullet$)$_2$ it is essentially zero, as already observed when discussing the calculated oscillator strength as a function of θ.

In summary, among the systems investigated, 5AP-(allyl$^\bullet$)$_2$ emerges as the most promising candidate for realizing optically addressable spin states. This molecule combines a sizable radiative decay rate, a finite ISC rate, and a comparatively slower RISC rate, thus satisfying the key requirements for effective spin polarization via an ODMR mechanism. While the rates for the C_2N_2-bridged diradical align with those obtained from the ab initio-based model, the ISC rates for 5AP-(allyl$^\bullet$)$_2$ are slightly smaller due to the larger S_1–T_1 gap predicted at the PPP level. This highlights the critical role of carefully tuning both the excited-state singlet–triplet energy gap and the SOC strength to engineer optimal optical–spin interfaces in organic diradicals. For completeness, we also evaluated the lowest quintet states at the PPP–RASCI level, finding them higher in energy (1.79 eV for 5AP-(allyl$^\bullet$)$_2$, 1.61 eV for C_2N_2-(trityl$^\bullet$)$_2$, and 2.00 eV for 5AP-(trityl$^\bullet$)$_2$) than the T_1 and S_1 levels, confirming that the photophysics is governed by singlet and triplet excitations, with negligible quintet contribution.

3.3 CT radicals

Apart from molecular qubits, another missing piece of hardware for the physical realization of molecular quantum computers is the molecular switch. Qubits are useless if not linked together in working circuits, with controlled methods to make them interact on command. To allow useful quantum computation, a molecule is needed that can change its magnetic state with nearly 100% efficiency and quickly (at least 10^3 times faster than the gate-application time). Taking inspiration from previous work

on switchable systems [45, 258, 259], we selected the tetrathiafulvalene-ethylene-perchlorotriphenylmethyl (TTF-PTM) donor-acceptor radical molecule, shown in Figure 16 as a candidate for a molecular switch.

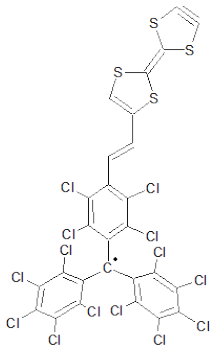

Figure 16: Kekulè structure of the tetrathiafulvalene-ethylen-perchlorotriphenylmethyl (TTF-PTM) radical

The TTF moiety is a strong donor molecule, widely studied as a building block in organic conductors and semiconductors [260–262]. PTM, on the other hand, is a stable radical acceptor, with the unpaired electron shielded by the 15 chlorines that surround the triphenyl group. The molecule of interest in Figure 16 is a donor-acceptor (DA) molecule, with the TTF fragment being the donor and the PTM the acceptor.It is well documented that a change in the solvent of TTF-PTM, specifically an increase in polarity, switches the molecule for a neutral (DA) to a zwitterionic state (D^+A^-) where the radical resides on the TTF unit. The tendency of TTF radicals to dimerize is very well known and indeed in polar solvent dimers of TTF-PTM are formed [45, 48, 258, 263, 264], a situation that can be reversed by another change in the polarity of the environment or by temperature. If the solvent polarity can drive the neutral to zwitterionic switch, it is likely that an applied field can produce a similar effect. In order to demonstrate the capabilities of TTF-PTM as a working molecular switch, we created an essential-state model inspired by previous work on the molecule[48, 263, 264] and attempted to validate and parametrize it against ab initio results. Here we present preliminary results.

3.3.1 Preliminary DFT calculation

We ran preliminary DFT ground state optimization under an electric field oriented along the molecular axis. The calculations were run using the UB3LYP functional and def2-tzvp basis set in QChem 6.0.2 [265]. To define the amount of charge transfer from the D to the A fragments, after optimization, we summed up the Mulliken charges and spin populations on the atoms residing on the three fragments: the TTF unit, the PTM unit, and the ethylene bridge. Results relevant to the spin-distributions are shown in Figure 17.For an electric field ~ 0.004 a.u. the unpaired electron, originally residing on the PTM unit, crosses over to the TTF unit. We mention that this electric field corresponds to $\sim 1 \cdot 10^9$ V/cm, in the range of electric fields that can be generated using a tip.

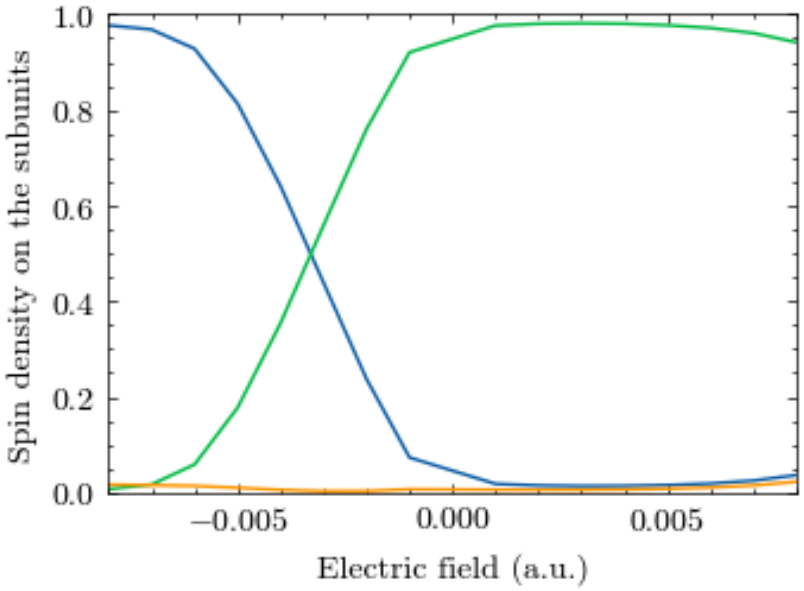

Figure 17: Mulliken spin population projected on the subunits of TTF-ethilen-PTM. Blue line: TTF fragment, green line: PTM fragment, orange line: ethylene fragment.

3.3.2 Essential state model and rate calculation

In line with previous work on the simulation of spectroscopic properties of DA dyes [256, 266] and TTF-PTM [45, 46], we developed an essential state model that contains the essential ingredients to simulate the properties of a switchable molecule. We use a minimal description of two diabatic electronic states, a neutral state $|N\rangle$ and a zwitterionic state $|Z\rangle$, representing the diabatic states D−A and D^+-A^-. A semiclassical vibrational mode is added, characterized by a displacement from the equilibrium position Q (in energy units) and a relaxation energy ε. The switching is possible due to the coupling between the dipole moment of the molecule $\hat{\boldsymbol{\mu}}$ and the electric field $\boldsymbol{E}$. For a molecule oriented along the z axis, only the z component of the electric field and of the dipole moment are relevant, so in the following we neglect the indices ($E = E_z$, $\hat{\mu} = \hat{\mu}_z$). In line with the Mulliken approach, the dipole moment operator is $\hat{\mu} = \mu_0\hat{\rho}$, with μ_0 being the value of the dipole moment of the zwitterionic state and $\hat{\rho} = |Z\rangle\langle Z|$ the ionicity operator [267, 268]. The adiabatic Hamiltonian reads:

$$\hat{H} = (2z_0 - Q - E\mu_0)\hat{\rho} - \tau\hat{\sigma} + \frac{1}{4\varepsilon}Q^2\hat{I} \tag{7}$$

Where $\hat{\sigma} = |N\rangle\langle Z| + |Z\rangle\langle N|$, $2z_0$ is the diabatic energy of the Z state taking the energy of the neutral state N as zero, τ is the diabatic coupling, and $\hat{I}$ is the identity matrix. The eigenvectors of the Hamiltonian are adiabatic Q-dependent electronic states $|G(Q)\rangle$ and $|E(Q)\rangle$. The assumptions for the validity of the model are:

- The two states must be the only states that have a relevant weight in the physics of the switching;
- the vibrational mode must be slow compared to the motion of the electron
- as we are dealing with a semiclassical mode, the switch of the electron must be fast and coherent. As we are dealing with a short-range CT in response to a sudden change of an external electrical field we expect this is the case.

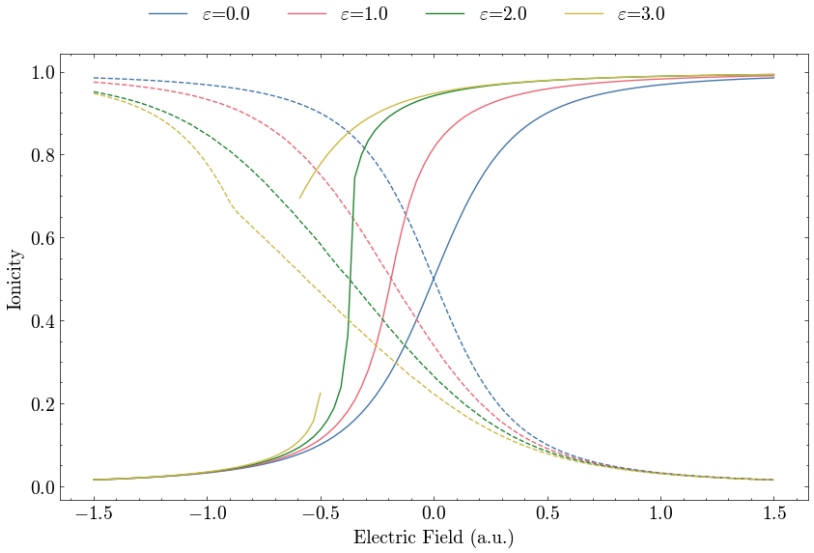

Figure 18: Ionicity of the minimum of the adiabatic states of the minimal model in Eq.7 against the applied external electric field . z=0, τ=1, μ_0 and E in arbitrary units of τ. ε is varied and reported on the top of the figure.Solid lines indicate the ground state, the dashed lines indicate the excited states. Where the line is not surjective, the zone indicates a double minimum for the state.

The properties of the model are analyzed in Figure 18 by varying ε and τ. Varying z only has the effect of rigidly translating the curves along the x axis. Upon increasing ε, the dependence of the ground state ionicity on the field becomes steeper, while the evolution of the excited state ionicity becomes smoother. Quite interestingly, the ground state becomes bistable for $\varepsilon > 2\tau$. This can create a very favorable situation for an applied field in the bistability region; small oscillations around it can cause a rapid change in the position of the electron.

Once the parameters are estimated, it is necessary to simulate the charge-transfer rate. We aim to do that by calculating the non-radiative electron-transfer mechanism using classical Marcus theory [269]:

$$k_{nr}^{M} = \frac{2\pi}{\hbar} \frac{\tau^2}{\sqrt{\pi \lambda T k_B}} e^{-\frac{1}{2}\frac{(\Delta E_{NZ}+\lambda)^2}{\lambda^2 k_B^2 T^2}} \tag{8}$$

where λ is the diabatic reorganization energy, so that $\Delta E_{NZ} + \lambda$ is the energy barrier between the two states. As a first guess, we estimate this energy in terms of the relaxation energy of the ab initio adiabatic vibrational modes, so the convention $\varepsilon = \lambda$ is taken.

3.3.3 Parametrization

The parametrization of the model Hamiltonian is a delicate issue that can dramatically change the calculated results. In the past, to reproduce the correct photophysics, a parametrization based on experimental spectra led to the use of electronic parameters $2z_0 = 0.45$ eV and $\tau = 0.1$ eV [48]. This parametrization allowed for the reproduction of the low-intensity CT band that can be seen in Figure 19 around 900 nm in DCM, as well as the photophysical behavior of the molecule in different solvents [48, 258]. The same band was used in this Chapter as a reference for the ab initio results.

A first brute-force way to parametrize the system is based on unrestricted TDDFT calculations. Under the hypothesis that only the two diabatic

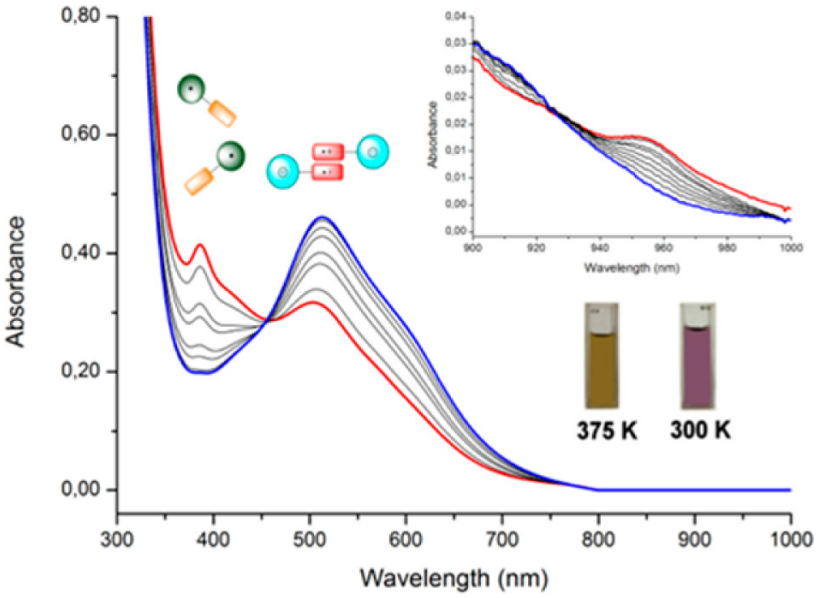

Figure 19: Experimental absorption spectra of TTF-PTM in DCM (0.1 mM) at 375 (red line), 365, 355, 350, 345, 340, 330, 320, and 300 K (blue line). As seen in the zoomed images in the upper right corner, at 900 nm (1.37 eV) a weak absorption signal appears at higher temperatures, where the system is not dimerized. This is the intramolecular CT transition of interest. Adapted with permission from Ref. [48]. Copyright (2013) American Chemical Society.

states N and Z are mixed to generate the first adiabatic TDDFT transition, it is possible to extract from adiabatic results important parameters as:

$$\rho_G = \frac{1}{2}(1 - \sqrt{1 - 4R}) \tag{9}$$

$$\tau = \sqrt{\rho(1-\rho)}\Delta E_{EG} \tag{10}$$

$$z_0 = \sqrt{\frac{\Delta E_{EG}^2}{4} - \tau^2} \tag{11}$$

with $R = \frac{\beta^2}{4\beta^2+1}$, $\beta = \frac{\mu_{EG}}{\Delta\mu}$, μ_{EG} being the TDDFT transition dipole moment between the ground state and the CT state, $\Delta\mu = \langle E|\,\hat{\mu}\,|E\rangle - \langle G|\,\hat{\mu}\,|G\rangle$ being the mesomeric dipole moment, and $\rho_G = \langle G|\,\hat{\rho}\,|G\rangle$.

Another approach relies on the direct diabatization of DFT, TDDFT, or post-HF results, by constraining specific expectation values of the density matrix, such as constrained-DFT-CI or the Boys algorithm. The latter defines the diabatic states $\{i\}$ that maximize the function:

$$f_{FB} = \sum_{ij} \left|\langle i|\,\hat{\mu}\,|i\rangle - \langle j|\,\hat{\mu}\,|i\rangle\right|^2 \tag{12}$$

Note that the diabatic basis so obtained is not diagonal in the dipole operator unless we are taking exactly 2 states and all the matrix elements of the dipole moment operator are oriented along the same axis. For these reasons, it is extremely improbable to obtain a basis in which the dipole moment operator is diagonal, and so post-diagonalization procedures are needed.

As for the vibrational parameters ε, unfortunately the only viable ab initio possibility is to rely on TDDFT results.

3.3.4 Results

The molecule was optimized using the QChem 6.0.2 Software at the B3LYP/def2-SVP level of theory. Then calculations were executed at the B3LYP/def2-TZVP level of theory. The results for the TTF-PTM dimer with different functionals are shown in Table 7.

Table 7: TDDFT results for the CT state of TTF-PTM at different functionals using def2-svp, RIJK with Automatic generated auxiliary basis set.

	ΔE_{TDDFT}	$\lvert\Delta\mu\rvert$	$\lvert\mu_{EG}\rvert$	ρ	τ	$2z_0$	$\langle\hat{S}^2\rangle$
CAM-B3LYP	2.151	17.8825	1.7385	0.009	0.205	2.111	2.217
B3LYP	0.918	49.0288	4.3851	0.008	0.081	0.904	2.589
B2PLYP	1.591	37.7369	3.8758	0.010	0.160	1.558	1.288
M062X	2.095	29.7116	2.3806	0.006	0.166	2.069	1.693
ωB97X	2.416	8.3611	0.7207	0.007	0.205	2.381	2.630

As can be seen, the calculated transitions are offset from the experimental measurement by at least 0.5 eV, a large number even considering the possible redshift caused by the solvent. Moreover, the states are not pure.

Before setting up post-HF calculations, we tried to extrapolate some results using cDFT and cDFT-CI [76]. The calculations were executed by building up a neutral "diabatic" state where the electron is completely confined on the PTM subunits by imposing the projected charges on the PTM units to be zero, and the projected spin multiplicity to be 2; and a zwitterionic state where the transfer of one electron from TTF to PTM gives the molecule a lone pair on the PTM units and an unpaired electron on the TTF units. The calculations were done using QChem 6.0.2 software [265], various different functionals, and the def2-SVP basis set; selected results are shown in Table 8. The method allows us to build diabatic states directly, and so τ and $2z_0$ are obtained without mathematical derivation. As can be seen, there is great variability on the results, with the ωB97V functional, apparently being best in line with experimental data.

Functionals	τ (eV)	$2z_0$ (eV)	$\lvert\Delta\mu\rvert$ (a.u.)	$\lvert\mu_{ZN}\rvert$ (a.u.)
B3LYP	1.28	2.30	45.11	6.67
CAM-B3LYP	-1.03	2.79	45.78	2.81
ωB97V	-0.22	1.53	33.13	5.93

Table 8: cDFT-CI diabatic results for TTF-PTM at different functionals using def2-svp, RIJK with Automatic generated auxiliary basis set on Qchem 6.0. 1. Notice that the diabatic dipole operator has not null coupling elements even in the diabatic basis.

We also attempted a parametrization relying on post-HF approaches. First of all, we calculated the orbitals of TTF-PTM at the geometry optimized at the B3LYP/def2-SVP level of theory and the ROHF calculation with the cc-pvdz basis set and RI approximation using an auxiliary basis set generated on the fly using the RICD method. All calculations were executed using Molcas 8 software [270]. Frontier orbitals are shown in Figure 20.

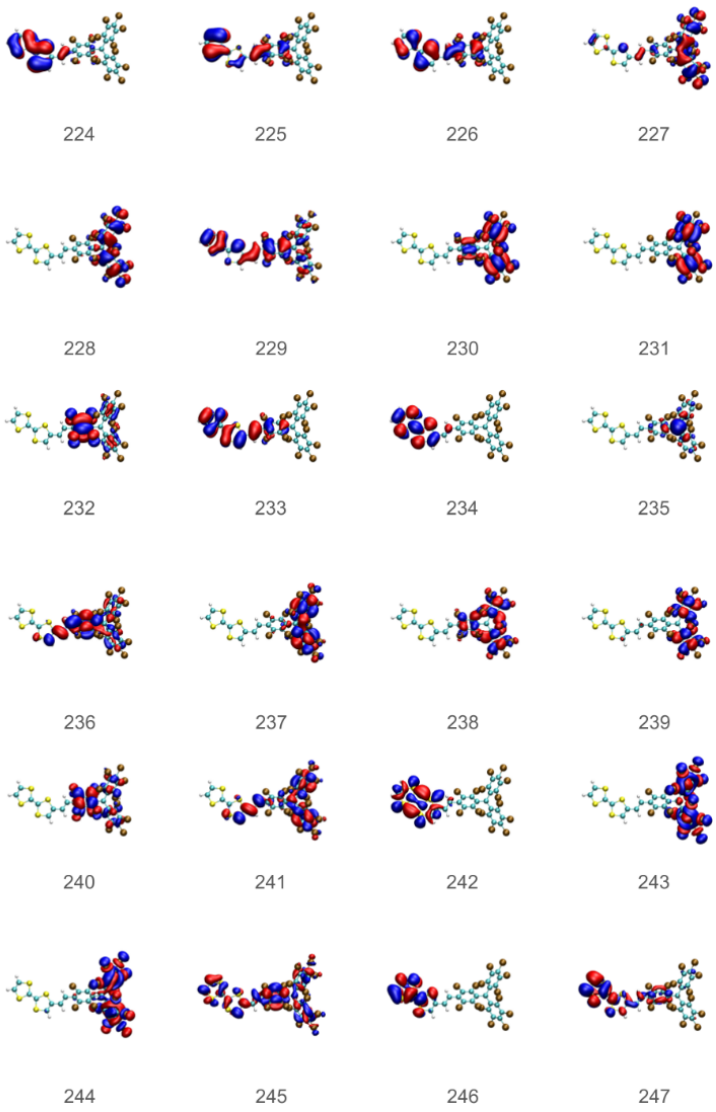

Figure 20: ccpvdz ROHF molcas orbitals obtained with Molcas progroam. Visualization. isovalues: 0.04 A. HOMO: 234. SOMO:235. LUMO:236.

Simulating charge-transfer transitions is a tough task. Ideally, it is necessary to include the fewest possible orbitals that can reproduce the character of the donor and the acceptor, while ensuring an active space large enough to regain static correlation. We started from a minimal description of HOMO and SOMO, and tried to include relevant orbitals as well (localized HOMO-n orbitals and LUMO, LUMO+m orbitals). We started with a CASSCF(3,3) calculation, and the energy was corrected using MC-PDFT with tPBE as a functional and CASPT2 with 0.25 IPEA shift and 0.3 imaginary shift, cutting a different number of orbitals to understand the effect, as for bigger AS not all orbitals can be considered when employing CASPT2. Results are reported in Table 9. All results show a low D_0 to D_1 transition energy, with a lowest value of 1.4 eV for the MC-PDFT method, comparable with the CASPT2 results of 1.8 eV without deleting virtual orbitals. On the other hand, other PT2 corrections lead to larger values.

The NTO analysis confirms that this is the CT transition we are looking for, as seen in Figure 21, where the hole is located entirely on the donor TTF units while the particle resides on the PTM.

Table 9: Results for CASSCF(3,3)/MCPDFT and CASSCF(3,3)/CASPT2 calculations on TTF-PTM, RICD approximation and cc-pvdz basis set. Various deletion of high-lying virtual orbitals were done to evaluate the changes.

CASSCF		MCPDFT T:PBE		
Eh	Tr.En. (eV)	Eh	Δ E (H)	Tr.En. (eV)
-9048.301	0.000	-9062.598	-14.297	0.000
-9048.198	2.788	-9062.546	-14.348	1.400
-9048.158	3.857	-9062.523	-14.364	2.037
-9048.117	4.983	-9062.506	-14.390	2.477
-9048.086	5.805	-9062.426	-14.339	4.669

CASPT2 DEL.400			CASPT2 DEL.200			CASPT2 DEL.0		
Eh	Δ E (H)	Tr.En. (eV)	Eh	Δ E (H)	Tr.En. (eV)	Eh	Δ E (H)	Tr.En. (eV)
-9049.646	-1.345	0.000	-9052.894	-4.593	0.000	-9054.313	-6.013	0.000
-9049.565	-1.367	2.182	-9052.818	-4.621	2.042	-9054.246	-6.048	1.835
-9049.523	-1.365	3.314	-9052.778	-4.620	3.146	-9054.204	-6.046	2.956
-9049.512	-1.395	3.624	-9052.771	-4.654	3.327	-9054.200	-6.083	3.088
-9049.478	-1.392	4.541	-9052.740	-4.653	4.179	-9054.162	-6.075	4.119

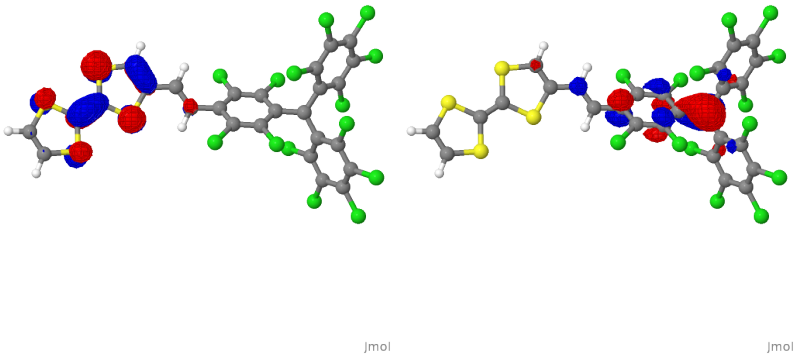

Figure 21: NTO for the CASSCF(3,3) calculations of ttf-ptm. Left: hole. Right particles. eigenvalue, 0.75, with a relative weight of 99%.

The states were diabatized using the Boys algorithm using the density matrix calculated at the CASSCF level of theory, while for the energy we used the CASSCF, MC-PDFT, and CASPT2 energies. The results reported in Table 10 show that the MC-PDFT diabatization seems to best reproduce the energy of the CT band in the experimental spectra.

	CASSCF	MCPDFT	CASPT2 DEL.0
$2z_0$ (eV)	2.754	1.383	1.812
τ (eV)	0.217	0.109	0.143
$\Delta\lvert\mu\rvert$	35.38	33.67	33.67
$\lvert\mu_{ZN}\rvert$	2.15	3.75	3.75

Table 10: Results of the diabatization for three of the cases reported in Table 9. The diabatic parameters are obtained using the Boys algorithm as implemented in molcas.

The results do not improve as we increase the active space. Indeed, upon extending the active space, several mixed CT/localized transitions can be found. Results for the calculations on the (5,5) and (7,7) AS are listed in Table 11 and Table 12. The lowest transition energy is located at too high energies (1.89 eV for CAS(5,5)/MC-PDFT and 2.64 eV for

CAS(7,7)/MC-PDFT).

Table 11: Results for CASSCF(5,5)/MCPDFT and CASSCF(5,5)/CASPT2 calculations on TTF-PTM, RICD approximation and cc-pvdz basis set.

CASSCF		MCPDFT			CASPT2 DEL.0		
Eh	Tr.En. (eV)	Eh	Δ E (H)	Tr.En. (eV)	Eh	Δ E (H)	Tr.En. (eV)
-9048.344	0.000	-9062.601	-14.258	0.000	-9054.314	-5.970	0.000
-9048.235	2.934	-9062.532	-14.296	1.894	-9054.232	-5.997	2.219
-9048.215	3.499	-9062.486	-14.272	3.122	-9054.198	-5.983	3.155
-9048.169	4.729	-9062.518	-14.349	2.264	-9054.210	-6.041	2.813
-9048.147	5.319	-9062.495	-14.347	2.894	-9054.187	-6.040	3.433
-9048.122	6.014	-9062.488	-14.367	3.065	-9054.206	-6.084	2.926

Table 12: Results for CASSCF(7,7)/MC-PDFT and CASSCF(5,5)/CASPT2 calculations on TTF-PTM, RICD approximation and cc-pvdz basis set.

CASSCF		MCPDFT			CASPT2 DEL.100		
Eh	Tr.En. (eV)	Eh	Δ E (H)	Tr.En. (eV)	Eh	Δ E (H)	Tr.En. (eV)
-9048.366	0.000	-9062.593	-14.227	0.000	-9053.755	-5.389	0.000
-9048.238	3.466	-9062.496	-14.257	2.638	-9053.656	-5.418	2.687
-9048.237	3.511	-9062.480	-14.243	3.069	-9053.640	-5.403	3.128
-9048.203	4.418	-9062.475	-14.272	3.196	-9053.631	-5.427	3.377
-9048.185	4.899	-9062.486	-14.301	2.885	-9053.661	-5.476	2.549
-9048.174	5.201	-9062.443	-14.268	4.063	-9053.589	-5.415	4.500
-9048.154	5.746	-9062.429	-14.276	4.415	-9053.581	-5.427	4.727
-9048.145	6.001	-9062.488	-14.343	2.842	-9053.610	-5.465	3.930
-9048.142	6.093	-9062.479	-14.338	3.074	-9053.605	-5.463	4.088
-9048.130	6.396	-9062.463	-14.333	3.506	-9053.604	-5.474	4.098
-9048.109	6.971	-9062.424	-14.315	4.585	-9053.555	-5.446	5.416
-9048.108	7.014	-9062.462	-14.354	3.544	-9053.570	-5.462	5.025
-9048.102	7.160	-9062.475	-14.373	3.196	-9053.579	-5.477	4.777
-9048.091	7.452	-9062.391	-14.299	5.477	-9053.563	-5.471	5.224
-9048.088	7.558	-9062.452	-14.365	3.812	-9053.558	-5.471	5.344
-9048.085	7.611	-9062.448	-14.363	3.914	-9053.569	-5.483	5.053

To set up the model and calculate the radiation-less rates, it is still necessary to calculate the diabatic relaxation energy ε. In this early stage of the work, we show preliminary results obtained by calculating the adiabatic vibrational modes at the DFT B3LYP level of theory using the Orca software, with the D3BJ dispersion correction and the RIJCOSX approximation with the def2/J auxiliary basis set. The estimated relaxation energy amounts to 0.117 eV. An effective vibrational mode is introduced that accounts for the whole relaxation energy of the system. We show here the results of a couple of calculations, adopting for the electronic parameters the TDDFT B3LYP results in Table 7, the cDFT-CI/ωB97X values in Table 8, and the CAS(3,3)/MC-PDFT results in Table 10. To visualize the switch, the ionicity of the ground and excited state against an electric field parallel to the axis of the molecule is shown in Figure 22. Bistability is not observed for any parametrization, and apart from a different crossing point, all curves display the switch around $8{\cdot}10^6$ V/cm, within the experimentally accessible range.

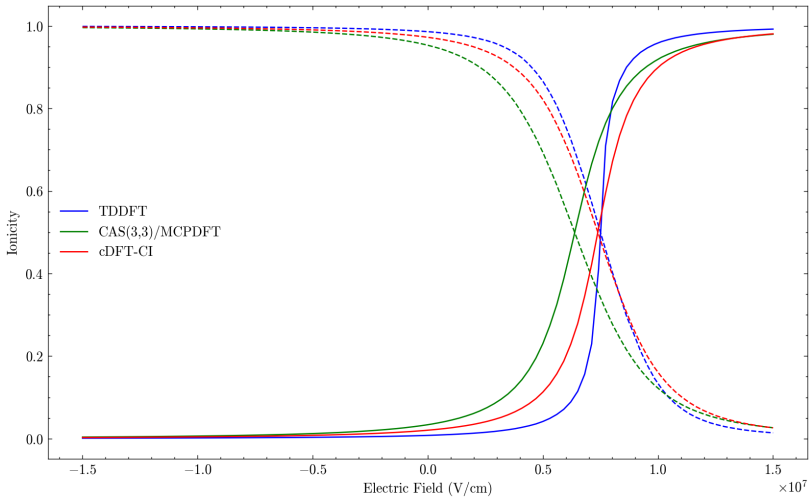

Figure 22: Ionicity of the ground states (solid lines) and excited states (dashed lines) for TDDFT/B3LYP (blue), CAS(3,3)/MC-PDFT with T:PBE (green) and cDFT-CI/ωB97X (red) using the semiclassical model in Eq. 7 and the values in the preceding tables.

Using the classical Marcus equation, we calculated the rates of the charge-transfer processes as a function of the electric field. We are interested in having a switch that can interconvert fast from one state to another without the inverse process being competitive. Results in Figure 23 show that a range of electric field values can always be found such that the rate of one process is ultrafast (in the range of fs^{-1}) with the inverse process at least 3 orders of magnitude slower. However, the inverse process (ps timescale) is still too fast for applications in experiments that, typically relying on magnetic techniques, have much longer timescales (μs). The window improve at a low temperature, as in Figure 24.

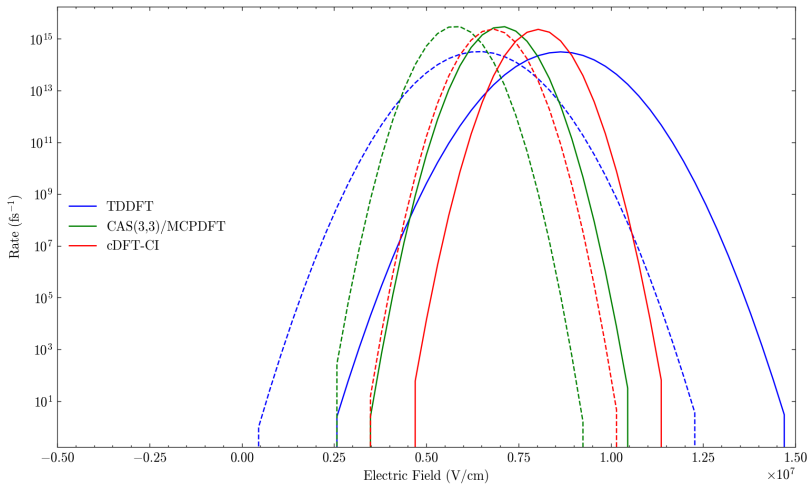

Figure 23: Charge-transfer rates for the $N \rightarrow Z$ processes (solid lines) and for the inverse process (dashed lines) for TDDFT/B3LYP (blue), CAS(3,3)/MCPDFT with T:PBE(green) and cDFT-CI/ωB97X (red) using the semiclassical model in 7, the Marcus rate equation in 8 at Room temperature (300 K) and the values in the precedent tables.

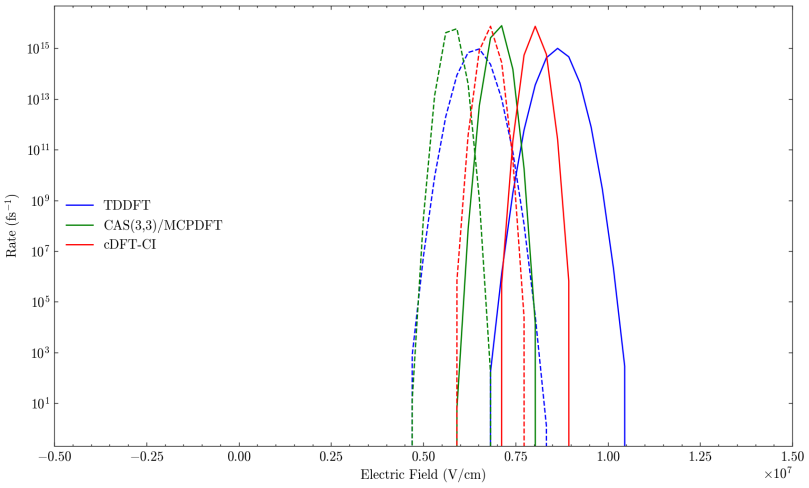

Figure 24: Charge-transfer rates for the $N \rightarrow Z$ processes (solid lines) and for the inverse process (dashed lines) for TDDFT/B3LYP (blue), CAS(3,3)/MCPDFT with T:PBE(green) and cDFT-CI/ωB97X (red) using the semiclassical model in 7, the Marcus rate equation in 8 at Low temperature (30 K) and the values in the precedent tables.

In conclusion, while this project is still ongoing, the preliminary results indicate that the TTF–PTM molecule shows the essential features to function as a molecular switch. The coexistence of two well-defined magnetic states, whose population can be selectively controlled through the application of an external electric field, highlights the potential of this system for molecular-scale information processing. These findings suggest that the interplay between charge transfer, spin localization, and field-induced stabilization could be exploited to achieve reproducible and reversible switching on ultrafast timescales.

Nevertheless, further work is required to consolidate these observations. In particular, additional electronic-structure calculations aimed at deriving reliable model parameters will be crucial to refine the picture. Equally important is the development of an experimental setup capable of validating the predicted switching behavior under realistic conditions. These steps represent mandatory milestones before proposing TTF–PTM as an operational molecular switch. Despite the remaining challenges, the encouraging preliminary evidence strongly supports the continuation of this research direction.

Appendix

3.A PPP approximation schemes

PPP-CI with PPP-HF-MOs

The operators $\hat{b}^{(\dagger)}_{k\sigma}$ that annihilate (create) an electron with spin σ in the k-th molecular orbital (MO) can be written as linear combination of the $\hat{a}^{(\dagger)}_{\mu\sigma}$ (on-site) operators:

$$\hat{b}_{k\sigma} = \sum_{\mu} c_{\mu,k}\hat{a}_{\mu\sigma} \tag{3.A.1}$$

$$\hat{b}^{\dagger}_{k\sigma} = \sum_{\mu} c_{\mu,k}\hat{a}^{\dagger}_{\mu\sigma} \tag{3.A.2}$$

where the expansion coefficients are obtained upon diagonalization of the Fock operator in Eq. 3, main text. With this transformation, the PPP model Hamiltonian is rewritten on the MO basis as:[165]

$$\begin{aligned}
\hat{H}^{CI}_{PPP} &= \sum_{ij}\sum_{\sigma}\left(\sum_{\mu}\varepsilon_{\mu}c_{\mu,i}c_{\mu,j}\right)\hat{b}^{\dagger}_{i\sigma}\hat{b}_{j\sigma} \\
&- t\sum_{ij}\sum_{\sigma}\left[\sum_{\mu\nu,\mu\neq\nu}\left(c_{\mu,i}c_{\nu,j}+c_{\nu,i}c_{\mu,j}\right)\right]\hat{b}^{\dagger}_{i\sigma}\hat{b}_{j\sigma} \\
&+ \sum_{ijkl}\left(\sum_{\mu}U_{\mu}c_{\mu,i}c_{\mu,j}c_{\mu,k}c_{\mu,l}\right)\hat{b}^{\dagger}_{i\uparrow}\hat{b}_{j\uparrow}\hat{b}^{\dagger}_{k\downarrow}\hat{b}_{l\downarrow} \\
&+ \sum_{ijkl}\sum_{\sigma\sigma'}\left(\sum_{\mu,\nu,\mu\neq\nu}\frac{V_{\mu\nu}}{2}c_{\mu,i}c_{\mu,j}c_{\nu,k}c_{\nu,l}\right)\hat{b}^{\dagger}_{i\sigma}\hat{b}_{j\sigma}\hat{b}^{\dagger}_{k\sigma'}\hat{b}_{l\sigma'} \\
&- \sum_{ij}\sum_{\sigma}\left[\sum_{\mu,\nu,\mu\neq\nu}\frac{V_{\mu\nu}}{2}\left(Z_{\nu}c_{\mu,i}c_{\mu,j}+Z_{\mu}c_{\nu,i}c_{\nu,j}\right)\right]\hat{b}^{\dagger}_{i\sigma}\hat{b}_{j\sigma}
\end{aligned} \tag{3.A.3}$$

where i, j, k and l run on the MOs, while μ and ν run on the AOs, and all the other symbols are defined in the main text, Section 2. The above Hamiltonian is written on the basis defined by the ground state configuration and the configurations obtained by accounting for a single electron moved from the occupied MO to the virtual MO (i.e., single CI case) or also accounting for double, triple, etc. excitations. Exact diagonalization[89] of the Hamiltonian in the selected basis returns the correlated eigenstates.

PPP-RASCI

To briefly describe it, in PPP-RASCI scheme the HF-MOs obtained from the PPP Hamiltonian are divided into three subspaces: RAS1, RAS2, and RAS3, ordered by increasing energy, and exactly as in the canonical RASCI approaches[149, 150], RAS1 includes occupied orbitals, RAS2 comprises a mix of occupied and low-lying virtual MOs, and RAS3 is composed of higher-energy virtual orbitals. This is extended through the hole-particle approximation, which allows a fixed number of excitations

out of RAS1 (holes) and a fixed number of electrons (particles) in RAS3. This increases the correlation effects captured in the RASCI solution.

The PPP SOMO-LUMO exchange integral

The $SOMO_1$-LUMO (equivalently $SOMO_2$-LUMO) exchange integral reads:

$$K_{SOMO_1-LUMO} = \frac{e^2}{4\pi\varepsilon_0}\left\langle \psi_{SOMO_1}(1)\psi_{LUMO}(2)\left|\frac{1}{r_{12}}\right|\psi_{LUMO}(1)\psi_{SOMO_1}(2)\right\rangle \tag{3.A.4}$$

By expanding the MOs on the $2p_z$ basis and adopting the zero differential overlap approximation, Eq. 3.A.4 becomes:

$$K_{SOMO_1-LUMO} = \sum_{\mu\nu} c_{SOMO_1,\nu}c_{LUMO,\nu}c_{LUMO,\mu}c_{SOMO_1,\mu}V_{\nu\mu} \tag{3.A.5}$$

where the double sum runs over the atomic orbitals, $c_{SOMO_1,\nu}$ is the coefficient of ν atomic orbital on the $SOMO_1$ ($c_{LUMO,\nu}$ is the same for LUMO) and $V_{\nu\mu}$ is the electrostatic repulsion between electrons on sites μ and ν, as introduced in Eq. 3. Looking at Eq. 3.A.4, the exchange energy becomes zero when SOMO and LUMO orbitals are disjoint, though it can remain small even when some overlap is present.

Quantum Treatment of the Torsional Degree of Freedom θ

With the diabatic model fully parametrized, we proceeded to compute the ISC (and RISC) rates. Due to the extremely small S_1–T_1 energy gap typical of InveST-bridged diradicals, an adiabatic treatment of the torsional coordinate is inadequate for accurately describing ISC dynamics. Instead, a fully quantum mechanical treatment of θ was adopted. To this end, the diabatic Hamiltonian was written on the basis obtained as the direct product of the four electronic diabatic states times the eigenstates of the harmonic oscillator associated with the θ-dependent torsional potential. The dimensionless conformational coordinate can be written as:

$$\theta = (a^\dagger + a)/\sqrt{2} \tag{3.A.6}$$

where $a^\dagger(a)$ is the bosonic creation (annihilation) operator. The infinite harmonic oscillator basis must be truncated to a large enough number of states to ensure convergence of the calculated quantities. Due to the very low frequency associated with the conformational mode, a large basis is required. In our case, 280 vibrational states were retained, resulting in a total Hamiltonian dimension of 560. Moreover, we used a polynomial expansion of $\cos 2\theta \sin 2\theta$, and, consistently with the quartic expansion of the potential, we truncated it at the third order:

$$\cos 2\theta \sin 2\theta \simeq 2\theta - \frac{8}{3}\theta^3 \tag{3.A.7}$$

Diagonalizing the resulting vibronic Hamiltonian with $V_{SOC} = 0$ provides the singlet and triplet vibronic eigenstates used for rate calculations.

Once these eigenstates are obtained, ISC and RISC rates are evaluated using Fermi Golden Rule.

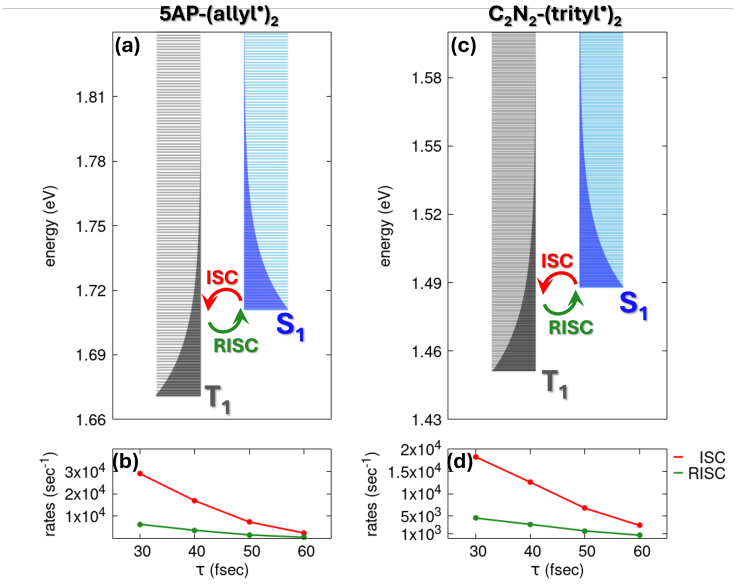

Figure 3.A.1: A schematic representation of the vibronic calculation of ISC rates and RISC rates for 5AP-(allyl$^\bullet$)$_2$ (panel a) and C_2N_2-(trityl$^\bullet$)$_2$ (panel c) starting from the PPP results shown in Figs. 2 and 3, main text. In both panels, gray and blue lines show the energy of the vibronic triplet and singlet eigenstates, respectively. The global ISC rate is calculated summing all the rates of the S_1 to T_1 processes, averaging on the thermal population of singlet states (graphically represented by the blue shaded area). RISC rates are evaluated from the ISC rate by imposing the microscopic reversibility condition. ISC and RISC rates calculated for different values of the relaxation time τ are reported in panels b and d. Parameters for 5AP-(allyl$^\bullet$)$_2$: $\tau_0 = 0.18$ eV, $\beta_0 = 0.21$ eV, $2z = 1.71$ eV, $2s = 1.67$ eV, $\hbar\omega_t = 1.3 \times 10^{-3}$ eV, $a = -0.15$ eV, $V_{SOC} = -0.09$ eV. Parameters for C_2N_2-(trityl$^\bullet$)$_2$: $\tau_0 = 0.20$ eV, $\beta_0 = 0.22$ eV, $2z = 1.49$ eV, $2s = 1.45$ eV, $\hbar\omega_t = 6.9 \times 10^{-4}$ eV, $a = -0.23$ eV, $V_{SOC} = -0.04$ eV.

The vibronic energy levels within the T_1 and S_1 manifolds, obtained by diagonalizing the vibronic Hamiltonian based on parameters fitted to the PPP-derived adiabatic potential energy curves, are shown as gray and blue lines in Figure 3.A.1, panels a and c, respectively. The corresponding ISC and RISC rates, computed for various relaxation times τ, are displayed in panels b and d. To complement the ISC and RISC analysis, we also evaluated the radiative decay rates from the S_1 and T_1 states using PPP-derived transition energies and transition dipole moments. As observed in the main text when discussing the oscillator strength of 5AP-(allyl$^\bullet$)$_2$ as a function of the torsional angle θ (cf. Fig. 2e, main text), the PPP model underestimates transition dipole moments compared to multireference ab initio methods (CASSCF/QD-NEVPT2). This discrepancy is reflected in the computed radiative rate, which amounts to 2.2×10^4 s^{-1} at the PPP level, in contrast to 3.5×10^7 s^{-1} from CASSCF/QD-NEVPT2 calculations. For the C_2N_2-(trityl$^\bullet$)$_2$ system, both S_1 and T_1 remain optically dark due to the symmetric nature of the InveST core, leading to vanishing transition dipole moments and, consequently, negligible radiative rates even at the PPP level.

Chirality-Induced Spin Selectivity

4

CISS is an intriguing yet poorly understood phenomenon observed when electrons travel through a chiral medium or molecule. In the first part of this chapter, we propose a current-constrained approach to drive a current through a linear Hubbard chain of twisted p orbitals, thus simulating electron motion through a chiral molecular system. CISS can be addressed in systems with correlated electrons coupled to non-adiabatic molecular vibrations. Sizable CISS responses are obtained in some parameter space, with a clear amplification of CISS in non half-filled systems. Peierls vibrations play a special role: CISS cannot be observed in a Hubbard chain in the lack of next nearest neighbor interactions, but an out-of-equilibrium stretching mode can lead to finite polarization even in these systems. In the second part of the chapter, we present a protocol to extrapolate Hubbard model parameters from ab initio results. A particular emphasis is given to the ab initio calculation that supports the validity of the protocol. *

4.1 A minimal model through the understanding of CISS

4.1.1 Introduction

Chirality, the property of systems not superimposable to their specular image, is intrinsically connected to symmetry[271]: chiral systems do not have roto-reflection axes of any order, including reflection planes and inversion centers. This requirement has a profound link with the nature of electric and magnetic fields that, corresponding to polar and axial vectors, respectively, may only mutually interact in chiral systems. The differential emission of left and right circularly polarized light (CPL) is a very hot topic these days, mainly in view of its applicative potential.[272–274] Molecular systems, due to their small size compared with the wavelength of light, typically have extremely small dissymmetry factors, orders of magnitude smaller than required for useful applications.[275] Efforts to amplify the CPL response exploit liquid crystals, plasmonic and/or supramolecular structures.[92]. Enantioselective interactions, the preferential interaction between enantiomeric species, are well-known in chemistry, providing the basis for asymmetric synthesis. [276–281]. The electron spin itself is non-chiral, but a moving electron carrying a spin is chiral[271] and therefore can specifically interact with chiral

* The first part of this chapter is based on work published in collaboration with the group of Prof. Stefano Carretta: Savi, L.; Celada, L.; Phan Huu, D. K. A.; Chiesa, A.; Carretta, S.; Painelli, A. Chirality-Induced Spin Selectivity: A Minimal Model. *J. Phys. Chem. Lett.* **2025**, 9107–9115. The work is presented in its entirety. The second part of the chapter consists of calculations performed to validate aspects of a model developed by collaborators in the Chemistry and Phyisics deparment: Phan Huu, D. K. A.; Cantarella, A.; Bonfà, P.; Savi, L.; Chiesa, A.; Painelli, A.; Carretta, S. ab initio Parametrization of a Generalized Hubbard Model in a Molecule Displaying Chirality-Induced Spin Selectivity. *Commun Mater* **2025**, *6* (1), 107. The results are reported here with the minimum context necessary to understand the rationale of the work.

molecules. This is the heart of the phenomenon dubbed *chirality induced spin selectivity* (CISS), that describes the differential transmission of spin up and spin down electrons traveling through a chiral medium.[282] CISS was observed when photoemitted electrons travel through layers of chiral molecules,[283] when a current is driven through chiral self-assembled monolayers[284] or through single chiral molecules,[285] and, more recently, when an electron travels through a molecule via photoinduced electron-transfer.[286–288] The issue here is not the observation of CISS, that is predictable in terms of symmetry considerations, the astonishing and so far not fully understood observation is the amount of CISS, leading to spin polarization well beyond 50%.

CISS requires the breaking of time-reversal symmetry, as guaranteed by traveling electrons, as well as the breaking of the spin degeneracy, as made possible by spin-orbit coupling (SOC).[289] In organic molecules, SOC is tiny,[282, 290] and several strategies for its amplification, as needed to explain the large spin polarizations observed experimentally, have been proposed, relying on electron-electron interactions,[289, 291, 292] electron-vibration coupling,[293, 294] quantum interference,[295] polaronic effects,[296–298] geometrical curvature in helical atomic chains,[299, 300] the close proximity to conical intersections,[301–303] and dephasing phenomena,[289, 304] to name just a few examples.

Modeling CISS is nontrivial not only because of the tiny and somewhat elusive nature of SOC but also because it requires addressing traveling electrons. To observe CISS, approaches must be devised to drive electrons through the system, either driving an electric current or via photoexcitation. Of course, the outcome of the simulation will vary depending on the way the system is prepared, giving rise to a large number of different approaches with sometimes contrasting results. Here, we propose forcing electron motion through the system exploiting a strategy that, to the best of our knowledge, has not been applied to CISS yet. Specifically, we rely on a current-constrained (CC) approach, which imposes a current through a system via the mathematical trick of Lagrange multipliers,[305–307] offering an easy and flexible way to mimic the electron motion through a molecule. Unlike conventional non-equilibrium Green's function methods [308, 309] that impose open boundary conditions through reservoir self-energies and often employ Büttiker probes to simulate dephasing and spin-flip scattering on an energy- and bias-resolved basis,[310] the CC formalism retains a closed-circuit, many-body perspective by enforcing a prescribed steady-state current through Lagrange multiplier constraints on bond-current operators. This choice obviates the need to specify chemical potentials or Fermi distributions for explicit leads and probes, embedding the non-equilibrium within the variational ground state of the augmented Hamiltonian. As a result, the CC formalism requires only the explicit form of the system Hamiltonian to compute the steady-state current, obviating the need to derive reservoir self-energies for each interaction, allowing one to explore regimes of strong interaction, such as photo-driven currents or persistent loop currents within a unified computational framework. Although non-equilibrium Green's function approaches offer direct control over bias voltage, temperature, and dephasing strength through adjustable self-energies and probe couplings,[311] the CC method trades this flexibility for a direct handle on the current magnitude, with the effective voltage drop inferred via

phenomenological relaxation parameters. CC provides complementary insights into correlation-driven spin polarization phenomena without recourse to explicit reservoirs and is therefore particularly well suited for the theoretical investigation of correlated transport in chiral systems.

4.1.2 The toy model

We consider the simplest model for correlated electrons, a linear Hubbard chain composed of N (typically 4) sites along the z axis. Structurally, the system is non-chiral, but electronic chirality, or electrohelicity,[312, 313] is introduced by accounting for a single p-type orbital on each site. The orbital is perpendicular to z, but twisted along the chain so that the orbital residing on site $i+1$ is rotated in the xy plane by an angle θ_i vs the orbital on site i, as shown in Figure 1a.

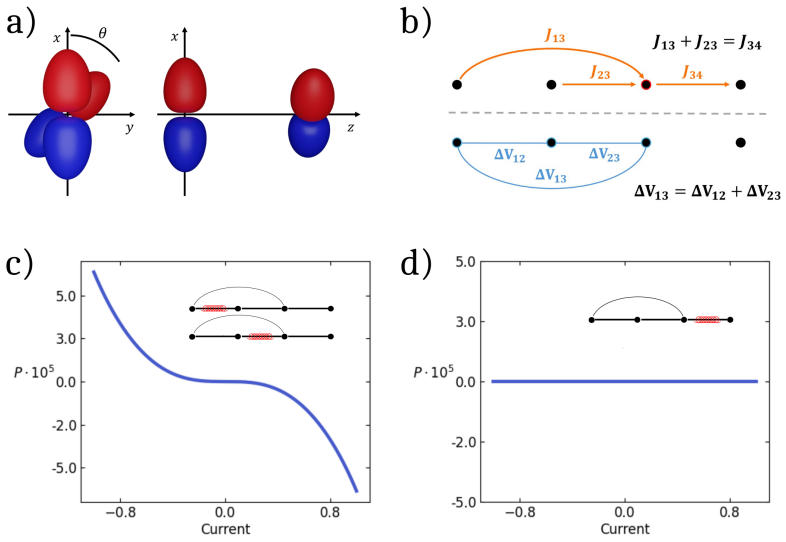

Figure 1: (a) Schematic front and side views of two adjacent p orbitals. (b) red: illustration of the constraint on the currents through site 3 to avoid charge accumulation; blue: illustration of the constraint on the potential drop. (c) and (d) The current dependent polarization for a four-site chain with $U = 5$, $\epsilon_1 = -\epsilon_4 = 2.5$, $t_{12} = t_{23} = 1$, $t_{13} = 0.01$ and $\chi = 0.01$. The insets show the relevant connectivity with black lines marking the electron-hopping channels, and the red helix marking the bond where SOC is introduced. The two structures depicted in panel (c) lead to the same result. The structure in panel (d) leads to vanishing polarization.

As explained in Chapter 2, Section 2.3.1, the Hubbard Hamiltonian reads:

$$H_{Hu} = \sum_{i=1}^{N} \epsilon_i \hat{n}_i - \sum_{i<j} t_{ij} \hat{b}_{ij} + \sum_{i=1}^{N} U_i \hat{n}_{i\alpha} \hat{n}_{i\beta}$$

In the above equation, $\hat{n}_i = \hat{n}_{i\alpha} + \hat{n}_{i,\beta}$ counts the total number of electrons on site i, $\hat{n}_{i\sigma} = a^{\dagger}_{i\sigma} a_{i\sigma}$ counts the electrons with spin σ on the same site, and $a^{\dagger}_{i\sigma}$ ($a_{i\sigma}$) creates (annihilates) an electron with spin $\sigma = \alpha, \beta$ on site i. The operator $\hat{b}_{ij} = \hat{b}_{ij\alpha} + \hat{b}_{ij\beta}$ with $\hat{b}_{ij,\sigma} = \left(a^{\dagger}_{i\sigma} a_{j\sigma} + H.c.\right)$, measures the bond-order between sites i and j. The on-site energy is ϵ_i, U_i is the repulsion between two electrons on the same site, t_{ij} is the hopping between site i and j.

We introduce SOC interactions accounting for the one-electron term of the Breit-Pauli Hamiltonian:[314]

$$\mathcal{H}_{SOC} = \frac{1}{2m_e^2 c^2} \sum_r \sum_i \frac{1}{r_{ri}^3} \boldsymbol{l}_{ri} \cdot \boldsymbol{s}_r \tag{1}$$

where $\boldsymbol{s_r}$ is the spin angular momentum of electron r, $\boldsymbol{l}_{ri}$ is its angular momentum with respect to the nucleus on site i and r_{ri} is the distance of the r electron from the i nucleus. The cubic distance in the denominator suggests that the dominant terms describe the interaction of an electron residing at site i with the i-th nucleus, so longer distance contributions are neglected. The p orbital on site i can be written as a linear combination of the p orbitals with $l_z = \pm 1$:

$$\left|\psi_i\right\rangle = \frac{1}{\sqrt{2}}\left(p^i_{-1}e^{\mathrm{i}\theta i} - p^i_1 e^{-\mathrm{i}\theta i}\right) \tag{2}$$

where i is the imaginary unit. The one-electron matrix elements of the $\boldsymbol{l}_{ri}\cdot\boldsymbol{s}_r$ operator reads:

$$\left\langle\psi_k(r)\sigma'(r)\right|\boldsymbol{l}_{ri}\cdot\boldsymbol{s}_r\left|\psi_i(r)\sigma(r)\right\rangle = \left\langle\psi_k(r)\right|l_{z,ri}\left|\psi_i(r)\right\rangle\left\langle\sigma(r)\right|\hat{s}_z\left|\sigma(r)\right\rangle\delta_{\sigma,\sigma'} \tag{3}$$

$\sigma(r)$ is the spin function associated with the electron located in r. Since the angular momentum of the electron is parallel to the z axis, the z component of the spin is conserved. Finally, in line with the choice made for the hopping integrals, the electronic matrix element is set proportional to the overlap between relevant orbitals, getting:

$$\left\langle\psi_k(r)\sigma'(r)\right|\boldsymbol{l}_{ri}\cdot\boldsymbol{s}_r\left|\psi_i(r)\sigma(r)\right\rangle \propto \cos\theta\sin\theta\left\langle\sigma(r)\right|\hat{s}_z\left|\sigma(r)\right\rangle\delta_{\sigma,\sigma'}\delta_{k,i\pm1} \tag{4}$$

Finally, the SOC Hamiltonian reduces to:

$$H_{SOC} = \mathrm{i}\sum_{i<j}\chi_{ij}\left(\hat{v}_{ij,\alpha} - \hat{v}_{ij,\beta}\right) \tag{5}$$

where χ_{ij} measures the strength of the SOC interaction between electrons residing on sites i and j and

$$\hat{v}_{ij,\sigma} = \hat{a}^\dagger_{i,\sigma}\hat{a}_{j,\sigma} - H.c. \tag{6}$$

is the velocity dipole operator. In the adopted model, the electron orbital momentum is aligned along the chain and the SOC interaction necessarily preserves the z component of the total spin, $\hat{S}_z$, so that spin-flips are not accounted for. This is an inherent feature of the proposed model, but investigating the role of spin flips in CISS would definitely be interesting, particularly in view of the contrasting opinions in recent literature. [289, 315]

A real-space basis will be adopted, with each basis state corresponding to a configuration obtained by assigning each electron to a specific site spin-orbital. A bit-representation is adopted to store each configuration as a single integer number. Specifically, each site orbital is represented by a bit, whose value is either 0 or 1 to represent a void or an occupied site orbital. Since in the adopted model $[\hat{S}_z, \hat{H}] = 0$, states with different $\langle\hat{S}_z\rangle$ stay unmixed, limiting attention to systems with an even number of electrons, we work in the $S_z = 0$ subspace. Table 1 shows the 36 basis states in the $S_z = 0$ subspace for a half-filled 4-site chain.

Integer representative number	bit representation	site representation
15	00 00 11 11	0 0 X X
27	00 01 10 11	0 β α X
30	00 01 11 10	0 β X α
39	00 10 01 11	0 α β X
45	00 10 11 01	0 α X β
51	00 11 00 11	0 X 0 X
54	00 11 01 10	0 X β α
57	00 11 10 01	0 X α β
60	00 11 11 00	0 X X 0
75	01 00 10 11	β 0 α X
78	01 00 11 10	β 0 X α
90	01 01 10 10	β β α α
99	01 10 00 11	β α 0 X
102	01 10 01 10	β α β α
105	01 10 10 01	β α α β
108	01 10 11 00	β α X 0
114	01 11 00 10	β X 0 α
120	01 11 10 00	β X α 0
135	10 00 01 11	α 0 β X
141	10 00 11 01	α 0 X β
147	10 01 00 11	α β 0 X
150	10 01 01 10	α β β α
153	10 01 10 01	α β α β
156	10 01 11 00	α β X 0
165	10 10 01 01	α α β β
177	10 11 00 01	α X 0 β
180	10 11 01 00	α X β 0
195	11 00 00 11	X 0 0 X
198	11 00 01 10	X 0 β α
201	11 00 10 01	X 0 α β
204	11 00 11 00	X 0 X 0
210	11 01 00 10	X β 0 α
216	11 01 10 00	X β α 0
225	11 10 00 01	X α 0 β
228	11 10 01 00	X α β 0
240	11 11 00 00	X X 0 0

Table 1: The real-space basis set for a 4-site, 4-electron system in the S_z = 0 subspace. Left column: The integer number representing each state. Central column: bit representation of the state. The spin-orbital on each site is represented by a bit in the order $1\alpha, 1\beta, 2\alpha, 2\beta, 3\alpha, 3\beta, 4\alpha, 4\beta$. 0 and 1 correspond to a void or occupied spin-orbital, respectively. Right column: site representation where X stands for doubly occupied sites, 0 for a void site and α, β indicate the spin of the electron in a single occupied site.

To describe electrons moving across the Hubbard chain, we rely on the CC approach. [305–307, 316–319] Specifically, to enforce a current J through the system, a set of Lagrange multipliers, λ_{lm}, enters the Hamiltonian, as follows:

$$H(J) = H - \sum_{l}^{1,N-1} \sum_{m}^{l+1,N} \lambda_{lm} \hat{j}_l^m \tag{7}$$

where $\hat{j}_l^m$ is the operator that measures the current flowing from site l to site m. The Lagrange multipliers are optimized so that in the ground state of the current carrying system, $|G(\{\lambda\})\rangle$, the incoming flux through the first site and the outcoming flux through the last site are equal to the current imposed through the system, J:

$$J = \sum_{i=2}^{N} \langle G(\{\lambda\})| \hat{j}_1^i |G(\{\lambda\})\rangle = \sum_{i=1}^{N-1} \langle G(\{\lambda\})| \hat{j}_i^N |G(\{\lambda\})\rangle \tag{8}$$

while ensuring a balanced incoming and outcoming flux on all other sites, and hence enforcing a steady-state current without charge accumulation:

$$\sum_{l=1}^{k-1} \langle G(\{\lambda\})| \hat{j}_l^k |G(\{\lambda\})\rangle - \sum_{l=k+1}^{N} \langle G(\{\lambda\})| \hat{j}_k^l |G(\{\lambda\})\rangle = 0 \tag{9}$$

The constraints in Eqs 8 and 9 fully define the Lagrange multipliers in a system with only nearest-neighbor (nn) hopping and SOC, but, in the presence of long-range hopping and/or SOC, other constraints are needed to ensure that the potential drop between two nodes is the same for different paths (cf. Figure 1b). This brings us to the delicate issue of the relationship between the Lagrange multipliers and the potential drop. As discussed in Ref. [307], the relation can be drawn by calculating the power spent on the system to maintain the current. Since the current is an off-diagonal operator on the eigenstates of the unperturbed Hamiltonian, the power spent on the system is governed by the relaxation of the off-diagonal elements of the density matrix, the coherences. In the simplifying hypothesis of a system with large inhomogeneous broadening, where the same relaxation time, $1/\Gamma$, can be applied to all coherences, the potential drop in each bond is simply proportional to the relevant Lagrange multiplier, $V_{ij} = \Gamma\lambda_{ij}$. Although this approximation can be relaxed, we will adopt it to keep the model as simple as possible. Accordingly, the Lagrange multipliers on next-nearest-neighbor (nnn) bonds are set as the sum of the two relevant nn Lagrange multipliers: $\lambda_{i,i+2} = \lambda_{i,i+1} + \lambda_{i+1,i+2}$.

The standard definition of the current operator, in terms of the velocity dipole,[320, 321] $\hat{j}_i^j \propto \hat{v}_{ij} = \hat{v}_{ij\alpha} + \hat{v}_{ij,\beta}$, leads to unphysical results: at zero external potential, opposite fluxes of α and β electrons are generated, as illustrated in Figure 2. A correct definition of the current operator must properly account for SOC. Specifically, the flux of electrons through site k, calculated as the time derivative of $\hat{n}_k$, is the sum of incoming currents from all sites connected to k from the left side minus the sum of all currents exiting site k toward all connected sites to the right of k, as sketched in Figure 1b . Accordingly:

$$\hat{\dot{n}}_k = i[H, \hat{n}_k] = \sum_{i}^{1,k-1} \hat{j}_i^k - \sum_{i}^{k+1,N} \hat{j}_k^i \tag{10}$$

where we use units with $\hbar = 1$ and

$$\hat{j}_l^m = it_{lm}(\hat{v}_{lm\alpha} + \hat{v}_{lm\beta}) - \chi_{lm}(\hat{b}_{lm\alpha} - \hat{b}_{lm\beta}) \tag{11}$$

Then SOC explicitly enters the definition of the current operator, with a contribution that has opposite sign for α and β electrons.

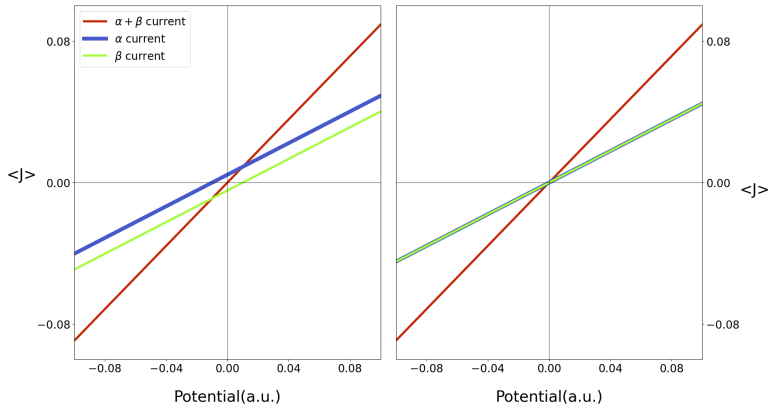

Figure 2: The two site Hubbard model with $t = 1$, $\chi = 0.01$, U=0, $\epsilon_1 = -\Delta/2$, $\epsilon_2 = \Delta/2$. Left: α- and β-spin current and the total current calculated setting the current operator proportional to the velocity operator, without accounting for the SOC contribution to the current operator. Right panel, the same quantities are calculated adopting the correct definition of the current, as defined by Eq. 11. Finite α and β currents calculated at zero potential in the left panel signal the incorrect definition of the current operator.

Having a model to drive electrons through a chiral Hubbard chain, we can address spin-selective behavior. We impose that charges do not accumulate in the current-carrying system, however, if the mobility of electrons depends on the spin, spin density can accumulate on the sites. The on-site spin-density is defined as: $\rho_i = \langle \hat{n}_{i\alpha} - \hat{n}_{i\beta} \rangle$ and the spin polarization across the system reads:

$$P = \frac{\rho_N - \rho_1}{2} \tag{12}$$

A second approach to address CISS mimics transport experiments, where a magnetized electrode is used to inject spin polarized electrons in a junction. To simulate this experiment, we use the same trick of the Lagrange multiplier to impose a current of electrons with α spin:

$$H(J_\alpha) = H - \sum_i \lambda_{i,\alpha} \hat{j}_{i,\alpha} \tag{13}$$

Then we do the same for β electrons. Of course, due to CISS, different potentials are needed to sustain the α or β-polarized current, or, in other terms, different spin-currents are calculated for the same potential drop. Accordingly, for each value of the total potential drop, we estimate the CISS efficiency as: $G = (J_\alpha - J_\beta)/(J_\alpha + J_\beta)$. In the literature, this quantity is typically referred to as spin-polarization. Here,to avoid confusion with the spin polarization defined in Eq. 12, we dub it as *current anisotropy*. It is important to stress that addressing the current anisotropy along these lines may only work in models where SOC does not flip the spins. In these conditions, the steady-state flux of spin-polarized electrons imposes a continuity relation on the spin current, a condition that would be broken in the presence of spin-flip events.

4.1.3 Results

The electronic system

It is well known that spin polarization cannot be supported in a linear chain featuring only nn interactions [322]. In Section 4.A of the Appendices of this chapter, we demonstrate that this result also holds true for current-carrying systems. Often, to allow for finite polarization,

next-nearest-neighbor (nnn) SOC interactions are introduced [291, 292], following an original suggestion by Kane and Mele for graphene-based systems [323, 324]. However, spin polarization can be observed in a linear chain without introducing nnn SOC, but by accounting for nnn hopping, as illustrated in Figure 1-c,d and in Figure 3.

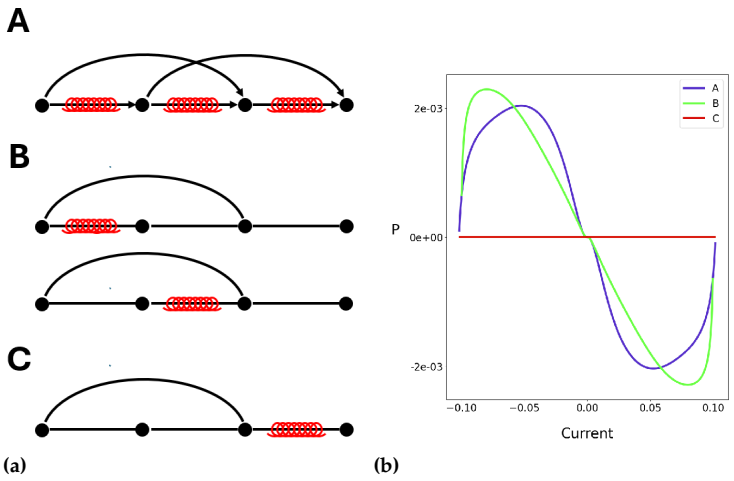

Figure 3: Illustrative examples of the role of the connectivity of a 4-site chain. (a) panel: a schematic view of the four site chain, where each black line refers to a hopping interaction and each red helix marks the SOC interaction. (b) panel: the spin polarization as a function of current calculated for the different configurations displayed in the left panel, setting $t_{23} = 1$ as the energy unit, $t_{12} = t_{34} = 0.05$ and the nnn hopping $t' = 0.01$. Moreover $\chi = 0.01, U = 2\Delta = 5$. The two systems marked as B lead to equivalent results.

Quite interestingly, a single nn SOC interaction in the current-carrying chain is enough to enable spin polarization, provided that it operates inside a loop generated by the electron hopping interactions, in a situation strongly reminiscent of the persistent spin currents induced by SOC in mesoscopic rings[325]. In the following, we will discuss results obtained introducing a tiny nnn hopping (typically two orders of magnitude smaller than the nn hopping); results obtained introducing nnn SOC are marginally different. To support a net spin polarization, non-equivalent sites must be present in the chain. Therefore, we will present results relevant to systems where the energy of the last and first sites differ by $\Delta = \epsilon_N - \epsilon_1$, while setting all other on-site energies to zero. Of course, a system with $\Delta = 0$ supports finite on-site spin densities and may sustain finite current anisotropy, as shown in Figure 4.

Before proceeding, it is important to illustrate how the relevant dimensionless quantities, current and potential drop, in the figures translate into dimensional quantities. The dimensionless current should be multiplied by $et/\hbar$ to get dimensional values. Then, setting e.g. $t \sim 0.1\,\text{eV}$, a dimensionless current $J = 1$ would correspond to $\sim 20\,\mu\text{A}$. The voltage drop should in turn be multiplied by $\hbar\Gamma/e$. Setting $1/\Gamma \sim 100\,\text{fs}$ as a typical lifetime of electronic states, $\lambda = 1$ would correspond to a potential drop $\sim 6\,\text{mV}$. For comparison, in a recent single molecule experiment,[285] current of the order of $\sim 1\,\mu\text{A}$ are obtained for potential drops of the order of 1 V.

Figure 9a shows results for a half-filled Hubbard chain with the nn hopping set to 1 as the energy unit, nnn hopping and nn SOC set to 0.01, $U = 5$ and variable Δ. In this system, a finite polarization is observed, which, however, remains very small, the largest value being reached for $U \sim \Delta$, where the current anisotropy also reaches its maximum value. Different calculations for variable U and Δ where done. In Figure 4, scans of different U with $\Delta = 0$ reveal a complex behavior. In the left panel, the spin accumulated on site 1 is shown (with $\Delta = 0$ the hole-particle

symmetry imposing vanishing polarization). The spin accumulation increases with U. In the right panel, the current anisotropy has a more complex behavior with a change of sign and a slight increase with U.

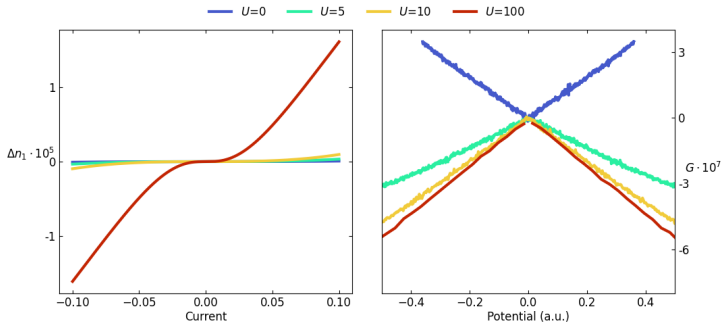

Figure 4: The 4-site Hubbard model with nn $t = 1$, and $\chi = 0.01$, the nnn $t' = 0.01$, $\epsilon_i = 0$. The results are shown for different U, as per the legend. Left panel: the spin density on the first site (equal to the spin density on the last site) as a function of the current; right panel: the current anisotropy vs the applied potential.

In Figure 5, Figure 6, and Figure 7, different results obtained for different Δ and U are shown, revealing a complex behavior for the current anisotropy, with a non-obvious relation between the measured maximum and the Δ/U ratio, while the polarization is always maximized for $2\Delta = U$.

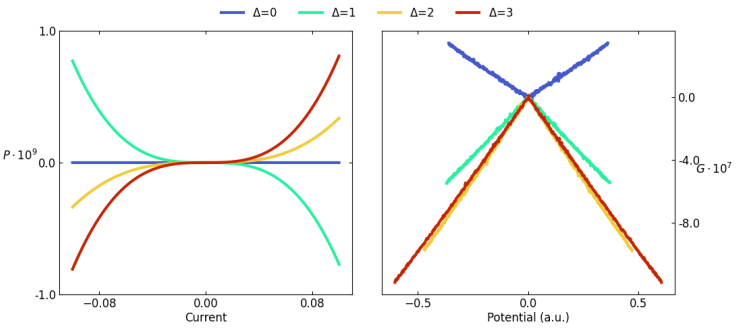

Figure 5: The 4-site Hubbard model with nn $t = 1$ and $\chi = 0.01$, nnn $t' = 0.01$, U=0. Results are shown for different Δ, as per the legend. Left panel: the polarization as a function of the current; right panel: the current anisotropy vs the applied potential.

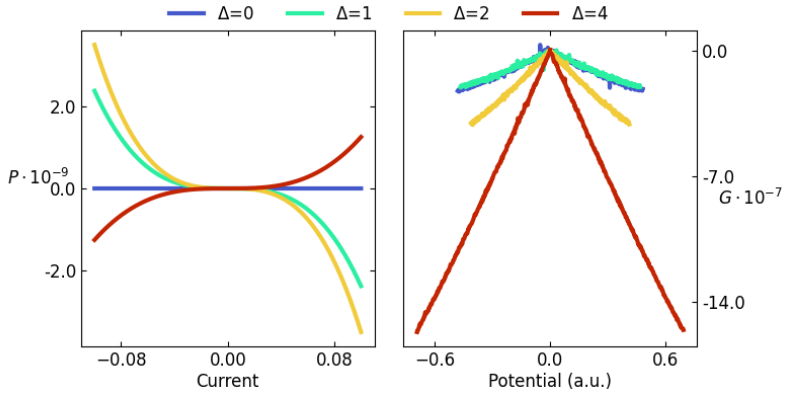

Figure 6: The 4-site Hubbard model with nn $t = 1$ and $\chi = 0.01$, nnn $t' = 0.01$, U=4. Results are shown fo different Δ, as per the legend. Left panel: the polarization as a function of the current; right panel: the current anisotropy vs the applied potential.

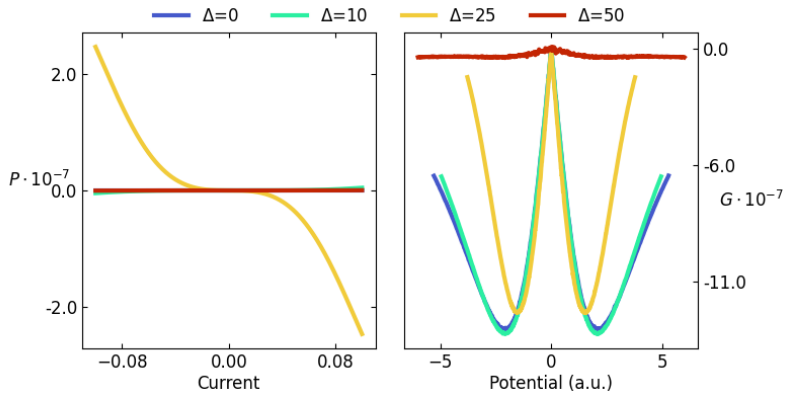

Figure 7: The 4-site Hubbard model with nn $t = 1$ and $\chi = 0.01$, nnn $t' = 0.01$, U=50. Results are shown fo different Δ, as per the legend. Left panel: the polarization as a function of the current; right panel: the current anisotropy vs the applied potential.

In any case, the polarization amplitudes and current anisotropies calculated so far are orders of magnitude smaller than those reported by experimentalists. Increasing the nnn hopping helps to increase the polarization and the current asymmetry (see Figure 8), but again, estimated values are far too small if compared with experiments.

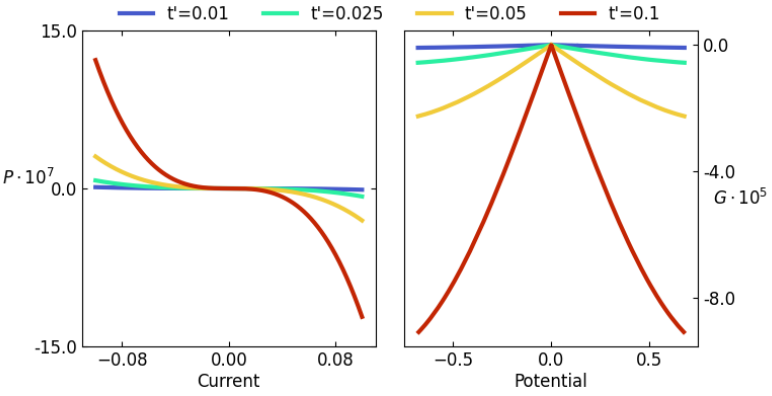

Figure 8: The 4-site Hubbard model with nn $t = 1$ and $\chi = 0.01$, U=10, $2\Delta = 5$. Results are shown for different nnn $t' =$, as per the legend. Left panel: the polarization as a function of the current; right panel: the current anisotropy vs the applied potential.

Moving away from half-filling is an interesting possibility towards amplified responses. Figure 9b shows a clear amplification of the responses for the same system as in Figure 9a for $2\Delta = U = 5$ when the number of electrons is either decreased from 4 to 2 or increased to 6. The first observation is that either non-nearest neighbor interactions or inequivalent on-site energies break electron-hole symmetry, so that results obtained for 4 or 6 electrons are not equivalent. To better picture this symmetry-breaking, in Figure 10 we show the difference between the absolute value of polarization obtained at 3/4 and 1/4 fillings for a range of parameters, clearly indicating that it does not get to zero.

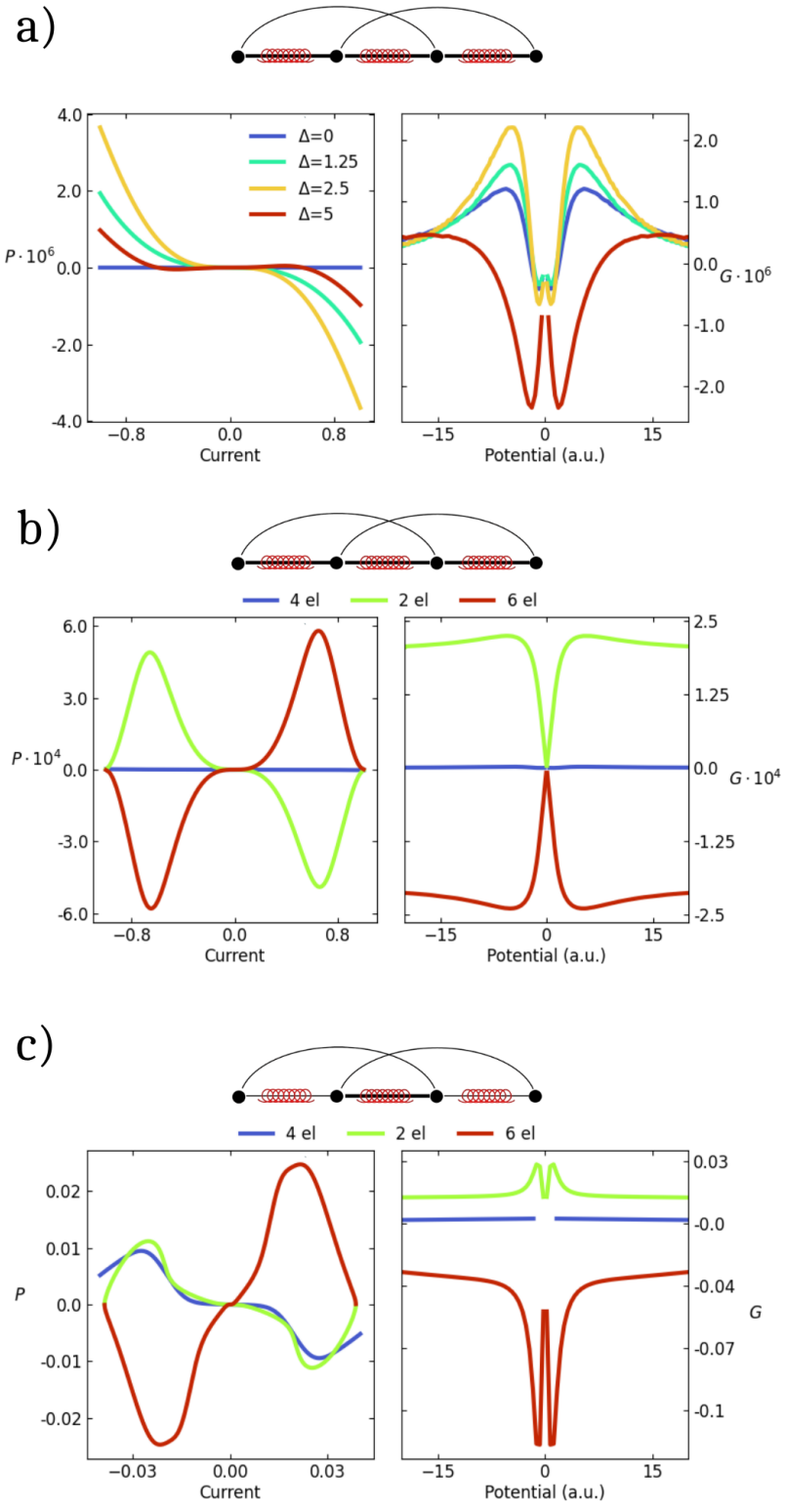

Figure 9: All panels: the 4 sites Hubbard chain with $U = 5$. Left: polarization vs current; Right: current anisotropy vs the voltage. (a) results are shown for nn hoppings $t = 1$ and SOC $\chi = 0.01$, nnn hoppings $t' = 0.01$, and variable Δ. (b) results for $2\Delta = 5$, nn $t = 1$ and and $\chi = 0.01$, nnn $t' = 0.01$. The blue curve refers to the half-filled case, the green and the red curves refer to a system with 2 and 6 electrons, respectively. (c) results for $2\Delta = 5$, nn hoppings: $t_{23} = 1, t_{12} = t_{34} = 0.01$, nnn $t' = 0.01$ and nn $\chi = 0.01$. The blue curve refers to the half-filled case, the green and the red curves refer to a system with 2 and 6 electrons, respectively.

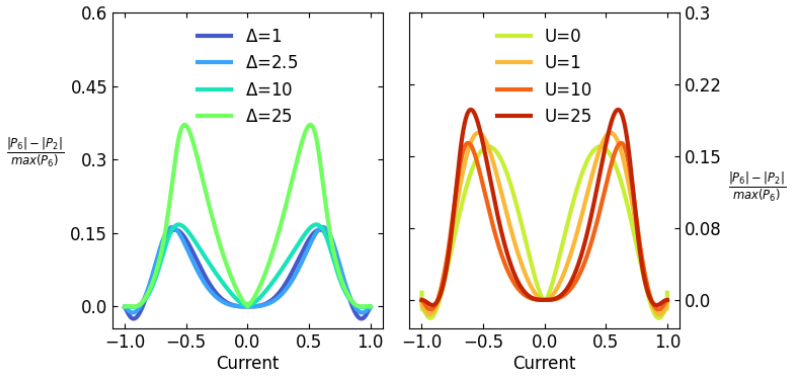

Figure 10: The 4-site Hubbard chain with nn $t = 1$ and $\chi = 0.01$, nnn $t' = 0.01$. Both panels display the difference in spin polarization between the 6-electron case and the 2-electron case, normalized for the maximum of the 6-electron case. Left: U=5, Δ varies as per the legend.Right: Δ=2.5, U varies as per the legend.

We also reproduced results for different values of model parameters, reported in Figure 11 and Figure 12. Figure 11 shows results for a non-correlated chain with all equivalent sites. Since the polarization vanishes under these conditions, the left panel shows the spin imbalance on site 1 (equal to that on site 4, causing the polarization to vanish). The effect of the electron number on the spin imbalance is marginal, while the current anisotropy increases by two orders of magnitude when going from 4 to either 2 or 6 electrons. Figure 12 shows results for a correlated system with nn $t = 1$ and $\chi = 0.01$, nnn $t' = 0.01$, $U = 2\Delta$=10. In this case, both the spin polarization and the current anisotropy display a two-order-of-magnitude amplification with respect to the half-filled case. These examples hint that investigating situations away from half-filling could help in modeling CISS quantitatively.

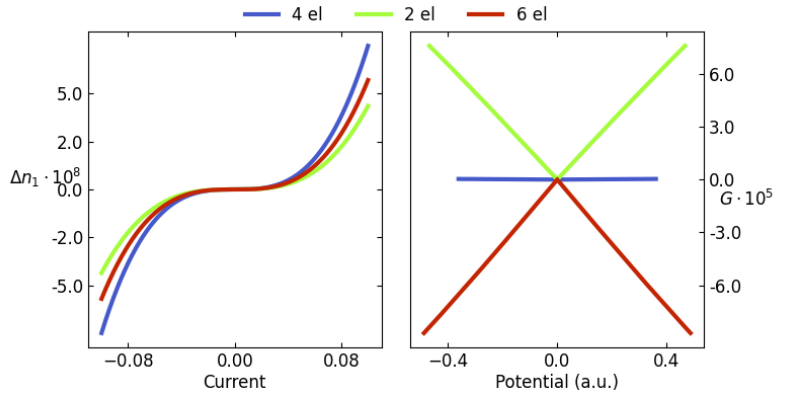

Figure 11: The 4-site Hubbard chain with $\epsilon_i = U = 0$, nn $t = 1$ and $\chi = 0.01$, nnn $t' = 0.01$. Blue lines: half-filled systems. Green and red lines refer to the system with 2 and 6 electrons,respectively. Left panel: the spin imbalance on site 1 as a function of the current; right panel: the current anisotropy vs the applied potential.

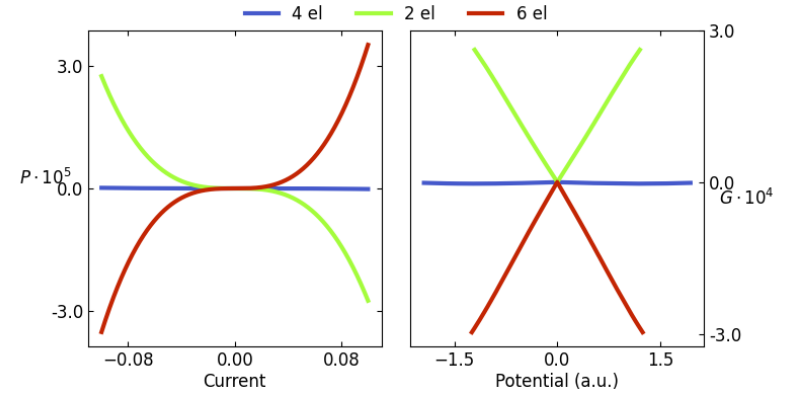

Figure 12: The 4-site half-filled Hubbard chain with $U = 2\Delta = 10$, nn $t = 1$ and $\chi = 0.01$, nnn $t' = 0.01$. Blue lines: half-filled chain. Green and red lines: 2 and 6 electrons, respectively. Left panel: the polarization as a function of the current; right panel: the current anisotropy vs the applied potential.

Introducing weak bonds also helps. Specifically, if we consider highly distorted bonds with $\theta \sim \pi/2$, the relevant hopping integral decreases, reaching values of the same order of magnitude as χ. In Figure 9b the blue line shows results for a chain with $U = \Delta = 5$, and where the lateral bonds are highly distorted as to set the relevant $\chi = t = 0.01$. Here the polarization reaches values up to 1%. Bringing together the two amplification strategies finally leads to the results in Figure 9c, where the spin polarization and current anisotropy reach values up to a few percent and to 10%, respectively. The observed amplification is much larger in this case for the 3/4 filled system than for the 1/2 filled chain. Less satisfying, yet qualitatively similar results are shown in Figure 13, for a system where the central bond is weak.

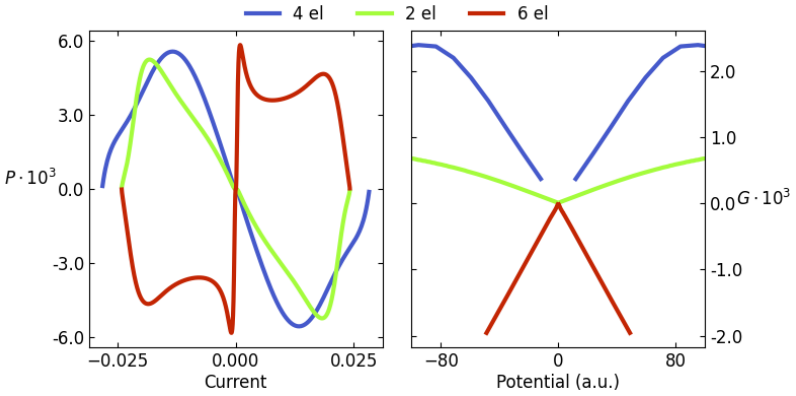

Figure 13: The 4-site half-filled Hubbard chain with $2\Delta = U = 5$, $t_{12} = t_{34} = 1$, $t_{23} = 0.01$, nn $\chi = 0.01$ and nnn $t' = 0.01$. Blu lines: half filled chain. Green and red lines: 2 and 6 electrons, respectively. Left panel: the polarization as a function of the current; right panel: the current anisotropy vs the applied potential.

Reaching a few percent of polarization or of current anisotropy is certainly encouraging. However, this result does not solve the CISS conundrum. Finding sizable polarization in a special parameter range does not fully explain CISS, a phenomenon that is observed in a very wide range of materials governed by qualitatively different physics. More robust results are needed, which apparently are hardly recovered in simple models for correlated electrons, a result that, in a different context, has been recently underlined.[326] On the positive side, results in Figure 9c could explain the large current anisotropies measured in transport experiments: the number of electrons inside the molecular junction depends on the circuit details,[327] and it is likely that in the steady-state regime the junction bears a number of electrons different from the isolated molecule. We notice that the spin polarization has a smooth evolution with the current, while the current anisotropy shows anomalies around $V = 0$. This anomaly is intrinsic to a quantity whose denominator vanishes at $V = 0$. Strong non-linearities of G around $V = 0$ have indeed been experimentally observed.[328–331]

Introducing vibrational coupling

Vibrations are often discussed as a possible source of spin polarization.[297, 332–334] In the CC approach, we can address non-adiabatic vibrations in a correlated electron model. A unitary transformation allows embedding the Holstein vibrations, modulating on-site energies, into the Hubbard Hamiltonian via a renormalization of model parameters (see Appendices, section 4.B). Accordingly, spin polarization cannot be

switched on by Holstein coupling when electrons travel in systems with only nn hopping and SOC terms. More generally, introducing Holstein modes in models with nnn hopping has marginal effects on the polarization, basically amounting to a renormalization of the on-site energies, ϵ_i and U_i.

The unitary transformation does not work for Peierls vibrations, leading to more interesting results. A Peierls mode modulating the coupling between sites l and m adds a vibronic term to the electronic Hamiltonian as follows:

$$\hat{H}_{vib} = \hbar\omega_v(\hat{a}_v^\dagger\hat{a}_v + \frac{1}{2}) + g_v(\hat{a}_v^\dagger + \hat{a}_v)\hat{b}_{lm} \tag{14}$$

where $\hat{a}_v^\dagger$, $\hat{a}_v$ are boson creation and annihilation operators, respectively, relevant to a mode with frequency ω_v. The vibrational mode modulates the $l-m$ hopping with a coupling constant g_v, the corresponding relaxation energy being $\epsilon_v = g_v^2/\omega$. The same vibration could also modulate the SOC, but the effect of SOC modulation is marginal. It must be recognized that if Peierls coupling is introduced, the current operator must be modified accordingly. In line with Eq.11 the current operator becomes:

$$\hat{j}_l^m = i\left[t_{lm} - g_v(\hat{a}_v^\dagger + \hat{a}_v)\right](\hat{v}_{lm\alpha} + \hat{v}_{lm\beta}) - \chi_{lm}(\hat{b}_{lm\alpha} - \hat{b}_{lm\beta}) \tag{15}$$

The vibronic Hamiltonian (including electron-electron interactions) is written on the basis obtained as the direct product of the real-space electronic basis times the eigenstates of the harmonic oscillator(s), truncating the vibrational basis up to a large enough number of vibrational quanta to obtain converged results. Direct numerical diagonalization leads to numerically exact non-adiabatic results for the current-carrying system. If several vibrational modes are introduced, the base grows rapidly, making the calculation computationally intensive. In the following, we will only address systems where a single mode is considered. Quite interestingly, we present for the first time results relevant to a system where electron-electron and non-adiabatic Peierls vibrations are accounted for at the same time.

Figure 14 shows results for a four-site Hubbard chain with nn t=1 and $\chi = 0.01$, nnn t'=0.01, and $U = 2\Delta = 5$. A Peierls mode with frequency ω =0.1 modulates the central hopping integral, with relaxation energy increasing from 0 to 0.1. The results are disappointing: both the polarization and the current anisotropy monotonously decrease upon increasing the strength of Peierls coupling. Similar results are obtained accounting for a vibrational mode that modulates either symmetrically or antisymmetrically the two lateral bonds (see in the appendices, Figure 4.C.1, Figure 4.C.2, Figure 4.C.3 and Figure 4.C.4).

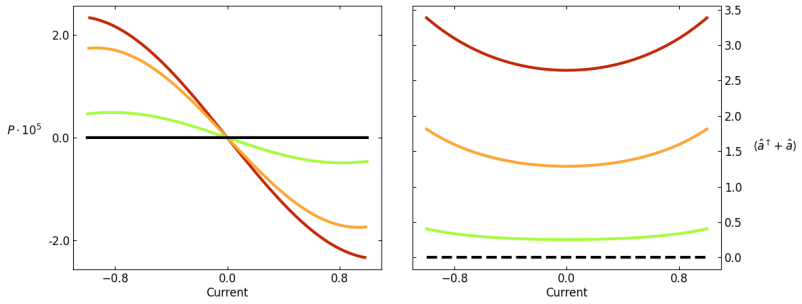

Figure 14: The half-filled 4-site Hubbard chain with nn hopping $t = 1$, nnn hopping $t' = 0.01$, $\chi = 0.01$, $U = 2\Delta = 5$. A Peierls mode modulates the hopping integral between the two central sites with $\omega = 0.1$. The spin polarization vs the current and the current anisotropy vs the potential drop calculated for different values of ϵ_v.

The calculation can be extended to finite temperatures by calculating all expectation values accounting for the Boltzmann population of the states. Figure 15 and Figure 16 show results for two different systems—one with regular bond strength and the other with two weaker terminal bonds—against different temperature values. Temperature has marginal effects as long as it stays lower than the singlet-triplet gap (0.7 for Figure 15, 0.002 for Figure 16), but both polarization and current anisotropy are suppressed at higher temperatures.

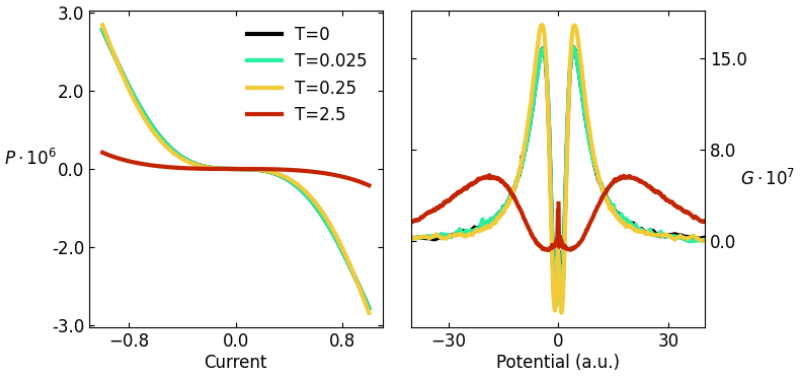

Figure 15: The half-filled 4-site Hubbard chain with nn hopping $t = 1$, nnn hopping $t' = 0.01$, $\chi = 0.01$, $U = 2\Delta = 5$. A Peierls mode modulates the hopping integral between the two central sites with $\omega = 0.1$,$\epsilon_v = 0.01$. The spin polarization vs the current and the current anisotropy vs the potential drop calculated for different temperatures.

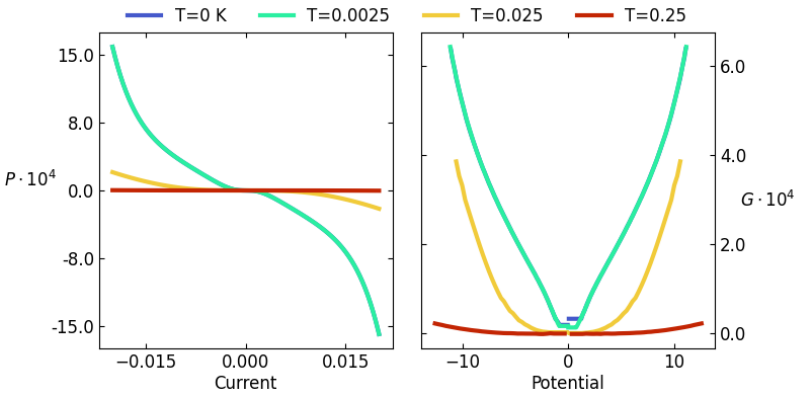

Figure 16: The 4-site Hubbard model with $t_{23} = 1$,$t_{12} = t_{23} = 0.05$ and $\chi = 0.01$, nnn $t' = 0.01$, $U = 2\Delta = 5$,, a vibrational mode is coupled to bond between sitew 1 and 2 and sites 3 and 4 in an anti-symmetric way is with $\omega = 0.1$ and $\epsilon_v = 0.01$. Results are shwon for different temperatures, as per the legend.

Peierls vibrations apparently do not lead to major effects, and, noteworthy, they do not relax the strict requirement of nnn interactions to observe CISS. Indeed, we checked explicitly that driving a current in systems with either Holstein or Peierls coupling always leads to vanishing polarization, as long as nnn interactions are disregarded. This result contrasts sharply with several reports showing CISS, and often quite substantial spin

polarization effects, in two-site systems (where nnn are obviously missing) or in systems with only nn hopping and SOC but in the presence of Peierls coupling.[293, 326, 334–337]

In the CC approach, the steady-state current is driven through a system where vibrations are always maintained in equilibrium. This represents a qualitative difference vs other approaches. To demonstrate this point, we consider the simplest system, a two-site Hubbard model, with Peierls coupling. As stated above, if the current operator is properly defined and the CC approach is adopted with equilibrated vibrations, CISS responses exactly vanish. However, a different picture emerges if, in the same spirit as in ref. [293], we adopt a mean-field approach to vibrations, basically blocking the coordinate to its equilibrium value in the system without current $Q_0 = \langle \hat{a}^\dagger + \hat{a} \rangle_0$. This approach could be applied to vibrational modes that are slow enough not to be able to readjust during the current flow.

Technically, to fix the vibrational coordinate to Q_0 we introduce an additional Lagrange multiplier in the Hamiltonian, as follows:

$$H(J, \alpha) = H_{vib} - \sum_{l}^{1,N-1} \sum_{m}^{l+1,N} \lambda_{lm} \hat{j}_l^m - \alpha \left(\langle \hat{a}^\dagger + \hat{a} \rangle - Q_0 \right) \tag{16}$$

Figure 17a collects results for a two-site Hubbard chain with $t = 1$ as the energy unit, $\chi = 0.01$, $U = 2\Delta = 5$, $\epsilon_v = 0.1$ and increasing frequency (or coupling constant). The right panel shows how the equilibrium value of the vibrational coordinate $\langle \hat{a}^\dagger + \hat{a} \rangle$ varies with the current in the fully equilibrated approach. In these conditions, the calculated spin polarization exactly vanishes for any value of the current (black line in the left panel of Figure 17a). In the left panel of Figure 17a, colored lines show instead the polarization calculated as a function imposing that, regardless of the current, the expectation value of the vibrational coordinate is fixed to Q_0. In this case, the spin polarization is finite and increases with the current and with the strength of the coupling.

Although the spin polarization remains small, the qualitative effect of out-of-equilibrium vibrational modes in allowing for finite spin-polarization even in the absence of nnn interactions is interesting, as it points to a major role of vibrations in CISS. Results in Figure 17 refer to a two-site Hubbard chain, a structurally non-chiral system, where chirality is enforced by the orbital twist. In this system, the stretching mode modulates the hopping integral and hence is not directly coupled to the spin degrees of freedom. Quite interestingly, the stretching mode, which by itself is clearly non-chiral, acquires a chiral nature due to the coupling to the electronic system, as demonstrated in Figure 17b that shows circular dichroism spectra calculated for the same systems as in Figure 17a in the absence of current (see Section 4.D for computational details).

Circular dichroism, measuring the differential absorption of left and right circularly polarized light,[275] is a clear signature of chirality. In the region of the electronic transitions (right panel of Figure 17b) Peierls coupling shows up, as expected, with the appearance of vibronic bands: besides the 0-0 band, the 0-1, 0-2 etc become progressively more intense upon increasing the strength of the coupling. More interesting is the region of vibrational transitions, where a signature appears in the circular dichroism spectrum whose intensity, while staying a few

orders of magnitude smaller than for the electronic transition, increases with the coupling strength, while the relevant transition energy slightly decreases. In chiral molecules, the chiral responses of vibrational states are well known and widely investigated;[338, 339] our results suggest that vibrational modes in chiral molecules may play a major role in CISS.

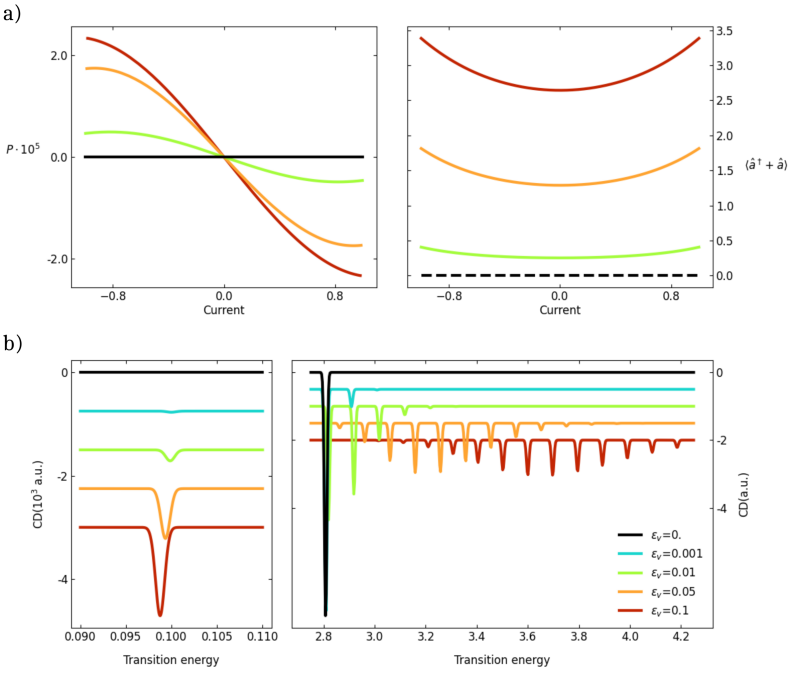

Figure 17: (a)The half-filled 2-site Hubbard model with $t = 1$, $\chi = 0.01$ and $U = 2\Delta = 5$. A Peierls mode with frequency $\omega = 0.1$ modulates the hopping integral between the two sites with different ε_v as per the legend in panel (b). The left panel shows the polarization against the current calculated with the phonon coordinate constrained to its equilibrium value in the absence of current. The right panel the equilibrium value of the coordinate vs the current. (b) Circular dichroism spectra (arbitrary units) for the same systems as in (a) without current. The two refer to the spectral region of vibrational (left) and electronic (right) transitions. The intensity of the spectra on the left panel are multiplied by a factor 10^3 for clarity.

4.1.4 Conclusions

We have presented an original discussion of CISS-related phenomena, where a CC approach is adopted to force electron motion through a chiral Hubbard chain. The approach is simple and allows us to explore large regions of parameter space. As expected, as long as only electronic degrees of freedom are considered, CISS is supported by electrons traveling along a simple Hubbard chain only if nnn hopping or SOC interactions are introduced. Spin polarization is in general small, for acceptable SOC values, but is amplified in non-half-filled systems and/or in the presence of weak bonds, leading in specific cases to spin polarization up to ~10%. However, since sizable CISS effects are observed in several systems of a very different nature, we conclude that electron correlations in the simple Hubbard chain hardly explain CISS. In the process, we learned an important lesson: when SOC enters the model, the standard definition of the current operator in terms of the velocity dipole is no longer adequate, since SOC itself enters the current operator.

The proposed approach lends itself quite naturally to address the role of non-adiabatic vibrational modes in correlated electron systems. Molecular vibrations modulating on-site energies, the Holstein modes, have no major effects. Peierls modes, modulating the hopping integrals, lead instead to more interesting physics. In the first place, Peierls modes, together with SOC, enter the definition of the current operator. As long as the current-carrying system is fully equilibrated in terms of both

electronic and vibrational degrees of freedom, vibrational coupling only marginally affects CISS. However, if the vibrational coordinate is kept out of equilibrium in the current-carrying system, a very interesting result is obtained in terms of a finite spin polarization in the two-site Hubbard chain. In other terms, if vibrational modes are maintained out of equilibrium, nnn interactions are not needed to observe spin-polarization. This impressive result, in line with recent theoretical work,[326, 334] suggests that the chiral nature acquired by the ubiquitous vibrational degrees of freedom in chiral molecules can be the key to unravel the CISS physics.

4.2 CISS in photoinduced electron transfers: ab-initio parametrization of a modified Hubbard model

Transport experiments are the most widely adopted experimental approach to CISS, but in these experiments it is difficult to disentangle the role of electrodes, with their large SOC, from the intrinsic properties of the chiral system. In this respect, the recent observation of CISS in a photoinduced electron transfer (PET) experiment sheds new light on the phenomenon.[286] In this novel experimental configuration, chiral molecules are composed of a donor, a chiral bridge, and acceptor moieties covalently linked in a specific architecture. These molecular triads are carefully designed to ensure that: (i) the photoexcitation of the system selectively populates the lowest excited state of the donor unit; (ii) after excitation, two fast electron transfer processes drive an electron across the bridge to the acceptor unit; and (iii) the resulting charge-separated (zwitterionic) state exhibits a long lifetime, extending into the microsecond regime.

In the initial study, the molecule peri-xanthenoxanthene-bis(naphthalene-1,8-dicarboximides)-naphthalene-1,8:4,5-bis(dicarboximide) (PXX-NMI_2-NDI, see Figure 18) was dissolved in a nematic liquid crystal, allowing the molecular axis to be aligned either parallel or perpendicular to an external magnetic field. Subsequently, the resulting spin polarization was characterized using time-resolved electron paramagnetic resonance (TREPR). The TREPR signals for both R and S enantiomers were found to be compatible with a spin polarization of 50%, a value supported by first-principles simulations. In contrast, spin polarization was not detected when an achiral reference molecule was employed. More recently, the CISS effect was investigated using a similar methodology in randomly oriented molecules in frozen glassy solvent. [287]

To simulate CISS in this peculiar setup, in line with recent advances in the field,[292] we adopt a modified Hubbard model to describe the basic physics of system, focusing attention on the bridge, constituted by a pair of twisted NMI units (Figure 18). Our aim is to reliably parametrize the Hubbard model for the bridge against ab initio results.

The proposed modified Hubbard model for the bridge takes into account two sites (corresponding to the two NMI units) accounting on each site for

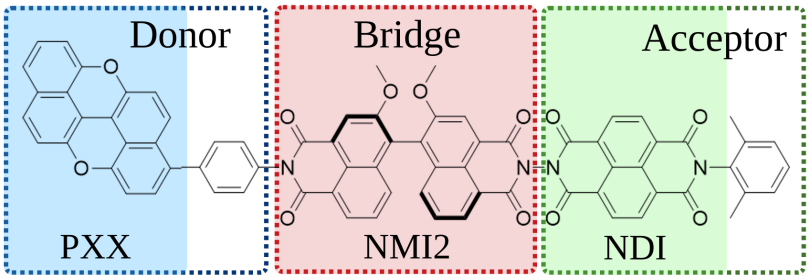

Figure 18: Kekule structure and fragments subdivision studied in the PET experiment by Wasielewski et al. [2]

two orbitals, namely the HOMO and LUMO. The Hamiltonian reads:

$$\begin{aligned}\mathscr{H} = &\sum_{I,i,\sigma} \varepsilon_i \hat{n}_{I,i,\sigma} - \sum_{I,i,j,\sigma} t_{ij} \hat{c}^{\dagger}_{Ii\sigma} \hat{c}_{\bar{I}j\sigma} + \\ &+ \frac{1}{2} \sum_{I,i,j,\sigma} U_{ij} \hat{n}_{Ii\sigma} \hat{n}_{Ij\bar{\sigma}} + \frac{1}{2} \sum_{I,i\neq j,\sigma} \left(U_{ij} - J_{ij}\right) \hat{n}_{Ii\sigma} \hat{n}_{Ij\sigma} + \\ &+ \frac{1}{2} \sum_{I,i\neq j,\sigma} J_{ij} \hat{c}^{\dagger}_{Ii\sigma} \hat{c}^{\dagger}_{Ij\bar{\sigma}} \hat{c}_{Ii\bar{\sigma}} \hat{c}_{Ij\sigma} + \\ &+ \frac{1}{2} \sum_{I,i,j,\sigma,\sigma'} V_{ij} \hat{n}_{Ii\sigma} \hat{n}_{\bar{I}j\sigma'} + \\ &+ \sum_{I,i\neq j,\sigma,\sigma'} J^{(exc)} \hat{c}^{\dagger}_{I,i,\sigma} \hat{c}_{I,\bar{i},\sigma} \hat{c}^{\dagger}_{\bar{I},j,\sigma'} \hat{c}_{\bar{I},\bar{j},\sigma'}\end{aligned} \tag{17}$$

where uppercase indices run on the two sites, lowercase indices run on site orbitals, and σ is the spin label, so that $\hat{c}^{\dagger}_{Ii\sigma}$, $\hat{c}_{Ii\sigma}$ and $\hat{n}_{Ii\sigma}$ are the creation, annihilation, and number operators for the σ-spin electron in the i-th spatial orbital of the I-th site. Barred indices indicate the other possible value for the site, orbital, or spin. The first line in Equation 17 collects the one-electron terms of the Hamiltonian, where ϵ_i is the energy for the i-th site orbital (equal on both fragments), and t_{ij} is the hopping integral between the i-th and j-th orbitals (on different fragments, on-site hopping integrals vanish). The second and third lines of Equation 17 collect the on-site two-electron terms, with U_{ij} measuring the repulsion between two electrons residing on the same site in the same or in different orbitals, and J_{ij} is the on-site exchange coupling. The fourth line of Eq. 17 describes inter-site electrostatic interactions. The fifth line in Eq. 17 introduces exciton coupling, a two-electron term that describes (in the point-dipole approximation) the interaction between on-site transition dipole moments, parameterized by the exciton coupling energy $J^{(exc)}$. This term does not appear in standard versions of the Hubbard model but should be accounted for when several orbitals are present on each site.

For the parametrization of the Hubbard Hamiltonian, we rely on the CASCI approach. CASCI offers several advantages, such as size insensitivity and comparatively well-behaved potential energy surfaces. Moreover, it was successfully adopted to describe electronic excitations in dimers, a problem somewhat relevant to our aim [340]. Specifically, we adopt CAS-sr-DFT, a variant of CASCI, to effectively account for dynamic correlation by incorporating short-range electron-electron interactions in a DFT framework [78]. The basis set for the CASCI and CAS-sr-DFT approaches are the electronic configurations, i.e., the states obtained by populating the active orbitals with the proper number of electrons. The

CASCI or CAS-sr-DFT eigenstates are obtained upon diagonalization of the relevant Hamiltonian matrix, which explicitly accounts for one- and two-electron terms. Specifically, in CAS-sr-DFT, a range separation parameter is defined (we set it to 0.2 to best fit the experimental excitation energy of NMI) on the electron-electron distance, so that two-electron terms are calculated using DFT in the short range and wavefunction theory in the long range, as explained in Chapter 2.

Before applying CAS-sr-DFT to our case, we calculated relevant transition energies with NEVPT2. The calculations were executed using the 6-31G* basis set and RI-JK approximation with the def2/JK auxiliary basis set, when applicable. The calculations were executed in ORCA 5.0.2 [222]. Hartree-Fock orbitals for the single NMI unit are reported in Figure 19. To model the Hamiltonian, two orbitals per site must be selected. As can be seen in Table 2, while the CASSCF transition energy displays a significant change from the (2,2) active space to the (10,10), the NEVPT2 energy is much more stable. Therefore, a (2,2) active space can be a good starting point to parametrize the effective Hamiltonian, provided a strategy is devised to recover the correlation energy.

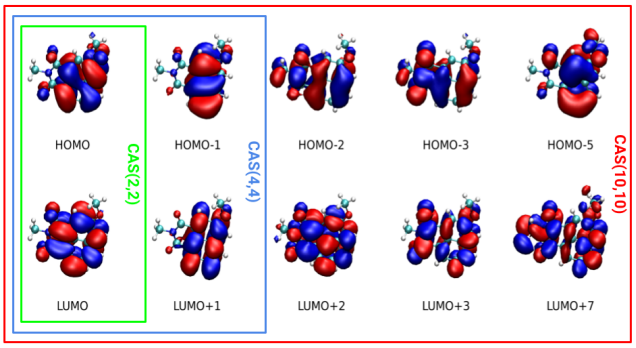

Figure 19: Hartree-Fockmolecularr orbitals of NMI used in the CAS-CI/NEVPT2 calculation. Different groupings refer to different active spaces.

Table 2: Transition energies for the lowest excited singlet, S_1, and triplet, T_1 of NMI. All values in eV. The active spaces for each calculation are displayed in Figure 19.

	T_1		S_1	
	CAS	NEVPT2	CAS	NEVPT2
CAS(2,2)	3.613	2.555	5.606	3.366
CAS(4,4)	3.810	2.504	5.391	3.640
CAS(10,10)*	3.134	2.646	4.907	3.675

We adopt CAS(2,2)-sr-DFT calculations to describe each NMI fragment, i.e., including two orbitals, the HOMO and LUMO, and two electrons in the active space. Analogously, NMI2 is described in CAS(4,4)-sr-DFT, accounting for 4 orbitals (HOMO-1, HOMO, LUMO, and LUMO+1) and 4 electrons. As a first step, we ran a HF calculation on the isolated NMI fragment and on an NMI $\cdots$ NMI system, corresponding to two NMI fragments set at a large distance (≈20 Å). This procedure allowed us to verify that the pair-degenerate canonical orbitals of NMI $\cdots$ NMI coincide with the canonical orbitals of the isolated NMI, so that all intersite interactions can be safely neglected in the NMI $\cdots$ NMI pair. The energy of the configurations E_i (the basis state of the CAS-CI calculation) can be obtained by rotating the eigenvalues of a CAS(4,4)-sr-DFT calculation on NMI $\cdots$ NMI onto the configuration basis. Once the energies of the configurations are known, the on-site parameters (U_{ij}, t_{ij}, J_{ij}) can

be easily obtained. Inter-site model parameters (t_{ij}, V_{ij}, $J^{(exc)}$) rely on CAS(4,4)-sr-DFT calculations on NMI2 and are extracted by adjusting the inter-site model parameters of the Hamiltonian to best fit the ab initio transition energies, while maintaining the on-site parameters fixed to the values obtained from NMI $\cdots$ NMI results. Results are listed in Table 3. Good agreement is obtained in terms of energy (RMSE of 0.045 eV). Results in the table show that the inclusion of the exciton coupling term in our Hamiltonian marginally affects the global quality of the fit, while it definitely improves the description of the lowest-lying excited states (i.e., the pair of local triplet states and the pair of local singlet states), suggesting that exciton coupling is required for a reliable description of the low-energy excited states. Moreover, accounting for exciton coupling does not significantly affect inter-site parameters, with the only exception of t_{22}, which goes from 80 meV if exciton coupling is disregarded, to 30 meV if it is accounted for. Overall, Hubbard eigenstates are a good approximation of CAS-sr-DFT eigenstates. Minor deviations can be ascribed to two main sources: (1) the MOs of NMI2 that enter the active space in the CAS(4,4)-sr-DFT calculation are not exactly linear combinations of the same on-site orbitals that enter the CAS(2,2)-sr-DFT calculation on the NMI dimer, and (2) some two-electron integrals that enter the CASCI calculations are not included in the neglect of differential overlap approximation adopted in the Hubbard model [341, 342]. The parameters obtained here show relatively high U values of about 3.4 eV, which was revealed to be important in simulating CISS in PET experiments [292].Furthermore, the introduction of vibrations caused the setup to acquire non-negligible spin polarization.

Generalized Hubbard parameters		
J_{12}	0.22	0.22
U_{12}	3.42	3.42
U_{11}	3.54	3.54
U_{22}	3.41	3.41
ΔE_{12}	3.40	3.40
t_{11}	-0.16	-0.16
t_{12}	-0.14	-0.14
t_{22}	-0.03	-0.08
V_{11}	2.06	2.06
V_{22}	2.21	2.22
V_{12}	2.09	2.10
$J^{(exc)}$	0.03	-
RMSE	0.05	0.05
RMSE'	0.02	0.04

Table 3: Hubbard parameters (eV) extracted by ab initio calculation. Parameters in the first column are obtained using the full Hamiltonian in eq.17, parameters in the second column are obtained neglecting exciton coupling. The last two lines show the root mean squared error calculated accounting for all transition energies (RMSE) and for the four lowest excited states (RMSE').

In conclusion, we introduced a generalized Hubbard model to describe the chiral bridge involved in the electron transfer process, i.e., the NMI2 fragment. Reliable model parameters are obtained through an original procedure that exploits complete active space methods, where dynamic correlations are effectively taken into account by treating short-range electron-electron interactions with DFT. The derivation of on-site parameters is exact, while intersite parameters are obtained via an eigenvalue fitting procedure, yielding good agreement between the Hubbard model and CAS-CI eigenstates. This approach could be extended to other homo- and hetero-dimers or larger molecular aggregates. The Hubbard model,

along with its PPP generalization, provides a powerful framework for addressing important problems in materials science, energy conversion, and quantum information. Understanding the interactions between localized, excitonic, and charge resonance states with different spin multiplicities is crucial for determining the photophysics of the system. Regarding CISS, SOC is predicted to be small in the NMI2 bridge, as expected for π-conjugated systems. However, strong correlations are found, with U values in the range of 3.4 eV. Despite this, the large HOMO-LUMO gap of NMI leads to a single channel for electron transfer, and thus leads to very small spin polarizations.

Appendix

4.A The gauge transformation for the Hubbard Hamiltonian with nearest-neighbor hopping

If nnn interactions are neglected, the current-carrying Hamiltonian reads:

$$\begin{aligned} H(\lambda) &= \sum_{i=1}^{N} \epsilon_i \hat{n}_i + \sum_{i=1}^{N} U_i \hat{n}_{i\alpha} \hat{n}_{i\beta} \\ &\quad + \sum_{i=1}^{N-1} \left[-t_i \hat{b}_{ij} + i\chi_i (\hat{v}_{i,i+1,\alpha} - \hat{v}_{i,i+1,\beta}) - \lambda_i \hat{j}_i^{i+1} \right] \end{aligned} \tag{4.A.1}$$

where, for the sake of simplicity, we have neglected the term accounting for intersite electrostatic interactions, which, however, does not affect the discussion below. The last line in the above Hamiltonian describes all hopping terms. Focusing on just one of these terms, we rewrite it as follows:

$$-t_i(1 + i\lambda_i)\mathbf{1}_{2\times 2} + \chi_i(i - \lambda)\sigma_z = A_i \cdot \mathbf{1}_{2\times 2} + B_i \cdot \sigma_z \tag{4.A.2}$$

where the unit and the σ_z matrices are defined on the two dimensional spin subspace. The following transformation is defined on each site as follows:

$$\hat{U}_j = e^{ij\phi_j \sigma_z} \tag{4.A.3}$$

since the transformation operators are unitary,

$$\hat{U}_j^\dagger \hat{U}_j = \hat{U}_j \hat{U}_j^\dagger = \mathbf{1}_{2\times 2}$$

we insert the identity in the Hamiltonian in Eq. 4.A.1:

$$\begin{aligned} \tilde{\boldsymbol{H}} &= \sum_{j=1}^{N} \sum_{\sigma} \epsilon_j c_{j,\sigma}^\dagger \hat{U}_j \hat{U}_j^\dagger c_{j,\sigma} + \sum_{j=1}^{N} U_j c_{j,\alpha}^\dagger \hat{U}_j \hat{U}_j^\dagger c_{j,\alpha} c_{j,\beta}^\dagger \hat{U}_j \hat{U}_j^\dagger c_{j,\beta} \\ &\quad + \sum_{j=1}^{N-1} \sum_{\sigma} c_{j,\sigma}^\dagger \hat{U}_j \hat{U}_j^\dagger \left[-t_j(1 + i\lambda_j) + \chi_j(i - \lambda_j)\sigma_z \right] \hat{U}_{j+1} \hat{U}_{j+1}^\dagger \, c_{j+1,\sigma} \text{h.c.} \\ &= \sum_{j=1}^{N} \sum_{\sigma} \epsilon_j d_{j,\sigma}^\dagger d_{j,\sigma} + \sum_{j=1}^{N} U_j d_{j,\alpha}^\dagger d_{j,\alpha} d_{j,\beta}^\dagger d_{j,\beta} \\ &\quad + \sum_{j=1}^{N-1} \sum_{\sigma} d_{j,\sigma}^\dagger \hat{U}_j^\dagger \left[-t_j(1 + i\lambda_j) + \chi_j(i - \lambda_j)\sigma_z \right] \hat{U}_{j+1} \, d_{2,\sigma} + \text{h.c.} \end{aligned}$$

Where:

$$d_{j,\sigma} = U_j^\dagger c_{j,\sigma} \qquad d_{j,\sigma}^\dagger = c_{j,\sigma}^\dagger U_j \tag{4.A.4}$$

We set:

$$\begin{aligned} &\hat{U}_j^\dagger \left[-t_j(1 + i\lambda_j) + \chi_j(i - \lambda_j)\sigma_z \right] \hat{U}_{j+1} = \\ &\left[A_j \cos(\phi_j) + iB_j \sin(\phi_j) \right] \mathbf{1}_{2\times 2} + \left[B_j \cos(\phi_j) + iA_j \sin(\phi_j) \right] \sigma_z \end{aligned}$$

To gauge the SOC term we impose:

$$\phi_j = \arctan\left(\frac{\chi_j}{t_j}\right)$$

while:

$$A_j \cos(\phi_j) + iB_j \sin(\phi_j) = -\sqrt{t_j^2 + \chi_j^2} - i\lambda_j \frac{t_j^2 - \chi_j^2}{\sqrt{t_j^2 + \chi_j^2}}$$

So the final hamiltonian is:

$$\begin{aligned}\tilde{\boldsymbol{H}} = &\sum_{j=1}^{2} \sum_{\sigma=\uparrow,\downarrow} \epsilon_j d_{j,\sigma}^\dagger d_{j,\sigma} \; + \sum_{j=1}^{2} U_j d_{j,\alpha}^\dagger d_{j,\alpha} d_{j,\beta}^\dagger d_{j,\beta} \\ &- \left[\sqrt{t^2 + \chi^2} + i\lambda \frac{t^2 - \chi^2}{\sqrt{t^2 + \chi^2}}\right] \sum_{\sigma=\uparrow,\downarrow} d_{1,\sigma}^\dagger d_{2,\sigma} + \text{ h.c.}\end{aligned} \tag{4.A.5}$$

The term SOC is completely gauged away setting

$$\hat{U}_j = e^{ij \arctan\left(\frac{\chi_j}{t_j}\right)\sigma_z} \tag{4.A.6}$$

Interestingly, the Lagrange multiplier does not appear in the transformation that holds true in the presence and in the absence of a running current. The Hamiltonian is no longer spin-dependent along $\hat{z}$ and therefore we cannot have any polarization along $\hat{z}$. Of course, the SOC cannot be gauged out if either nnn hopping or nnn SOC interactions are accounted for.

4.B Introducing Holstein phonons

A Holstein vibration is introduced on each site, which modulates the on-site energy, so that the nn Hamiltonian in Eq. 4.A.1 reads:

$$\begin{aligned}H(\lambda) = &\sum_{j=1}^{N} \sum_{\sigma} c_{j,\sigma}^\dagger c_{j,\sigma} \left[\epsilon_j + g_j(a_j^\dagger + a_j)\right] + \sum_{j=1}^{N} U_j c_{j,\alpha}^\dagger c_{j,\alpha} c_{j,\beta}^\dagger c_{j,\beta} \\ &+ \sum_{j=1}^{N} \hbar\omega_j \left(a_j^\dagger a_j + \frac{1}{2}\right) + \sum_{\sigma} c_{1,\sigma}^\dagger \left[-t + i\chi\sigma_z\right] c_{2,\sigma} + \text{h.c.} \\ &- \lambda \left[it \left(\sum_{\sigma=\uparrow,\downarrow} c_{1,\sigma}^\dagger c_{2,\sigma} + \text{h.c.}\right) - \chi \left(\sum_{\sigma=\uparrow,\downarrow} c_{1,\sigma}^\dagger \sigma_z c_{2,\sigma} + \text{h.c.}\right)\right]\end{aligned} \tag{4.B.1}$$

We apply the Lang-Firsov transformation with the following ansatz:

$$S_j = \sum_{\sigma} \frac{g_j}{\hbar\omega_j} c_{j,\sigma}^\dagger c_{j,\sigma} \left(a_j^\dagger - a_j\right) \tag{4.B.2}$$

From $S_j^\dagger = -S_j$, it follows $e^{S_j} = \left(e^{-S_j}\right)^\dagger$. Applying the unitary transfor-

mation $\tilde{\boldsymbol{H}} = e^{s_j} \boldsymbol{H} e^{-s_j}$, the transformed operators on site j read:

$$\tilde{a}_j = a_j - \sum_{\sigma=\uparrow,\downarrow} \frac{g_j}{\hbar\omega_{0,j}} c^\dagger_{j,\sigma} c_{j,\sigma} \qquad \tilde{a}^\dagger_j = a_j - \sum_{\sigma=\uparrow,\downarrow} \frac{g_j}{\hbar\omega_{0,j}} c^\dagger_{j,\sigma} c_{j,\sigma} \quad (4.B.3)$$

$$\tilde{c}_{j,\sigma} = c_{j,\sigma}\, e^{-\frac{g_j}{\hbar\omega_{0,j}}(a^\dagger_j - a_j)} \qquad \tilde{c}^\dagger_{j,\sigma} = c^\dagger_{j,\sigma} e^{+\frac{g_j}{\hbar\omega_{0,j}}(a^\dagger_j - a_j)} \quad (4.B.4)$$

while, for site $i \neq j$ the operators stay unchanged:

$$\tilde{c}_{i,\sigma'} = c_{i,\sigma'}$$
$$\tilde{a}_i = a_i$$

Repeating the transformation on each site, we end up with the transformed operator:

$$\tilde{c}^\dagger_{j,\sigma} \tilde{c}_{j,\sigma} = c^\dagger_{j,\sigma} c_{j,\sigma}$$

$$\tilde{c}^\dagger_{j,\sigma} \tilde{c}_{j',\sigma} = c^\dagger_{j,\sigma} c_{j',\sigma} \exp\left\{ \frac{g_j}{\hbar\omega_{0,j}} (a^\dagger_j - a_j) \; - \; \frac{g_{j'}}{\hbar\omega_{0,j'}} (a^\dagger_{j'} - a_{j'}) \right\} = c^\dagger_{j,\sigma} c_{j',\sigma} \Lambda_{j,j'}$$

$$\tilde{a}^\dagger_j + \tilde{a}_j = a^\dagger_j + a_j - 2 \sum_{j=1}^{2} \sum_{\sigma=\uparrow,\downarrow} \frac{g_j}{\hbar\omega_0} c^\dagger_{j,\sigma} c_{j,\sigma}$$

$$\tilde{a}^\dagger_j \tilde{a}_j + \frac{1}{2} = a^\dagger_j a_j + \frac{1}{2} - \sum_{j=1}^{2} \sum_{\sigma=\uparrow,\downarrow} \frac{g_j}{\hbar\omega_j} c^\dagger_{j,\sigma} c_{j,\sigma} (a^\dagger_j + a_j) + \left[\sum_{j=1}^{2} \sum_{\sigma=\uparrow,\downarrow} \frac{g_j}{\hbar\omega_0} c^\dagger_{j,\sigma} c_{j,\sigma} \right]^2$$

First we evaluate:

$$\sum_{j=1}^{2} \sum_{\sigma=\uparrow,\downarrow} \epsilon_j \tilde{c}^\dagger_{j,\sigma} \tilde{c}_{j,\sigma} \; + \; \sum_{j=1}^{2} \hbar\omega_j \left(\tilde{a}_j{}^\dagger \tilde{a}_j + \frac{1}{2} \right) + \sum_{j=1}^{2} \sum_{\sigma=\uparrow,\downarrow} \frac{g_j}{\hbar\omega_j} \tilde{c}^\dagger_{j,\sigma} \tilde{c}_{j,\sigma} \left(\tilde{a}^\dagger_j + \tilde{a}_j \right)$$
$$= \sum_{j=1}^{2} \sum_{\sigma=\uparrow,\downarrow} \epsilon_j c^\dagger_{j,\sigma} c_{j,\sigma} \; + \; \sum_{j=1}^{2} \hbar\omega_j \left(a^\dagger_j a_j + \frac{1}{2} \right)$$
$$- \sum_{j=1}^{2} \sum_{\sigma=\uparrow,\downarrow} \frac{g_j^2}{\hbar\omega_j} n_{j,\sigma} \; - \; 2 \sum_{j=1}^{2} \frac{g_j^2}{\hbar\omega_j} n_{j,\uparrow} n_{j,\downarrow}$$

So in the end we get:

Finally, the trasformed Hamiltonain is:

$$\begin{aligned} \tilde{\boldsymbol{H}} = & \sum_{j=1}^{N} \sum_{\sigma} \left[\epsilon_j - \frac{g_j^2}{\hbar\omega_j} \right] c^\dagger_{j,\sigma} c_{j,\sigma} \\ & + \sum_{j=1}^{N} \hbar\omega_j \left(a^\dagger_j a_j + \frac{1}{2} \right) + \sum_{j=1}^{2} \left(U_j - \frac{2 g_j^2}{\hbar\omega_j} \right) c^\dagger_{j,\alpha} c_{j,\alpha} c^\dagger_{j,\beta} c_{j,\beta} \\ & + \sum_{j=1}^{N-1} \sum_{\sigma} \left[-t_j (1 + i\lambda) + \chi_j (i - \lambda) \sigma_z \right] c^\dagger_{j,\sigma} c_{i+1,\sigma} \Lambda_{i,i+1} + \text{ h.c.} \end{aligned} \quad (4.B.5)$$

Apart from a renormalization of the on-site energies and of the on-site electron-electron repulsion, the electronic part of the Hamiltonian has the same form as the purely electronic Hamiltonian in Eq. 4.A.1. Accordingly, as long as only nn interactions are accounted for, the same gauge transformation can be applied as discussed in Section 4.A, proving

that Holstein phonons cannot lead to spin polarization in a system with only nn hopping terms.

4.C Introducing Peierls phonons

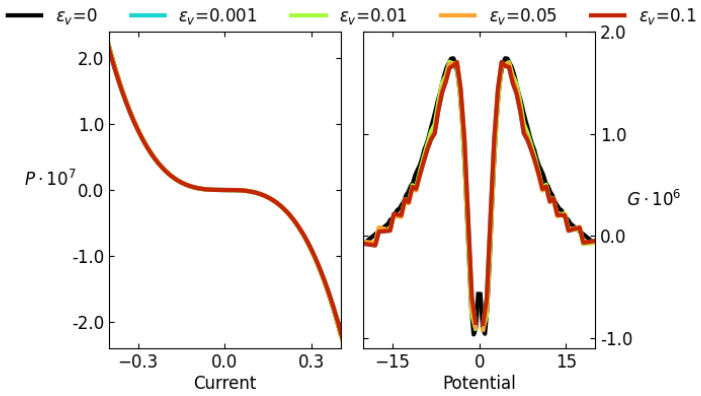

Figure 4.C.1: The 4-site Hubbard chain with nn $t = 1$ and $\chi = 0.01$, nnn $t' = 0.01$, $U = 2\Delta = 5$, a vibrational mode is coupled in an anti-symmetric way to the bond between site 1 and 2 and sites 3 and 4 with interaction term: $g_v(\hat{a}_v^\dagger + \hat{a}_v)(\hat{b}_{12} - \hat{b}_{34})$ with $\omega = 0.1$ and different ϵ_v, as per the legend.

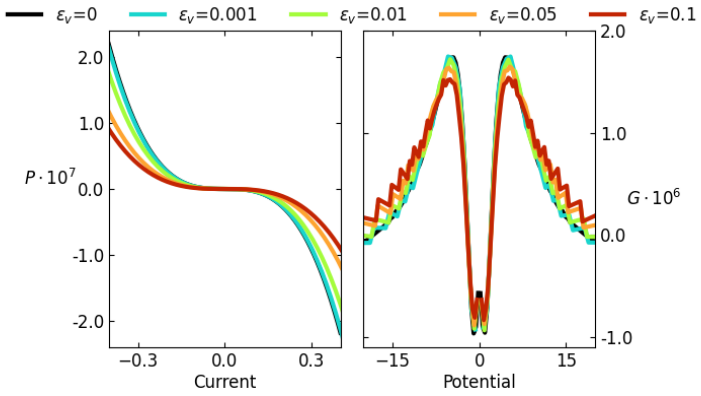

Figure 4.C.2: The same as Figure 4.C.1 but for symmetric coupling: $g_v(\hat{a}_v^\dagger + \hat{a}_v)(\hat{b}_{12} + \hat{b}_{34})$.

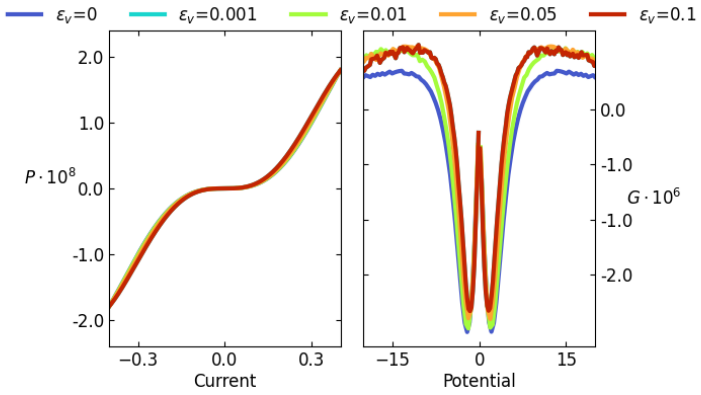

Figure 4.C.3: The same as Figure 4.C.1 but for U=0.

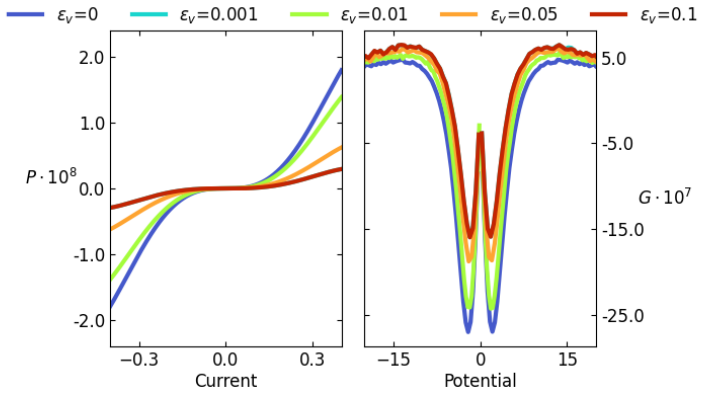

Figure 4.C.4: The same as Figure 4.C.2 but for U=0.

4.D CD spectra

The calculation of CD spectra in isotropic samples requires the calculation of the rotational strength $R(\omega)$:

$$R(\omega) \propto \sum_f \frac{Im\{\vec{\mu}_{gf} \cdot \vec{m}_{fg}\}}{\omega - \omega_{fg}} \tag{4.D.1}$$

where the sum runs over the excited states, $\vec{\mu}_{gf}$ and $\vec{m}_{fg}$ are the transition dipole moment and the magnetic dipole moment between the ground g and the f state (the expression holds in the hypothesis that only the ground state is populated, extending the expression to finite temperature is trivial). In the adopted model, the electric and magnetic dipole moments are collinear and are directed along the z axis. Specifically, in the real space basis the dipole moment operator is diagonal and reads:

$$\hat{\mu}_z = \sum_j (Z_j - \hat{n}_j) j \tag{4.D.2}$$

In the same basis, the magnetic dipole moment is:

$$\hat{m}_z \propto i[\hat{r}, \hat{H}] = i \sum_{j<k,\sigma} t_{jk} \hat{c}^\dagger_{j\sigma} \hat{c}_{k\sigma} + h.c. \tag{4.D.3}$$

After having diagonalized the Hamiltonian, relevant transition elements are calculated, and the CD spectra are then plotted.

Addressing crystallochromism: a hybrid model for Quinacridone polymorphs

5

The evolution of the optical properties of a molecule from solution to a crystalline phase is nontrivial, as it results from a complex interplay of several interactions, including electrostatic and charge-transfer intermolecular interactions and the coupling with molecular vibrations. In order to address the crystallochromism observed in quinacridone (QA), a hybrid modeling strategy is presented that successfully describes the optical properties (absorption and emission) of the βQA and γQA crystalline phases. The proposed protocol relies on the parameterization of the Frenkel-Holstein Hamiltonian against quantum chemical calculations. Periodic Density Functional Theory (DFT) is adopted to optimize the crystallographic geometry and to extract effective atomic charges. TD-DFT results on the isolated molecule are exploited to parametrize the Holstein coupling, while TD-DFT on the embedded molecules and on embedded clusters of increasing size are finally exploited to extract the exciton model parameters. For safe validation, missing optical spectra of the two polymorphs were measured. The approach is general and paves the way for a rationalization of crystallochromism of molecular condensed phases.

5.1 Introduction

The control and interpretation of the optical properties of functional molecular materials is a fundamental research topic in material science, with a wide range of applications in the color industry, [343] optoelectronic devices, [344, 345] fluorescent sensing,[346] and bio-imaging.[347] The precisely engineered energy fluxes driven by intermolecular interactions in molecular assemblies are crucial to the photosynthetic processes and, if properly designed, can be exploited for quantum computing.[55, 56] A recent challenge in the field is the design of molecular luminophores for light generation and amplification.[348] Luminescence, the radiative relaxation from excited states (fluorescence or phosphorescence), is rare in the solid state due to dominant non-radiative decay pathways.[349]. The introduction of aggregation-induced emission (AIE) in 2001 [344, 350] pushed new possibilities for material design, fabrication, and device applications, particularly in achieving multi-color and white-light emission [351]. Along these lines, several luminescence-related properties of condensed phases were discovered, including thermochromism, [352] mechanochromism, [353, 354] and piezochromism.[355] At a more fundamental level, crystallochromism describes the property of a crystalline material to show different colors in the solid state. As with other complex phenomena, crystallochromism relies on a subtle interplay of different interactions.

Here we will focus on a specific form of crystallochromism, sometimes dubbed *color polymorphism*,[356] that applies to systems showing different colors in different polymorphs. In these systems, the presence of specific interactions (such as hydrogen bonds, charge transfer, or

$\pi \cdots \pi$ interactions) can give rise to new electronic transitions or even suppress transitions present at the molecular level. In this direction, crystal engineering is a helpful strategy to govern intermolecular interactions towards specific properties.[357] In a broader perspective, crystallochromism sometimes refers to crystals where different optical spectra are due to different molecular configurations inside the crystal, as due to the presence of different conformers or rotamers building up the crystal.

Crystallochromism finds several technological applications in temperature sensing,[358–360] optoelectronic devices and multiplexing capabilities.[361] Among the most studied examples of crystallochromic molecular systems we mention *N*-(4-methyl-2-nitrophenyl)acetamide [362], the ROY pigment [363], *N*-picryl-*p*-toluidine[364] and quinacridone[365] - which is the system tested in this work.

Quinacridone (QA) (5,12-Dihydroquinolino[2,3-b]acridine-7,14-dione) belongs to a well known class of organic dye and crystallochromic system composed of 3 benzenes and 2 pyridin-4-one rings arranged alternately. The molecule belongs to the C_{2h} point group. QA, commonly known as "Pigment Violet 19", has an intense violet colour. The QA scaffold can be easily functionalized to tune its properties. Several QA derivatives are known, displaying different colours. For these reasons, QA and its derivatives are widely used in industry as organic pigments [366–368]. QA is used in inks as the main product, but also in the sectors of digital printing, paints and coatings, plastics industry, textiles industry, and others[369]. With its highly conjugated scaffold, QA has semiconducting properties: QA and its derivatives are extensively used for organic light-emitting devices (OLED) [370], organic field-effect transistors (OFET) [371], organic solar cells (OSC) [372] and other organic electronic devices. While its electronic structure and transport properties have been deeply investigated [373–376], less comprehensive studies deal with its optical properties.

The accurate prediction and simulation of optical properties of molecular crystals remains a challenging theoretical and computational task. Excited states in molecular condensed phases are typically described as Frenkel excitons (FEs), to account for the delocalization of the molecular excitation as a result of electrostatic intermolecular interactions.[377]. Intermolecular charge-transfer (CT) excitations may also be involved, leading to a considerably more complex picture.[94, 378–380] Moreover, molecular vibrations have a large impact on spectral line shapes and therefore must be taken into account to properly simulate the color of the crystal[91, 96, 381].

Model Hamiltonians have proved useful to describe low-energy excited states in supramolecular systems, including molecular aggregates and crystals. Excited states and FEs can be described by means of a Frenkel-Holstein Hamiltonian accounting for electrostatic interactions among states with one excitation per molecular site and for electron-vibration coupling in the linear approximation[90, 96, 382]. Essential-state models [383–385] have been widely employed to describe charge-transfer transitions in donor-acceptor molecular systems, including aggregates [94, 379, 386–392]. Essential-state Hamiltonians can be parametrized against experimental data[384, 385] and/or against results of quantum chemical calculations.[389, 393]

At the electronic level, density functional theory (DFT) and its time-dependent implementation (TD-DFT) [79] have been largely and successfully applied to describe the excited states of isolated molecular systems, provided a proper functional is selected. Some critical aspects of DFT when dealing with organic conjugated systems, [394] have recently been mitigated by a number of improvements, with double hybrid[395] and long-range corrected functionals.[394, 396] However, the simulation of spectral properties in a crystalline environment hardly remains approachable with first-principle electronic structure calculations. With few exceptions, [397] the simulation of emission with periodic ab initio methods is not available in any electronic structure codes and, therefore, is hardly applied in systematic approaches. More generally, addressing optical properties of molecular crystals requires several approximations, such as multi-methods, such as for spectral warping [398] or approximated Becke's virial exciton model to entirely bypass conventional excited-state methods [399]. A strategy that combines DFT with classical embedding (QM:MM), has been proposed by Adamo et al.[400, 401], and applied to model luminescence of various molecular crystals. Finally, the Crespo-Otero group has proposed a cluster-based QM:QM' protocol for electrostatic embedding, useful not only for optical properties but also for excited-state dynamics and photochemistry.[402]. Lately, they have been benchmarking several approaches for embedding [403].

To step in a different direction and overcome some of the limitations of DFT, we propose here a hybrid modeling strategy that combines first-principle calculations and model Hamiltonians. Specifically, we run TD-DFT calculations on isolated molecules (monomers) and on molecular clusters derived from the crystal structure. These small crystal fragments are electrostatically embedded in a large portion of the crystal, following the charge distribution evaluated with periodic DFT. Relevant results are then exploited to parametrize a periodic model Hamiltonian that describes FE in the presence of electron-vibration coupling (Frenkel-Holstein), fully accounting for the excitonic dispersion in different directions.

In the FE model, the proper definition of the exciton coupling J is crucial. It measures the electrostatic interaction between electronic excitations on different molecules, and several strategies have been proposed for its estimate. The simplest approach relies on the point dipole approximation. More sophisticated strategies have been developed, including (cube) transition densities [404] and approaches based on dimer adiabatic excited states[405], successfully employed by some of us to describe triplet exciton couplings.[406] Time-Dependent tight-binding-based Density Functional Theory was also attempted to go beyond the point-dipole approximation. [407] In this work, we propose an original strategy inspired by the reverse eigenvalue problem. Specifically, the exciton couplings relevant to a crystal fragment are adjusted to reproduce the excitation energies and oscillator strengths obtained from TD-DFT calculations on molecular clusters of increasing size. The proposed general workflow has a modular structure, applicable to different molecular crystals. The method is validated against absorption and fluorescence spectra of two QA polymorphs. Reliable fluorescence data are available on films,[408] but information on absorption spectra is very limited.[368] To fill this gap, we collected experimental absorption and fluorescence spectra of

the two polymorphs.

In the next section, we introduce the general theoretical methodological workflow and provide details about computational and experimental techniques. In the Results and Discussion section, the approach is applied to the QA polymorphs and calculated spectra are compared with experimental data.

5.2 Methods

To model the optical properties of QA,we employ a hybrid modeling approach with a modular structure, as illustrated in Figure 1. First-principle calculations are exploited to evaluate the parameters to be plugged into an effective Frenkel-Holstein Hamiltonian that accounts for exciton delocalization and for vibrational degrees of freedom in a linear coupling approach.

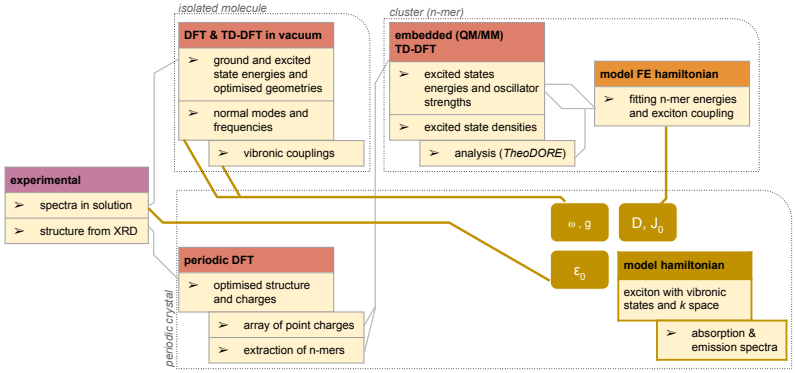

Figure 1: A schematic representation of the hybrid computational methodology.

5.2.1 Model Selection

The structure of βQA and γQA is taken from literature.[365] In βQA [365] each molecule is bonded to the two nearest neighbor molecules via two hydrogen bonds each, forming alternate chains that are not parallel. Half of the chains run in the [110] direction and the other half run in the [1$\bar{1}$0] direction. All chains are equivalent by symmetry. The molecules form stacks through $\pi \cdots \pi$ interactions in the b direction, in 2D layers parallel to the [001] direction that are held together by Van der Waals interactions. To sum up, the three-dimensional crystal can be described as set of non-interacting 2D sheets, held together by independent hydrogen bonds and π stacking interactions.

In γQA [365], each molecule is connected through a single hydrogen bond to the four nearest neighbor molecules, forming a criss-cross pattern. The hydrogen-bond network develops along a unique direction roughly parallel to the [001] direction. Alongside the hydrogen bonds network, the molecules form stacks through $\pi \cdots \pi$ interactions in the b direction. The crystal can be described as non-interacting 2D sheets parallel to the [100] direction, held together by hydrogen bonds and π stacking, but at variance with βQA, the interactions are not independent and each molecule that belongs to a sheet is part of the unique hydrogen-bond

network of that sheet. Both phases can be seen in Figure 2, panels a) and c).

As can be seen, quasi-independent 2D layers are found in both the phases. Figure 2 panels b) and d) offer a schematic representation of the structures and of the main intermolecular interactions.

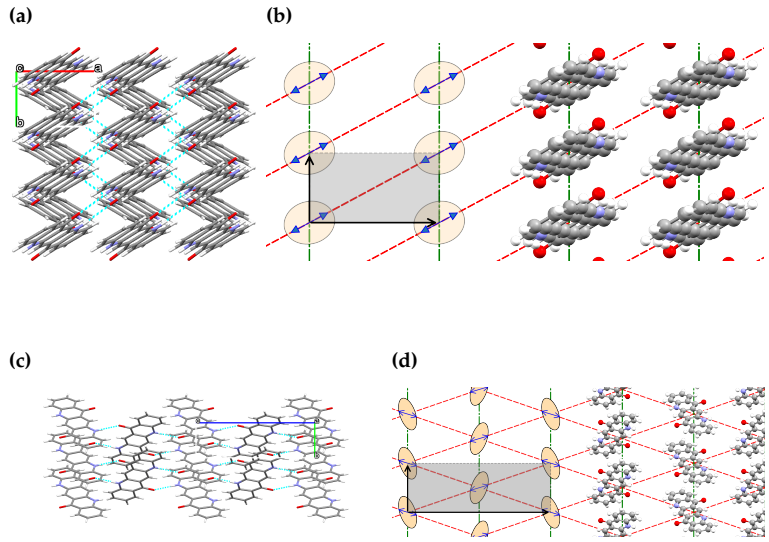

(a) βQA viewed from the ab plane. (b) Schematic representation of relevant interactions in βQA. (c-d): γQA crystal structure. (c) γQA viewed from the bc plane. (d) Schematic representation of relevant interactions in γQA. In panels (b) and (d) the gray box shows the unit cell, green lines mark π-π stacking interactions, red lines mark the hydrogen-bond interactions, blue arrows are aligned with the molecular transition dipole moment.

Figure 2: (a-b): βQA crystal structure.

5.2.2 Electronic structure calculation: pDFT and TDDFT

Periodic DFT (pDFT) calculations were performed using Quantum Espresso (QE) v 6.8 with vdw-df-cx functional [409] to accurately establish the atomic positions and the electrostatic landscape (electron density), fully accounting for periodicity. GBRV ultrasoft PBE pseudopotentials are employed with fixed electronic occupation for the wavefunction with a 5×10×2=100 K-point grid. Kinetic-energy cutoffs of 60 Ry for the wavefunction and of 600 Ry for charge density were chosen. Default QE options were adopted, but with a tighter threshold for SCF convergence (10^{-8} a.u.). Initial coordinates from experimental CCDC structures βQA: QNACRD07 (# 620258) and γQA: QNACRD07 (# 620259) were relaxed according to the BFGS algorithm with variable cell.

Starting from the optimized periodic structures, crystalline fragments (monomer, dimer and 1D molecular clusters) were selected across preferential interaction directions, e.g. along the π stacking direction or the hydrogen-bond direction. TD-DFT calculations with a QM/MM embedding (vide infra) were run to estimate transition energies and dipole moments on the embedded crystalline fragments. The ωB97X-D3BJ [410] functional with the def2-TZVP basis set[411] was selected. As available in Orca[412] 5, it is actually corresponding to the 10-parameters ωB97X-V

[413] functional with dispersion corrections (D3BJ version). The choice of the functional for the DFT part of our workflow is motivated by the good balance between accuracy and computational cost achieved by range-separated DFT functionals. Their performance was confirmed by recent benchmark studies [414–416].

For these Gaussian-based DFT calculations, we employed the Orca 5.0.2 package [412], (by default) taking advantage of the resolution of identity approximation and of the Tamm-Dancoff approximation, TDA (for TD-DFT)[417]. TDA was adopted to achieve convergence and good stability of excited state solutions as well as to reduce the computational burden for large clusters. The analysis of the nature of excited states was performed using the `TheoDORE` 3.0 package.[418–421] Of special interest is the calculation of the electron-hole correlation Ω matrix defined over a set of fragments, where each $\Omega(A, B)$ element quantifies the degree of electronic transfer associated with a given electronic transition when the hole is restricted to a fragment A of the system and the electron to fragment B. In other words, Ω matrices map the transfer of electronic population between the occupied A (x-axis) and virtual states B (y-axis) according to the predefined partition into fragments. [421] Upon subdividing the system of interest into fragments, electron-hole correlation plots are reported in terms of such Ω matrices. From this analysis, reliable information is retrieved on the nature of excited states, including their CT character and the exciton delocalization.

5.2.3 Electrostatic embedding

The QA molecule or QA clusters defined above were inserted into a large grid of point charges, to effectively create a QM/MM-like crystalline embedding (in house code). Specifically, atomic point charges obtained via a Löwdin analysis from the pDFT calculations were located at the atomic positions.Figure 3 illustrates the impact of embedding a monomer in successive layers of charges (for the central monomer, one layer corresponds to $3^3 - 1 = 26$ molecules of point charge arrays, two layers correspond to $5^3 - 1 = 124$, etc.). Acceptable convergence is reached at 3 layers, i.e. introducing 26 unit cells with point-charges around the DFT unit cell.

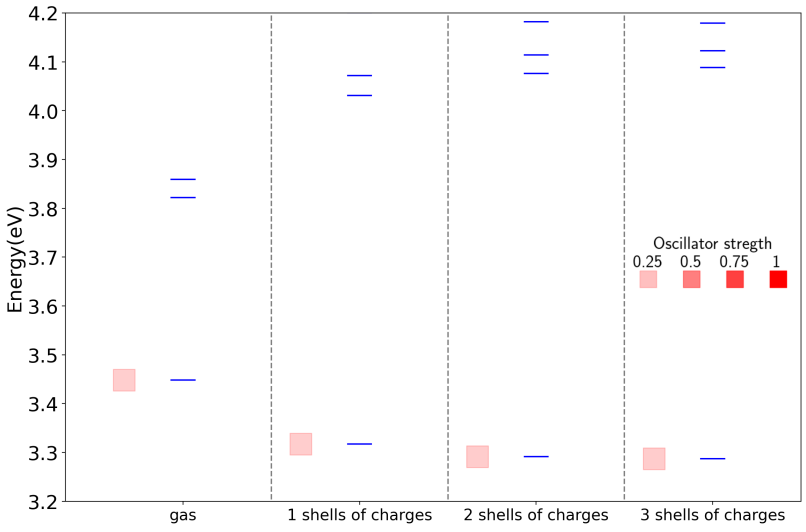

Figure 3: βQA monomer in gas phase, one, two and three shells of molecular charges. In blue the transition energy; in red the oscillator strength. ωB97X functional, def2-TZVP basis set.

5.2.4 Exciton model parameters

To estimate the exciton coupling strength, we adopt an inverse-eigenvalue problem approach. Specifically, we focus on embedded 1D clusters of N molecules, as extracted from the relaxed crystalline structure. Following Section 2.3.2, the exciton Hamiltonian in the tight-binding approximation reads:

$$\hat{H}_{exc} = \epsilon \sum_{i}^{N} |i\rangle \langle i| + J \sum_{i}^{N-1} (|i+1\rangle \langle i| + |i\rangle \langle i+1|) \quad (1)$$

where i runs on the N molecular sites, $|i\rangle$ defines the state where the exciton resides on site i, ϵ is the excitation energy and J is the site-independent exciton interaction energy. We adopted the open-boundary condition to better reproduce the finite-size effects.

For each embedded hexamer, the TD-DFT (ωB97X, def2-TZVP basis set—see above) transition energies of the first excitonic manifold (a set of six excited states) are fitted by tuning the coupling and the diagonal energies of the exciton model, the sign of J being defined by the distribution of the TD-DFT oscillator strength. Notably, while not fitted, the distribution of oscillator strengths of the different eigenstates is well reproduced by the model. The electron-hole correlation analysis described above was used to confirm the excitonic character of TD-DFT states and, in one case, spurious excitations caused by finite-size effects were removed. As seen in Figure 4, the calculation converges rapidly. Hexamers are then selected, offering a good compromise between accuracy and computational feasibility.

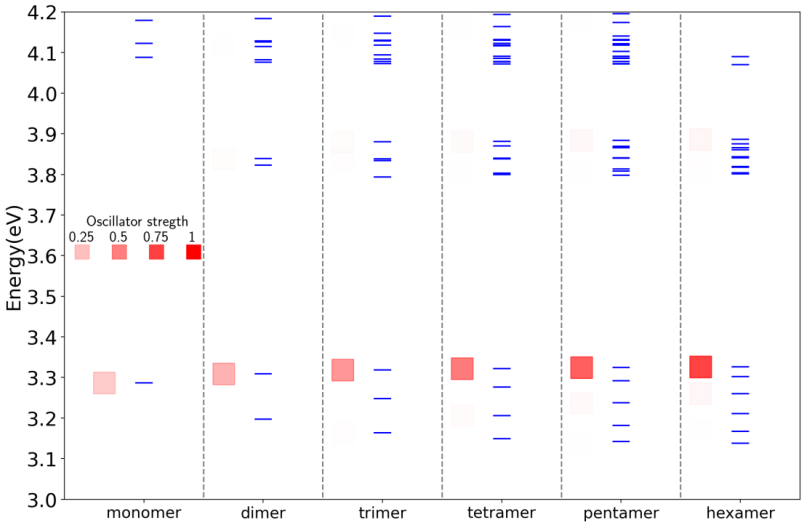

Figure 4: TD-DFT results βQA embedded π-stacked aggregates with increasing dimension. While this case is presented here as an example, similar trends were analyzed for all the four linear aggregates.

For each hexamer aggregate, electron-hole correlation analysis was performed. We derfined four different aggregates, two for each phase, namely γQA$_H$,γQA$_\pi$, βQA$_H$ and βQA$_\pi$. These aggregates are defined by either H-bond or π-π stacking interactions, and they can be individuated following the green and red scattered lines in Figure 2. In the case of γQA$_H$,γQA$_\pi$ and βQA$_\pi$, the first N= 6 excited states are essentially purely excitonic and were safely selected to build the exciton model. For βQA$_H$ (see Figure 5), the two lowest-energy states are not pure exciton states, as they include sizable CT contributions and are somewhat localized on the two molecules at the ends of the linear cluster

suggesting important finite-size effects. We solved the issue by selecting the remaining (N-2) states corresponding to excitonic states delocalized on the (N-2) inner molecules. Summarizing, we selected the first six states of γQA$_H$,γQA$_\pi$ and βQA$_\pi$ embedded hexamers against TDDFT results, and the third to the sixth states of the βQA$_H$ embedded hexamers. The other useful analysis can be found in the Appendix of this Chapter,

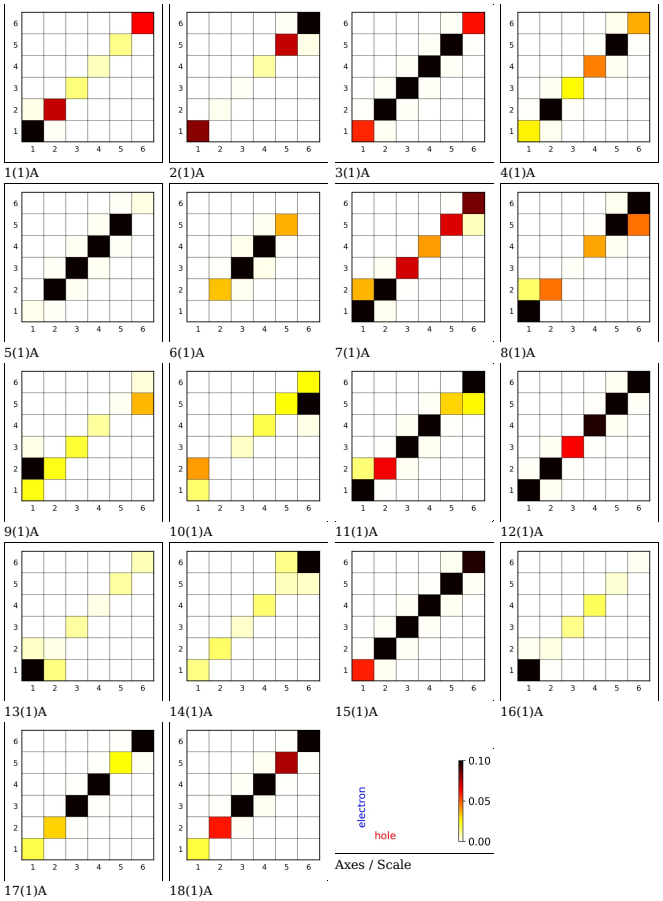

Figure 5: βQA embedded dimer electron-hole correlation analysis represented as Ω matrices as obtained from `TheoDORE`[421] with TDDFT at ωB97X with def2-TZVP basis set. Excited states (1A, 2A, etc.) ordered from top left by rows. The colorscale is defined in the last box. Corresponding transition energies and dipole moments are listed in Table 5.A.12.

section 5.A. All of them showed a remarkable excitonic character for the first N states of the N-mer.

Once the relevant states are properly selected, we employed an in-house code to fit the TD-DFT energies to find the best exciton model parameters (ϵ and J) for each aggregate. The fitting was performed using the `leastsq` least-square algorithm from `SciPy Python` [422]. Indeed, as discussed below, to get rid of the uncertainties in the TD-DFT estimates of the absolute transition energies, we will rely on experimental data for the estimate of ϵ, so that the fitting procedure is actually exploited only to estimate the excitonic couplings J (Table 2).

We note that the oscillator strengths are not fitted, but their relative magnitude is naturally obtained by the eigenvectors of the fitting Hamiltonian. Indeed, the sign of J is fixed by the clustering of the oscillator strength at the bottom or top of the exciton band. Of course, in the exciton model we only get the relative oscillator strengths, and for the sake of comparison in Figure 6, we have normalized them to the value of the brightest transition.

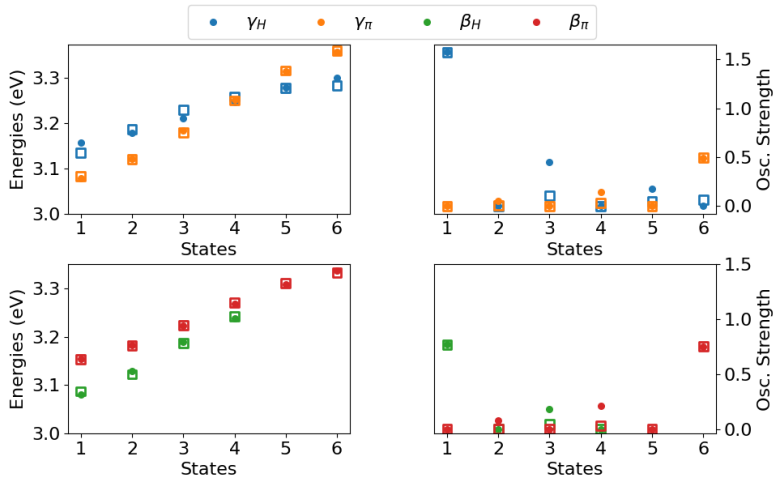

Figure 6: Results of the fitting using the model exciton Hamiltonian (circles) against TDDFT results (squares) for the embedded hexamers. On the left: fitted transition energies. On the right: resulting oscillator strength, rescaled to match the brightest transition. Following the oscillator strength trends, γQA$_\pi$,βQA$_\pi$ are H-aggregates, while βQA$_H$,γQA$_H$ are J-aggregates. RMS Errors (in meV): γ_H=36.6, γ_π=6.3, β_H=10.1,β_π=5.2

The analysis is performed on 1D clusters developing along different directions, getting information on exciton interactions arising in the different clusters. The exciton interaction energies obtained from the analysis of TD-DFT results account for the presence of fixed atomic charges in the surrounding crystal, but not for the polarizability of the crystal. To partially correct for this, the J values extracted from the analysis of TD-DFT results are divided by the squared refractive index of the crystal to obtain the effective $J_{H,\pi}$ to be inserted in the exciton model (Eqns 4,5). The refractive index of the two polymorphs is η =2.04 for γQA and η =2.02 for βQA.[423]

In principle, the fit of TD-DFT data with the Hamiltonian in Eq. 1 would also lead to an estimate of the on-site energies, ϵ. However, as a common practice, TD-DFT calculated spectra are rigidly shifted to improve the agreement with experiment. Here, we prefer a different strategy. QA, a symmetric non-polar dye, is marginally solvatochromic and the position of the maximum of its absorption band in solution offers a good estimate of ϵ_0, the transition energy of an isolated QA in a polarizable environment. The absorption spectrum of QA in dioxane [424] has a maximum at ϵ_0=2.43 eV. A TD-DFT calculation (ωB97X-D3BJ functional and def2-TZVP basis set, using the Adiabatic Hessian After a Step technique as available on ORCA package) quite accurately simulates the experimental spectrum if the calculated spectrum is rigidly redshifted by $\Delta = 0.92$ eV. Since the on-site energies entering Eq. 1 must also account for the shift of the transition energies of the molecule caused by the presence of the surrounding crystal, we set $\epsilon = \epsilon_0 + \Delta$.

5.2.5 DFT-based vibrational and vibronic properties

Vibrational frequencies, ω_i, and Huang-Rhys factors, S_i, are obtained from TD-DFT calculation on a single isolated monomer using the Orca package, employing the Adiabatic Hessian After a Step (AHAS) approximation, where a single optimization step is done in the excited-state geometry and then the Hessian is recalculated in that geometry [425]. The results are shown in Table 1 As can be seen in Figure 7, the calculated vibronic absorption spectrum can be approximated using a single effective mode. With this information, a single effective coupled vibrational

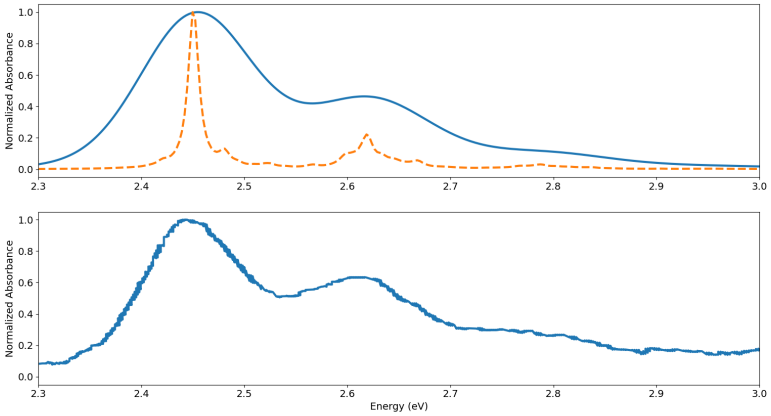

Figure 7: Top: spectra simulated with the AHAS (Adiabatic Hessian After a Step) technique. Harmonic mode calculated on the optimized structure at the ωB97X-D3BJ/def2-TZVP level of theory as in Table 1. Yellow: the raw spectrum obtained from Orca. Blue: the same spectra broadened by convolution with a sum of Gaussian functions with $\sigma = 0.05$eV. Both spectra were redshifted by 0.92 eV to maximize the overlap with the experimental spectrum, corresponding to an ϵ_0 value of 2.43 eV. Bottom: experimental spectrum of QA in dioxane [424].

mode is defined with a frequency that is the weighted average of the vibrational frequencies:[426, 427]

$$\omega_{eff} = \frac{\sum_i S_i \omega_i}{\sum_i S_i} \tag{2}$$

and a relaxation energy that is the sum of all relaxation energies, $\lambda = \sum_i \lambda_i$ (with $\lambda_i = S_i \omega_i$). Accordingly, the coupling constant of the effective coupled mode is:

$$g = \sqrt{\omega_{eff} \lambda} \tag{3}$$

In this approach, the (typically minor) effect of the crystalline environment on intramolecular vibrational modes is neglected.

5.2.6 Frenkel-Holstein model Hamiltonian

We employed a classical Frenkel-Holstein (see Results and eq 8), parametrized according to the protocol described above. It is convenient to exploit the translational symmetry and rewrite the 2D periodic Hamiltonian in the reciprocal space. For the βQA phase with a single molecule per unit cell, the π-stacking interaction develops along the **b** axis, while H-bonds develop along the **a** + **b** direction and the Hamiltonian in the reciprocal space reads:

$$\begin{aligned} \hat{H}^{\beta} = & \sum_{\boldsymbol{k}} [\epsilon_0 + D + 2J_{\pi}^{\beta} cos(\boldsymbol{kb}) + 2J_{H}^{\beta} cos(\boldsymbol{k}(\boldsymbol{a}+\boldsymbol{b}))] \tilde{b}_{\boldsymbol{k}}^{\dagger} \tilde{b}_{\boldsymbol{k}} + \\ & + h\omega_{eff} \sum_{\boldsymbol{q}} (\tilde{a}_{\boldsymbol{q}}^{\dagger} \tilde{a}_{\boldsymbol{q}} + \frac{1}{2}) + \frac{g}{\sqrt{N}} \sum_{\boldsymbol{k},\boldsymbol{q}} \left[\tilde{a}_{\boldsymbol{q}}^{\dagger} \tilde{b}_{\boldsymbol{k}}^{\dagger} \tilde{b}_{\boldsymbol{k}+\boldsymbol{q}} + \tilde{a}_{-\boldsymbol{q}}^{\dagger} \tilde{b}_{\boldsymbol{k}}^{\dagger} \tilde{b}_{\boldsymbol{k}+\boldsymbol{q}} \right] \end{aligned} \tag{4}$$

where $\boldsymbol{k}$ and $\boldsymbol{q}$ are the electronic and vibrational wavevectors, respectively, while $a_{\boldsymbol{i}}^{\dagger}$ and $a_{\boldsymbol{i}}$ are the vibrational creation and annihilation operators for the effective vibrational mode on the i-th molecule, $b_{\boldsymbol{i}}^{\dagger}$ and $b_{\boldsymbol{i}}$ as the creation and annihilation operators for the electronic excitation, g is the vibronic coupling constant, $2J_H^{\beta}$ and J_{π}^{β} define the two excitonic couplings between nearest neighbors.

For γQA the transformed Hamiltonian is more complex, due to the

n	S	ω(eV)	g(eV)	n	S	ω(eV)	g(eV)	n	S	ω(eV)	g(eV)
1	0.000	0.004	0.000	**35**	0.000	0.092	0.000	**69**	0.035	0.165	0.031
2	0.000	0.007	0.000	**36**	0.000	0.093	0.000	**70**	0.000	0.166	0.000
3	0.000	0.008	0.000	**37**	0.002	0.095	0.004	**71**	0.000	0.168	0.000
4	0.000	0.014	0.000	**38**	0.000	0.097	0.000	**72**	0.175	0.169	0.071
5	0.000	0.015	0.000	**39**	0.000	0.097	0.000	**73**	0.000	0.172	0.001
6	0.000	0.017	0.000	**40**	0.000	0.103	0.000	**74**	0.000	0.172	0.000
7	0.000	0.024	0.000	**41**	0.000	0.103	0.000	**75**	0.000	0.177	0.000
8	0.000	0.024	0.000	**42**	0.000	0.104	0.000	**76**	0.054	0.183	0.043
9	0.009	0.029	0.003	**43**	0.000	0.110	0.000	**77**	0.000	0.187	0.000
10	0.045	0.030	0.006	**44**	0.000	0.110	0.000	**78**	0.000	0.189	0.000
11	0.000	0.034	0.000	**45**	0.004	0.111	0.007	**79**	0.006	0.190	0.014
12	0.000	0.035	0.000	**46**	0.000	0.113	0.000	**80**	0.000	0.193	0.000
13	0.000	0.038	0.000	**47**	0.006	0.116	0.009	**81**	0.028	0.194	0.033
14	0.014	0.043	0.005	**48**	0.008	0.116	0.010	**82**	0.000	0.199	0.000
15	0.000	0.049	0.000	**49**	0.000	0.117	0.002	**83**	0.001	0.205	0.007
16	0.000	0.052	0.000	**50**	0.000	0.123	0.000	**84**	0.000	0.207	0.001
17	0.000	0.054	0.000	**51**	0.000	0.125	0.000	**85**	0.004	0.207	0.013
18	0.000	0.055	0.000	**52**	0.000	0.125	0.000	**86**	0.000	0.211	0.000
19	0.000	0.056	0.000	**53**	0.000	0.126	0.000	**87**	0.002	0.211	0.008
20	0.000	0.056	0.000	**54**	0.000	0.126	0.000	**88**	0.000	0.214	0.003
21	0.003	0.058	0.003	**55**	0.003	0.132	0.007	**89**	0.000	0.218	0.000
22	0.001	0.058	0.002	**56**	0.000	0.133	0.000	**90**	0.034	0.220	0.040
23	0.000	0.060	0.000	**57**	0.001	0.140	0.005	**91**	0.000	0.396	0.002
24	0.014	0.068	0.008	**58**	0.000	0.141	0.000	**92**	0.000	0.396	0.002
25	0.000	0.069	0.000	**59**	0.000	0.143	0.000	**93**	0.000	0.398	0.001
26	0.000	0.069	0.000	**60**	0.013	0.144	0.017	**94**	0.000	0.398	0.003
27	0.000	0.070	0.000	**61**	0.000	0.147	0.000	**95**	0.000	0.398	0.001
28	0.018	0.074	0.010	**62**	0.040	0.147	0.029	**96**	0.000	0.398	0.006
29	0.000	0.078	0.000	**63**	0.000	0.152	0.000	**97**	0.000	0.399	0.000
30	0.000	0.079	0.000	**64**	0.030	0.154	0.027	**98**	0.000	0.399	0.000
31	0.001	0.081	0.002	**65**	0.009	0.157	0.015	**99**	0.000	0.401	0.000
32	0.000	0.087	0.000	**66**	0.000	0.158	0.000	**100**	0.000	0.401	0.002
33	0.000	0.087	0.000	**67**	0.000	0.161	0.000	**101**	0.000	0.456	0.001
34	0.009	0.089	0.008	**68**	0.013	0.161	0.018	**102**	0.002	0.456	0.018

Table 1: Vibrational modes, Huang-Rhys factors, frequency in eV, coupling relative to the vibronic spectrum for the first transition of QA. Harmonic mode calculated on the optimized ωB97X-D3BJ/def2-TZVP structure in vacuum with the ωB97X-D3BJ/def2-TZVP level of theory; vibronic progression calculated with the AHAS (Adiabatic Hessian After a Step) method and the ωB97X-D3BJ/def2-tzvp level of theory.

presence of two molecules per unit cell.

$$
\begin{aligned}
\hat{H}^{\gamma} = \sum_{\boldsymbol{k}} \Big\{ & \{\epsilon_0 + D + 2J_{\pi}^{\gamma} cos(\boldsymbol{kb}) + \\
& + 2J_{H}^{\gamma} cos[\boldsymbol{k}(\frac{\boldsymbol{a}+\boldsymbol{b}}{2})] + 2J_{H}^{\gamma} cos[\boldsymbol{k}(\frac{\boldsymbol{a}-\boldsymbol{b}}{2})]\} b_{1,\boldsymbol{k}}^{\dagger} b_{1,\boldsymbol{k}} + \\
& + \{\epsilon_0 + D + 2J_{\pi}^{\gamma} cos(\boldsymbol{kb}) + \\
& - 2J_{H}^{\gamma} cos[\boldsymbol{k}(\frac{\boldsymbol{a}+\boldsymbol{b}}{2})] - 2J_{H}^{\gamma} cos[\boldsymbol{k}(\frac{\boldsymbol{a}-\boldsymbol{b}}{2})]\} b_{2,\boldsymbol{k}}^{\dagger} b_{2,\boldsymbol{k}} \Big\} + \\
& + h\omega \sum_{Q} (a_{1,Q}^{\dagger} a_{1,Q} + a_{2,Q}^{\dagger} a_{2,Q}) + \\
& + \frac{g}{\sqrt{2N}} \sum_{\boldsymbol{k},Q} \Big\{ a_{1,Q}^{\dagger} b_{1,\boldsymbol{k}}^{\dagger} b_{1,\boldsymbol{k}+Q} + a_{1,Q}^{\dagger} b_{2,\boldsymbol{k}}^{\dagger} b_{2,\boldsymbol{k}+Q} + \\
& + a_{2,Q}^{\dagger} b_{1,\boldsymbol{k}}^{\dagger} b_{2,\boldsymbol{k}+Q} + a_{2,Q}^{\dagger} b_{2,\boldsymbol{k}}^{\dagger} b_{1,\boldsymbol{k}+Q} + h.c. \Big\}
\end{aligned}
\tag{5}
$$

where notation equivalent to that in Eq. 4 is employed. Further details on the derivation of the Hamiltonians are in the Appendices, Section 5.B.

The Frenkel-Holstein Hamiltonian is diagonalized at the specific points of the Brillouin zone as relevant to spectroscopy (see Results). Absorption and emission spectra are calculated by assigning a Gaussian lineshape to each transition:

$$
I_{abs}(\omega) \propto \frac{\hbar\omega}{\sigma} \sum_{f>i} \left| \langle f | \hat{\mu} | i \rangle \right|^2 e^{-\frac{\hbar^2}{2\sigma^2}(\omega_{fi}-\omega)^2} \tag{6}
$$

$$
I_{emi}(\omega) \propto \frac{(\hbar\omega)^3}{\sigma} \sum_{f<i} \left| \langle f | \hat{\mu} | i \rangle \right|^2 e^{-\frac{\hbar^2}{2\sigma^2}(\omega_{fi}-\omega)^2} \tag{7}
$$

where I is the intensity of the spectra at frequency ω, σ is the Gaussian width, $\hbar\omega_{if}$ is the energy of the transition between states i and f. In absorption (emission) experiments, f runs on all states with energy

higher (lower) than the ground (Kasha) state. For an easier comparison with experiments, all spectra are normalized.

Color as RGB-tuple is finally calculated starting from the absorption spectra by in-house code. These RGBs define the simulated corresponding colors except for an arbitrary extinction coefficient (or a color depth, equivalently).

Absorption and fluorescence measurements. UV-Vis absorption spectra were recorded with a PerkinElmer Lambda650 spectrophotometer. Fluorescence measurements were performed on a FLS1000 Edinburgh Fluorometer. For each sample, a small quantity of the solid dispersed in nujol oil was ground in a mortar, and a thin layer of the material was then applied on a quartz plate. Absorption spectra were collected in transmission, with the light beam perpendicular to the sample. A quartz plate was used as a reference. Emission spectra were acquired by exciting at 450 nm the same thin layers used for absorption. The sample was slightly off 45^o with respect to the excitation beam to minimize the interference from reflected light. To remove artifacts due to scattering and stray light, appropriate longpass filters were inserted in the emission path.

The spectra were plotted with the absorption spectrum of quinacridone in dioxane solution as reported by Mizuguchi [424] in Figure 8.

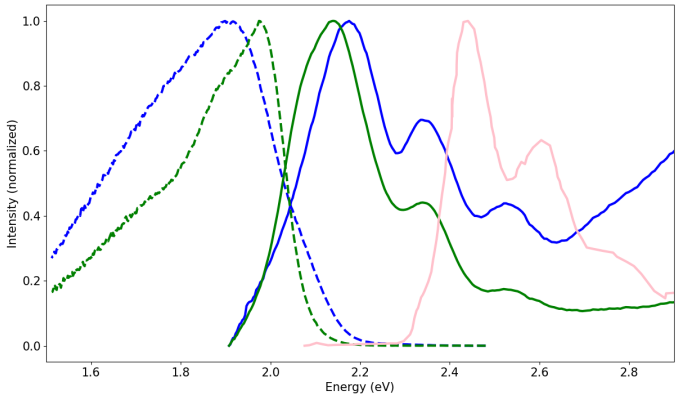

Figure 8: Experimental absorption (continuous lines) and emission (dashed lines) spectra of βQA (green), γQA (blue) (obtained in this work). Pink lines show the absorption spectrum of QA in dioxane solution from literature.[424]

5.3 Results

We first investigated the properties of the QA monomer. TD-DFT results (Figure 9a(i)) demonstrate that the lowest energy excited state of QA is well separated from higher excited states and has a sizable transition dipole moment. In order to discriminate the role of different functional groups and identify the nature of low-lying excited states, the QA molecule was first partitioned into 6 fragments, as shown in Figure 9b(i). The Ω matrix in the top panel of Figure 9c(i) safely ascribes the lowest transition to a delocalized $\pi \rightarrow \pi*$ excitation. Higher energy excited states, with a localized $n \rightarrow \pi*$ nature involving the carbonyl units (see bottom of Figure 9c(i) and Figure 5.A.1 in the Appendices of this chapter), are optically dark, as expected. When embedding the monomer in the

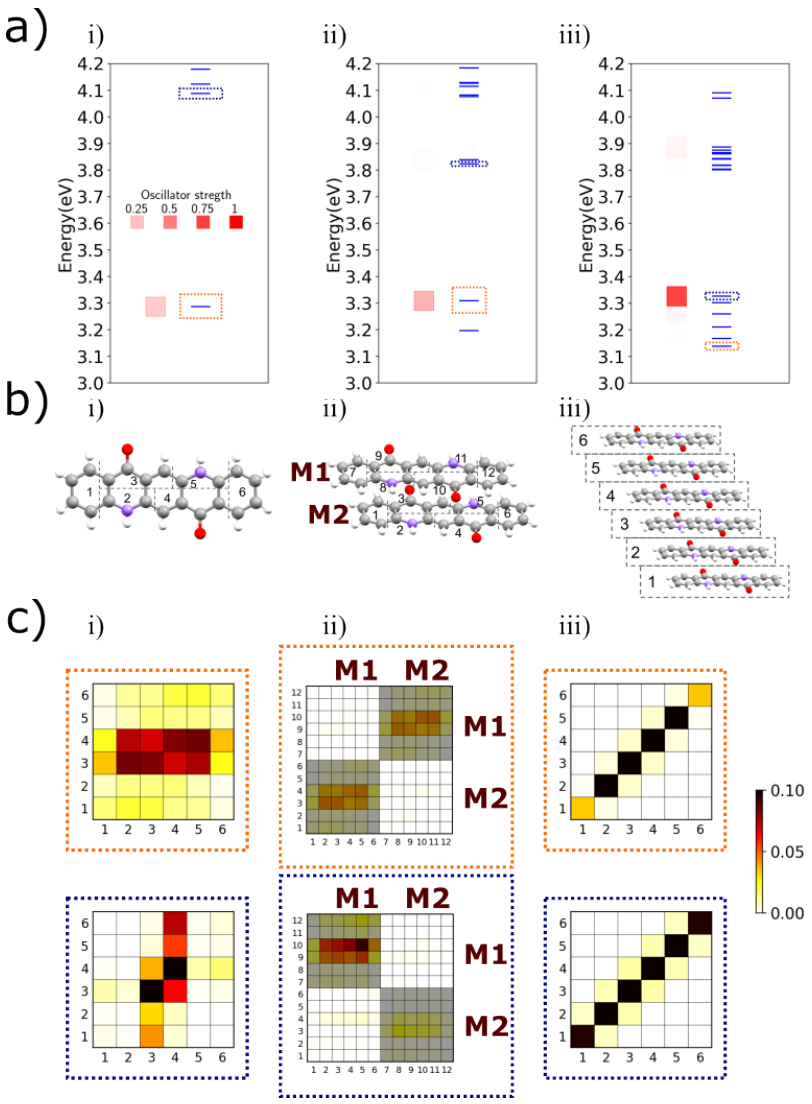

Figure 9: Understanding the exciton model for QA from monomer to βQA hexamer. a) Transition energy diagrams: blue bars representing the TD-DFT excitation energies of the embedded monomer (i), dimer (ii), and hexamer (iii). The color intensity of the red square represents the transition dipole moment according to the scale in panel a(i). The blue and orange dotted frames in panels i-iii mark the states represented in panels c i)-iii). b) The molecular structure of the monomer (i), the dimer (ii) and the hexamer (iii) and their fragment subdivision for this analysis. M1 and M2 are shown for the dimers to help interpreting molecular vs. fragment information. c) Electron-hole correlation analysis of selected transition for the monomer (i), dimer (ii) and hexamer (iii), as carried out by `TheoDORE` version 3.0 (Ω matrices). Colorbar on the right represent the degree of transferred electronic population.

electrostatic field generated by the atomic charges of the surrounding medium, the lowest energy transition is stabilized by ~ 0.2 eV, while its nature is not affected.

For a specific cluster obtained from the βQA structure along axis b, Figure 9 shows the evolution of the excited states from the monomer, to a dimer and an hexamer. In the dimer, the same partitioning of the molecular units as performed in the monomer is adopted, while the hexamer is partitioned into molecular units. Accordingly, in the electron-hole correlation analysis, excited states with (delocalized intermolecular) excitonic nature would generate block-diagonal (dimer, Figure 9c(ii)) or diagonal (hexamer, Figure 9c(iii)) elements in the Ω matrix. Intermolecular CT states are signaled by non-vanishing elements off-diagonal or in off-diagonal blocks.

In the dimer (Figure 9a(ii)), in line with the Kasha's exciton model for H-aggregates, the two low-lying monomer excitations recombine into two states of different energy, with all oscillator strength collapsed into the highest energy state. At higher energy, two dark transitions appear with a dominant CT character (see Figure 9c(ii)). A similar behavior is observed for the hexamer, where, of course, each manifold contains 6

Table 2: Model parameters. All the values are in eV. J_π and J_H corresponds to the two possible excitonic interactions - see text.

phase	βQA	γQA
ϵ_0	2.43	2.43
Δ	0.160	0.145
J_H	-0.011	-0.008
J_π	0.009	0.019
ω	0.168	0.168
g	0.120	0.120

states. The same analysis is performed on other clusters: the clusters obtained from γQA along the b direction shows H-aggregate behavior; the βQA cluster along the $a + b$ direction and the γQA cluster along $\frac{1}{2}[a+b]$ and $\frac{1}{2}[a-b]$ directions all show J-aggregate behavior (see Section 5.A, Hexamers subsection).

In general, both Frenkel and CT excitons can play a role in optical spectra for molecular crystals and aggregates. [94, 379, 381, 428–431] CT excitons typically have negligible oscillator strengths, but they can interact with nearby excited states leading to important spectroscopic effects.[381] In the case of acene crystals, for example, their role has been discussed in the literature and considered from a computational perspective [378, 432, 433] In line with previous work,[368, 408] our results confirm that CT states do not play a major role in the low-energy optical properties of QA. (Figure 9). Accordingly, we will not discuss CT states any further and will focus on the low-energy excited state manifold, with a well-defined exciton nature.

Following the strategy described in the Methods section, from the analysis of TD-DFT results on embedded clusters we obtain a reliable estimate of J-couplings between nearest-neighbor molecules. Relevant results for the two crystals are reported in Table 2. In the same table we also show the other parameters of the Frenkel-Holstein model, obtained following the approaches detailed in Methods section.

Vibrational degrees of freedom enter the model in terms of molecular vibrations modulating on-site energies, in the classical Frenkel-Holstein model. Accounting for a single effective molecular vibration on each site with frequency ω_{eff} the Hamiltonian reads:

$$\hat{H} = \sum_i \left\{ \left[\epsilon_0 + D - g(\hat{a}_i^\dagger + \hat{a}_i) \right] \hat{b}_i^\dagger \hat{b}_i + \hbar\omega_{eff}(\hat{a}_i^\dagger \hat{a}_i + \frac{1}{2}) + \sum_j J_{ij}(\hat{b}_i^\dagger \hat{b}_j + \hat{b}_j^\dagger \hat{b}_i) \right\} \tag{8}$$

$a_i^\dagger$ and a_i are the vibrational creation and annihilation operators for the effective vibrational mode on the i-th molecule, $b_i^\dagger$ and b_i are the creation and annihilation operators for the electronic excitation, g is the vibronic coupling constant, J_{ij} measures the coupling between the molecules on the site $\boldsymbol{i}$ and $\boldsymbol{j}$.

As detailed above, we only account for excitonic interactions between nearest-neighbors sites linked by either hydrogen-bonds or π stacking acting in the two dimensional crystallographic planes of interest for the two crystals. The single-mode approximation is often adopted in the framework of the Frenkel-Holstein model[381]. To further validate this approximation, Figure 10 shows the vibronic coupling strength partitioned in the different contributions. It is clear that the coupling strength clusters around the frequency of the effective mode. The 2D

periodic Hamiltonian written in the reciprocal space, is fully reported in the Method section Eq. 4 and 5.

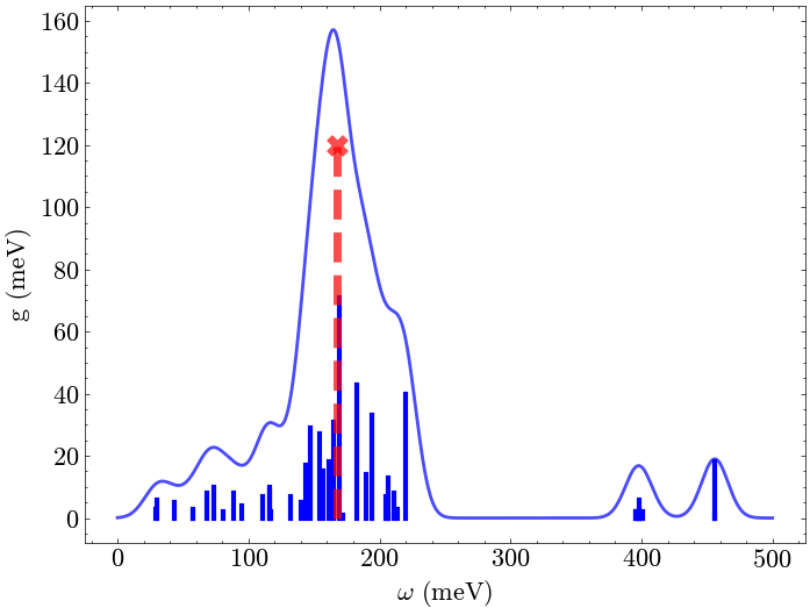

Figure 10: g_i at each corresponding ω_i in meV for the vibrational modes analyzed in Table 1. Bars: g values as shown in the table. Blue line: convolution of the bars with a Gaussian lineshape with $\sigma = 0.01eV$ to simulate a frequency distribution. Red line and red cross: coupling mode at the average effective mode frequency ω.

To start with, we consider the electronic problem, setting $g = 0$. In these conditions, only the electronic wavevector is of relevance. For the βQA phase with a single molecule per unit cell, the first line in Eq. 4 defines the energy of the exciton in the momentum space. Results are plotted in Figure 11. In the γQA phase, the presence of two molecules per unit cell leads to a slightly more complex problem, with the first two lines in Eq. 5 defining a two-dimensional Hamiltonian in each point of the Brillouin zone. The diagonalization of the two dimensional matrix leads to two exciton bands, as plotted in Figure 11. The ground state in the electronic model is a single point at $\boldsymbol{K} = \boldsymbol{k} = 0$, and the selection rule of optical spectroscopy, $\Delta\boldsymbol{K} = 0$, allows us to immediately recognize the states that can be reached upon photoexcitation, marked with a black star in the right-hand side panels of Figure 11. In the γQA phase, the two states reached upon photoexcitation have very similar energies and transition dipole moments. After photoexcitation, according to the Kasha rule[434], the system typically relaxes very quickly to the lowest energy state in the lowest exciton surface (marked as a white star in the right-hand panels of Figure 11a-b). In both polymorphs, the Kasha state is located at the border of the Brillouin zone so that emission is forbidden. However, this result is strictly valid only in the absence of vibrational coupling.

When vibrational coupling is switched on, the wavevector is the sum of the electronic and vibrational wavevectors, $\boldsymbol{K} = \boldsymbol{k} + \boldsymbol{q}$. In the low temperature limit, vibrational states are not thermally populated and the ground state is located at $\boldsymbol{K} = \boldsymbol{k} = 0$. States reached upon absorption can have population on the vibrational levels, but the optical selection rules impose that $\boldsymbol{K} = \boldsymbol{k} + \boldsymbol{q} = 0$ or $\boldsymbol{k} = -\boldsymbol{q} = -\sum_\nu n_\nu \boldsymbol{q}_\nu$, where $\boldsymbol{q}_\nu$ are the occupation numbers for the vibrational wavevectors $\boldsymbol{q}_\nu$. Emission occurs from the Kasha state, the lowest energy state in the excited state manifold, characterized by a total wavevector $\boldsymbol{K}_{Kasha}$. Upon emission, the optical selection rule imposes that a state is reached in the ground state manifold with the same total wavevector, $\boldsymbol{K}_{Kasha}$. Accordingly, since the

electronic ground state has $\boldsymbol{k} = 0$, the relevant state in the ground state manifold has $\sum_\nu n_\nu \boldsymbol{q}_\nu = \boldsymbol{K}_{Kasha}$. To calculate spectra, we considered 2D aggregates comprising 4×4 unit cells (16 and 32 molecules for βQA and γQA, respectively) limiting the total number of vibrational quanta to 3 (we explicitly checked the quasi-convergence of calculated spectra). Temperature effects were tested, accounting for a Boltzmann energy distribution, but only marginal broadening effects were detected.

Focusing on absorption, vibronic coupling gives rise to a manifold of vibronic states on each exciton surface and is therefore responsible for the appearance of a vibronic structure. The role of molecular vibrations is even more important in emission. Specifically, the ground state is itself dressed by vibrational modes, so that states are present in the ground state manifold at the border of the Brillouin zone, making emission possible. Emission originates from the lowest energy states in the excited state manifold and it ends up in states with finite vibrational population on the ground state manifold. The emission band edge is therefore red-shifted with respect to absorption.

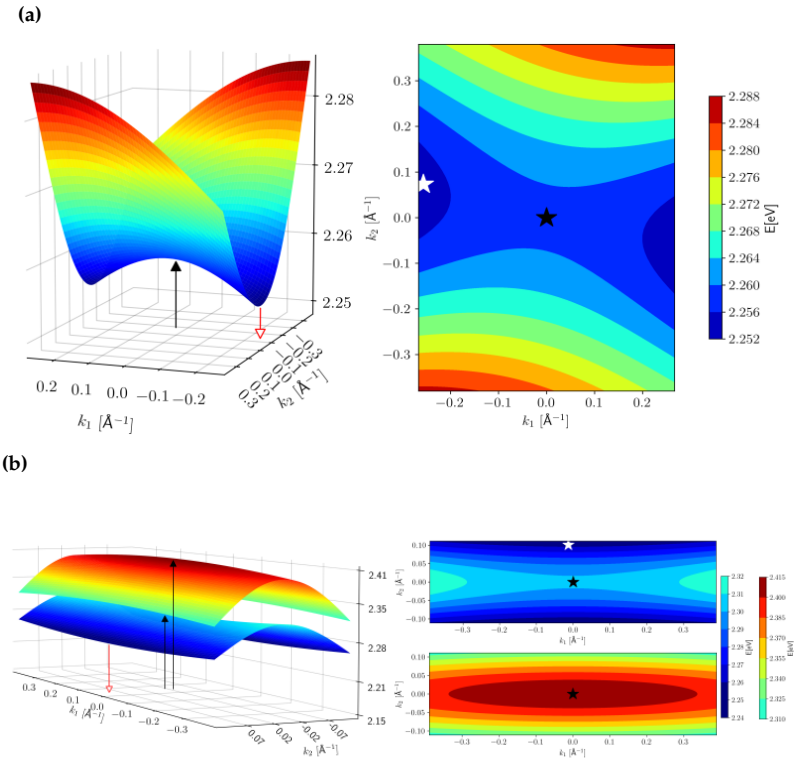

Figure 11: Electronic energy surfaces for the band of βQA (a) and γQA (b). On the left side: 3D representation, on the right: 2D colormap representation. The colorscale is displayed on the right. The black arrow (left) and the black stars (right) represent the center zone, the sole point in which the absorption takes place. The red arrow (left) and white star (right) represent the point of the emission.

Figure 12 compares experimental and simulated spectra. For both polymorphs, absorption and emission band shapes agree very well with experiment. The agreement is particularly striking since there are no adjustable parameters in the adopted model. In fact, all model parameters are extracted from ab initio simulations, with the only exception of ϵ_0, the exciton energy, which is extracted from experimental data relevant to QA in solution. This choice is motivated by the well-known problem of TD-DFT in the calculation of accurate absolute transition energies, as already discussed for QA[435]. Our results overestimate transition energies by roughly 0.9 eV (see Figure 7 and Table 5.A.1-Table 5.A.16).

To reproduce experimental spectra, a fairly large width is assigned to the Gaussian bands associated to each transition. This effectively accounts for inhomogeneous broadening phenomena that are not included in the FE model. Specifically, low-frequency vibrational modes are responsible for broadening, as well as disorder and structural defects that are absent in the adopted perfect crystalline model.

The major discrepancy between calculated and experimental spectra is seen in emission, with the experimental band showing a broad component to the red that is missing in the simulation. This is ascribed to the presence of defects and trap states in the sample that may contribute to the actual emission and are not accounted for in our model for the perfect crystal. In any case, the overall quality of the simulated spectra is very satisfactory and validates the proposed approach.

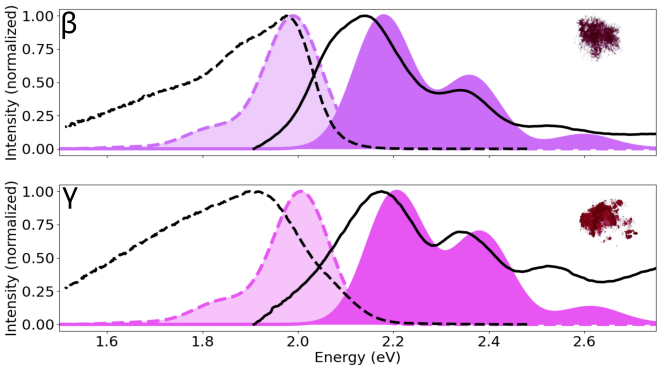

Figure 12: Calculated absorption and emission spectra of βQA (top) and γQA (bottom) compared with experimental measurements (this work). The experimental spectra are indicated in black thick lines, while the calculated ones are filled in dark purple(βQA, RGB: 204,109,249) and magenta(γQA, RGB:231,85,243), i.e. the colors calculated using the corresponding simulated absorption spectra. Areas under the emission spectra are filled with a variant of the corresponding absorption colors with arbitrary transparency. Solid lines are used for absorption spectra and dashed lines for emission spectra. In the insets on the right-top side we show photographs of the crystal powders taken for the two phases.

Looking at Figure 12, we notice the prominent role of vibrational states in determining the optical signatures of QA in absorption and emission. This suggests that quantum treatment of coupled excitonic-vibrational states, as suggested in our hybrid approach, is a fundamental step towards reliable spectra simulation. Conversely, electronic methods based on QM or QM/MM methods would fail to capture these features even though they offer an accurate description of the embedding.

Based on the simulated absorption spectra it is possible to simulate the corresponding color. These colors are reported in Figure 12 as a filled area under the absorption spectra. Unfortunately, reversely re-obtaining quantitative components in color space from the experimental spectra is not straightforward due to the scattering artifacts on the high-energy side of the bands. In addition to this, the effective color appearance perceived by human eyes for the two polymorphs is not necessarily easy to quantify nor can be accurately reproduced on the reading format (paper or screen). However, we are able to capture the amount of blue vs. red hue dominance in βQA vs. γQA, respectively.

5.4 Discussion and conclusions

The evolution of the optical properties of a molecule from solution to a crystalline phase is highly nontrivial, being dominated by intermolecular

interactions with the appearance of collective excitations or, in other terms, of delocalized excited states. Molecular vibrations add a layer of complexity in this scenario and, as discussed above, profoundly alter the spectral properties in terms of bandshapes and/or emissive properties. Here we introduced a comparatively simple and computationally accessible hybrid modeling protocol, relying on the parameterization of the Frenkel-Holstein Hamiltonian against quantum chemical calculations. Specifically, periodic DFT was adopted to optimize the crystallographic geometry and to extract effective atomic charges. TD-DFT results on the isolated molecule are exploited to parametrize the Holstein coupling. TD-DFT calculations on the embedded molecule and clusters of increasing size are finally exploited to extract the exciton model parameters. The only phenomenological inputs are the refractive index of the crystal and ϵ_0, the absorption frequency of the molecule in solution that enters to recalibrate the TD-DFT absolute energies. Specifically, the squared refractive index enters into the renormalization of the exciton couplings as extracted from TD-DFT, in line with recent theoretical discussions [436]. Indeed, simulated spectra calculated without accounting for dielectric screening poorly agree with experiment, as seen in Figure 13. For ϵ_0, we prefer to refer to the experimental transition energy of QA in solution rather than introduce an arbitrarily rigid shift of the TD-DFT energies.

Exciton couplings are often estimated in the point dipole approximation. In this approximation the estimated J (in Table 3) are much larger than in our current approach, leading to a poor agreement between calculated and experimental spectra, in Figure 14.

Table 3: Excitonic couplings calculated following different methods for βQA and γQA. Up: fitting with TDDFT and dividing by the squared refractive index as discussed in the main text. Middle: point-dipole approximation (again accounting for the refractive index correction). Bottom: as the top line but without accounting for the refractive index correction.

	βQA		γQA	
	J_H	J_π	J_H	J_π
This work	-0.013	0.008	-0.008	0.020
Dipole approximation	-0.012	0.036	-0.016	0.011
This work (no refractive index correction)	-0.052	0.033	-0.031	0.078

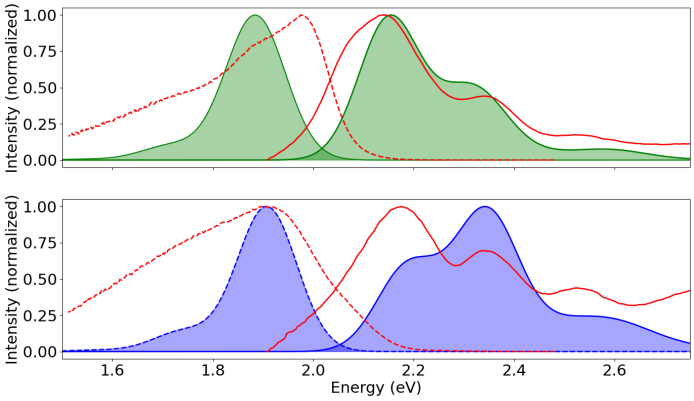

Figure 13: Calculated absorption and emission spectra of QA β (top) and γQA (bottom) using directly the fitted J (without correction for the squared refractive index), compared with experimental measurements (red lines). Calculated spectra are shown in green(βQA) and blue (γQA). Solid lines are used for experimental absorption spectra and dashed lines for experimental emission spectra.

The approach is validated against the interesting case of QA, a molecular system featuring two polymorphs with distinctly different optical spectra (and colors). In the process, we collected a set of new experimental absorption and emission spectra for the β and γ phases of QA, in

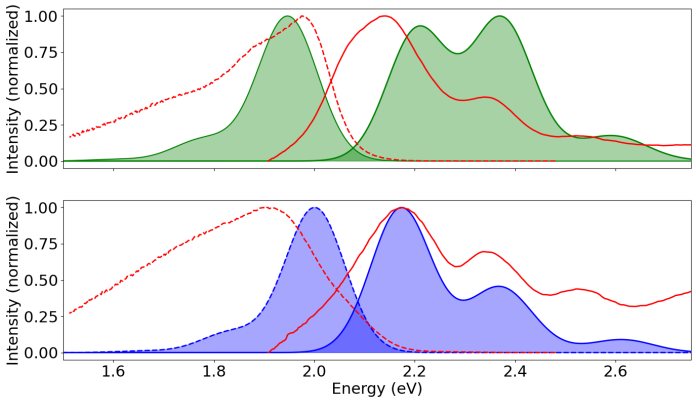

Figure 14: Calculated absorption and emission spectra of QA β (top) and γQA (bottom) using the J calculated with the dipole moment approximation, compared with experimental measurements (red lines). Calculated spectra are shown in green(βQA) and blue (γQA). Solid lines are used for experimental absorption spectra and dashed lines for experimental emission spectra.

order to fill a gap in the available literature data for these crystals. The agreement between simulated and experimental spectra is very good, demonstrating the validity of the proposed method. The proposed multiscale approach applies to molecular crystals where CT transitions are marginally involved in low-energy excited states. In principle, it could be automated once a dictionary of symmetries is established. Finally, having access to experimental absorption spectra in solution may help to fine tune ϵ_0.

Recently, Giannini et al. have addressed the spectral properties of a non-fullerene acceptor labeled Y6.[380] Their model includes FEs, CTs and vibrational states, and it is based on a similar hybrid strategy of a model Frenkel-Holstein Hamiltonian supplemented by ab initio calculations. They were able to describe the spectral evolution from the solution to the thin film and the crystal. For Y6 it was shown that CTs and FEs can strongly mix due to a favorable energy alignment. By accounting for their combined mixing with vibronic states, the authors accurately reproduced the absorption in the visible and infrared. Although emission spectra were not addressed, their strategy proved to be successful in explaining the photophysics of Y6 and interpreting additional features observed in the experiments.

Multiscale flavors were also suggested in a conceptual workflow proposed by Bondarenko et al. [437], with the aim to simulate optical properties of a large supramolecular aggregate of dyes. Their iterative multiscale approach combines molecular dynamics and quantum mechanical exciton modeling. However, vibrational states were not included in their model, which was limited to the case of J-aggregates with large excitonic coupling. A multiscale bottom-up scheme has also been suggested to compute non-linear properties of molecular crystal [438].

Our work is aligned with this promising direction of multiscale approaches. An important novelty is the actual simulation of emission spectra. In the case of QA, we observe that emission is only permitted as a consequence of mixing with vibronic states. Our robust parametrization, combined with the proper building of a model Hamiltonian, well explains the different absorption and emissions measured for the polymorphs of QA, hence paving the way to a rationalization of crystallochromism of molecular condensed phases.

Appendix

5.A TD-DFT excitations and analysis

TD-DFT calculations were performed with `Orca 5` at ωB97X-D3BJ (equivalently ωB97X for TDDFT transitions) with def2-TZVP basis set. See Methods for all details. For both βQA and γQA we present additional figures and tables for:

- monomers in-vacuum (include frequency and vibronic coupling calculations) and embedded (including evaluation of embedding)
- dimers (H-Bond and π-stacked), both in-vacuum (tables only) and embedded
- hexamers (H-Bond and π-stacked), both in-vacuum (tables only) and embedded

5.A.1 Monomer

Table 5.A.1: Results for the βQA in-vacuum (a) and embedded (b) monomer obtained with TDDFT at ωB97X with def2-TZVP basis set. The calculation for the embedded monomer employs 3 layers of point-charges that simulate the βQA environment around the molecule. Rows marked in green correspond to the selected electronic states possessing excitonic features.

a)	State	Energy (eV)	Wavelength (nm)	Oscillator Strength	μ_x(au)	μ_y(au)	μ_z(au)
	1	3.44791	359.6	0.194233	-1.251360	0.785020	0.342590
	2	3.82177	324.4	0.000000	-0.000070	0.000040	0.000030
	3	3.85967	321.3	0.000313	-0.029600	0.029150	0.039840
	4	4.29990	288.4	0.000000	0.000000	0.000000	0.000020
	5	4.40580	281.4	0.085870	0.251170	-0.214530	-0.828540
	6	5.22019	237.5	0.000000	-0.000010	0.000090	0.000560
b)	State	Energy (eV)	Wavelength (nm)	Oscillator Strength	μ_x(au)	μ_y(au)	μ_z(au)
	1	3.28738	377.2	0.199489	-1.292640	0.810850	0.386070
	2	4.08836	303.3	0.000001	-0.002320	0.002410	0.001910
	3	4.12371	300.7	0.000146	-0.021360	0.020670	0.023750
	4	4.17931	296.7	0.000007	0.004410	-0.003160	-0.006430
	5	4.30406	288.1	0.071344	0.250540	-0.203780	-0.756610
	6	5.07989	244.1	0.001754	0.000460	0.011330	0.118150

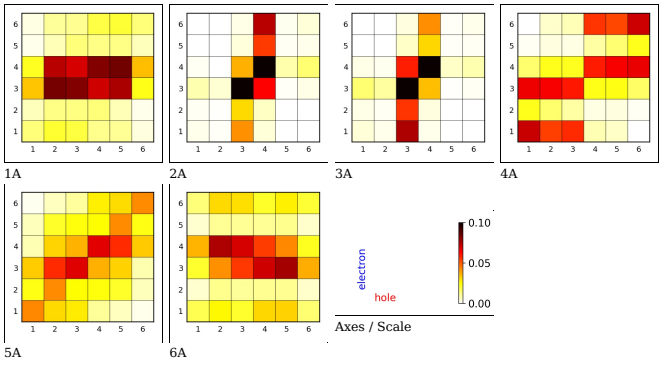

Figure 5.A.1: βQA embedded monomer electron-hole correlation analysis represented as Ω matrices as obtained from `TheoDORE` at ωB97X with def2-TZVP basis set. Excited states (1A, 2A, etc.) ordered from top left by rows. The colorscale is reported in the last box. [421].

Table 5.A.2: Results for the γQA in-vacuum (a) and embedded (b) monomer obtained with TDDFT at ωB97X with def2-TZVP basis set. The calculation for the embedded monomer employs 3 layers of point-charges that simulate the γQA environment around the molecule. Rows marked in green correspond to the selected electronic states possessing excitonic features.

a)	State	Energy (eV)	Wavelength (nm)	Oscillator Strength	μ_x(au)	μ_y(au)	μ_z(au)
	1	3.43745	360.7	0.194425	0.537130	-0.362980	-1.374240
	2	3.80076	326.2	0.000000	0.000290	-0.000170	-0.000290
	3	3.83411	323.4	0.000154	-0.030600	0.025860	0.006180
	4	4.29182	288.9	0.000000	-0.000630	-0.000070	0.000130
	5	4.39957	281.8	0.084573	-0.775020	0.404400	0.143110
	6	5.20749	238.1	0.000005	-0.004790	0.002210	-0.002930
b)	State	Energy (eV)	Wavelength (nm)	Oscillator Strength	μ_x(au)	μ_y(au)	μ_z(au)
	1	3.29241	376.8	0.202047	-0.563280	0.378990	1.433510
	2	4.12187	300.8	0.000000	0.000210	-0.000180	0.000320
	3	4.15014	298.8	0.000075	0.020920	-0.016080	0.006440
	4	4.16512	297.7	0.000000	0.000390	-0.000500	-0.000270
	5	4.28967	289	0.048471	-0.572430	0.301510	0.206540
	6	5.06301	244.9	0.000003	-0.000020	-0.000260	-0.005110

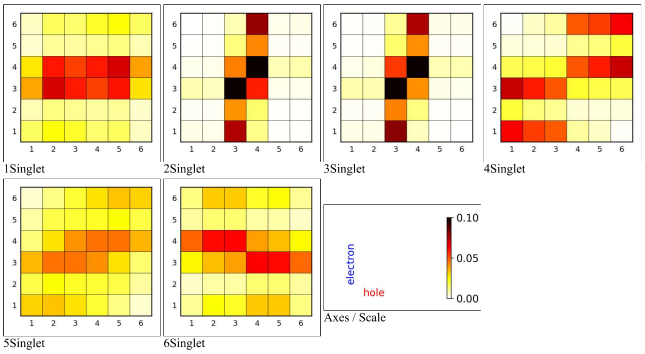

Figure 5.A.2: γQA embedded monomer electron-hole correlation analysis represented as Ω matrices as obtained from `TheoDORE` at ωB97X with def2-TZVP basis set. Excited states (1A, 2A, etc.) ordered from top left by rows. The colorscale is reported in the last box. [421].

5.A.2 Dimers

Table 5.A.3: Results for the βQA gas-phase dimer obtained with TDDFT at ωB97X with def2-TZVP basis set. Rows marked in green correspond to the selected electronic states possessing excitonic features.

State	Energy (eV)	Wavelength (nm)	Oscillator Strength	μ_x(au)	μ_y(au)	μ_z(au)
1	3.25838	380.5	0.475739246	2.02869	-1.27746	-0.46045
2	3.32478	372.9	0.000000031	-0.00052	0.00032	0.00011
3	3.81206	325.2	0.000198540	-0.01978	0.02533	0.03306
4	3.81209	325.2	0.000000971	-0.00135	0.00177	0.00233
5	4.16212	297.9	0.000000000	-0.00001	0.00001	0.00003
6	4.22884	293.2	0.000149094	-0.02498	0.01993	0.02044
7	4.22911	293.2	0.000000006	0.00016	-0.00019	0.00000
8	4.24318	292.2	0.011718787	-0.18620	0.08474	-0.26623
9	4.3323	286.2	0.000001039	-0.00123	0.00094	0.00272
10	4.33543	286.0	0.099420779	0.39206	-0.29582	-0.83355
11	4.57182	271.2	0.004930381	-0.16728	0.10935	0.06386
12	4.57281	271.1	0.000000223	0.00111	-0.00075	-0.00044

Table 5.A.4: Results for the βQA embedded dimer obtained with TDDFT at ωB97X with def2-tzvp basis set and employing 3 layers of point-charges around the molecule. Rows marked in green correspond to the selected electronic states possessing excitonic features.

State	Energy (eV)	Wavelength (nm)	Oscillator Strength	μ_x(au)	μ_y(au)	μ_z(au)
1	3.125	396.8	0.471923692	2.06597	-1.29728	-0.46140
2	3.2014	387.3	0.001620569	0.11992	-0.07513	-0.02521
3	4.06316	305.1	0.000055956	-0.00314	0.00304	0.02330
4	4.14344	299.2	0.045359596	0.00972	-0.02581	-0.66789
5	4.15483	298.4	0.000615543	0.01764	-0.00942	0.07515
6	4.16045	298.0	0.000309917	0.01948	-0.01027	0.05055
7	4.23139	293.0	0.003202061	0.05909	-0.05110	-0.15743
8	4.23809	292.5	0.006853556	0.09168	-0.07512	-0.22795
9	4.23934	292.5	0.025663848	-0.18434	0.13973	0.43999
10	4.24379	292.2	0.045006957	-0.25053	0.18808	0.57857
11	4.60888	269.0	0.000191800	0.03235	-0.02081	-0.01481
12	4.62418	268.1	0.000148597	0.02717	-0.01781	-0.01601

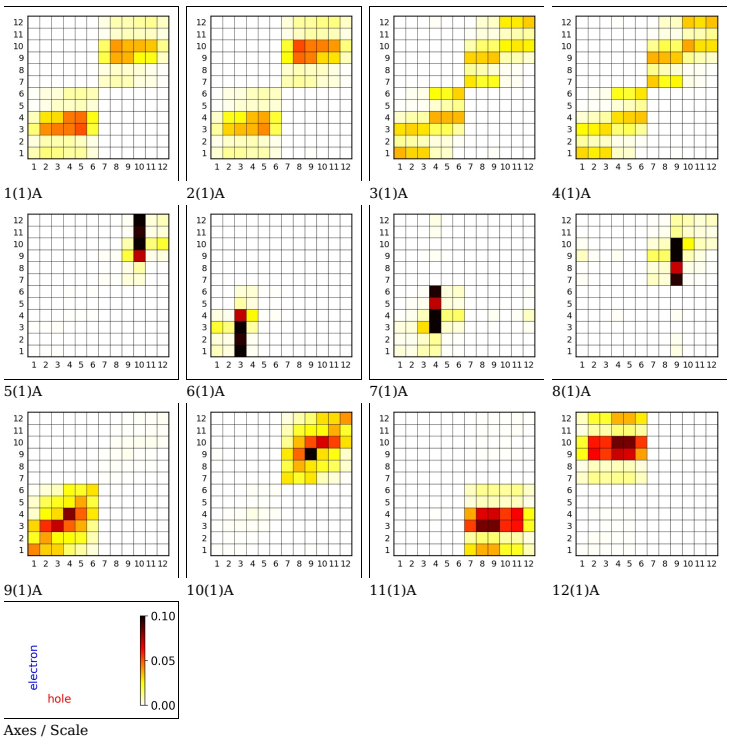

Figure 5.A.3: βQA gas phase dimer electron-hole correlation analysis represented as Ω matrices as obtained through `TheoDORE`[421] with def2-TZVP basis set and employing 3 layers of point-charges around the molecule. Excited states (1A, 2A, etc.) ordered from top left by rows. The colorscale is reported in the last box.

Table 5.A.5: Results for the βQA gas-phase dimer obtained with TDDFT at ωB97X with def2-TZVP basis set. Rows marked in green correspond to the selected electronic states possessing excitonic features.

State	Energy (eV)	Wavelength (nm)	Oscillator Strength	μ_x(au)	μ_y(au)	μ_z(au)
1	3.39819	364.9	0.000000006	-0.00021	0.00014	0.00006
2	3.50325	353.9	0.294780438	-1.46607	1.05865	0.40553
3	3.82699	324.0	0.000000000	-0.00000	0.00006	0.00004
4	3.82871	323.8	0.000014054	-0.00401	-0.00668	-0.00944
5	3.86906	320.5	0.000583918	-0.05525	0.04867	0.02720
6	3.87101	320.3	0.000000011	0.00023	-0.00021	-0.00013
7	4.0655	305.0	0.000000002	0.00009	-0.00006	0.00012
8	4.07093	304.6	0.005719503	-0.17569	0.11679	-0.11331
9	4.26933	290.4	0.002935783	0.01425	0.03180	0.16387
10	4.33146	286.2	0.000000000	0.00000	-0.00000	0.00001
11	4.42026	280.5	0.000000025	-0.00014	0.00014	0.00043
12	4.42982	279.9	0.090254278	-0.34519	0.30097	0.78860

Table 5.A.6: Results for the βQA embedded dimer obtained with TDDFT at ωB97X with def2-TZVP basis set and employing 3 layers of point-charges around the molecule. Rows marked in green correspond to the selected electronic states possessing excitonic features.

State	Energy (eV)	Wavelength (nm)	Oscillator Strength	μ_x(au)	μ_y(au)	μ_z(au)
1	3.20991	386.3	0.000001079	0.00265	-0.00191	-0.00176
2	3.31774	373.7	0.303420197	-1.52191	1.09838	0.45853
3	3.84988	322.0	0.000922684	0.07979	-0.05536	0.01873
4	3.86386	320.9	0.009288988	-0.24989	0.17699	-0.06603
5	4.0921	303.0	0.000041995	-0.00521	0.01213	0.01564
6	4.09789	302.6	0.000064844	0.00485	-0.01380	-0.02078
7	4.12985	300.2	0.004356302	0.01657	0.02606	0.20519
8	4.14175	299.4	0.000385288	-0.02254	0.02443	0.05189
9	4.14447	299.2	0.000247708	-0.01933	0.01977	0.04093
10	4.19876	295.3	0.000004378	0.00265	-0.00245	-0.00544
11	4.29941	288.4	0.000007729	0.00213	-0.00262	-0.00787
12	4.31398	287.4	0.075798414	0.35439	-0.29897	-0.70866

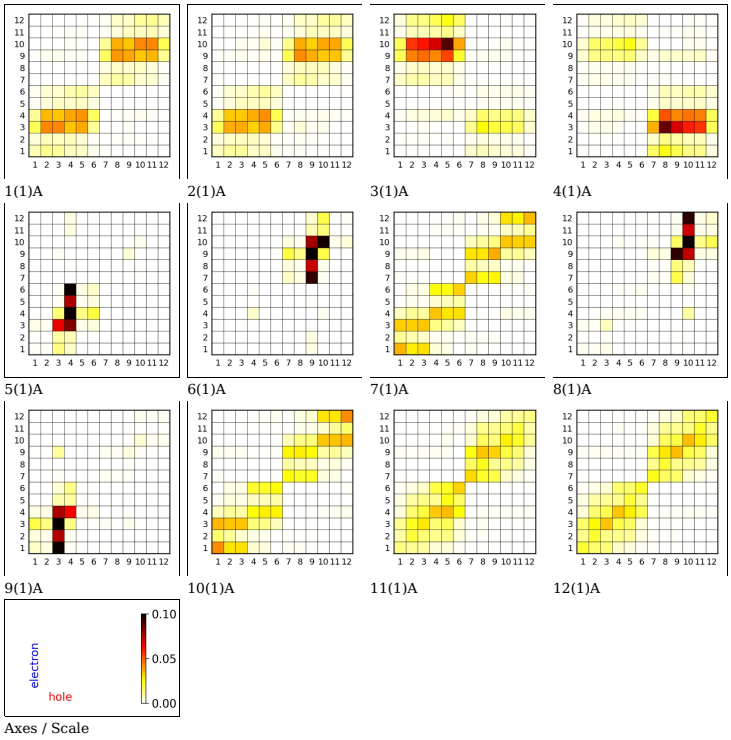

Figure 5.A.4: βQA embedded dimer electron-hole correlation analysis represented as Ω matrices as obtained from `TheoDORE`[421] with TDDFT at ωB97X with def2-TZVP basis set. Excited states (1A, 2A, etc.) ordered from top left by rows. The colorscale is defined in the last box. Corresponding transition energies and dipole moments are listed in Table 5.A.6.

Table 5.A.7: Results for the βQA gas-phase dimer obtained with TDDFT at ωB97X with def2-TZVP basis set. Rows marked in green correspond to the selected electronic states possessing excitonic features.

State	Energy (eV)	Wavelength (nm)	Oscillator Strength	μ_x(au)	μ_y(au)	μ_z(au)
1	3.32872	372.5	0.443340057	0.79344	0.04895	-2.19189
2	3.39125	365.6	0.023808317	0.00370	-0.51731	0.13761
3	3.78501	327.6	0.000078057	0.02079	0.01991	-0.00365
4	3.83644	323.2	0.000006829	0.00485	-0.00681	0.00166
5	3.87599	319.9	0.000128342	-0.02871	0.02287	0.00204
6	4.06124	305.3	0.000979200	-0.00163	0.02233	-0.09664
7	4.21854	293.9	0.004468782	0.06028	0.12187	-0.15733
8	4.22712	293.3	0.000909010	0.02918	0.05871	-0.06692
9	4.26165	290.9	0.006901507	0.17274	-0.09876	0.16281
10	4.35646	284.6	0.087717747	-0.76077	0.47538	0.13078
11	4.38247	282.9	0.040947969	0.49873	0.27528	-0.23847
12	4.98476	248.7	0.479448401	0.90736	-1.53775	0.85903

Table 5.A.8: Results for the γQA embedded dimer obtained with TDDFT at ωB97X with def2-TZVP basis set and employing 3 layers of point-charges around the molecule. Rows marked in green correspond to the selected electronic states possessing excitonic features.

State	Energy (eV)	Wavelength (nm)	Oscillator Strength	μ_x(au)	μ_y(au)	μ_z(au)
1	3.21911	385.2	0.461103949	-0.81007	-0.05235	2.27765
2	3.28817	377.1	0.024222186	-0.00899	0.53343	-0.12669
3	4.12292	300.7	0.003545342	-0.01283	-0.10811	0.15247
4	4.13769	299.6	0.000244743	-0.03529	-0.03088	0.01468
5	4.14998	298.8	0.000286338	-0.02226	0.02519	-0.04106
6	4.1731	297.1	0.004007037	-0.16282	0.02982	-0.10859
7	4.18497	296.3	0.000250206	-0.04106	0.01405	-0.02360
8	4.26126	291.0	0.000398715	0.00724	0.03269	-0.05194
9	4.27993	289.7	0.044747757	-0.52607	0.32831	0.20548
10	4.29156	288.9	0.034916802	0.43397	0.25545	-0.28020
11	4.39446	282.1	0.000717994	0.00396	-0.02825	0.07652
12	4.98742	248.6	0.000944376	0.03284	-0.02627	0.07720

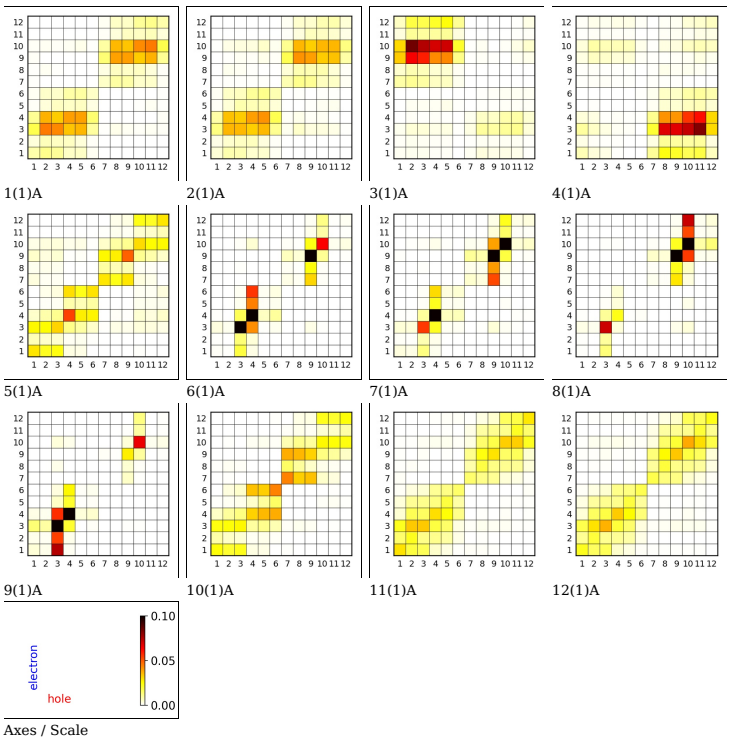

Figure 5.A.5: γQA embedded dimer electron-hole correlation analysis represented as Ω matrices as obtained from `TheoDORE`[421] with TDDFT at ωB97X with def2-TZVP basis set. Excited states (1A, 2A, etc.) ordered from top left by rows. The colorscale is defined in the last box. Corresponding transition energies and dipole moments are listed in Table 5.A.8

Table 5.A.9: Results for the γQA gas-phase dimer obtained with TDDFT at ωB97X with def2-TZVP basis set. Rows marked in green correspond to the selected electronic states possessing excitonic features.

State	Energy (eV)	Wavelength (nm)	Oscillator Strength	μ_x(au)	μ_y(au)	μ_z(au)
1	3.346	370.5	0.000000036	0.00015	-0.00021	-0.00061
2	3.50375	353.9	0.254968727	0.54637	-0.41563	-1.58083
3	3.7894	327.2	0.000113258	0.02168	-0.02106	-0.01750
4	3.78966	327.2	0.000000004	-0.00009	0.00004	0.00019
5	3.84359	322.6	0.000181713	0.03213	-0.02935	0.00599
6	3.84382	322.6	0.000001415	0.00280	-0.00262	0.00057
7	3.95411	313.6	0.016357749	0.33673	-0.15055	-0.18112
8	3.96065	313.0	0.000064464	0.02109	-0.00946	-0.01141
9	4.25217	291.6	0.004736467	-0.17461	0.12209	0.00852
10	4.33573	286.0	0.000000067	0.00074	0.00012	-0.00027
11	4.39095	282.4	0.000000047	0.00054	-0.00034	-0.00019
12	4.41682	280.7	0.083800787	-0.70492	0.46740	0.24303

Table 5.A.10: Results for the γQA embedded dimer obtained with TDDFT at ωB97X with def2-TZVP basis set and employing 3 layers of point-charges around the molecule. Rows marked in green correspond to the selected electronic states possessing excitonic features.

State	Energy (eV)	Wavelength (nm)	Oscillator Strength	μ_x(au)	μ_y(au)	μ_z(au)
1	3.16156	392.2	0.000000056	-0.00023	0.00020	0.00080
2	3.32858	372.5	0.262155584	-0.58488	0.44320	1.63591
3	3.73429	332.0	0.003851017	-0.12748	0.06611	0.14653
4	3.74246	331.3	0.015695600	-0.25950	0.13411	0.29302
5	4.10743	301.9	0.002596576	-0.12251	0.10303	0.01335
6	4.11611	301.2	0.000010705	0.00852	-0.00567	-0.00121
7	4.11803	301.1	0.000285130	0.04526	-0.02731	-0.00565
8	4.14684	299.0	0.000151783	-0.03010	0.01914	-0.01489
9	4.14737	298.9	0.000024220	-0.01234	0.00768	-0.00520
10	4.20577	294.8	0.000000069	-0.00042	0.00066	0.00025
11	4.27877	289.8	0.000002870	0.00391	-0.00297	-0.00180
12	4.29706	288.5	0.052487490	-0.52116	0.37291	0.29648

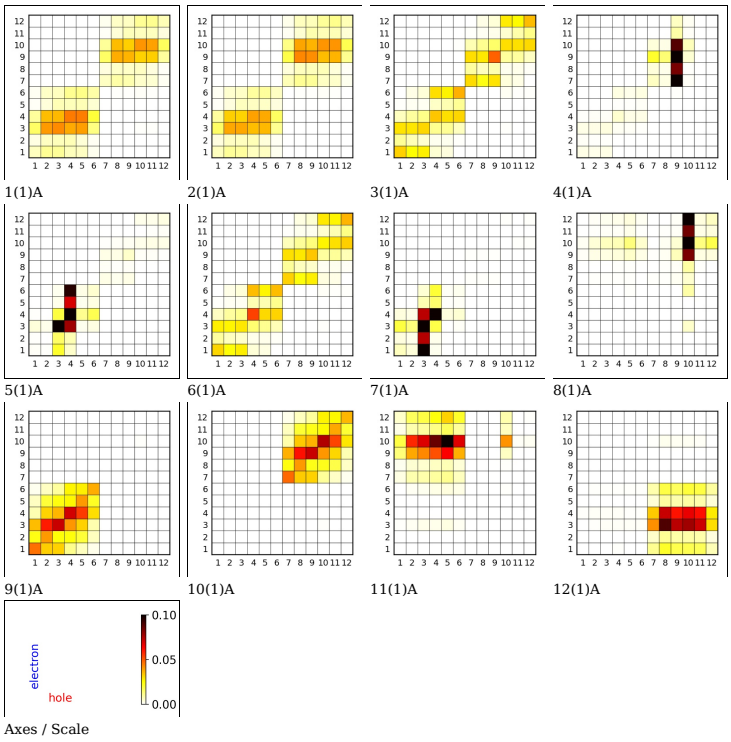

Figure 5.A.6: γQA embedded dimer electron-hole correlation analysis represented as Ω matrices as obtained from `TheoDORE`[421] with TDDFT at ωB97X with def2-TZVP basis set. Excited states (1A, 2A, etc.) ordered from top left by rows. The colorscale is defined in the last box. Corresponding transition energies and dipole moments are listed in Table 5.A.10.

5.A.3 Hexamers

Table 5.A.11: Results for the βQA gas-phase hexamer obtained with TDDFT at ωB97X with def2-TZVP basis set. Rows marked in green correspond to the selected electronic states possessing excitonic features.

State	Energy (eV)	Wavelength (nm)	Oscillator Strength	μ_x(au)	μ_y(au)	μ_z(au)
1	3.12036	397.3	1.700501399	3.96180	-2.49057	-0.58764
2	3.183	389.5	0.000000000	0.00002	-0.00001	0.00001
3	3.23101	383.7	0.117669412	-1.01497	0.63909	0.21888
4	3.26323	379.9	0.000000000	-0.00003	0.00002	0.00003
5	3.29274	376.5	0.105529747	0.94328	-0.59507	-0.25353
6	3.29397	376.4	0.000007856	0.00814	-0.00514	-0.00216
7	3.80542	325.8	0.000097612	-0.01347	0.01803	0.02325
8	3.80543	325.8	0.000090460	-0.01293	0.01736	0.02240
9	4.03302	307.4	0.000000002	0.00011	-0.00005	0.00001
10	4.07182	304.5	0.001423097	0.08147	-0.04200	0.07658
11	4.12091	300.9	0.000000000	-0.00001	-0.00000	-0.00002
12	4.16816	297.5	0.002651132	0.09937	-0.04810	0.11736
13	4.20052	295.2	0.000006795	0.00656	-0.00447	0.00173
14	4.20055	295.2	0.000144517	0.03025	-0.02061	0.00803
15	4.21483	294.2	0.000000037	-0.00041	0.00019	-0.00040
16	4.21815	293.9	0.005596338	0.14456	-0.07047	0.16820
17	4.21871	293.9	0.000030967	-0.01033	0.00492	-0.01299
18	4.22204	293.7	0.002159156	0.05417	-0.01636	0.13294

Table 5.A.12: Results for the βQA embedded hexamer obtained with TDDFT at ωB97X with def2-TZVP basis set and employing 3 layers of point-charges around the molecule. Rows marked in green correspond to the selected electronic states possessing excitonic features.

State	Energy (eV)	Wavelength (nm)	Oscillator Strength	μ_x(au)	μ_y(au)	μ_z(au)
1	2.98084	415.9	0.739952469	2.66074	-1.67610	-0.49339
2	2.99371	414.2	0.240360110	-1.51382	0.95348	0.27637
3	3.09924	400.0	0.769191155	-2.67648	1.69046	0.33034
4	3.13439	395.6	0.001106024	0.10103	-0.06382	-0.01108
5	3.19802	387.7	0.042911214	-0.62354	0.39216	0.07139
6	3.25357	381.1	0.000000204	-0.00135	0.00084	0.00017
7	3.98838	310.9	0.006912707	-0.03744	0.03512	0.26098
8	3.99483	310.4	0.053242517	-0.10038	0.09455	0.72456
9	4.0256	308.0	0.001104622	-0.00281	0.00755	0.10552
10	4.02842	307.8	0.002283174	0.00098	-0.00906	-0.15183
11	4.04176	306.8	0.000010998	-0.00140	0.00156	0.01033
12	4.07065	304.6	0.012965191	-0.01360	0.01847	0.35983
13	4.10386	302.1	0.000596476	-0.00380	-0.00948	-0.07634
14	4.10828	301.8	0.000647490	-0.00540	-0.00977	-0.07943
15	4.11643	301.2	0.000014260	-0.00033	-0.00073	-0.01186
16	4.16481	297.7	0.049032992	0.08585	-0.09865	-0.68077
17	4.17032	297.3	0.026196665	-0.07485	0.07849	0.49461
18	4.17301	297.1	0.016550912	-0.03549	0.04981	0.39768

Table 5.A.13: Results for the βQA gas-phase hexamer obtained with TDDFT at ωB97X with def2-TZVP basis set and employing 3 layers of point-charges around the molecule. Rows marked in green correspond to the selected electronic states possessing excitonic features.

State	Energy (eV)	Wavelength (nm)	Oscillator Strength	μ_x(au)	μ_y(au)	μ_z(au)
1	3.36786	368.1	0.000000002	-0.00012	0.00007	0.00004
2	3.3891	365.8	0.018094111	0.38549	-0.24351	-0.10010
3	3.42519	362.0	0.000000001	0.00008	-0.00005	-0.00003
4	3.47	357.3	0.075186365	0.75244	-0.52543	-0.20535
5	3.51342	352.9	0.000000005	0.00017	-0.00017	-0.00003
6	3.54315	349.9	0.672298506	2.02169	-1.84124	-0.51721
7	3.82486	324.2	0.000000000	0.00003	0.00000	0.00003
8	3.82571	324.1	0.000000397	-0.00157	0.00103	0.00084
9	3.82677	324.0	0.000000000	-0.00002	-0.00000	-0.00005
10	3.82774	323.9	0.000004282	0.00219	0.00491	0.00409
11	3.82847	323.8	0.000000001	-0.00002	0.00003	-0.00008
12	3.8287	323.8	0.000004196	0.00298	0.00398	0.00447
13	3.86006	321.2	0.001124744	0.06905	-0.08226	-0.01893
14	3.86124	321.1	0.000000000	-0.00003	0.00000	-0.00005
15	3.86264	321.0	0.000119527	0.02425	-0.02485	-0.00760
16	3.86382	320.9	0.000000000	-0.00002	0.00004	-0.00002
17	3.86988	320.4	0.000499862	0.04538	-0.05004	-0.02664
18	3.86998	320.4	0.000001556	-0.00255	0.00285	0.00133

Table 5.A.14: Results for the βQA embedded hexamer obtained with TDDFT at ωB97X with def2-TZVP basis set and employing 3 layers of point-charges around the molecule. Rows marked in green correspond to the selected electronic states possessing excitonic features.

State	Energy (eV)	Wavelength (nm)	Oscillator Strength	μ_x(au)	μ_y(au)	μ_z(au)
1	3.15303	393.2	0.000000005	0.00005	-0.00007	-0.00023
2	3.1813	389.7	0.004460019	-0.20823	0.10608	0.05109
3	3.22315	384.7	0.000000296	0.00135	-0.00107	-0.00088
4	3.2704	379.1	0.030941792	0.52273	-0.29877	-0.15384
5	3.31129	374.4	0.000000502	0.00210	-0.00130	-0.00030
6	3.33315	372.0	0.752660546	-2.21086	1.98301	0.62991
7	3.83107	323.6	0.000314230	0.04502	-0.02873	0.02227
8	3.8336	323.4	0.001429573	-0.09437	0.06342	-0.04788
9	3.84644	322.3	0.000300603	-0.03348	0.01760	-0.04195
10	3.84772	322.2	0.000062713	0.01542	-0.00766	0.01921
11	3.86695	320.6	0.000089670	0.02239	-0.02044	0.00524
12	3.8707	320.3	0.003275203	-0.13880	0.11830	-0.03574
13	3.88466	319.2	0.000083607	0.01361	-0.00106	-0.02631
14	3.89094	318.7	0.000010001	-0.00571	0.00746	-0.00408
15	3.89914	318.0	0.000002289	-0.00165	0.00426	-0.00175
16	3.90902	317.2	0.029900360	0.35682	-0.41832	0.09953
17	4.08551	303.5	0.000320744	-0.00210	-0.00964	-0.05574
18	4.10571	302.0	0.000001143	-0.00041	0.00076	0.00326

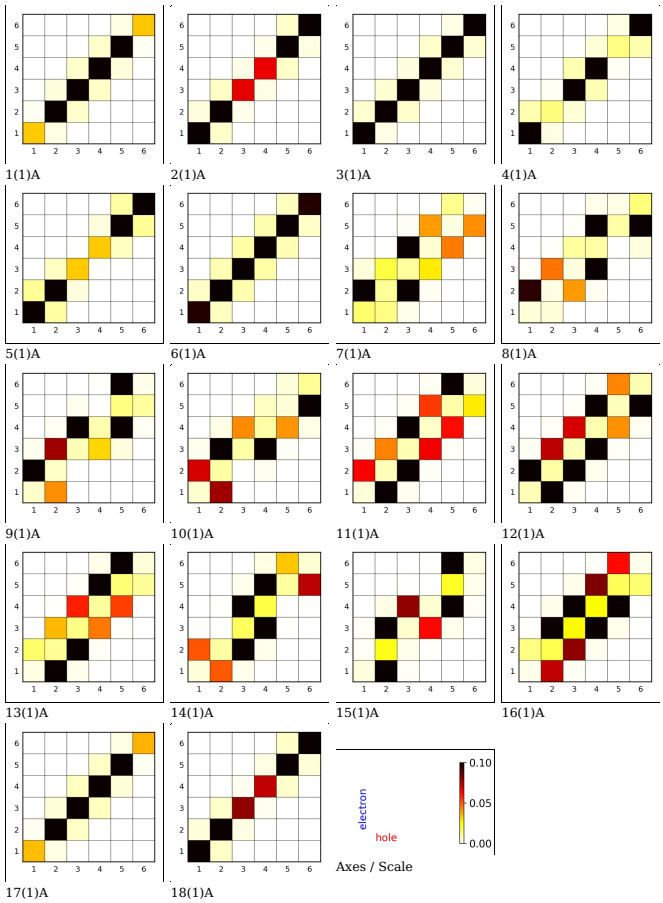

Figure 5.A.7: βQA embedded hexamer electron-hole correlation analysis represented as Ω matrices as obtained from TheoDORE[421] with TDDFT at ωB97X with def2-TZVP basis set. Excited states (1A, 2A, etc.) ordered from top left by rows. The colorscale is defined in the last box. Corresponding transition energies and dipole moments are listed in Table 5.A.14.

Table 5.A.15: Results for the βQA gas-phase hexamer obtained with TDDFT at ωB97X with def2-TZVP basis set. Rows marked in green correspond to the selected electronic states possessing excitonic features.

State	Energy (eV)	Wavelength (nm)	Oscillator Strength	μ_x(au)	μ_y(au)	μ_z(au)
1	3.2097	386.3	1.494468804	1.29117	0.01849	-4.16383
2	3.26595	379.6	0.000114830	-0.02900	-0.01738	0.01710
3	3.30954	374.6	0.112566966	-0.39381	-0.01910	1.11034
4	3.33977	371.2	0.008390210	-0.03094	-0.31826	0.01727
5	3.36525	368.4	0.078934804	0.33325	-0.38485	-0.83561
6	3.36883	368.0	0.072909711	0.17926	0.71430	-0.58397
7	3.77042	328.8	0.000075317	0.02034	0.01980	-0.00309
8	3.80533	325.8	0.000083095	0.02262	-0.01923	-0.00312
9	3.81376	325.1	0.000075667	0.02126	0.01859	-0.00351
10	3.8147	325.0	0.000077673	-0.02166	0.01856	0.00418
11	3.82278	324.3	0.000075324	-0.02135	-0.01814	0.00441
12	3.84145	322.8	0.000004785	0.00150	-0.00690	0.00097
13	3.87986	319.6	0.000129829	-0.02983	0.02179	0.00107
14	4.12994	300.2	0.025342656	0.10659	0.02549	-0.48832
15	4.15486	298.4	0.000868888	0.06850	0.01814	0.05929
16	4.18179	296.5	0.002262748	0.04981	0.04817	-0.13147
17	4.20263	295.0	0.003685260	-0.05684	-0.17588	-0.04036
18	4.25018	291.7	0.000254292	0.02128	-0.02900	0.03389

Table 5.A.16: Results for the γQA embedded hexamer obtained with TDDFT at ωB97X with def2-TZVP basis set and employing 3 layers of point-charges around the molecule. Rows marked in green correspond to the selected electronic states possessing excitonic features.

State	Energy (eV)	Wavelength (nm)	Oscillator Strength	μ_x(au)	μ_y(au)	μ_z(au)
1	3.13411	395.6	1.573583859	1.32995	0.02244	-4.32717
2	3.18658	389.1	0.000149768	-0.03491	0.02611	-0.00421
3	3.22893	384.0	0.107125721	-0.39349	-0.02707	1.09482
4	3.25919	380.4	0.000125414	-0.03353	-0.01126	-0.01788
5	3.27784	378.3	0.046436573	-0.26488	0.14944	0.69696
6	3.28362	377.6	0.066068288	0.04637	0.88006	-0.21122
7	4.0708	304.6	0.020619950	-0.03270	-0.03234	0.45237
8	4.09396	302.8	0.001813854	0.11548	0.00877	0.06836
9	4.12133	300.8	0.001200576	-0.00723	-0.05977	0.09091
10	4.13021	300.2	0.000176600	0.03597	0.02041	-0.00589
11	4.14506	299.1	0.002268234	0.12319	0.01917	0.08242
12	4.15228	298.6	0.000019633	0.00567	-0.01262	0.00126
13	4.15313	298.5	0.000249215	0.01832	-0.02046	0.04117
14	4.15603	298.3	0.000278394	0.04886	-0.00171	0.01854
15	4.1587	298.1	0.000308816	0.04043	0.01303	0.03503
16	4.16059	298.0	0.000201343	0.03946	0.01947	0.00626
17	4.16567	297.6	0.000658401	0.02566	-0.07282	0.02214
18	4.16944	297.4	0.001924279	0.09359	-0.08152	0.05861

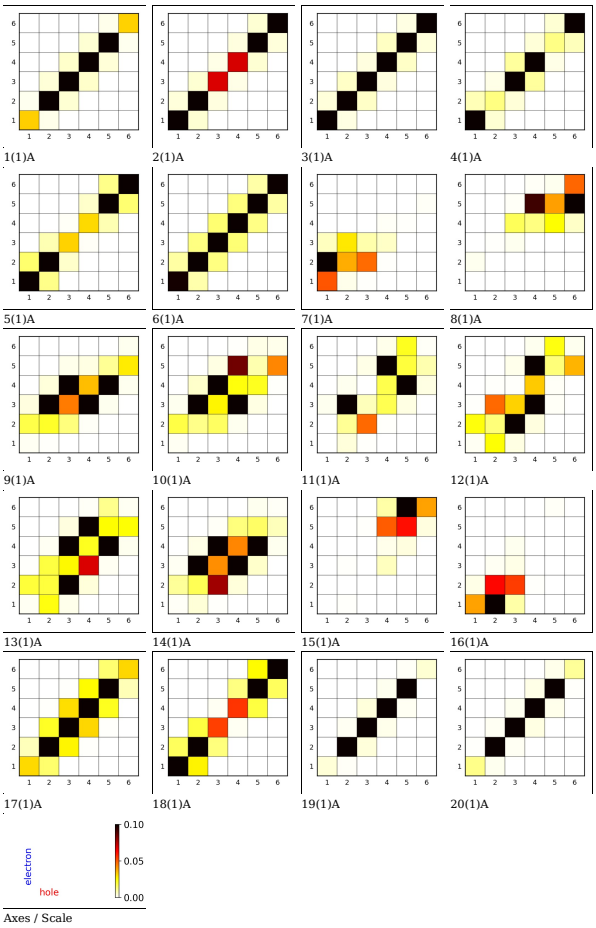

Figure 5.A.8: γQA embedded hexamer electron-hole correlation analysis represented as Ω matrices as obtained from `TheoDORE`[421] with TDDFT at ωB97X with def2-TZVP basis set. Excited states (1A, 2A, etc.) ordered from top left by rows. The colorscale is defined in the last box. Corresponding transition energies and dipole moments are listed in Table 5.A.12.

Table 5.A.17: Results for the γQA gas-phase hexamer obtained with TDDFT at ωB97X with def2-TZVP basis set. Rows marked in green correspond to the selected electronic states possessing excitonic features.

State	Energy (eV)	Wavelength (nm)	Oscillator Strength	μ_x(au)	μ_y(au)	μ_z(au)
1	3.28733	377.2	0.000000005	-0.00007	0.00009	0.00022
2	3.32086	373.4	0.008049508	0.11557	-0.08142	-0.28098
3	3.37362	367.5	0.000000010	-0.00005	0.00012	0.00032
4	3.4381	360.6	0.040592013	-0.23996	0.17063	0.62866
5	3.50038	354.2	0.000000126	-0.00025	0.00036	0.00113
6	3.54411	349.8	0.466558632	-0.65044	0.61750	2.13751
7	3.77955	328.0	0.000000232	-0.00027	-0.00139	-0.00071
8	3.77978	328.0	0.000000002	0.00001	0.00003	0.00014
9	3.78013	328.0	0.000002087	0.00114	-0.00292	-0.00356
10	3.78045	328.0	0.000000010	0.00002	-0.00009	-0.00031
11	3.78925	327.2	0.000083754	-0.01694	0.01885	0.01612
12	3.78926	327.2	0.000077192	-0.01626	0.01806	0.01553
13	3.81251	325.2	0.000590076	-0.05529	0.05708	0.00164
14	3.81256	325.2	0.000000582	-0.00174	0.00178	0.00007
15	3.81271	325.2	0.000014596	-0.00830	0.00934	0.00012
16	3.8128	325.2	0.000000691	0.00186	-0.00198	-0.00008
17	3.84472	322.5	0.000100863	0.02209	-0.02213	0.00967
18	3.84473	322.5	0.000045547	-0.01442	0.01487	-0.00737

Table 5.A.18: Results for the γQA embedded hexamer obtained with TDDFT at ωB97X with def2-TZVP basis set and employing 3 layers of point-charges around the molecule. Rows marked in green correspond to the selected electronic states possessing excitonic features.

State	Energy (eV)	Wavelength (nm)	Oscillator Strength	μ_x(au)	μ_y(au)	μ_z(au)
1	3.08224	402.3	0.000000003	0.00005	-0.00005	-0.00017
2	3.12082	397.3	0.004877294	0.09179	-0.05986	-0.22756
3	3.17983	389.9	0.000000017	0.00010	-0.00011	-0.00045
4	3.25015	381.5	0.031135518	-0.22131	0.14573	0.56640
5	3.31617	373.9	0.000000899	0.00083	-0.00091	-0.00309
6	3.35948	369.1	0.492767625	-0.73502	0.68768	2.23022
7	3.696	335.5	0.003806643	-0.12080	0.07134	0.14952
8	3.70169	334.9	0.002439649	0.09822	-0.05672	-0.11848
9	3.71998	333.3	0.000980486	0.06423	-0.03826	-0.07190
10	3.72944	332.4	0.000115760	-0.01974	0.01494	0.02557
11	3.73466	332.0	0.000968397	-0.05864	0.04182	0.07346
12	3.74163	331.4	0.003058747	-0.10721	0.07418	0.12795
13	3.7536	330.3	0.000922476	0.05909	-0.04129	-0.06953
14	3.76073	329.7	0.045584402	0.41578	-0.29363	-0.48545
15	3.77136	328.8	0.008837951	0.18774	-0.11777	-0.21573
16	3.77809	328.2	0.011867586	0.21870	-0.13832	-0.24749
17	4.07396	304.3	0.000224846	0.03771	-0.02874	-0.00223
18	4.09114	303.1	0.000000146	-0.00034	0.00088	-0.00075

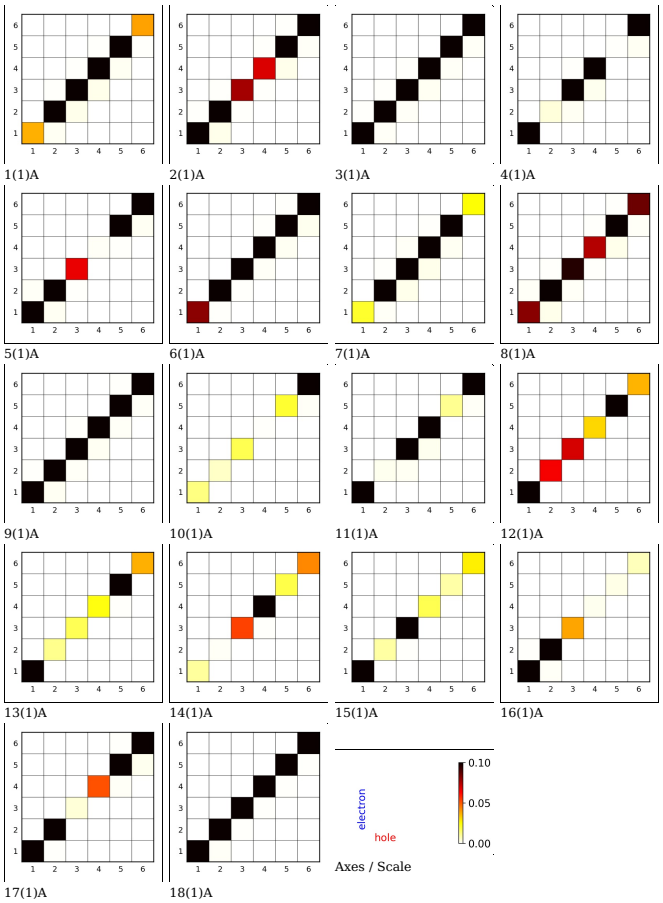

Figure 5.A.9: βQA embedded hexamer electron-hole correlation analysis represented as Ω matrices as obtained from `TheoDORE`[421] with TDDFT at ωB97X with def2-TZVP basis set. Excited states (1A, 2A, etc.) ordered from top left by rows. The colorscale is defined in the last box. Corresponding transition energies and dipole moments are listed in Table 5.A.18

5.B Model Hamiltonians

5.B.1 βQA

βQA can be modeled using a 2D lattice with a single molecule per unit cell. This type of crystal was already employed by Anzola at al. [96, 392], with the only difference that the directions of interaction are not perpendicular to the unit-cell axis. Following a similar analysis, the Hamiltonian in the reciprocal space reads:

$$\begin{aligned}\hat{H}^{\beta} = \sum_{\boldsymbol{k}}[\epsilon_0 + D + 2J_{\pi}^{\beta}cos(\boldsymbol{kb}) + 2J_{H}^{\beta}cos(\boldsymbol{k}(\boldsymbol{a}+\boldsymbol{b}))]\tilde{b}_{\boldsymbol{k}}^{\dagger}\tilde{b}_{\boldsymbol{k}} + \\ + h\omega_{eff}\sum_{\boldsymbol{q}}(\tilde{a}_{\boldsymbol{q}}^{\dagger}\tilde{a}_{\boldsymbol{q}} + \frac{1}{2}) + \frac{g}{\sqrt{N}}\sum_{\boldsymbol{k},\boldsymbol{q}}\tilde{a}_{\boldsymbol{q}}^{\dagger}\tilde{b}_{\boldsymbol{k}}^{\dagger}\tilde{b}_{\boldsymbol{k}+\boldsymbol{q}} + \tilde{a}_{-\boldsymbol{q}}^{\dagger}\tilde{b}_{\boldsymbol{k}}^{\dagger}\tilde{b}_{\boldsymbol{k}+\boldsymbol{q}}\end{aligned} \tag{5.B.1}$$

and the dipole moment operator:

$$\hat{\boldsymbol{\mu}} = \boldsymbol{\mu}_0 \cdot \sqrt{N}(\tilde{b}_{\boldsymbol{K}=0}^{\dagger} + \tilde{b}_{\boldsymbol{K}=0}) \tag{5.B.2}$$

5.B.2 γQA

While the dipole moment operator retains the same formula used for βQA, γQA possesses two molecules per unit cell, and the treatment is more complex. Following Agranovich [439] creation (annihilation) operators in reciprocal space can be defined. Defininig α and β the two molecules in the unit cell and 1 and 2 the two resulting branches, the creation (annihilation) operator for the excitation on the α/β molecule in the $\boldsymbol{n}$ unit cell are written in terms of the operators in the reciprocal space as follows:

$$b_{\boldsymbol{n}\alpha}^{\dagger} = \frac{\sqrt{2}}{2\sqrt{N}}\sum_{\boldsymbol{k}} e^{i\boldsymbol{k}(\boldsymbol{n}+r_{\alpha})}(b_{1,\boldsymbol{k}}^{\dagger} + b_{2,\boldsymbol{k}}^{\dagger}) \tag{5.B.3}$$

$$b_{\boldsymbol{n}\beta}^{\dagger} = \frac{\sqrt{2}}{2\sqrt{N}}\sum_{\boldsymbol{k}} e^{i\boldsymbol{k}(\boldsymbol{n}+r_{\beta})}(b_{1,\boldsymbol{k}}^{\dagger} - b_{2,\boldsymbol{k}}^{\dagger}) \tag{5.B.4}$$

where $b_{1,\boldsymbol{k}}^{\dagger}, b_{2,\boldsymbol{k}}^{\dagger}$ create an exciton on the first and the second branches, respectively. Since all molecules are equivalent by symmetry, the on-site energies for the α and β sites are the same and the Hamiltonian in the real space is:

$$\begin{aligned}\hat{H} = \sum_{\boldsymbol{i}\sigma}\Big\{\Big[\epsilon_0 + D - g(\hat{a}_{\boldsymbol{i}}^{\dagger} + \hat{a}_{\boldsymbol{i}})\Big]\hat{b}_{\boldsymbol{i}\sigma}^{\dagger}\hat{b}_{\boldsymbol{i}\sigma} + \hbar\omega_{eff}(\hat{a}_{\boldsymbol{i}}^{\dagger}\hat{a}_{\boldsymbol{i}} + \frac{1}{2}) \\ + \sum_{\boldsymbol{j}}\sum_{int} J_{\boldsymbol{i}\sigma,\boldsymbol{j}\sigma',int}(\hat{b}_{\boldsymbol{i}\sigma}^{\dagger}\hat{b}_{\boldsymbol{j}\sigma'} + \hat{b}_{\boldsymbol{j}\sigma'}^{\dagger}\hat{b}_{\boldsymbol{i}}\sigma)\Big\}\end{aligned} \tag{5.B.5}$$

Going to the reciprocal space the diagonal term simply remains diagonal:.

$$\sum_{\boldsymbol{n}\sigma} b_{\boldsymbol{n}\sigma}^{\dagger}b_{\boldsymbol{n}\sigma} = \sum_{\boldsymbol{k}} b_{1,\boldsymbol{k}}^{\dagger}b_{1,\boldsymbol{k}} + b_{2,\boldsymbol{k}}^{\dagger}b_{2,\boldsymbol{k}} \tag{5.B.6}$$

More delicate are the off-diagonal terms:

$$\sum_{\boldsymbol{n},\boldsymbol{m}}\sum_{\sigma,\sigma'} J_{\boldsymbol{n}\sigma,\boldsymbol{m}\sigma'}b_{\boldsymbol{n}\sigma}^{\dagger}b_{\boldsymbol{m}\sigma'} \tag{5.B.7}$$

where $\boldsymbol{n}, \boldsymbol{m}$ run over the cells and σ, σ' run on the two molecules inside the unit cells. For the γ phase of quinacridone, using the vector $\boldsymbol{b} = (b, 0)$ and $\boldsymbol{a} = (0, a)$ as the unit cell vectors, and recalling that there are two molecules per unit cell ($\sigma = \alpha, \beta$) the following interactions are defined:

$$J_{\boldsymbol{n}\sigma,\boldsymbol{m}\sigma'} \begin{cases} \sigma = \alpha : \begin{cases} \boldsymbol{m} = \boldsymbol{n} \pm \boldsymbol{b}, \sigma' = \alpha \xrightarrow{J_{\boldsymbol{n}\sigma,\boldsymbol{m}\sigma'}} J_\pi^\gamma \\ \begin{cases} \boldsymbol{m} = \boldsymbol{n}, \sigma' = \beta \xrightarrow{J_{\boldsymbol{n}\sigma,\boldsymbol{m}\sigma'}} J_H^\gamma \\ \boldsymbol{m} = \boldsymbol{n} - \boldsymbol{b}, \sigma' = \beta \xrightarrow{J_{\boldsymbol{n}\sigma,\boldsymbol{m}\sigma'}} J_H^\gamma \\ \boldsymbol{m} = \boldsymbol{n} - \boldsymbol{a}, \sigma' = \beta \xrightarrow{J_{\boldsymbol{n}\sigma,\boldsymbol{m}\sigma'}} J_H^\gamma \\ \boldsymbol{m} = \boldsymbol{n} - (\boldsymbol{a} + \boldsymbol{b}), \sigma' = \beta \xrightarrow{J_{\boldsymbol{n}\sigma,\boldsymbol{m}\sigma'}} J_H^\gamma \end{cases} \end{cases} \\ \sigma = \beta : \begin{cases} \boldsymbol{m} = \boldsymbol{n} \pm \boldsymbol{b}, \sigma' = \beta \xrightarrow{J_{\boldsymbol{n}\sigma,\boldsymbol{m}\sigma'}} J_\pi^\gamma \\ \begin{cases} \boldsymbol{m} = \boldsymbol{n}, \sigma' = \alpha \xrightarrow{J_{\boldsymbol{n}\sigma,\boldsymbol{m}\sigma'}} J_H^\gamma \\ \boldsymbol{m} = \boldsymbol{n} + \boldsymbol{b}, \sigma' = \alpha \xrightarrow{J_{\boldsymbol{n}\sigma,\boldsymbol{m}\sigma'}} J_H^\gamma \\ \boldsymbol{m} = \boldsymbol{n} + \boldsymbol{a}, \sigma' = \alpha \xrightarrow{J_{\boldsymbol{n}\sigma,\boldsymbol{m}\sigma'}} J_H^\gamma \\ \boldsymbol{m} = \boldsymbol{n} + (\boldsymbol{a} + \boldsymbol{b}), \sigma' = \alpha \xrightarrow{J_{\boldsymbol{n}\sigma,\boldsymbol{m}\sigma'}} J_H^\gamma \end{cases} \end{cases} \end{cases} \tag{5.B.8}$$

Looking at the interaction J_P that links two molecules of types σ, σ' located in the unit cells, $\boldsymbol{n}, \boldsymbol{m} = \boldsymbol{n} + \boldsymbol{s}$ we can use Eq 5.B.4 and generalize the interactions in Eq. 5.B.8 as:

$$\sum_{\boldsymbol{m},\boldsymbol{n}} J_P b^\dagger_{\boldsymbol{n},\sigma} b_{\boldsymbol{m},\sigma'} == \frac{J_P}{2} \sum_{\boldsymbol{k}\boldsymbol{s}} e^{i(\boldsymbol{r}_\sigma - \boldsymbol{r}_{\sigma'} - \boldsymbol{s})\boldsymbol{k}} (b^\dagger_{1,\boldsymbol{k}} \pm_\sigma b^\dagger_{2,\boldsymbol{k}})(b_{1,\boldsymbol{k}} \pm_{\sigma'} b_{2,\boldsymbol{k}}) \tag{5.B.9}$$

where with $\pm_\sigma$ I have indicated that the sign follows from the type of the molecule as in 5.B.4.

γ phase:J_π^γ terms

We apply 5.B.9 to the case in which $\sigma = \sigma' = \alpha$, as in 5.B.8.

$$\begin{aligned} J_\pi^\gamma \sum_{\boldsymbol{n}} b^\dagger_{\boldsymbol{n},\alpha} b_{\boldsymbol{n}+\boldsymbol{b},\alpha} + b^\dagger_{\boldsymbol{n},\alpha} b_{\boldsymbol{n}-\boldsymbol{b},\alpha} = \frac{J_\pi^\gamma}{2} [& \sum_{\boldsymbol{k}} e^{-i\boldsymbol{b}\boldsymbol{k}} (b^\dagger_{1,\boldsymbol{k}} + b^\dagger_{2,\boldsymbol{k}})(b_{1,\boldsymbol{k}} + b_{2,\boldsymbol{k}}) \\ & + \sum_{\boldsymbol{k}} e^{i\boldsymbol{b}\boldsymbol{k}} (b^\dagger_{1,\boldsymbol{k}} + b^\dagger_{2,\boldsymbol{k}})(b_{1,\boldsymbol{k}} + b_{2,\boldsymbol{k}})] \end{aligned} \tag{5.B.10}$$

Doing the same with $\sigma = \sigma' = \beta$ takes to:

$$\begin{aligned} \frac{J_\pi^\gamma}{2} \sum_{\boldsymbol{n}} b^\dagger_{\boldsymbol{n},\beta} b_{\boldsymbol{n}+\boldsymbol{b},\beta} + b^\dagger_{\boldsymbol{n},\beta} b_{\boldsymbol{n}-\boldsymbol{b},\beta} = \frac{J_\pi^\gamma}{2} [& \sum_{\boldsymbol{k}} e^{-i\boldsymbol{b}\boldsymbol{k}} (b^\dagger_{1,\boldsymbol{k}} - b^\dagger_{2,\boldsymbol{k}})(b_{1,\boldsymbol{k}} - b_{2,\boldsymbol{k}}) \\ & + \sum_{\boldsymbol{k}} e^{i\boldsymbol{b}\boldsymbol{k}} (b^\dagger_{1,\boldsymbol{k}} - b^\dagger_{2,\boldsymbol{k}})(b_{1,\boldsymbol{k}} - b_{2,\boldsymbol{k}})] \end{aligned} \tag{5.B.11}$$

Finally, if we sum together these two results we obtain:

$$\begin{aligned} & J_\pi^\gamma \sum_{\boldsymbol{n}} b^\dagger_{\boldsymbol{n},\alpha} b_{\boldsymbol{n}+\boldsymbol{b},\alpha} + b^\dagger_{\boldsymbol{n},\alpha} b_{\boldsymbol{n}-\boldsymbol{b},\alpha} + b^\dagger_{\boldsymbol{n},\beta} b_{\boldsymbol{n}+\boldsymbol{b},\beta} + b^\dagger_{\boldsymbol{n},\beta} b_{\boldsymbol{n}-\boldsymbol{b},\beta} = \\ & = 2 J_\pi^\gamma \sum_{\boldsymbol{k}} cos(\boldsymbol{k}\boldsymbol{b}) (b^\dagger_{1,\boldsymbol{k}} b_{1,\boldsymbol{k}} + b^\dagger_{2,\boldsymbol{k}} b_{2,\boldsymbol{k}}) \end{aligned} \tag{5.B.12}$$

All the cross terms cancel out and only the diagonal terms remain.

γ phase:J_H^γ terms

All terms have $\sigma \neq \sigma'$ and the phase exponentials do not expire. We then have 8 different terms:

$$J_H^\gamma \sum_{\boldsymbol{n}} b^\dagger_{\boldsymbol{n},\alpha} b_{\boldsymbol{n},\beta} = \frac{J_H^\gamma}{2} \sum_{\boldsymbol{k}} e^{i(\boldsymbol{r}_\beta - \boldsymbol{r}_\alpha - \boldsymbol{b} - \boldsymbol{a})\boldsymbol{k}} (b^\dagger_{1,\boldsymbol{k}} - b^\dagger_{2,\boldsymbol{k}})(b_{1,\boldsymbol{k}} + b_{2,\boldsymbol{k}}) \quad (5.B.13)$$

We expanded the relations in 5.B.8 using 5.B.9 The first thing to note is that, for the γ phase of QA, $\boldsymbol{r}_\beta - \boldsymbol{r}_\alpha = \frac{\boldsymbol{a}+\boldsymbol{b}}{2}$. So we can transform everything as:

$$J_H^\gamma \sum_{\boldsymbol{n}} b^\dagger_{\boldsymbol{n},\alpha} b_{\boldsymbol{n},\beta} = \frac{J_H^\gamma}{2} \sum_{\boldsymbol{k}} e^{-i(\frac{\boldsymbol{a}+\boldsymbol{b}}{2})\boldsymbol{k}} (b^\dagger_{1,\boldsymbol{k}} + b^\dagger_{2,\boldsymbol{k}})(b_{1,\boldsymbol{k}} - b_{2,\boldsymbol{k}}) \quad (5.B.14)$$

$$J_H^\gamma \sum_{\boldsymbol{n}} b^\dagger_{\boldsymbol{n},\alpha} b_{\boldsymbol{n}-\boldsymbol{b},\beta} = \frac{J_H^\gamma}{2} \sum_{\boldsymbol{k}} e^{-i(\frac{\boldsymbol{a}-\boldsymbol{b}}{2})\boldsymbol{k}} (b^\dagger_{1,\boldsymbol{k}} + b^\dagger_{2,\boldsymbol{k}})(b_{1,\boldsymbol{k}} - b_{2,\boldsymbol{k}}) \quad (5.B.15)$$

$$J_H^\gamma \sum_{\boldsymbol{n}} b^\dagger_{\boldsymbol{n},\alpha} b_{\boldsymbol{n}-\boldsymbol{a},\beta} = \frac{J_H^\gamma}{2} \sum_{\boldsymbol{k}} e^{-i(\frac{-\boldsymbol{a}+\boldsymbol{b}}{2})\boldsymbol{k}} (b^\dagger_{1,\boldsymbol{k}} + b^\dagger_{2,\boldsymbol{k}})(b_{1,\boldsymbol{k}} - b_{2,\boldsymbol{k}}) \quad (5.B.16)$$

$$J_H^\gamma \sum_{\boldsymbol{n}} b^\dagger_{\boldsymbol{n},\alpha} b_{\boldsymbol{n}-\boldsymbol{a}-\boldsymbol{b},\beta} = \frac{J_H^\gamma}{2} \sum_{\boldsymbol{k}} e^{-i(\frac{-\boldsymbol{a}-\boldsymbol{b}}{2})\boldsymbol{k}} (b^\dagger_{1,\boldsymbol{k}} + b^\dagger_{2,\boldsymbol{k}})(b_{1,\boldsymbol{k}} - b_{2,\boldsymbol{k}}) \quad (5.B.17)$$

$$J_H^\gamma \sum_{\boldsymbol{n}} b^\dagger_{\boldsymbol{n},\beta} b_{\boldsymbol{n},\alpha} = \frac{J_H^\gamma}{2} \sum_{\boldsymbol{k}} e^{i(\frac{\boldsymbol{a}+\boldsymbol{b}}{2})\boldsymbol{k}} (b^\dagger_{1,\boldsymbol{k}} - b^\dagger_{2,\boldsymbol{k}})(b_{1,\boldsymbol{k}} + b_{2,\boldsymbol{k}}) \quad (5.B.18)$$

$$J_H^\gamma \sum_{\boldsymbol{n}} b^\dagger_{\boldsymbol{n},\beta} b_{\boldsymbol{n}+\boldsymbol{b},\alpha} = \frac{J_H^\gamma}{2} \sum_{\boldsymbol{k}} e^{i(\frac{\boldsymbol{a}-\boldsymbol{b}}{2})\boldsymbol{k}} (b^\dagger_{1,\boldsymbol{k}} - b^\dagger_{2,\boldsymbol{k}})(b_{1,\boldsymbol{k}} + b_{2,\boldsymbol{k}}) \quad (5.B.19)$$

$$J_H^\gamma \sum_{\boldsymbol{n}} b^\dagger_{\boldsymbol{n},\beta} b_{\boldsymbol{n}+\boldsymbol{a},\alpha} = \frac{J_H^\gamma}{2} \sum_{\boldsymbol{k}} e^{i(\frac{-\boldsymbol{a}+\boldsymbol{b}}{2})\boldsymbol{k}} (b^\dagger_{1,\boldsymbol{k}} - b^\dagger_{2,\boldsymbol{k}})(b_{1,\boldsymbol{k}} + b_{2,\boldsymbol{k}}) \quad (5.B.20)$$

$$J_H^\gamma \sum_{\boldsymbol{n}} b^\dagger_{\boldsymbol{n},\beta} b_{\boldsymbol{n}+\boldsymbol{b}+\boldsymbol{a},\alpha} = \frac{J_H^\gamma}{2} \sum_{\boldsymbol{k}} e^{i(\frac{-\boldsymbol{a}-\boldsymbol{b}}{2})\boldsymbol{k}} (b^\dagger_{1,\boldsymbol{k}} - b^\dagger_{2,\boldsymbol{k}})(b_{1,\boldsymbol{k}} + b_{2,\boldsymbol{k}}) \quad (5.B.21)$$

we can now group the terms in couples:

$$\begin{aligned}
\boldsymbol{s} = \boldsymbol{0} : \frac{J_H^\gamma}{2} \sum_{\boldsymbol{k}} & e^{-i(\frac{\boldsymbol{a}+\boldsymbol{b}}{2})\boldsymbol{k}} (b^\dagger_{1,\boldsymbol{k}} + b^\dagger_{2,\boldsymbol{k}})(b_{1,\boldsymbol{k}} - b_{2,\boldsymbol{k}}) \\
& + e^{i(\frac{\boldsymbol{a}+\boldsymbol{b}}{2})\boldsymbol{k}} (b^\dagger_{1,\boldsymbol{k}} - b^\dagger_{2,\boldsymbol{k}})(b_{1,\boldsymbol{k}} + b_{2,\boldsymbol{k}}) \\
\boldsymbol{s} = \pm\boldsymbol{b} : \frac{J_H^\gamma}{2} \sum_{\boldsymbol{k}} & e^{-i(\frac{\boldsymbol{a}-\boldsymbol{b}}{2})\boldsymbol{k}} (b^\dagger_{1,\boldsymbol{k}} + b^\dagger_{2,\boldsymbol{k}})(b_{1,\boldsymbol{k}} - b_{2,\boldsymbol{k}}) \\
& + e^{i(\frac{\boldsymbol{a}-\boldsymbol{b}}{2})\boldsymbol{k}} (b^\dagger_{1,\boldsymbol{k}} - b^\dagger_{2,\boldsymbol{k}})(b_{1,\boldsymbol{k}} + b_{2,\boldsymbol{k}}) \\
\boldsymbol{s} = \pm\boldsymbol{a} : \frac{J_H^\gamma}{2} \sum_{\boldsymbol{k}} & e^{-i(\frac{-\boldsymbol{a}+\boldsymbol{b}}{2})\boldsymbol{k}} (b^\dagger_{1,\boldsymbol{k}} + b^\dagger_{2,\boldsymbol{k}})(b_{1,\boldsymbol{k}} - b_{2,\boldsymbol{k}}) \\
& + e^{i(\frac{-\boldsymbol{a}+\boldsymbol{b}}{2})\boldsymbol{k}} (b^\dagger_{1,\boldsymbol{k}} - b^\dagger_{2,\boldsymbol{k}})(b_{1,\boldsymbol{k}} + b_{2,\boldsymbol{k}}) \\
\boldsymbol{s} = \pm(\boldsymbol{a}+\boldsymbol{b}) : \frac{J_H^\gamma}{2} \sum_{\boldsymbol{k}} & e^{-i(\frac{-\boldsymbol{a}-\boldsymbol{b}}{2})\boldsymbol{k}} (b^\dagger_{1,\boldsymbol{k}} + b^\dagger_{2,\boldsymbol{k}})(b_{1,\boldsymbol{k}} - b_{2,\boldsymbol{k}}) \\
& + e^{i(\frac{-\boldsymbol{a}-\boldsymbol{b}}{2})\boldsymbol{k}} (b^\dagger_{1,\boldsymbol{k}} - b^\dagger_{2,\boldsymbol{k}})(b_{1,\boldsymbol{k}} + b_{2,\boldsymbol{k}})
\end{aligned}$$

expanding the products and the exponentials with the Euler formula and summing everything takes to:

$$\frac{J_H^\gamma}{2}\sum_{\boldsymbol{k}}\{2cos\left[\boldsymbol{k}\frac{(\boldsymbol{a}+\boldsymbol{b})}{2}\right]\left(b_{1,\boldsymbol{k}}^\dagger b_{1,\boldsymbol{k}}-b_{2,\boldsymbol{k}}^\dagger b_{2,\boldsymbol{k}}\right)-2isin\left[\boldsymbol{k}\frac{(\boldsymbol{a}+\boldsymbol{b})}{2}\right](b_{1,\boldsymbol{k}}^\dagger b_{2,\boldsymbol{k}}-b_{2,\boldsymbol{k}}^\dagger b_{1,\boldsymbol{k}})+$$
$$+2cos\left[\boldsymbol{k}\frac{(\boldsymbol{a}-\boldsymbol{b})}{2}\right](b_{1,\boldsymbol{k}}^\dagger b_{1,\boldsymbol{k}}-b_{2,\boldsymbol{k}}^\dagger b_{2,\boldsymbol{k}})-2isin\left[\boldsymbol{k}\frac{(\boldsymbol{a}-\boldsymbol{b})}{2}\right](b_{1,\boldsymbol{k}}^\dagger b_{2,\boldsymbol{k}}-b_{2,\boldsymbol{k}}^\dagger b_{1,\boldsymbol{k}})+$$
$$+2cos\left[\boldsymbol{k}\frac{(-\boldsymbol{a}+\boldsymbol{b})}{2}\right](b_{1,\boldsymbol{k}}^\dagger b_{1,\boldsymbol{k}}-b_{2,\boldsymbol{k}}^\dagger b_{2,\boldsymbol{k}})-2isin\left[\boldsymbol{k}\frac{(-\boldsymbol{a}+\boldsymbol{b})}{2}\right](b_{1,\boldsymbol{k}}^\dagger b_{2,\boldsymbol{k}}-b_{2,\boldsymbol{k}}^\dagger b_{1,\boldsymbol{k}})+$$
$$+2cos\left[\boldsymbol{k}\frac{(-\boldsymbol{a}-\boldsymbol{b})}{2}\right](b_{1,\boldsymbol{k}}^\dagger b_{1,\boldsymbol{k}}-b_{2,\boldsymbol{k}}^\dagger b_{2,\boldsymbol{k}})-2isin\left[\boldsymbol{k}\frac{(-\boldsymbol{a}-\boldsymbol{b})}{2}\right](b_{1,\boldsymbol{k}}^\dagger b_{2,\boldsymbol{k}}-b_{2,\boldsymbol{k}}^\dagger b_{1,\boldsymbol{k}})\}$$

Finally, we use the fact that the sine is an odd function while the cosine is odd. The cosine terms with opposite signs do sum up, while the sine terms cancel each other, so that:

$$2J_H^\gamma\sum_{\boldsymbol{k}}\{cos\left[\boldsymbol{k}\frac{(\boldsymbol{a}+\boldsymbol{b})}{2}\right](b_{1,\boldsymbol{k}}^\dagger b_{1,\boldsymbol{k}}-b_{2,\boldsymbol{k}}^\dagger b_{2,\boldsymbol{k}})+cos\left[\boldsymbol{k}\frac{(\boldsymbol{a}-\boldsymbol{b})}{2}\right](b_{1,\boldsymbol{k}}^\dagger b_{1,\boldsymbol{k}}-b_{2,\boldsymbol{k}}^\dagger b_{2,\boldsymbol{k}})\}$$

Finally, the complete electronic exciton Hamiltonian in the reciprocal space reads:

$$\hat{H}_{el}=\sum_{\boldsymbol{k}}\Big\{\{\epsilon_0+D+2J_\pi^\gamma cos(\boldsymbol{kb})+2J_H^\gamma cos[\boldsymbol{k}(\frac{\boldsymbol{a}+\boldsymbol{b}}{2})]+2J_H^\gamma cos[\boldsymbol{k}(\frac{\boldsymbol{a}-\boldsymbol{b}}{2})]\}b_{1,\boldsymbol{k}}^\dagger b_{1,\boldsymbol{k}}+$$
$$+\{\epsilon_0+D+2J_\pi^\gamma cos(\boldsymbol{kb})-2J_H^\gamma cos[\boldsymbol{k}(\frac{\boldsymbol{a}+\boldsymbol{b}}{2})]-2J_H^\gamma cos[\boldsymbol{k}(\frac{\boldsymbol{a}-\boldsymbol{b}}{2})]\}b_{2,\boldsymbol{k}}^\dagger b_{2,\boldsymbol{k}}\Big\} \tag{5.B.22}$$

Vibrations

A similar procedure is adopted to deal with vibrations.

$$a_{\boldsymbol{n}\alpha}^\dagger=\frac{1}{\sqrt{2N}}\sum_{\boldsymbol{Q}}e^{i\boldsymbol{Q}(\boldsymbol{n}+r_\alpha)}(a_{1,\boldsymbol{Q}}^\dagger+a_{2,\boldsymbol{Q}}^\dagger) \tag{5.B.23}$$

$$a_{\boldsymbol{n}\beta}^\dagger=\frac{1}{\sqrt{2N}}\sum_{\boldsymbol{Q}}e^{i\boldsymbol{Q}(\boldsymbol{n}+r_\beta)}(a_{1,\boldsymbol{Q}}^\dagger-a_{2,\boldsymbol{Q}}^\dagger) \tag{5.B.24}$$

Exactly as the electronic Hamiltonian, the diagonal term of the vibrations remains diagonal:

$$\sum_{\boldsymbol{n},\sigma}a_{\boldsymbol{n},\sigma}^\dagger a_{\boldsymbol{n},\sigma}=\sum_{\boldsymbol{Q}}a_{1,\boldsymbol{Q}}^\dagger a_{1,\boldsymbol{Q}}+a_{2,\boldsymbol{Q}}^\dagger a_{2,\boldsymbol{Q}} \tag{5.B.25}$$

We can then work out the vibronic coupling term:

$$g\sum_{\boldsymbol{n},\sigma}(a_{\boldsymbol{n},\sigma}^\dagger+a_{\boldsymbol{n},\sigma})b_{\boldsymbol{n},\sigma}^\dagger b_{\boldsymbol{n},\sigma}=$$
$$+\frac{g}{\sqrt{2N}}\sum_{\boldsymbol{k},\boldsymbol{Q}}\{a_{1,\boldsymbol{Q}}^\dagger b_{1,\boldsymbol{k}}^\dagger b_{1,\boldsymbol{k}+\boldsymbol{Q}}+a_{1,\boldsymbol{Q}}^\dagger b_{2,\boldsymbol{k}}^\dagger b_{2,\boldsymbol{k}+\boldsymbol{Q}}+a_{2,\boldsymbol{Q}}^\dagger b_{1,\boldsymbol{k}}^\dagger b_{2,\boldsymbol{k}+\boldsymbol{Q}}+a_{2,\boldsymbol{Q}}^\dagger b_{2,\boldsymbol{k}}^\dagger b_{1,\boldsymbol{k}+\boldsymbol{Q}}+h.c.\} \tag{5.B.26}$$

Only the terms with an even number of creation/annihilation operators concerning the second branches survive. The final Hamiltonian reads:

$$\begin{aligned}\hat{H} = \sum_{\boldsymbol{k}} \Big\{ &\{\epsilon_0 + D + 2J_\pi^\gamma cos(\boldsymbol{kb}) + 2J_H^\gamma cos[\boldsymbol{k}(\frac{\boldsymbol{a}+\boldsymbol{b}}{2})] + 2J_H^\gamma cos[\boldsymbol{k}(\frac{\boldsymbol{a}-\boldsymbol{b}}{2})]\} b_{1,\boldsymbol{k}}^\dagger b_{1,\boldsymbol{k}} + \\ &+\{\epsilon_0 + D + 2J_\pi^\gamma cos(\boldsymbol{kb}) - 2J_H^\gamma cos[\boldsymbol{k}(\frac{\boldsymbol{a}+\boldsymbol{b}}{2})] - 2J_H^\gamma cos[\boldsymbol{k}(\frac{\boldsymbol{a}-\boldsymbol{b}}{2})]\} b_{2,\boldsymbol{k}}^\dagger b_{2,\boldsymbol{k}} \Big\} + \\ &+h\omega \sum_{\boldsymbol{Q}} (a_{1,\boldsymbol{Q}}^\dagger a_{1,\boldsymbol{Q}} + a_{2,\boldsymbol{Q}}^\dagger a_{2,\boldsymbol{Q}}) + \\ &+\frac{g}{\sqrt{2N}} \sum_{\boldsymbol{k},\boldsymbol{Q}} \Big\{ a_{1,\boldsymbol{Q}}^\dagger b_{1,\boldsymbol{k}}^\dagger b_{1,\boldsymbol{k}+\boldsymbol{Q}} + a_{1,\boldsymbol{Q}}^\dagger b_{2,\boldsymbol{k}}^\dagger b_{2,\boldsymbol{k}+\boldsymbol{Q}} \\ &+a_{2,\boldsymbol{Q}}^\dagger b_{1,\boldsymbol{k}}^\dagger b_{2,\boldsymbol{k}+\boldsymbol{Q}} + a_{2,\boldsymbol{Q}}^\dagger b_{2,\boldsymbol{k}}^\dagger b_{1,\boldsymbol{k}+\boldsymbol{Q}} + h.c. \Big\}\end{aligned} \tag{5.B.27}$$

where J_π^γ, J_H^γ are the π/hydrogen bond interactions, $\boldsymbol{a}, \boldsymbol{b}$ are the unit cell vector, $b_{i,\boldsymbol{k}}^\dagger / b_{i,\boldsymbol{k}}$ creates/annihilates an exciton on the i branch at wavevector $\boldsymbol{k}$, $a_{i,\boldsymbol{Q}}^\dagger / a_{i,\boldsymbol{Q}}$ crates/annihilates a phonon on the i branch at wavevector $\boldsymbol{Q}$.

Dipole moment operator

$$\begin{aligned}\hat{\boldsymbol{\mu}} &= \sum_{\boldsymbol{n}\sigma} \boldsymbol{\mu}_{\boldsymbol{n}\sigma} (b_{\boldsymbol{n}\sigma}^\dagger + b_{\boldsymbol{n}\sigma}) = \sum_{\boldsymbol{n}} \boldsymbol{\mu}_\alpha (b_{\boldsymbol{n}\alpha}^\dagger + b_{\boldsymbol{n}\alpha}) + \boldsymbol{\mu}_\beta (b_{\boldsymbol{n}\beta}^\dagger + b_{\boldsymbol{n}\beta}) = \\ &= \sqrt{N}[(\boldsymbol{\mu}_\alpha + \boldsymbol{\mu}_\beta)(b_{1,\boldsymbol{k}=0}^\dagger + b_{1,\boldsymbol{k}=0}) + (\boldsymbol{\mu}_\alpha - \boldsymbol{\mu}_\beta)(b_{2,\boldsymbol{k}=0}^\dagger + b_{2,\boldsymbol{k}=0})]\end{aligned} \tag{5.B.28}$$

Conclusion and Future Perspectives

6

The aim of the work summarized in this thesis is to build a bridge across the critical interface between chemistry and quantum technology, demonstrating that molecular systems offer a versatile and highly tunable toolkit to engineer the next generation of quantum hardware. The work progresses from the rigorous calibration of theoretical methods to the ab initio design of isolated molecular qubits, the investigation of spin-selective transport phenomena, and finally, the simulation of complex exciton behavior in crystalline environments. By bridging the gap between microscopic Hamiltonian models and macroscopic observables, we have highlighted how the specific chemical structure and connectivity, electronic correlation and vibrations in organic media can be manipulated to possibly satisfy the DiVincenzo criteria for quantum computation.

We began by establishing robust computational protocols, validating the computationally efficient Pariser-Parr-Pople (PPP) model for the radical species. Quite interestingly, we went beyond HF, augmenting the standard PPP solution to include CASCI-based extensions. This hybrid approach proved essential to address organic radicals, characterized by strong electron correlations. Investigating molecular qubits, we demonstrated that triangulene-based radicals have a tunable electronic structure, suitable for qubit operations. Furthermore, the design of InveST-bridged diradicals highlighted a specific pathway to create optically addressable molecular spin qubits (optical-spin interfaces), satisfying a critical requirement for quantum networking. The study of new organic diradicals will be a natural continuation of this work. On a parallel track, further studies are needed to propose realistic models for decoherence effects due to the environment surrounding the diradicals, to be dealt with, possibly, by exploiting an effective embedding as demonstrated in Chapter 5.

Another hot topic in the field of quantum technologies is Chirality-Induced Spin Selectivity (CISS). A minimal Hubbard model, where chirality is due to orbital twisting, offers an interesting and comparatively simple playground to address this intriguing topic. By driving a current flux through the Hubbard chain, adopting a current-constrained approach, we studied how the connectivity affects CISS. Moreover, investigating a wide range of model parameters, we were able to observe large CISS responses in a very specific and tiny parameter range. The inclusion of electron-vibration coupling leads to particularly insightful findings. As long as the nuclear geometry is maintained in equilibrium with the current flux, vibrational coupling has marginal effects of CISS responses. However, non-equilibrium vibrational modes serve as a crucial amplifier of the CISS effect. Our results suggest that the chiral character acquired by ubiquitous vibrational degrees of freedom may be the key to unraveling the physics of CISS; consequently, elucidating the roles of thermal populations and out-of-equilibrium vibrations emerges as a necessary further step. As the mechanism underpinning CISS remains not fully understood, insights derived from novel methodological approaches could drive significant advancements in the field. In the future, the introduction of full spin-orbit coupling terms, including two-electron contributions,

could be useful for gaining deeper insights. To this end, Hubbard-like models represent a robust starting point, offering an optimal balance between a realistic representation of electron correlation and computational cost. Crucially, two-electron SOC terms can be explicitly accounted for in these models without the need for mean-field approximations, which, although ubiquitous in standard quantum chemistry packages, are hardly adequate for strongly correlated systems.

Finally, moving from isolated molecules to the solid state, our study on quinacridone crystallochromism provided a comprehensive framework for understanding exciton behavior in crystalline environments. By combining periodic DFT for electrostatic embedding with a Frenkel-Holstein model parametrized via TD-DFT, we successfully rationalized the crystallochromism of the β and γ polymorphs. This work bridges the gap between single-molecule quantum properties and the macroscopic matrices required to host and protect them, emphasizing the role of intermolecular coupling and vibronic interactions in defining the optical landscape.

In conclusion, this work reinforces that organic molecules are not merely passive elements but active, tunable platforms with a strong potential to meet fundamental criteria of quantum information technology: initialization, manipulation, and readout.

List of pubblication A

(1) Dubbini, Matteo, Federico Bonvini, Lorenzo Savi, and Francesco Di Maiolo. 2024. "Turning on Organic Radical Emitters." The Journal of Physical Chemistry C 128 (43): 18158–69. https://doi.org/10.1021/acs.jpcc.4c04362.

(2) D.K. Andrea Phan Huu, Arianna Cantarella, Pietro Bonfà, Lorenzo Savi, Alessandro Chiesa, Anna Painelli, Stefano Carretta, 2025. "Ab Initio Parametrization of a Generalized Hubbard Model in a Molecule Displaying Chirality-Induced Spin Selectivity." Communications Materials 6 (1): 107. https://doi.org/10.1038/s43246-025-00821-3.

(3) Savi, Lorenzo, Leonardo Celada, D.K. Andrea Phan Huu, Alessandro Chiesa, Stefano Carretta, and Anna Painelli. 2025. "Chirality-Induced Spin Selectivity: A Minimal Model." The Journal of Physical Chemistry Letters, August 26, 9107–15. https://doi.org/10.1021/acs.jpclett.5c01813.

(4) Savi, Lorenzo, Matteo Masino, Anna Painelli, and Luca Grisanti. 2025. "Crystallochromism: A Hybrid Model for the Spectral Properties of Quinacridone Polymorphs." Journal of Chemical Theory and Computation 21 (21): 11179–89. https://doi.org/10.1021/acs.jctc.5c01022.

(5) Savi, Lorenzo, Marco Tommaso Barreca, Matteo Bedogni, and Francesco Di Maiolo. 2025. "Organic Diradicals Bridged by Inverted Singlet–Triplet Units for Optical–Spin Interfaces." Journal of Chemical Theory and Computation, ahead of print, November 29. https://doi.org/10.1021/acs.jctc.5c01571.

Bibliography

Here are the references in citation order.

[1] Roman S. Ingarden. 'Quantum information theory'. In: *Reports on Mathematical Physics* 10.1 (Aug. 1976), pp. 43–72. DOI: 10.1016/0034-4877(76)90005-7. (Visited on 06/10/2025) (cited on page 1).

[2] Michael R. Wasielewski et al. 'Exploiting chemistry and molecular systems for quantum information science'. en. In: *Nature Reviews Chemistry* 4.9 (Sept. 2020). Publisher: Nature Publishing Group, pp. 490–504. DOI: 10.1038/s41570-020-0200-5. (Visited on 07/03/2024) (cited on pages 1, 5, 83).

[3] Alyssa Ney. 'Do our observations make reality happen?' en. In: *Nature* 642.8067 (June 2025). Bandiera_abtest: a Cg_type: Essay Publisher: Nature Publishing Group Subject_term: Quantum physics, Philosophy, Physics, Quantum information, pp. 294–297. DOI: 10.1038/d41586-025-01773-x. (Visited on 06/10/2025) (cited on page 1).

[4] C. E. Shannon. 'A mathematical theory of communication'. In: *The Bell System Technical Journal* 27.3 (July 1948), pp. 379–423. DOI: 10.1002/j.1538-7305.1948.tb01338.x. (Visited on 09/15/2025) (cited on page 1).

[5] J. S. Bell. 'On the Einstein Podolsky Rosen paradox'. In: *Physics Physique Fizika* 1.3 (1964), pp. 195–200. DOI: 10.1103/PhysicsPhysiqueFizika.1.195 (cited on page 1).

[6] Alain Aspect. 'Experimental Test of Bell's Inequalities Using Time-Varying Analyzers'. In: *Physical Review Letters* 49.25 (1982), pp. 1804–1807. DOI: 10.1103/PhysRevLett.49.1804 (cited on page 1).

[7] M.A. Nielsen and I.L. Chuang. *Quantum Computation and Quantum Information: 10th Anniversary Edition*. Cambridge University Press, 2010 (cited on page 3).

[8] W. K. Wootters and W. H. Zurek. 'A single quantum cannot be cloned'. en. In: *Nature* 299.5886 (Oct. 1982). Publisher: Nature Publishing Group, pp. 802–803. DOI: 10.1038/299802a0. (Visited on 09/15/2025) (cited on page 3).

[9] L. Hales and S. Hallgren. 'An improved quantum Fourier transform algorithm and applications'. In: *Proceedings 41st Annual Symposium on Foundations of Computer Science*. ISSN: 0272-5428. Nov. 2000, pp. 515–525. DOI: 10.1109/SFCS.2000.892139. (Visited on 09/15/2025) (cited on page 3).

[10] Nicolas Gisin et al. 'Quantum cryptography'. In: *Reviews of Modern Physics* 74.1 (Mar. 2002). Publisher: American Physical Society, pp. 145–195. DOI: 10.1103/RevModPhys.74.145. (Visited on 09/15/2025) (cited on page 3).

[11] Lov K. Grover. 'A fast quantum mechanical algorithm for database search'. In: *Proceedings of the twenty-eighth annual ACM symposium on Theory of Computing*. STOC '96. New York, NY, USA: Association for Computing Machinery, 1996, pp. 212–219. DOI: 10.1145/237814.237866. (Visited on 09/15/2025) (cited on page 3).

[12] Charles H. Bennett and Stephen J. Wiesner. 'Communication via one- and two-particle operators on Einstein-Podolsky-Rosen states'. In: *Physical Review Letters* 69.20 (Nov. 1992). Publisher: American Physical Society, pp. 2881–2884. DOI: 10.1103/PhysRevLett.69.2881. (Visited on 09/15/2025) (cited on page 3).

[13] Charles H. Bennett et al. 'Teleporting an unknown quantum state via dual classical and Einstein-Podolsky-Rosen channels'. In: *Physical Review Letters* 70.13 (Mar. 1993). Publisher: American Physical Society, pp. 1895–1899. DOI: 10.1103/PhysRevLett.70.1895. (Visited on 09/15/2025) (cited on page 3).

[14] David P. DiVincenzo. 'The Physical Implementation of Quantum Computation'. en. In: *Fortschritte der Physik* 48.9-11 (2000). _eprint: https://onlinelibrary.wiley.com/doi/pdf/10.1002/1521-3978%28200009%2948%3A9/11%
PROP771%3E3.0.CO%3B2-E, pp. 771–783. DOI: 10.1002/1521-3978(200009)48:9/11<771::AID-PROP771>3.0.CO;2-E. (Visited on 07/29/2025) (cited on page 3).

[15] Akshaya Jayashankar and Prabha Mandayam. 'Quantum Error Correction: Noise-Adapted Techniques and Applications'. en. In: *Journal of the Indian Institute of Science* 103.2 (Apr. 2023), pp. 497–512. DOI: 10.1007/s41745-022-00332-x. (Visited on 07/29/2025) (cited on page 4).

[16] A. A. Golubov, M. Yu. Kupriyanov, and E. Il'ichev. 'The current-phase relation in Josephson junctions'. In: *Reviews of Modern Physics* 76.2 (Apr. 2004). Publisher: American Physical Society, pp. 411–469. DOI: 10.1103/RevModPhys.76.411. (Visited on 07/16/2025) (cited on page 4).

[17] John M Martinis and Kevin Osborne. 'Superconducting Qubits and the Physics of Josephson Junctions'. en. In: () (cited on page 4).

[18] Anton Frisk Kockum and Franco Nori. 'Quantum Bits with Josephson Junctions'. en. In: *Fundamentals and Frontiers of the Josephson Effect*. Ed. by Francesco Tafuri. Cham: Springer International Publishing, 2019, pp. 703–741. DOI: 10.1007/978-3-030-20726-7_17. (Visited on 07/16/2025) (cited on page 4).

[19] D. Ristè et al. 'Initialization by Measurement of a Superconducting Quantum Bit Circuit'. In: *Physical Review Letters* 109.5 (Aug. 2012). Publisher: American Physical Society, p. 050507. DOI: 10.1103/PhysRevLett.109.050507. (Visited on 07/17/2025) (cited on page 4).

[20] Daniel Barredo et al. 'An atom-by-atom assembler of defect-free arbitrary two-dimensional atomic arrays'. In: *Science* 354.6315 (Nov. 2016). Publisher: American Association for the Advancement of Science, pp. 1021–1023. DOI: 10.1126/science.aah3778. (Visited on 07/29/2025) (cited on page 4).

[21] Xiaoling Wu et al. 'A concise review of Rydberg atom based quantum computation and quantum simulation*'. en. In: *Chinese Physics B* 30.2 (Feb. 2021). Publisher: Chinese Physical Society and IOP Publishing Ltd, p. 020305. DOI: 10.1088/1674-1056/abd76f. (Visited on 07/17/2025) (cited on pages 4, 22, 23).

[22] Daniel Comparat and Pierre Pillet. 'Dipole blockade in a cold Rydberg atomic sample [Invited]'. EN. In: *JOSA B* 27.6 (June 2010). Publisher: Optica Publishing Group, A208–A232. DOI: 10.1364/JOSAB.27.00A208. (Visited on 07/29/2025) (cited on pages 4, 23).

[23] Colin D. Bruzewicz et al. 'Trapped-ion quantum computing: Progress and challenges'. In: *Applied Physics Reviews* 6.2 (May 2019), p. 021314. DOI: 10.1063/1.5088164. (Visited on 07/17/2025) (cited on page 4).

[24] Philipp Schindler et al. 'A quantum information processor with trapped ions'. en. In: *New Journal of Physics* 15.12 (Dec. 2013). Publisher: IOP Publishing, p. 123012. DOI: 10.1088/1367-2630/15/12/123012. (Visited on 07/17/2025) (cited on page 4).

[25] M. AbuGhanem. *Photonic Quantum Computers*. arXiv:2409.08229 [quant-ph]. Sept. 2024. DOI: 10.48550/arXiv.2409.08229. URL: http://arxiv.org/abs/2409.08229 (visited on 07/17/2025) (cited on page 4).

[26] Sergei Slussarenko and Geoff J. Pryde. 'Photonic quantum information processing: A concise review'. In: *Applied Physics Reviews* 6.4 (Oct. 2019), p. 041303. DOI: 10.1063/1.5115814. (Visited on 07/29/2025) (cited on page 4).

[27] Jianwei Wang et al. 'Multidimensional quantum entanglement with large-scale integrated optics'. In: *Science* 360.6386 (Apr. 2018). Publisher: American Association for the Advancement of Science, pp. 285–291. DOI: 10.1126/science.aar7053. (Visited on 07/29/2025) (cited on page 4).

[28] Chung-Jui Yu et al. 'Long Coherence Times in Nuclear Spin-Free Vanadyl Qubits'. In: *Journal of the American Chemical Society* 138.44 (Nov. 2016). Publisher: American Chemical Society, pp. 14678–14685. DOI: 10.1021/jacs.6b08467. (Visited on 07/29/2025) (cited on page 4).

[29] Simon G. McAdams et al. 'Molecular single-ion magnets based on lanthanides and actinides: Design considerations and new advances in the context of quantum technologies'. In: *Coordination Chemistry Reviews*. SI: 42 iccc, Brest– by invitation 346 (Sept. 2017), pp. 216–239. DOI: 10.1016/j.ccr.2017.03.015. (Visited on 07/29/2025) (cited on page 4).

[30] Selena J. Lockyer et al. 'Five-Spin Supramolecule for Simulating Quantum Decoherence of Bell States'. In: *Journal of the American Chemical Society* 144.35 (Sept. 2022). Publisher: American Chemical Society, pp. 16086–16092. DOI: 10.1021/jacs.2c06384. (Visited on 07/29/2025) (cited on page 4).

[31] Daniel Čavlović and Michal Juríček. 'Molecular Magnetic Switches'. en. In: *CHIMIA* 73.4 (Apr. 2019). Number: 4, pp. 313–313. DOI: 10.2533/chimia.2019.313. (Visited on 06/26/2024) (cited on page 4).

[32] J. R. Weber et al. 'Quantum computing with defects'. EN. In: *Proceedings of the National Academy of Sciences* 107.19 (May 2010). Company: National Academy of Sciences Distributor: National Academy of Sciences Institution: National Academy of Sciences Label: National Academy of Sciences Publisher: Proceedings of the National Academy of Sciences, pp. 8513–8518. DOI: 10.1073/pnas.1003052107. (Visited on 07/29/2025) (cited on page 4).

[33] David D. Awschalom et al. 'Quantum Spintronics: Engineering and Manipulating Atom-Like Spins in Semiconductors'. In: *Science* 339.6124 (Mar. 2013). Publisher: American Association for the Advancement of Science, pp. 1174–1179. DOI: 10.1126/science.1231364. (Visited on 07/29/2025) (cited on page 4).

[34] Ke Wang et al. 'Spin manipulation in semiconductor quantum dots qubit*'. en. In: *Chinese Physics B* 27.9 (Sept. 2018). Publisher: Chinese Physical Society and IOP Publishing Ltd, p. 090308. DOI: 10.1088/1674-1056/27/9/090308. (Visited on 07/29/2025) (cited on page 4).

[35] M. A. Eriksson, S. N. Coppersmith, and M. G. Lagally. 'Semiconductor quantum dot qubits'. en. In: *MRS Bulletin* 38.10 (Oct. 2013), pp. 794–801. DOI: 10.1557/mrs.2013.208. (Visited on 07/29/2025) (cited on page 4).

[36] Simone Chicco et al. 'Controlled coherent dynamics of [VO(TPP)], a prototype molecular nuclear qudit with an electronic ancilla'. en. In: *Chemical Science* 12.36 (Sept. 2021). Publisher: The Royal Society of Chemistry, pp. 12046–12055. DOI: 10.1039/D1SC01358K. (Visited on 02/14/2023) (cited on page 4).

[37] A. Chiesa et al. 'Theoretical Design of Optimal Molecular Qudits for Quantum Error Correction'. In: *The Journal of Physical Chemistry Letters* 13.28 (July 2022). Publisher: American Chemical Society, pp. 6468–6474. DOI: 10.1021/acs.jpclett.2c01602. (Visited on 02/14/2023) (cited on page 4).

[38] Y. Olivier et al. 'Computational Design of Thermally Activated Delayed Fluorescence Materials: The Challenges Ahead'. In: *The Journal of Physical Chemistry Letters* 9.20 (2018), pp. 6149–6163. DOI: 10.1021/acs.jpclett.8b02327 (cited on pages 4, 27).

[39] Yong Rui Poh et al. 'Alternant Hydrocarbon Diradicals as Optically Addressable Molecular Qubits'. In: *Journal of the American Chemical Society* 146.22 (June 2024). Publisher: American Chemical Society, pp. 15549–15561. DOI: 10.1021/jacs.4c04360. (Visited on 12/04/2025) (cited on page 4).

[40] Rituparno Chowdhury et al. 'Bright triplet and bright charge-separated singlet excitons in organic diradicals enable optical read-out and writing of spin states'. en. In: *Nature Chemistry* 17.9 (Sept. 2025). Publisher: Nature Publishing Group, pp. 1410–1417. DOI: 10.1038/s41557-025-01875-z. (Visited on 12/04/2025) (cited on page 4).

[41] Rituparno Chowdhury et al. *Room temperature optical control of spin states in organic diradicals*. arXiv:2510.09440 [cond-mat]. Oct. 2025. DOI: 10.48550/arXiv.2510.09440. URL: http://arxiv.org/abs/2510.09440 (visited on 12/04/2025) (cited on page 4).

[42] Rituparno Chowdhury et al. 'Optical read and write of spin states in organic diradicals'. In: *Nature Chemistry* 17.9 (Sept. 2025). arXiv:2406.03365 [cond-mat], pp. 1410–1417. DOI: 10.1038/s41557-025-01875-z. (Visited on 12/04/2025) (cited on page 4).

[43] Sebastian Gorgon et al. 'Reversible spin-optical interface in luminescent organic radicals'. en. In: *Nature* 620.7974 (Aug. 2023). Publisher: Nature Publishing Group, pp. 538–544. DOI: 10.1038/s41586-023-06222-1. (Visited on 12/04/2025) (cited on page 4).

[44] Lujo Matasovic et al. *Coulombic control of charge transfer in luminescent radicals with long-lived quartet states*. arXiv:2508.06945 [cond-mat]. Aug. 2025. DOI: 10.48550/arXiv.2508.06945. URL: http://arxiv.org/abs/2508.06945 (visited on 12/04/2025) (cited on page 4).

[45] Manuel Souto et al. 'Intramolecular electron transfer and charge delocalization in bistable donor–acceptor systems based on perchlorotriphenylmethyl radicals linked to ferrocene and tetrathiafulvalene units'. en. In: *Journal of Physical Organic Chemistry* 27.6 (2014). _eprint: https://onlinelibrary.wiley.com/doi/pdf/10.1002/poc.32 pp. 465–469. DOI: 10.1002/poc.3296. (Visited on 06/22/2023) (cited on pages 5, 51, 52).

[46] Manuel Souto et al. 'Self-Assembled Architectures with Segregated Donor and Acceptor Units of a Dyad Based on a Monopyrrolo-Annulated TTF–PTM Radical'. en. In: *Chemistry – A European Journal* 21.24 (2015). _eprint: https://onlinelibrary.wiley.com/doi/pdf/10.1002/chem.201500497, pp. 8816–8825. DOI: 10.1002/chem.201500497. (Visited on 06/26/2023) (cited on pages 5, 52).

[47] Manuel Souto et al. 'Influence of the donor unit on the rectification ratio in tunnel junctions based on donor–acceptor SAMs using PTM units as acceptors'. en. In: *Physical Chemistry Chemical Physics* 20.40 (Oct. 2018). Publisher: The Royal Society of Chemistry, pp. 25638–25647. DOI: 10.1039/C8CP05488F. (Visited on 08/17/2023) (cited on page 5).

[48] Manuel Souto et al. 'Thermomagnetic Molecular System Based on TTF-PTM Radical: Switching the Spin and Charge Delocalization'. In: *The Journal of Physical Chemistry Letters* 4.16 (Aug. 2013). Publisher: American Chemical Society, pp. 2721–2726. DOI: 10.1021/jz4013855. (Visited on 06/22/2023) (cited on pages 5, 51, 53, 54).

[49] Clarice D. Aiello et al. 'A Chirality-Based Quantum Leap'. In: *ACS Nano* 16.4 (Apr. 2022). Publisher: American Chemical Society, pp. 4989–5035. DOI: 10.1021/acsnano.1c01347. (Visited on 12/04/2025) (cited on page 5).

[50] A. Chiesa et al. 'Assessing the Nature of Chiral-Induced Spin Selectivity by Magnetic Resonance'. In: *The Journal of Physical Chemistry Letters* 12.27 (July 2021). Publisher: American Chemical Society, pp. 6341–6347. DOI: 10.1021/acs.jpclett.1c01447. (Visited on 12/04/2025) (cited on page 5).

[51] Alessandro Chiesa et al. 'Chirality-Induced Spin Selectivity: An Enabling Technology for Quantum Applications'. en. In: *Advanced Materials* 35.28 (2023). _eprint: https://advanced.onlinelibrary.wiley.com/doi/pdf/10.1002/ p. 2300472. DOI: 10.1002/adma.202300472. (Visited on 12/04/2025) (cited on page 5).

[52] Emilio Macaluso et al. 'Chiral-induced spin selectivity in photo-induced electron transfer: Investigating charge and spin dynamics in a master equation framework'. In: *The Journal of Chemical Physics* 159.8 (Aug. 2023), p. 084301. DOI: 10.1063/5.0160149. (Visited on 12/04/2025) (cited on page 5).

[53] Ron Naaman, Yossi Paltiel, and David H. Waldeck. 'Chiral molecules and the electron spin'. en. In: *Nature Reviews Chemistry* 3.4 (Apr. 2019), pp. 250–260. DOI: 10.1038/s41570-019-0087-1. (Visited on 03/19/2025) (cited on page 5).

[54] B. P. Bloom et al. 'Asymmetric reactions induced by electron spin polarization'. en. In: *Physical Chemistry Chemical Physics* 22.38 (Oct. 2020), pp. 21570–21582. DOI: 10.1039/D0CP03129A. (Visited on 03/19/2025) (cited on page 5).

[55] Maria A. Castellanos and Adam P. Willard. 'Designing excitonic circuits for the Deutsch–Jozsa algorithm: mitigating fidelity loss by merging gate operations'. In: *Physical Chemistry Chemical Physics* 23.28 (2021), pp. 15196–15208. DOI: 10.1039/d1cp01643a (cited on pages 5, 93).

[56] Bernard Yurke, Richard Elliott, and Aaron Sup. 'Implementation of a Frenkel exciton-based controlled phase shifter'. In: *Physical Review A* 107.1 (Jan. 2023), p. 012603. DOI: 10.1103/physreva.107.012603 (cited on pages 5, 93).

[57] Casandra M. Moisanu et al. 'Crystalline Arrays of Copper Porphyrin Qubits Based on Ion-Paired Frameworks'. In: *Journal of the American Chemical Society* 145.33 (Aug. 2023). Publisher: American Chemical Society, pp. 18447–18454. DOI: 10.1021/jacs.3c04786. (Visited on 12/04/2025) (cited on page 5).

[58] Casandra M. Moisanu et al. 'A Paired-Ion Framework Composed of Vanadyl Porphyrin Molecular Qubits Extends Spin Coherence Times'. In: *Journal of the American Chemical Society* 146.41 (Oct. 2024). Publisher: American Chemical Society, pp. 28088–28094. DOI: 10.1021/jacs.4c07288. (Visited on 12/04/2025) (cited on page 5).

[59] Jonathan R. Palmer et al. 'Oriented Triplet Excitons as Long-Lived Electron Spin Qutrits in a Molecular Donor–Acceptor Single Cocrystal'. In: *Journal of the American Chemical Society* 146.1 (Jan. 2024). Publisher: American Chemical Society, pp. 1089–1099. DOI: 10.1021/jacs.3c12277. (Visited on 12/04/2025) (cited on page 5).

[60] Isaiah Shavitt. 'Matrix element evaluation in the unitary group approach to the electron correlation problem'. en. In: *International Journal of Quantum Chemistry* 14.S12 (1978). _eprint: https://onlinelibrary.wiley.com/doi/pd pp. 5–32. DOI: 10.1002/qua.560140803. (Visited on 07/08/2025) (cited on page 7).

[61] Giovanni Li Manni et al. 'Multiconfiguration Pair-Density Functional Theory'. In: *Journal of Chemical Theory and Computation* 10.9 (Sept. 2014). Publisher: American Chemical Society, pp. 3669–3680. DOI: 10.1021/ct500483t. (Visited on 03/25/2025) (cited on pages 7, 16).

[62] Per E. M. Siegbahn et al. 'The complete active space SCF (CASSCF) method in a Newton–Raphson formulation with application to the HNO molecule'. In: *The Journal of Chemical Physics* 74.4 (Feb. 1981), pp. 2384–2396. DOI: 10.1063/1.441359. (Visited on 07/08/2025) (cited on pages 8, 10).

[63] *ORCA Forum - Downloads*. URL: https://orcaforum.kofo.mpg.de/app.php/dlext/?cat=4 (visited on 09/05/2025) (cited on pages 9, 10).

[64] Jeppe Olsen et al. 'Determinant based configuration interaction algorithms for complete and restricted configuration interaction spaces'. In: *The Journal of Chemical Physics* 89.4 (Aug. 1988), pp. 2185–2192. DOI: 10.1063/1.455063. (Visited on 09/05/2025) (cited on page 9).

[65] Timo Fleig, Jeppe Olsen, and Christel M. Marian. 'The generalized active space concept for the relativistic treatment of electron correlation. I. Kramers-restricted two-component configuration interaction'. In: *The Journal of Chemical Physics* 114.11 (Mar. 2001), pp. 4775–4790. DOI: 10.1063/1.1349076. (Visited on 09/05/2025) (cited on page 10).

[66] Björn O. Roos, Peter R. Taylor, and Per E. M. Sigbahn. 'A complete active space SCF method (CASSCF) using a density matrix formulated super-CI approach'. In: *Chemical Physics* 48.2 (May 1980), pp. 157–173. DOI: 10.1016/0301-0104(80)80045-0. (Visited on 07/08/2025) (cited on page 10).

[67] Frank Neese. 'Importance of Direct SpinSpin Coupling and Spin-Flip Excitations for the Zero-Field Splittings of Transition Metal Complexes: A Case Study'. In: *Journal of the American Chemical Society* 128.31 (Aug. 2006). Publisher: American Chemical Society, pp. 10213–10222. DOI: 10.1021/ja061798a. (Visited on 05/11/2024) (cited on page 11).

[68] Björn O. Roos and Kerstin Andersson. 'Multiconfigurational perturbation theory with level shift — the Cr2 potential revisited'. In: *Chemical Physics Letters* 245.2 (Oct. 1995), pp. 215–223. DOI: 10.1016/0009-2614(95)01010-7. (Visited on 07/09/2025) (cited on page 12).

[69] Kenneth G. Dyall. 'The choice of a zeroth-order Hamiltonian for second-order perturbation theory with a complete active space self-consistent-field reference function'. In: *The Journal of Chemical Physics* 102.12 (Mar. 1995), pp. 4909–4918. DOI: 10.1063/1.469539. (Visited on 07/09/2025) (cited on page 12).

[70] Giovanni Ghigo, Björn O. Roos, and Per-Åke Malmqvist. 'A modified definition of the zeroth-order Hamiltonian in multiconfigurational perturbation theory (CASPT2)'. In: *Chemical Physics Letters* 396.1 (Sept. 2004), pp. 142–149. DOI: 10.1016/j.cplett.2004.08.032. (Visited on 09/05/2025) (cited on page 12).

[71] Niclas Forsberg and Per-Åke Malmqvist. 'Multiconfiguration perturbation theory with imaginary level shift'. In: *Chemical Physics Letters* 274.1 (Aug. 1997), pp. 196–204. DOI: 10.1016/S0009-2614(97)00669-6. (Visited on 07/09/2025) (cited on page 12).

[72] Jae Woo Park et al. 'Imaginary Shift in CASPT2 Nuclear Gradient and Derivative Coupling Theory'. In: *Journal of Chemical Theory and Computation* 15.7 (July 2019). Publisher: American Chemical Society, pp. 4088–4098. DOI: 10.1021/acs.jctc.9b00368. (Visited on 07/04/2025) (cited on page 12).

[73] C. Angeli et al. 'Introduction of n-electron valence states for multireference perturbation theory'. In: *The Journal of Chemical Physics* 114.23 (June 2001), pp. 10252–10264. DOI: 10.1063/1.1361246. (Visited on 07/07/2025) (cited on page 13).

[74] Celestino Angeli et al. 'A quasidegenerate formulation of the second order n-electron valence state perturbation theory approach'. In: *The Journal of Chemical Physics* 121.9 (Sept. 2004), pp. 4043–4049. DOI: 10.1063/1.1778711. (Visited on 01/10/2025) (cited on page 14).

[75] Walter Kohn and Lu Jeu Sham. 'Self-consistent equations including exchange and correlation effects'. In: *Physical review* 140.4A (1965), A1133 (cited on page 15).

[76] Benjamin Kaduk, Tim Kowalczyk, and Troy Van Voorhis. 'Constrained Density Functional Theory'. In: *Chemical Reviews* 112.1 (Jan. 2012). Publisher: American Chemical Society, pp. 321–370. DOI: 10.1021/cr200148b. (Visited on 11/28/2023) (cited on pages 16, 55).

[77] Qin Wu and Troy Van Voorhis. 'Extracting electron transfer coupling elements from constrained density functional theory'. In: *The Journal of Chemical Physics* 125.16 (Oct. 2006), p. 164105. DOI: 10.1063/1.2360263. (Visited on 11/30/2023) (cited on page 16).

[78] David Casanova. 'Short-range density functional correlation within the restricted active space CI method'. In: *The Journal of Chemical Physics* 148.12 (Mar. 2018), p. 124118. DOI: 10.1063/1.5018895. (Visited on 09/01/2025) (cited on pages 17, 83).

[79] Andreas Dreuw and Martin Head-Gordon. 'Single-reference ab initio methods for the calculation of excited states of large molecules'. In: *Chemical reviews* 105.11 (2005), pp. 4009–4037 (cited on pages 17, 95).

[80] Mark E Casida. 'Time-dependent density-functional theory for molecules and molecular solids'. In: *Journal of Molecular Structure: THEOCHEM* 914.1-3 (2009), pp. 3–18 (cited on page 17).

[81] Carsten A Ullrich. *Time-dependent density-functional theory: concepts and applications*. OUP Oxford, 2011 (cited on pages 17, 18).

[82] Erich Runge and Eberhard KU Gross. 'Density-functional theory for time-dependent systems'. In: *Physical Review Letters* 52.12 (1984), p. 997 (cited on page 17).

[83] Robert Van Leeuwen. 'Mapping from densities to potentials in time-dependent density-functional theory'. In: *Physical review letters* 82.19 (1999), p. 3863 (cited on page 18).

[84] Mark E Casida. 'Time-dependent density functional response theory for molecules'. In: *Recent Advances In Density Functional Methods: (Part I)*. World Scientific, 1995, pp. 155–192 (cited on pages 18, 19).

[85] Dionys Baeriswyl. *The Hubbard Model: Its Physics and its Mathematical Physics*. Vol. 343. Springer Science & Business Media, 1995 (cited on page 20).

[86] Rudolph Pariser and Robert G. Parr. 'A Semi-Empirical Theory of the Electronic Spectra and Electronic Structure of Complex Unsaturated Molecules. I.' In: *The Journal of Chemical Physics* 21.3 (1953), pp. 466–471 (cited on pages 20, 28, 39).

[87] Rudolph Pariser. 'Theory of the Electronic Spectra and Structure of the Polyacenes and of Alternant Hydrocarbons'. In: *The Journal of Chemical Physics* 24.2 (1956), pp. 250–268. DOI: https://doi.org/10.1063/1.1742461 (cited on pages 20, 28).

[88] Rudolph Pariser. 'Electronic Spectrum and Structure of Azulene'. In: *The Journal of Chemical Physics* 25.6 (1956), pp. 1112–1116. DOI: https://doi.org/10.1063/1.1743159 (cited on pages 20, 28).

[89] R. Lehoucq, D. Sorensen, and C. Yang. *ARPACK Users' Guide*. Society for Industrial and Applied Mathematics, 1998 (cited on pages 21, 29, 61).

[90] Frank C Spano. 'Excitons in conjugated oligomer aggregates, films, and crystals'. In: *Annu. Rev. Phys. Chem.* 57 (2006), pp. 217–243 (cited on pages 22, 94).

[91] Frank C Spano. 'The spectral signatures of Frenkel polarons in H-and J-aggregates'. In: *Accounts of chemical research* 43.3 (2010), pp. 429–439 (cited on pages 22, 94).

[92] Francesco Bertocchi et al. 'Chiroptical properties of cyanine aggregates: hierarchical modelling from monomers to bundles'. In: *Chemical Science* 15.39 (2024), pp. 16103–16111. DOI: 10.1039/d4sc04968c (cited on pages 22, 65).

[93] Aleksandr Sergeevich Davydov. 'The theory of molecular excitons'. In: *Soviet Physics Uspekhi* 7.2 (1964), p. 145 (cited on page 22).

[94] Davide Giavazzi et al. 'A marvel of chiral squaraine aggregates: chiroptical spectra beyond the exciton model'. In: *Journal of Materials Chemistry C* (2023) (cited on pages 22, 94, 106).

[95] Michael Kasha, Henry R Rawls, and M Ashraf El-Bayoumi. 'The exciton model in molecular spectroscopy'. In: *Pure and applied Chemistry* 11.3-4 (1965), pp. 371–392 (cited on pages 22, 23).

[96] M Anzola, F Di Maiolo, and A Painelli. 'Optical spectra of molecular aggregates and crystals: testing approximation schemes'. In: *Physical Chemistry Chemical Physics* 21.36 (2019), pp. 19816–19824 (cited on pages 22, 94, 125).

[97] Manthos G Papadopoulos, Andrzej J Sadlej, Jerzy Leszczynski, et al. *Non-linear optical properties of matter*. Springer, 2006 (cited on page 23).

[98] Leticia Gonzalez. *Quantum Chemistry and Dynamics of Excited States: Model and Applications* (cited on page 24).

[99] Yang Guo et al. 'Approximations of density matrices in N-electron valence state second-order perturbation theory (NEVPT2). II. The full rank NEVPT2 (FR-NEVPT2) formulation'. eng. In: *The Journal of Chemical Physics* 154.21 (June 2021), p. 214113. DOI: 10.1063/5.0051218 (cited on page 25).

[100] Yang Guo, Kantharuban Sivalingam, and Frank Neese. 'Approximations of density matrices in N-electron valence state second-order perturbation theory (NEVPT2). I. Revisiting the NEVPT2 construction'. In: *The Journal of Chemical Physics* 154.21 (June 2021), p. 214111. DOI: 10.1063/5.0051211. (Visited on 07/11/2025) (cited on page 25).

[101] Francesco Di Maiolo et al. 'Shedding light on thermally-activated delayed fluorescence'. In: *Chemical Science* 15.15 (2024), pp. 5434–5450. DOI: 10.1039/D4SC00033A (cited on pages 27, 45).

[102] M. A. Baldo et al. 'Highly efficient phosphorescent emission from organic electroluminescent devices'. In: *Nature* 395.6698 (Sept. 1998), pp. 151–154. DOI: 10.1038/25954 (cited on page 27).

[103] Chihaya Adachi et al. 'Nearly 100% internal phosphorescence efficiency in an organic light-emitting device'. In: *Journal of Applied Physics* 90.10 (Nov. 2001), pp. 5048–5051 (cited on page 27).

[104] Zhiyong Yang et al. 'Recent advances in organic thermally activated delayed fluorescence materials'. In: *Chemical Society Reviews* 46.3 (2017), pp. 915–1016. DOI: 10.1039/c6cs00368k (cited on page 27).

[105] Yuchao Liu et al. 'All-organic thermally activated delayed fluorescence materials for organic light-emitting diodes'. In: *Nature Reviews Materials* 3.4 (Apr. 2018), p. 18020. DOI: 10.1038/natrevmats.2018.20 (cited on page 27).

[106] Yi-Zhong Shi et al. 'Recent progress in thermally activated delayed fluorescence emitters for nondoped organic light-emitting diodes'. In: *Chemical Science* 13.13 (2022), pp. 3625–3651. DOI: 10.1039/d1sc07180g (cited on page 27).

[107] Yuxin Xiao et al. 'NIR TADF emitters and OLEDs: challenges, progress, and perspectives'. In: *Chemical Science* 13.31 (2022), pp. 8906–8923. DOI: 10.1039/d2sc02201j (cited on page 27).

[108] Bowen Li et al. 'Role of the Intramolecular-Locking Strategy in the Construction of Organic Thermally Activated Delayed Fluorescence Emitters with Rotation-Restricted Acceptors'. In: *Advanced Optical Materials* 11.7 (Jan. 2023), p. 2202610. DOI: 10.1002/adom.202202610 (cited on page 27).

[109] T. Northey and T.J. Penfold. 'The intersystem crossing mechanism of an ultrapure blue organoboron emitter'. In: *Organic Electronics* 59 (2018), pp. 45–48. DOI: https://doi.org/10.1016/j.orgel.2018.04.038 (cited on page 27).

[110] Mariana T. do Casal et al. 'First-Principles Calculations of Excited-State Decay Rate Constants in Organic Fluorophores'. In: *The Journal of Physical Chemistry A* (2023), pp. 10033–10053. DOI: 10.1021/acs.jpca.3c06191 (cited on page 27).

[111] Kleitos Stavrou et al. 'Key requirements for ultraefficient sensitization in hyperfluorescence organic light-emitting diodes'. In: *Nature Photonics* 18.6 (Feb. 2024), pp. 554–561. DOI: 10.1038/s41566-024-01395-1 (cited on page 27).

[112] Naoya Aizawa et al. 'Delayed fluorescence from inverted singlet and triplet excited states'. In: *Nature* 609.7927 (2022), pp. 502–506. DOI: 10.1038/s41586-022-05132-y (cited on pages 27, 38).

[113] Johannes Ehrmaier et al. 'Singlet–triplet inversion in heptazine and in polymeric carbon nitrides'. In: *The Journal of Physical Chemistry A* 123.38 (2019), pp. 8099–8108 (cited on pages 27, 38).

[114] Robert Pollice et al. 'Organic molecules with inverted gaps between first excited singlet and triplet states and appreciable fluorescence rates'. In: *Matter* 4.5 (2021), pp. 1654–1682 (cited on page 27).

[115] David Hall et al. 'Modeling of Multiresonant Thermally Activated Delayed Fluorescence Emitters-sProperly Accounting for Electron Correlation Is Key!' In: *Journal of Chemical Theory and Computation* 18.8 (2022), pp. 4903–4918. DOI: 10.1021/acs.jctc.2c00141 (cited on page 27).

[116] Matteo Bedogni et al. 'Shining Light on Inverted Singlet–Triplet Emitters'. In: *Journal of Chemical Theory and Computation* 20.2 (Nov. 2023), pp. 902–913. DOI: https://doi.org/10.1021/acs.jctc.3c01112 (cited on pages 27–31, 38–40).

[117] Ömer H. Omar et al. 'Identification of Unknown Inverted Singlet–Triplet Cores by High-Throughput Virtual Screening'. In: *Journal of the American Chemical Society* 145.36 (Aug. 2023), pp. 19790–19799. DOI: https://doi.org/10.1021/jacs.3c05452?urlappend=%3Fref%3DPDF&jav=VoR&rel=cite-as (cited on page 27).

[118] Kjell Jorner et al. 'Ultrafast Computational Screening of Molecules with Inverted Singlet–Triplet Energy Gaps Using the Pariser–Parr–Pople Semiempirical Quantum Chemistry Method'. In: *The Journal of Physical Chemistry A* 128.12 (Mar. 2024), pp. 2445–2456. DOI: 10.1021/acs.jpca.3c06357 (cited on pages 27–29, 39).

[119] Leonardo Barneschi, Leonardo Rotondi, and Daniele Padula. 'Molecular Geometry Impact on Deep Learning Predictions of Inverted Singlet–Triplet Gaps'. In: *The Journal of Physical Chemistry A* 128.12 (Mar. 2024), pp. 2417–2426. DOI: 10.1021/acs.jpca.4c00172 (cited on page 27).

[120] Asier E. Izu, Jon M. Matxain, and David Casanova. 'Reverse intersystem crossing mechanisms in doped triangulenes'. In: *Physical Chemistry Chemical Physics* 26.15 (2024), pp. 11459–11468. DOI: 10.1039/d4cp00304g (cited on page 27).

[121] Atreyee Majumdar and Raghunathan Ramakrishnan. 'Resilience of Hund's rule in the chemical space of small organic molecules'. In: *Physical Chemistry Chemical Physics* 26.20 (2024), pp. 14505–14513. DOI: 10.1039/d4cp00886c (cited on page 27).

[122] Pijush Karak et al. 'Reverse Intersystem Crossing Dynamics in Vibronically Modulated Inverted Singlet–Triplet Gap System: A Wigner Phase Space Study'. In: *The Journal of Physical Chemistry Letters* 15.30 (2024), pp. 7603–7609. DOI: 10.1021/acs.jpclett.4c01437 (cited on page 27).

[123] Kenneth D. Wilson et al. 'Spectroscopic Quantification of the Inverted Singlet–Triplet Gap in Pentaazaphenalene'. In: *Journal of the American Chemical Society* 146.23 (May 2024), pp. 15688–15692. DOI: https://doi.org/10.1021/jacs.4c05043 (cited on pages 27, 38).

[124] Qiming Peng et al. 'Organic Light-Emitting Diodes Using a Neutral π Radical as Emitter: The Emission from a Doublet'. In: *Angewandte Chemie International Edition* 54.24 (Apr. 2015), pp. 7091–7095. DOI: 10.1002/anie.201500242 (cited on pages 28, 29).

[125] Xin Ai et al. 'Efficient radical-based light-emitting diodes with doublet emission'. In: *Nature* 563.7732 (Nov. 2018), pp. 536–540. DOI: 10.1038/s41586-018-0695-9 (cited on pages 28, 29).

[126] Shun Kimura et al. 'A luminescent organic radical with two pyridyl groups: high photostability and dual stimuli-responsive properties, with theoretical analyses of photophysical processes'. In: *Chemical Science* 9.7 (2018), pp. 1996–2007. DOI: 10.1039/c7sc04034b (cited on pages 28, 29).

[127] Haoqing Guo et al. 'High stability and luminescence efficiency in donor–acceptor neutral radicals not following the Aufbau principle'. In: *Nature Materials* 18.9 (July 2019), pp. 977–984. DOI: 10.1038/s41563-019-0433-1 (cited on pages 28, 29).

[128] Chuhuan He et al. 'Unraveling the Emission Mechanism of Radical-Based Organic Light-Emitting Diodes'. In: *The Journal of Physical Chemistry Letters* 10.3 (Jan. 2019), pp. 574–580. DOI: 10.1021/acs.jpclett.8b03864 (cited on pages 28, 29).

[129] Alim Abdurahman et al. 'Understanding the luminescent nature of organic radicals for efficient doublet emitters and pure-red light-emitting diodes'. In: *Nature Materials* 19.11 (June 2020), pp. 1224–1229. DOI: 10.1038/s41563-020-0705-9 (cited on pages 28, 29).

[130] Eunkyung Cho, Veaceslav Coropceanu, and Jean-Luc Brédas. 'Organic Neutral Radical Emitters: Impact of Chemical Substitution and Electronic-State Hybridization on the Luminescence Properties'. In: *Journal of the American Chemical Society* 142.41 (Sept. 2020), pp. 17782–17786. DOI: 10.1021/jacs.0c08997 (cited on pages 28, 29).

[131] Z.X. Chen, Y. Li, and F. Huang. 'Persistent and Stable Organic Radicals: Design, Synthesis, and Applications'. In: *Chem* 7.2 (Feb. 2021), pp. 288–332. DOI: https://doi.org/10.1016/j.chempr.2020.09.024 (cited on pages 28, 29).

[132] John M. Hudson, Timothy J. H. Hele, and Emrys W. Evans. 'Efficient light-emitting diodes from organic radicals with doublet emission'. In: *Journal of Applied Physics* 129.18 (May 2021), p. 180901. DOI: 10.1063/5.0047636 (cited on pages 28, 29).

[133] Sebastian Gorgon et al. 'Reversible spin-optical interface in luminescent organic radicals'. In: *Nature* 620.7974 (Aug. 2023), pp. 538–544. DOI: 10.1038/s41586-023-06222-1 (cited on pages 28, 29).

[134] J. A. Vergés et al. 'Fit of Pariser-Parr-Pople and Hubbard model Hamiltonians to charge and spin states of polycyclic aromatic hydrocarbons'. In: *Physical Review B* 81.8 (Feb. 2010), p. 085120. DOI: 10.1103/PhysRevB.81.085120 (cited on page 28).

[135] Antoine Marie and Hugh G. A. Burton. 'Excited States, Symmetry Breaking, and Unphysical Solutions in State-Specific CASSCF Theory'. In: *The Journal of Physical Chemistry A* 127.20 (May 2023), pp. 4538–4552. DOI: 10.1021/acs.jpca.3c00603 (cited on page 28).

[136] Shaoqin Zhang, Zhongjun Zhou, and Zexing Qu. 'Diradical-Based Strategy in Designing Narrowband Thermally Activated Delayed Fluorescence Molecules with Tunable Emission Wavelengths'. In: *The Journal of Physical Chemistry Letters* 15.10 (Mar. 2024), pp. 2723–2731. DOI: 10.1021/acs.jpclett.4c00146 (cited on page 28).

[137] Butong Li et al. 'CAS Calculation of the Excited States of the Methylthio Neutral Radical and Its Ions'. In: *ACS Omega* 5.38 (Sept. 2020), pp. 24204–24210. DOI: https://dx.doi.org/10.1021/acsomega.0c01883?ref=pdf (cited on page 28).

[138] Sudip Chattopadhyay et al. 'State-specific multireference perturbation theory: development and present status'. In: *WIREs Computational Molecular Science* 6.3 (Feb. 2016), pp. 266–291. DOI: 10.1002/wcms.1248 (cited on page 28).

[139] Christopher E. Smith, Rollin A. King, and T. Daniel Crawford. 'Coupled cluster methods including triple excitations for excited states of radicals'. In: *The Journal of Chemical Physics* 122.5 (Jan. 2005), p. 054110. DOI: 10.1063/1.1835953 (cited on page 28).

[140] Arkajyoti Sengupta, Raghunath O. Ramabhadran, and Krishnan Raghavachari. 'Breaking a bottleneck: Accurate extrapolation to "gold standard" CCSD(T) energies for large open shell organic radicals at reduced computational cost'. In: *Journal of Computational Chemistry* 37.2 (Aug. 2015), pp. 286–295. DOI: https://doi.org/10.1002/jcc.24050 (cited on page 28).

[141] Soumyajit Das et al. 'Fully Fused Quinoidal/Aromatic Carbazole Macrocycles with Poly-radical Characters'. In: *Journal of the American Chemical Society* 138.24 (June 2016), pp. 7782–7790. DOI: http://dx.doi.org/10.1021/jacs.6b04539 (cited on page 28).

[142] Rui Huang et al. 'Higher Order π-Conjugated Polycyclic Hydrocarbons with Open-Shell Singlet Ground State: Nonazethrene versus Nonacene'. In: *Journal of the American Chemical Society* 138.32 (Aug. 2016), pp. 10323–10330. DOI: 10.1021/jacs.6b06188 (cited on page 28).

[143] Maude Desroches et al. 'Breaking Bonds and Forming Nanographene Diradicals with Pressure'. In: *Angewandte Chemie International Edition* 56.51 (Nov. 2017), pp. 16212–16217. DOI: 10.1002/anie.201708740 (cited on page 28).

[144] Xuefeng Lu et al. 'Fluorenyl Based Macrocyclic Polyradicaloids'. In: *Journal of the American Chemical Society* 139.37 (Sept. 2017), pp. 13173–13183. DOI: 10.1021/jacs.7b07335 (cited on page 28).

[145] Chunchen Liu et al. 'Macrocyclic Polyradicaloids with Unusual Super-ring Structure and Global Aromaticity'. In: *Chem* 4.7 (July 2018), pp. 1586–1595. DOI: https://doi.org/10.1016/j.chempr.2018.03.020 (cited on page 28).

[146] A. Pérez-Guardiola et al. 'The role of topology in organic molecules: origin and comparison of the radical character in linear and cyclic oligoacenes and related oligomers'. In: *Physical Chemistry Chemical Physics* 20.10 (2018), pp. 7112–7124. DOI: https://doi.org/10.1039/C8CP00135A (cited on page 28).

[147] A. Pérez-Guardiola et al. 'From cyclic nanorings to single-walled carbon nanotubes: disclosing the evolution of their electronic structure with the help of theoretical methods'. In: *Physical Chemistry Chemical Physics* 21.5 (2019), pp. 2547–2557. DOI: 10.1039/C8CP06615A (cited on page 28).

[148] Yong Ni et al. '[n]Cyclo-para-biphenylmethine Polyradicaloids: [n]Annulene Analogs and Unusual Valence Tautomerization'. In: *Chem* 5.1 (Jan. 2019), pp. 108–121. DOI: https://doi.org/10.1016/j.chempr.2018.09.025 (cited on page 28).

[149] María E. Sandoval-Salinas, Abel Carreras, and David Casanova. 'Triangular graphene nanofragments: open-shell character and doping'. In: *Physical Chemistry Chemical Physics* 21.18 (2019), pp. 9069–9076. DOI: 10.1039/c9cp00641a (cited on pages 28, 61).

[150] David Casanova. 'Restricted active space configuration interaction methods for strong correlation: Recent developments'. In: *WIREs Computational Molecular Science* 12.1 (2022), e1561. DOI: https://doi.org/10.1002/wcms.1561 (cited on pages 28, 61).

[151] Preethanuj Preethalayam et al. '3,4-Dimethylenecyclobutene: A Building Block for Design of Macrocycles with Excited State Aromatic Low-Lying High-Spin States'. In: *Chemistry – A European Journal* 30.27 (2024), e202303549. DOI: https://doi.org/10.1002/chem.202303549 (cited on page 28).

[152] T. Ukai et al. 'CASCI-DFT study of the phenalenyl radical system'. In: *Polyhedron* 26.9–11 (June 2007), pp. 2313–2319. DOI: https://doi.org/10.1016/j.poly.2006.11.028 (cited on page 28).

[153] Yasushi Morita et al. 'Topological Symmetry Control in Spin Density Distribution: Spin Chemistry of Phenalenyl-Based Neutral Monoradical Systems'. In: *Organic Letters* 5.18 (Aug. 2003), pp. 3289–3291. DOI: 10.1021/ol0352097 (cited on page 28).

[154] Yasushi Morita et al. 'Synthetic organic spin chemistry for structurally well-defined open-shell graphene fragments'. In: *Nature Chemistry* 3.3 (Feb. 2011), pp. 197–204. DOI: 10.1038/nchem.985 (cited on page 28).

[155] Yohei Hattori, Tetsuro Kusamoto, and Hiroshi Nishihara. 'Luminescence, Stability, and Proton Response of an Open-Shell (3,5-Dichloro-4-pyridyl)bis(2,4,6-trichlorophenyl)methyl Radical'. In: *Angewandte Chemie International Edition* 53.44 (Sept. 2014), pp. 11845–11848. DOI: 10.1002/anie.201407362 (cited on page 28).

[156] Valentín Diez-Cabanes et al. 'Design of Perchlorotriphenylmethyl (PTM) Radical-Based Compounds for Optoelectronic Applications: The Role of Orbital Delocalization'. In: *ChemPhysChem* 19.19 (July 2018), pp. 2572–2578. DOI: https://doi.org/10.1002/cphc.201800321 (cited on page 28).

[157] Claire Tonnelé and David Casanova. 'Rationalization and tuning of doublet emission in organic radicals'. In: *Journal of Materials Chemistry C* 10.37 (2022), pp. 13826–13833. DOI: https://doi.org/10.1039/D2TC01632J (cited on page 28).

[158] Tong Shen et al. 'Fused Triangulene Dimers: Facile Synthesis by Intramolecular Radical-Radical Coupling and Application for Near-Infrared Lasers'. In: *Angewandte Chemie International Edition* 62.27 (2023), e202304197. DOI: https://doi.org/10.1002/anie.202304197 (cited on page 28).

[159] Cheng-Wei Ju et al. 'Accurate Electronic and Optical Properties of Organic Doublet Radicals Using Machine Learned Range-Separated Functionals'. In: *The Journal of Physical Chemistry A* 128.12 (Feb. 2024), pp. 2457–2471. DOI: 10.1021/acs.jpca.3c07437 (cited on page 28).

[160] Jie Su et al. 'Triangulenes: From Precursor Design to On-Surface Synthesis and Characterization'. In: *Angewandte Chemie International Edition* 59.20 (Feb. 2020), pp. 7658–7668. DOI: 10.1002/anie.201913783 (cited on page 28).

[161] Rudolph Pariser and Robert G. Parr. 'A Semi-Empirical Theory of the Electronic Spectra and Electronic Structure of Complex Unsaturated Molecules. II'. In: *The Journal of Chemical Physics* 21.5 (1953), pp. 767–776. DOI: https://doi.org/10.1063/1.1699030 (cited on pages 28, 30, 39).

[162] J. A. Pople. 'Electron interaction in unsaturated hydrocarbons'. In: *Transactions of the Faraday Society* 49 (1953), p. 1375. DOI: https://doi.org/10.1039/TF9534901375 (cited on pages 28, 39).

[163] Giorgio Favini, Ida Vandoni, and Massimo Simonetta. 'Calculation of electronic spectra of aza-benzenes and aza-naphthalenes by the Pariser-Parr-Pople method'. In: *Theoretica Chimica Acta* 3.1 (1965), pp. 45–58. DOI: https://doi.org/10.1007/BF00526532 (cited on pages 28, 30).

[164] I. D. L. Albert, S. Ramasesha, and P. K. Das. 'Properties of some low-lying electronic states in polymethineimines and poly(2,3-diazabutadienes)'. In: *Physical Review B* 43.9 (1991), pp. 7013–7019. DOI: 10.1103/PhysRevB.43.7013 (cited on pages 28, 30).

[165] S. Mukhopadhyay et al. 'Neutral and Charged Excited States in Polar Organic Films: Origin of Unusual Electroluminescence in Tri-*p*-tolylamine-Based Hole Conductors'. In: *The Journal of Physical Chemistry A* 112.31 (2008), pp. 7271–7279. DOI: https://doi.org/10.1021/jp8012078 (cited on pages 28, 30, 61).

[166] Manoranjan Kumar, Y. Anusooya Pati, and S. Ramasesha. 'A density matrix renormalization group method study of optical properties of porphines and metalloporphines'. In: *The Journal of Chemical Physics* 136.1 (2012), p. 014112. DOI: https://doi.org/10.1063/1.3671946 (cited on pages 28, 30, 40).

[167] Simil Thomas, YA Pati, and S Ramasesha. 'Linear and nonlinear optical properties of expanded porphyrins: A DMRG study'. In: *The Journal of Physical Chemistry A* 117.33 (2013), pp. 7804–7809 (cited on pages 28, 30, 39).

[168] Karan Aryanpour, Alok Shukla, and Sumit Mazumdar. 'Electron correlations and two-photon states in polycyclic aromatic hydrocarbon molecules: A peculiar role of geometry'. In: *The Journal of Chemical Physics* 140.10 (2014), p. 104301. DOI: https://doi.org/10.1063/1.4867363 (cited on pages 28, 39).

[169] Pritam Bhattacharyya, Deepak Kumar Rai, and Alok Shukla. 'Pariser–Parr–Pople Model Based Configuration-Interaction Study of Linear Optical Absorption in Lower-Symmetry Polycyclic Aromatic Hydrocarbon Molecules'. In: *The Journal of Physical Chemistry C* 124.26 (2020), pp. 14297–14305. DOI: https://doi.org/10.1021/acs.jpcc.0c01719 (cited on pages 28, 39).

[170] Yong Rui Poh et al. 'Alternant Hydrocarbon Diradicals as Optically Addressable Molecular Qubits'. In: *Journal of the American Chemical Society* 146.22 (May 2024), pp. 15549–15561. DOI: https://doi.org/10.1021/jacs.4c04360 (cited on pages 28, 29, 38, 39, 41, 42).

[171] Matteo Bedogni and Francesco Di Maiolo. 'Singlet–Triplet Inversion in Triangular Boron Carbon Nitrides'. In: *Journal of Chemical Theory and Computation* (2024). DOI:10.1021/acs.jctc.4c00706 (cited on pages 28, 38, 39).

[172] Timothy J. H. Hele. 'On the electronic structure of alternant conjugated organic radicals for light-emitting diode applications'. In: *Physical Chemistry of Semiconductor Materials and Interfaces XX*. Ed. by Andrew J. Musser and Derya Baran. Vol. 11799. International Society for Optics and Photonics. SPIE, 2021, 117991A. DOI: 10.1117/12.2593712 (cited on pages 28, 29).

[173] James D. Green and Timothy J. H. Hele. 'ExROPPP: Fast, accurate, and spin-pure calculation of the electronically excited states of organic hydrocarbon radicals'. In: *The Journal of Chemical Physics* 160.16 (Apr. 2024), p. 164110. DOI: 10.1063/5.0191373 (cited on pages 28, 29, 31, 39).

[174] R. L. Ellis, G. Kuehnlenz, and H. H. Jaffé. 'The use of the CNDO method in spectroscopy: VI. further n-π^* transitions'. In: *Theoretica Chimica Acta* 26.2 (1972), pp. 131–140. DOI: https://doi.org/10.1007/BF00526540 (cited on pages 29, 39).

[175] Péter R. Surján and Hans Kuzmany. 'Interruption of conjugations of polyacetylene chains'. In: *Physical Review B* 33.4 (1986), pp. 2615–2624. DOI: https://doi.org/10.1103/PhysRevB.33.2615 (cited on pages 29, 39).

[176] Timothy J. H. Hele et al. 'Anticipating Acene-Based Chromophore Spectra with Molecular Orbital Arguments'. In: *The Journal of Physical Chemistry A* 123.13 (Feb. 2019), pp. 2527–2536. DOI: https://doi.org/10.1021/acs.jpca.8b12222 (cited on pages 29, 39).

[177] James D. Green, Eric G. Fuemmeler, and Timothy J. H. Hele. 'Inverse molecular design from first principles: Tailoring organic chromophore spectra for optoelectronic applications'. In: *The Journal of Chemical Physics* 156.18 (May 2022). DOI: https://doi.org/10.1063/5.0082311 (cited on pages 29, 39).

[178] Ljubisa R. Radovic et al. 'The role of substitutional boron in carbon oxidation'. In: *Carbon* 36.12 (1998), pp. 1841–1854. DOI: https://doi.org/10.1016/S0008-6223(98)00156-0 (cited on page 29).

[179] P. G. Perkins and D. H. Wall. 'Self-consistent molecular-orbital calculations on borazines'. In: *Journal of the Chemical Society A: Inorganic, Physical, Theoretical* (1966), p. 235. DOI: https://doi.org/10.1039/J19660000235 (cited on page 29).

[180] H. Jensen et al. 'Semi-empirical Parameters in pi-Electron Systems. V. The Carbonyl Group.' In: *Acta Chemica Scandinavica* 22 (1968), pp. 2899–2909. DOI: 10.3891/acta.chem.scand.22-2899 (cited on page 29).

[181] Prakash Chandra Jha et al. 'Nonlinear optical properties of linear chain phosphazenes, (PN)x'. In: *The Journal of Chemical Physics* 117.6 (Aug. 2002), pp. 2873–2881. DOI: https://doi.org/10.1063/1.1491878 (cited on page 29).

[182] Mousumi Das. 'Low-lying excitations of poly-fused thiophene within Pariser–Parr–Pople model: A density matrix renormalization group study'. In: *The Journal of Chemical Physics* 132.19 (May 2010). DOI: 10.1063/1.3425882 (cited on page 29).

[183] C. A. Coulson and G. S. Rushbrooke. 'Note on the method of molecular orbitals'. In: *Mathematical Proceedings of the Cambridge Philosophical Society* 36.2 (Apr. 1940), pp. 193–200. DOI: 10.1017/S0305004100017163 (cited on page 29).

[184] A.D. McLachlan. 'The pairing of electronic states in alternant hydrocarbons'. In: *Molecular Physics* 2.3 (July 1959), pp. 271–284. DOI: 10.1080/00268975900100261 (cited on page 29).

[185] Jaroslav Koutecký. 'Contribution to the Theory of Alternant Systems'. In: *The Journal of Chemical Physics* 44.10 (May 1966), pp. 3702–3706. DOI: https://doi.org/10.1063/1.1726522 (cited on page 29).

[186] Elliott H. Lieb and F. Y. Wu. 'Absence of Mott Transition in an Exact Solution of the Short-Range, One-Band Model in One Dimension'. In: *Physical Review Letters* 20.25 (June 1968), pp. 1445–1448. DOI: https://doi.org/10.1103/PhysRevLett.20.1445 (cited on page 29).

[187] Ole J. Heilmann and Elliott H. Lieb. 'VIOLATION OF THE NONCROSSING RULE: THE HUBBARD HAMILTONIAN FOR BENZENE'. In: *Annals of the New York Academy of Sciences* 172.15 (Oct. 1971), pp. 584–617. DOI: https://doi.org/10.1111/j.1749-6632.1971.tb34956.x (cited on page 29).

[188] A. Laforgue, J. Čížek, and J. Paldus. 'Study of the correlation effects in a three-electron model system using the projected Hartree-Fock method and the natural spin orbital formalism'. In: *The Journal of Chemical Physics* 59.5 (Sept. 1973), pp. 2560–2571. DOI: https://doi.org/10.1063/1.1680372 (cited on page 29).

[189] J. Čížek, J. Paldus, and I. Hubač. 'Correlation effects in the low–lying excited states of the PPP models of alternant hydrocarbons. I. Qualitative rules for the effect of limited configuration interaction'. In: *International Journal of Quantum Chemistry* 8.6 (Nov. 1974), pp. 951–970. DOI: https://doi.org/10.1002/qua.560080610 (cited on page 29).

[190] S.R. Bondeson and Z.G. Soos. 'Charge transfer transitions in extended correlated electronic systems'. In: *Chemical Physics* 44.3 (Dec. 1979), pp. 403–414. DOI: https://doi.org/10.1016/0301-0104(79)85223-4 (cited on page 29).

[191] I. R. Ducasse, T. E. Miller, and Z. G. Soos. 'Correlated states in finite polyenes: Exact PPP results'. In: *The Journal of Chemical Physics* 76.8 (Apr. 1982), pp. 4094–4104. DOI: https://doi.org/10.1063/1.443484 (cited on page 29).

[192] Zoltán G. Soos. 'Electronic Structure of Ion-Radical Organic Solids and Polyenes'. In: *Israel Journal of Chemistry* 23.1 (Jan. 1983), pp. 37–48. DOI: https://doi.org/10.1002/ijch.198300005 (cited on page 29).

[193] T. P. Živković. 'Particle-hole symmetry and complementary quantum systems'. In: *International Journal of Quantum Chemistry* 34.4 (Oct. 1988), pp. 333–359. DOI: 10.1002/qua.560340404 (cited on page 29).

[194] Péter R. Surján. *Second Quantized Approach to Quantum Chemistry*. Springer Berlin Heidelberg, 1989 (cited on page 29).

[195] R. B. Mallion and D. H. Rouvray. 'The golden jubilee of the Coulson-Rushbrooke pairing theorem'. In: *Journal of Mathematical Chemistry* 5.1 (Mar. 1990), pp. 1–21. DOI: 10.1007/BF01166272 (cited on page 29).

[196] I A Misurkin and Aleksandr A Ovchinnikov. 'The Electronic Structure of Conjugated Systems in Terms of the Pariser–Parr–Pole Approximation'. In: *Russian Chemical Reviews* 43.12 (1974), p. 1072. DOI: 10.1070/RC1974v043n12ABEH001881 (cited on page 29).

[197] Joseph R. Lakowicz. *Principles of fluorescence spectroscopy / Joseph R. Lakowicz.* eng. 3rd ed. New York: Springer, 2006 (cited on page 30).

[198] D.H. Reid. 'Stable π-electron systems and new aromatic structures'. In: *Tetrahedron* 3.3 (Jan. 1958), pp. 339–352. DOI: https://doi.org/10.1016/0040-4020(58)80039-3 (cited on page 30).

[199] F. Gerson. 'Notiz über das ESR.-Spektrum des Phenalenyl-Radikals'. In: *Helvetica Chimica Acta* 49.5 (Jan. 1966), pp. 1463–1467. DOI: https://doi.org/10.1002/hlca.19660490506 (cited on page 30).

[200] Kosaburo Goto et al. 'A Stable Neutral Hydrocarbon Radical: Synthesis, Crystal Structure, and Physical Properties of 2,5,8-Tri-tert-butyl-phenalenyl'. In: *Journal of the American Chemical Society* 121.7 (Feb. 1999), pp. 1619–1620. DOI: 10.1021/ja9836242 (cited on page 30).

[201] K. Fukui et al. 'Electronic structure of a stable phenalenyl radical in crystalline state as studied by SQUID measurements, cw-ESR, and 13C CP/MAS NMR spectroscopy'. In: *Synthetic Metals* 103.1–3 (June 1999), pp. 2257–2258. DOI: https://doi.org/10.1016/S0379-6779(98)00396-8 (cited on page 30).

[202] M. E. Itkis et al. 'Magneto-Opto-Electronic Bistability in a Phenalenyl-Based Neutral Radical'. In: *Science* 296.5572 (May 2002), pp. 1443–1445. DOI: 10.1126/science.1071372 (cited on page 30).

[203] D. H. Reid. 'The chemistry of the phenalenes'. In: *Quarterly Reviews, Chemical Society* 19.3 (1965), p. 274. DOI: https://doi.org/10.1039/QR9651900274 (cited on pages 30, 35).

[204] W.P. Cofino et al. 'Jahn-Teller effect in highly resolved optical spectra of the phenalenyl radical'. In: *Molecular Physics* 51.3 (Feb. 1984), pp. 537–550. DOI: https://doi.org/10.1080/00268978400100381 (cited on pages 30, 35).

[205] Shijun Zheng et al. 'Synthesis, Characterization, and Coordination Chemistry of the 2-Azaphenalenyl Radical'. In: *Journal of the American Chemical Society* 125.19 (Apr. 2003), pp. 5786–5791. DOI: https://doi.org/10.1021/ja029236o (cited on page 30).

[206] Yasushi Morita et al. 'A New Trend in Phenalenyl Chemistry: A Persistent Neutral Radical, 2,5,8-Tri-tert-butyl-1,3-diazaphenalenyl, and the Excited Triplet State of the Gablesyn-Dimer in the Crystal of Column Motif'. In: *Angewandte Chemie International Edition* 41.10 (May 2002), pp. 1793–1796. DOI: https://doi.org/10.1002/1521-3773(20020517)41:10%3C1793::AID-ANIE1793%3E3.0.CO;2-G (cited on page 30).

[207] Shijun Zheng et al. 'Perchloro-2,5,8-triazaphenalenyl Radical'. In: *Organic Letters* 7.9 (Apr. 2005), pp. 1861–1863. DOI: https://doi.org/10.1021/ol050570+ (cited on page 30).

[208] Shuichi Suzuki et al. 'Hexaazaphenalenyl Anion Revisited: A Highly Symmetric Planar π System with Multiple-Networking Ability for Self-Assembled Metal Complexation'. In: *Inorganic Chemistry* 44.23 (Oct. 2005), pp. 8197–8199. DOI: 10.1021/ic051583m (cited on page 30).

[209] Shingo Ito. 'The Rapid Synthesis of π-Extended Azacorannulenes'. In: *Journal of Synthetic Organic Chemistry, Japan* 77.11 (Nov. 2019), pp. 1128–1135. DOI: https://doi.org/10.5059/yukigoseikyokaishi.77.1128 (cited on page 30).

[210] Z. G. Soos and S. Ramasesha. 'Valence-bond theory of linear Hubbard and Pariser-Parr-Pople models'. In: *Physical Review B* 29.10 (1984), pp. 5410–5422. DOI: 10.1103/PhysRevB.29.5410 (cited on page 30).

[211] Suryoday Prodhan, Zoltán G. Soos, and S. Ramasesha. 'Model for triplet state engineering in organic light emitting diodes'. In: *The Journal of Chemical Physics* 140.21 (2014), p. 214313. DOI: 10.1063/1.4880276 (cited on page 30).

[212] Kichisuke Nishimoto and Leslie S. Forster. 'SCFMO calculations of heteroatomic systems with the variable? approximation'. In: *Theoretica Chimica Acta* 4.2 (1966), pp. 155–165. DOI: https://doi.org/10.1007/BF01007291 (cited on page 30).

[213] Josef Michl et al. 'A note on the parameters for heteroatoms in Pariser-Parr-Pople (PPP) calculations'. In: *Theoretica Chimica Acta* 19.1 (1970), pp. 92–97. DOI: https://doi.org/10.1007/BF00527381 (cited on page 30).

[214] Juergen Hinze and David L. Beveridge. 'Parametrization of semiempirical π-electron molecular orbital calculations. π Systems containing carbon, nitrogen, oxygen, and fluorine'. In: *Journal of the American Chemical Society* 93.13 (1971), pp. 3107–3114. DOI: https://doi.org/10.1021/ja00742a002 (cited on page 30).

[215] R. Zahradník, I. Tesařová, and J. Pancíř. 'Experimental and theoretical (HMO and LCI-SCF) study of singlet-triplet transitions in conjugated hydrocarbons and their derivatives'. In: *Collection of Czechoslovak Chemical Communications* 36.8 (1971), pp. 2867–2880. DOI: https://doi.org/10.1135/cccc19712867 (cited on page 30).

[216] John Griffiths. 'Practical aspects of colour prediction of organic dye molecules'. In: *Dyes and Pigments* 3.2-3 (1982), pp. 211–233. DOI: https://doi.org/10.1016/0143-7208(82)80024-7 (cited on page 30).

[217] Michael F. Grossjean and Paul Tavan. 'Wavelength regulation in bacteriorhodopsin and halorhodopsin: A Pariser–Parr–Pople multireference double excitation configuration interaction study of retinal dyes'. In: *The Journal of Chemical Physics* 88.8 (1988), pp. 4884–4896. DOI: https://doi.org/10.1063/1.454701 (cited on page 30).

[218] I. D. L. Albert, P. K. Das, and S. Ramasesha. 'Optical nonlinearities in symmetric cyanine dyes and related systems'. In: *Journal of the Optical Society of America B* 10.8 (1993), p. 1365. DOI: https://doi.org/10.1364/JOSAB.10.001365 (cited on page 30).

[219] Matteo Dubbini et al. 'Turning on Organic Radical Emitters'. In: *The Journal of Physical Chemistry C* 128.43 (Oct. 2024). Publisher: American Chemical Society, pp. 18158–18169. DOI: 10.1021/acs.jpcc.4c04362. (Visited on 08/14/2025) (cited on pages 30, 36).

[220] Kimio Ohno. 'Some remarks on the Pariser-Parr-Pople method'. In: *Theoretica chimica acta* 2.3 (1964), pp. 219–227 (cited on page 30).

[221] David Maurice and Martin Head-Gordon. 'On the Nature of Electronic Transitions in Radicals: An Extended Single Excitation Configuration Interaction Method'. In: *The Journal of Physical Chemistry* 100.15 (1996), pp. 6131–6137. DOI: 10.1021/jp952754j (cited on page 31).

[222] F. Neese. 'The ORCA program system'. In: *WIRES Comput. Molec. Sci.* 2.1 (2012), pp. 73–78. DOI: 10.1002/wcms.81 (cited on pages 32, 42, 84).

[223] Rudraditya Sarkar et al. 'Assessing the Performances of CASPT2 and NEVPT2 for Vertical Excitation Energies'. In: *Journal of Chemical Theory and Computation* 18.4 (Mar. 2022), pp. 2418–2436. DOI: 10.1021/acs.jctc.1c01197 (cited on page 32).

[224] S. Ramasesha and Z.G. Soos. 'Magnetic and optical properties of exact PPP states of naphthalene'. In: *Chemical Physics* 91.1 (Nov. 1984), pp. 35–42. DOI: https://doi.org/10.1016/0301-0104(84)80040-3 (cited on page 35).

[225] Edan Scriven and B. J. Powell. 'Toward the parametrization of the Hubbard model for salts of bis(ethylenedithio)tetrathiafulvalene: A density functional study of isolated molecules'. In: *The Journal of Chemical Physics* 130.10 (Mar. 2009), p. 104508. DOI: 10.1063/1.3080543 (cited on page 37).

[226] Francesco Di Maiolo, Matteo Masino, and Anna Painelli. 'Terahertz-pulse driven modulation of electronic spectra: Modeling electron-phonon coupling in charge-transfer crystals'. In: *Physical Review B* 96.7 (Aug. 2017), p. 075106. DOI: 10.1103/PhysRevB.96.075106 (cited on page 37).

[227] M. J. Frisch et al. *Gaussian~16 Revision B.01*. Gaussian Inc. Wallingford CT. 2016 (cited on pages 37, 41).

[228] F. Dolde et al. 'Electric-field sensing using single diamond spins'. In: *Nature Physics* 7.6 (Apr. 2011), pp. 459–463. DOI: 10.1038/nphys1969 (cited on page 38).

[229] Marcus W. Doherty et al. 'The nitrogen-vacancy colour centre in diamond'. In: *Physics Reports* 528.1 (July 2013), pp. 1–45. DOI: 10.1016/j.physrep.2013.02.001 (cited on page 38).

[230] L Rondin et al. 'Magnetometry with nitrogen-vacancy defects in diamond'. In: *Reports on Progress in Physics* 77.5 (May 2014), p. 056503. DOI: 10.1088/0034-4885/77/5/056503 (cited on page 38).

[231] Francesco Casola, Toeno van der Sar, and Amir Yacoby. 'Probing condensed matter physics with magnetometry based on nitrogen-vacancy centres in diamond'. In: *Nature Reviews Materials* 3.1 (Jan. 2018). DOI: 10.1038/natrevmats.2017.88 (cited on page 38).

[232] Sebastian Gorgon et al. 'Reversible spin-optical interface in luminescent organic radicals'. In: *Nature* 620.7974 (Aug. 2023), pp. 538–544. DOI: 10.1038/s41586-023-06222-1 (cited on page 38).

[233] Hongde Yu and Thomas Heine. 'Magnetic Coupling Control in Triangulene Dimers'. In: *Journal of the American Chemical Society* 145.35 (Aug. 2023), pp. 19303–19311. DOI: 10.1021/jacs.3c05178 (cited on page 38).

[234] Sebastian M. Kopp et al. 'Luminescent Organic Triplet Diradicals as Optically Addressable Molecular Qubits'. In: *Journal of the American Chemical Society* 146.40 (Sept. 2024), pp. 27935–27945. DOI: 10.1021/jacs.4c11116 (cited on page 38).

[235] Yong Rui Poh and Joel Yuen-Zhou. 'Enhancing the Optically Detected Magnetic Resonance Signal of Organic Molecular Qubits'. In: *ACS Central Science* 11.1 (Jan. 2025), pp. 116–126. DOI: 10.1021/acscentsci.4c01632 (cited on page 38).

[236] Qi Sun, Jean-Luc Brédas, and Hong Li. 'Reliable Diradical Characterization via Precise Singlet–Triplet Gap Calculations: Application to Thiele, Chichibabin, and Müller Analogous Diradicals'. In: *Journal of Chemical Theory and Computation* 21.3 (Jan. 2025), pp. 1194–1202. DOI: 10.1021/acs.jctc.4c01384 (cited on page 38).

[237] Davide Mesto et al. 'Luminescent Trityl-based Diradicaloids: A Theoretical and Experimental Assessment of Charge-Resonance in Low-Lying Excited States'. In: *Chemistry – A European Journal* 31.23 (Mar. 2025). DOI: 10.1002/chem.202500749 (cited on page 38).

[238] Raul Santiago et al. 'Rational design of organic diradicals with robust high-spin ground state based on antiaromatic linkers'. In: *Chemical Science* 16.1 (2025), pp. 430–447. DOI: 10.1039/d4sc05225k (cited on page 38).

[239] Sebastian M. Kopp et al. 'Optically Detected Coherent Spin Control of Organic Molecular Color Center Qubits'. In: *Journal of the American Chemical Society* (June 2025). DOI: 10.1021/jacs.5c05718 (cited on page 38).

[240] Ángel José Pérez-Jiménez, Yoann Olivier, and Juan Carlos Sancho-García. 'The Role of Theoretical Calculations for INVEST Systems: Complementarity Between Theory and Experiments and Rationalization of the Results'. In: *Advanced Optical Materials* n/a.n/a (), p. 2403199 (cited on page 38).

[241] Makhvela Anwer and Shiwei Yin. 'Recent progress and prospects of inverted singlet-triplet energy gap (INVEST) materials in OLEDs'. In: *Organic Electronics* 144 (Sept. 2025), p. 107282. DOI: 10.1016/j.orgel.2025.107282 (cited on page 38).

[242] H. Kollmar and V. Staemmler. 'A theoretical study of the structure of cyclobutadiene'. In: *Journal of the American Chemical Society* 99.11 (1977), pp. 3583–3587. DOI: https://doi.org/10.1021/ja00453a009 (cited on page 38).

[243] H. Kollmar and V. Staemmler. 'Violation of Hund's rule by spin polarization in molecules'. In: *Theoretica Chimica Acta* 48.3 (1978), pp. 223–239. DOI: https://doi.org/10.1007/BF00549021 (cited on page 38).

[244] Shiro Koseki, Takeshi Nakajima, and Azumao Toyota. 'Violation of Hund's multiplicity rule in the electronically excited states of conjugated hydrocarbons'. In: *Canadian Journal of Chemistry* 63.7 (1985), pp. 1572–1579 (cited on page 38).

[245] Azumao Toyota and Takeshi Nakajima. 'Violation of Hund's multiplicity rule in the lowest excited singlet–triplet pairs of cyclic bicalicene and its higher homologues'. In: *J. Chem. Soc., Perkin Trans. 2* 11 (1986), pp. 1731–1734. DOI: 10.1039/P29860001731 (cited on page 38).

[246] Azumao Toyota. 'Violation of Hund's rule in the lowest excited singlet-triplet pairs of dicyclohepta[cd,gh]pentalene and dicyclopenta[ef,kl]heptalene'. In: *Theoretica Chimica Acta* 74.3 (1988), pp. 209–217. DOI: https://doi.org/10.1007/BF00527144 (cited on page 38).

[247] D. K. Andrea Phan Huu et al. 'Ab initio parametrization of a generalized Hubbard model in a molecule displaying chirality-induced spin selectivity'. In: *Communications Materials* 6.1 (May 2025). DOI: https://doi.org/10.1038/s43246-025-00821-3 (cited on page 39).

[248] Tzay-Ming Hong and Hsin-Fei Meng. 'Spin-dependent recombination and electroluminescence quantum yield in conjugated polymers'. In: *Physical Review B* 63.7 (Jan. 2001). DOI: 10.1103/physrevb.63.075206 (cited on page 41).

[249] J. Rybicki and M. Wohlgenannt. 'Spin-orbit coupling in singly charged π-conjugated polymers'. In: *Physical Review B* 79.15 (Apr. 2009). DOI: 10.1103/physrevb.79.153202 (cited on page 41).

[250] William Barford, Robert J. Bursill, and Dmitry V. Makhov. 'Spin-orbit interactions between interchain excitations in conjugated polymers'. In: *Physical Review B* 81.3 (Jan. 2010). DOI: 10.1103/physrevb.81.035206 (cited on pages 41, 44).

[251] Max Marcus and William Barford. 'Triplet-triplet decoherence in singlet fission'. In: *Physical Review B* 102.3 (July 2020). DOI: 10.1103/physrevb.102.035134 (cited on page 41).

[252] Michael Franz, Frank Neese, and Sabine Richert. 'Calculation of exchange couplings in the electronically excited state of molecular three-spin systems'. In: *Chemical Science* 13.42 (2022), pp. 12358–12366. DOI: 10.1039/d2sc04701b (cited on page 42).

[253] Rama Dhali et al. 'Understanding TADF: a joint experimental and theoretical study of DMAC-TRZ'. In: *Physical Chemistry Chemical Physics* 23.1 (2021), pp. 378–387. DOI: 10.1039/d0cp05982j (cited on page 45).

[254] Abel Carreras et al. 'Calculation of spin–orbit couplings using RASCI spinless one-particle density matrices: Theory and applications'. In: *The Journal of Chemical Physics* 153.21 (Dec. 2020). DOI: 10.1063/5.0029146 (cited on page 45).

[255] DK Andrea Phan Huu, Sangeeth Saseendran, and Anna Painelli. 'Effective models for TADF: the role of the medium polarizability'. In: *Journal of Materials Chemistry C* 10.12 (2022), pp. 4620–4628 (cited on pages 48, 49).

[256] D. K. Andrea Phan Huu, Sangeeth Saseendran, and Anna Painelli. 'Effective models for TADF: the role of the medium polarizability'. In: *Journal of Materials Chemistry C* 10.12 (2022), pp. 4620–4628. DOI: 10.1039/d1tc05296a (cited on pages 49, 52).

[257] Rodney Loudon. *The Quantum Theory of Light*. Oxford University PressOxford, Sept. 2000 (cited on page 50).

[258] Manuel Souto et al. 'TTF–PTM dyads: from switched molecular self assembly in solution to radical conductors in solid state'. en. In: *CrystEngComm* 19.2 (2017). Publisher: Royal Society of Chemistry, pp. 197–206. DOI: 10.1039/C6CE01660J. (Visited on 06/27/2023) (cited on pages 51, 53).

[259] Manuel Souto et al. 'Synthesis and Characterization of Ethylenedithio-MPTTF-PTM Radical Dyad as a Potential Neutral Radical Conductor'. en. In: *Magnetochemistry* 2.4 (Dec. 2016). Number: 4 Publisher: Multidisciplinary Digital Publishing Institute, p. 46. DOI: 10.3390/magnetochemistry2040046. (Visited on 08/17/2023) (cited on page 51).

[260] José L Segura and Nazario Martín. 'New concepts in tetrathiafulvalene chemistry'. In: *Angewandte Chemie International Edition* 40.8 (2001), pp. 1372–1409 (cited on page 51).

[261] Nazario Martín. 'Tetrathiafulvalene: the advent of organic metals'. In: *Chemical Communications* 49.63 (2013), pp. 7025–7027 (cited on page 51).

[262] David Canevet et al. 'Tetrathiafulvalene (TTF) derivatives: key building-blocks for switchable processes'. In: *Chemical Communications* 17 (2009), pp. 2245–2269 (cited on page 51).

[263] Judith Guasch et al. 'Induced Self-Assembly of a Tetrathiafulvalene-Based Open-Shell Dyad through Intramolecular Electron Transfer'. In: *Angewandte Chemie International Edition* 51.44 (2012). _eprint: https://onlinelibrary.wiley.com/doi/pdf/10.1002/anie.201203448, pp. 11024–11028. DOI: 10.1002/anie.201203448. (Visited on 01/06/2024) (cited on page 51).

[264] Judith Guasch et al. 'Intra- and Intermolecular Charge Transfer in Aggregates of Tetrathiafulvalene-Triphenylmethyl Radical Derivatives in Solution'. In: *Journal of the American Chemical Society* 135.18 (May 2013). Publisher: American Chemical Society, pp. 6958–6967. DOI: 10.1021/ja400281b. (Visited on 02/14/2023) (cited on page 51).

[265] Evgeny Epifanovsky et al. 'Software for the frontiers of quantum chemistry: An overview of developments in the Q-Chem 5 package'. In: *The Journal of Chemical Physics* 155.8 (Aug. 2021), p. 084801. DOI: 10.1063/5.0055522. (Visited on 09/18/2025) (cited on pages 51, 55).

[266] Luca Grisanti et al. 'Essential State Models for Solvatochromism in Donor Acceptor Molecules: The Role of the Bridge'. In: *The Journal of Physical Chemistry B* 113.14 (Apr. 2009). Publisher: American Chemical Society, pp. 4718–4725. DOI: 10.1021/jp809771d. (Visited on 06/22/2023) (cited on page 52).

[267] Mulliken, R. S. 'Molecular Compounds and their Spectra. II'. In: *J. Am. Chem. Soc.* 74.3 (1952), pp. 811–824 (cited on page 52).

[268] Anna Painelli. 'Vibronic contribution to static NLO properties: exact results for the DA dimer'. In: *Chemical physics letters* 285.5-6 (1998), pp. 352–358 (cited on page 52).

[269] R. A. Marcus. 'On the Theory of Oxidation-Reduction Reactions Involving Electron Transfer. I'. In: *The Journal of Chemical Physics* 24.5 (May 1956), pp. 966–978. DOI: 10.1063/1.1742723. (Visited on 11/20/2025) (cited on page 53).

[270] Francesco Aquilante et al. 'Molcas 8: New capabilities for multiconfigurational quantum chemical calculations across the periodic table'. en. In: *Journal of Computational Chemistry* 37.5 (2016). _eprint: https://onlinelibrary.wiley.com/doi/pdf/10.1002/jcc.24221, pp. 506–541. DOI: 10.1002/jcc.24221. (Visited on 11/18/2025) (cited on page 55).

[271] Laurence D. Barron. *Molecular Light Scattering and Optical Activity*. Cambridge University Press, 2009 (cited on page 65).

[272] Jianmei Han et al. 'Recent Progress on Circularly Polarized Luminescent Materials for Organic Optoelectronic Devices'. In: *Advanced Optical Materials* 6.17 (2018), p. 1800538. DOI: 10.1002/adom.201800538 (cited on page 65).

[273] Li Wan et al. 'Inverting the Handedness of Circularly Polarized Luminescence from Light-Emitting Polymers Using Film Thickness'. In: *ACS Nano* 13.7 (2019), pp. 8099–8105. DOI: 10.1021/acsnano.9b02940 (cited on page 65).

[274] Rituparno Chowdhury et al. 'Circularly polarized electroluminescence from chiral supramolecular semiconductor thin films'. In: *Science* 387.6739 (2025), pp. 1175–1181. DOI: 10.1126/science.adt3011 (cited on page 65).

[275] N. S. Shahana Nizar et al. 'Emergent chiroptical properties in supramolecular and plasmonic assemblies'. In: *Chemical Society Reviews* 50.20 (2021), pp. 11208–11226. DOI: 10.1039/d0cs01583k (cited on pages 65, 80).

[276] Kyle W. Quasdorf and Larry E. Overman. 'Catalytic enantioselective synthesis of quaternary carbon stereocentres'. en. In: *Nature* 516.7530 (Dec. 2014), pp. 181–191. DOI: 10.1038/nature14007. (Visited on 03/24/2025) (cited on page 65).

[277] Elisa González-Fernández et al. 'Enantioselective Synthesis of [6]Carbohelicenes'. In: *Journal of the American Chemical Society* 139.4 (Feb. 2017), pp. 1428–1431. DOI: 10.1021/jacs.6b12443. (Visited on 03/24/2025) (cited on page 65).

[278] Jacob S. DeHovitz et al. 'Static to inducibly dynamic stereocontrol: The convergent use of racemic β-substituted ketones'. In: *Science* 369.6507 (2020), pp. 1113–1118. DOI: 10.1126/science.abc9909 (cited on page 65).

[279] Tzuriel S. Metzger et al. 'Dynamic Spin-Controlled Enantioselective Catalytic Chiral Reactions'. In: *The Journal of Physical Chemistry Letters* 12.23 (June 2021), pp. 5469–5472. DOI: 10.1021/acs.jpclett.1c01518. (Visited on 03/19/2025) (cited on page 65).

[280] Wei Liu et al. 'Catalytic Enantioselective Synthesis of Helicenes'. In: *Chemistry – A European Journal* 28.68 (Dec. 2022), e202202369. DOI: 10.1002/chem.202202369. (Visited on 03/24/2025) (cited on page 65).

[281] Rosario R. Riso, Enrico Ronca, and Henrik Koch. 'Strong Coupling to Circularly Polarized Photons: Toward Cavity-Induced Enantioselectivity'. In: *The Journal of Physical Chemistry Letters* 15.34 (2024), pp. 8838–8844. DOI: 10.1021/acs.jpclett.4c01701 (cited on page 65).

[282] Brian P. Bloom et al. 'Chiral Induced Spin Selectivity'. In: *Chemical Reviews* 124.4 (2024), pp. 1950–1991. DOI: 10.1021/acs.chemrev.3c00661 (cited on page 66).

[283] K. Ray et al. 'Asymmetric Scattering of Polarized Electrons by Organized Organic Films of Chiral Molecules'. In: *Science* 283.5403 (1999), pp. 814–816. DOI: 10.1126/science.283.5403.814 (cited on page 66).

[284] Zouti Xie et al. 'Spin Specific Electron Conduction through DNA Oligomers'. In: *Nano Letters* 11.11 (2011), pp. 4652–4655. DOI: 10.1021/nl2021637 (cited on page 66).

[285] Anil-Kumar Singh et al. 'Single-molecule junctions map the interplay between electrons and chirality'. In: *Nature Communications* 16.1 (2025), p. 1759 (cited on pages 66, 72).

[286] Hannah J. Eckvahl et al. 'Direct observation of chirality-induced spin selectivity in electron donor–acceptor molecules'. In: *Science* 382.6667 (2023), pp. 197–201. DOI: 10.1126/science.adj5328 (cited on pages 66, 82).

[287] Hannah J. Eckvahl et al. 'Detecting Chirality-Induced Spin Selectivity in Randomly Oriented Radical Pairs Photogenerated by Hole Transfer'. In: *Journal of the American Chemical Society* 146.34 (2024), pp. 24125–24132. DOI: 10.1021/jacs.4c08706 (cited on pages 66, 82).

[288] Ron Naaman and David H. Waldeck. 'What Can CISS Teach Us about Electron Transfer?' In: *The Journal of Physical Chemistry Letters* 15.44 (2024), pp. 11002–11006. DOI: 10.1021/acs.jpclett.4c02617 (cited on page 66).

[289] Jonas Fransson. 'Chiral Induced Spin Polarized Electron Current: Origin of the Chiral Induced Spin Selectivity Effect'. In: *The Journal of Physical Chemistry Letters* 16.17 (2025), pp. 4346–4353. DOI: 10.1021/acs.jpclett.5c00104 (cited on pages 66, 68).

[290] Ferdinand Evers et al. 'Theory of Chirality Induced Spin Selectivity: Progress and Challenges'. In: *Advanced Materials* 34.13 (2022). DOI: 10.1002/adma.202106629 (cited on page 66).

[291] Jonas Fransson. 'Chirality-induced spin selectivity: The role of electron correlations'. In: *The journal of physical chemistry letters* 10.22 (2019), pp. 7126–7132 (cited on pages 66, 72).

[292] Alessandro Chiesa et al. 'Many-Body Models for Chirality-Induced Spin Selectivity in Electron Transfer'. In: *Nano Letters* 24.39 (Oct. 2024), pp. 12133–12139. DOI: 10.1021/acs.nanolett.4c02912. (Visited on 10/24/2024) (cited on pages 66, 72, 82, 85).

[293] Gui-Fang Du, Hua-Hua Fu, and Ruqian Wu. 'Vibration-enhanced spin-selective transport of electrons in the DNA double helix'. In: *Physical Review B* 102.3 (July 2020), p. 035431. DOI: 10.1103/PhysRevB.102.035431. (Visited on 03/19/2025) (cited on pages 66, 80).

[294] Akihito Kato, Hiroshi M. Yamamoto, and Jun-ichiro Kishine. 'Chirality-induced spin filtering in pseudo Jahn-Teller molecules'. In: *Physical Review B* 105.19 (May 2022), p. 195117. DOI: 10.1103/PhysRevB.105.195117. (Visited on 03/19/2025) (cited on page 66).

[295] Song Chen and Hua-Hua Fu. 'Spin-Dependent Destructive and Constructive Quantum Interference Associated with Chirality-Induced Spin Selectivity in Single Circular Helix Molecules'. In: *The Journal of Physical Chemistry Letters* 14.49 (2023), pp. 11076–11083. DOI: 10.1021/acs.jpclett.3c02648 (cited on page 66).

[296] Longlong Zhang et al. 'Chiral-induced spin selectivity: A polaron transport model'. In: *Physical Review B* 102.21 (Dec. 2020), p. 214303. DOI: 10.1103/PhysRevB.102.214303. (Visited on 03/19/2025) (cited on page 66).

[297] Dan Klein and Karen Michaeli. 'Giant chirality-induced spin selectivity of polarons'. In: *Physical Review B* 107.4 (Jan. 2023), p. 045404. DOI: 10.1103/PhysRevB.107.045404. (Visited on 03/19/2025) (cited on pages 66, 77).

[298] Tapan Kumar Das, Ron Naaman, and Jonas Fransson. 'Insights into the Mechanism of Chiral-Induced Spin Selectivity: The Effect of Magnetic Field Direction and Temperature'. In: *Advanced Materials* 36.29 (2024), p. 2313708. DOI: 10.1002/adma.202313708 (cited on page 66).

[299] Ryosuke Otsuto, Yuya Yatabe, and Hiroshi Akera. 'Orbital and spin polarizations induced by current through a helical atomic chain'. In: *Physical Review B* 104.3 (2021), p. 035431. DOI: 10.1103/physrevb.104.035431 (cited on page 66).

[300] Yuya Yatabe and Hiroshi Akera. 'Coupling of orbital and spin polarizations to interatomic hopping in a helical atomic chain'. In: *The Journal of Chemical Physics* 159.7 (2023), p. 074701. DOI: 10.1063/5.0156461 (cited on page 66).

[301] Yanze Wu and Joseph E. Subotnik. 'Electronic spin separation induced by nuclear motion near conical intersections'. In: *Nature Communications* 12.1 (2021), p. 700. DOI: 10.1038/s41467-020-20831-8 (cited on page 66).

[302] Hung-Hsuan Teh, Wenjie Dou, and Joseph E. Subotnik. 'Spin polarization through a molecular junction based on nuclear Berry curvature effects'. In: *Physical Review B* 106.18 (2022), p. 184302. DOI: 10.1103/physrevb.106.184302 (cited on page 66).

[303] Zhi-Gang Yu. 'Spin-Charge Conversion in Chiral Polymers with Hopping Conduction'. In: *The Journal of Physical Chemistry Letters* 15.30 (2024), pp. 7770–7774. DOI: 10.1021/acs.jpclett.4c01597 (cited on page 66).

[304] Tian-Yi Zhang et al. 'Dynamical theory of chiral-induced spin selectivity in electron donor–chiral molecule–acceptor systems'. In: *Physical Review B* 111.20 (2025), p. 205417. DOI: 10.1103/physrevb.111.205417 (cited on page 66).

[305] D.S Kosov and J.C Greer. 'Many-electron systems with constrained current'. In: *Physics Letters A* 291.1 (2001), pp. 46–50. DOI: 10.1016/s0375-9601(01)00701-0 (cited on pages 66, 69).

[306] D. S. Kosov. 'Schrödinger equation for current carrying states'. In: *The Journal of Chemical Physics* 116.14 (2002), pp. 6368–6375. DOI: 10.1063/1.1460857 (cited on pages 66, 69).

[307] Anna Painelli. 'Real-space description of current-constrained molecular junctions'. In: *Physical Review B* 74.15 (2006), p. 155305. DOI: 10.1103/physrevb.74.155305 (cited on pages 66, 69, 70).

[308] Irene Burghardt et al., eds. *Energy Transfer Dynamics in Biomaterial Systems*. en. Vol. 93. Springer Series in Chemical Physics. Berlin, Heidelberg, 2009. (Visited on 05/22/2025) (cited on page 66).

[309] Mark R Hirsbrunner et al. 'A review of modeling interacting transient phenomena with non-equilibrium Green functions'. en. In: *Reports on Progress in Physics* 82.4 (Mar. 2019), p. 046001. DOI: 10.1088/1361-6633/aafe5f. (Visited on 05/22/2025) (cited on page 66).

[310] Ai-Min Guo and Qing-feng Sun. 'Spin-Selective Transport of Electrons in DNA Double Helix'. In: *Physical Review Letters* 108.21 (May 2012), p. 218102. DOI: 10.1103/PhysRevLett.108.218102. (Visited on 05/22/2025) (cited on page 66).

[311] Ai-Min Guo et al. 'Contact effects in spin transport along double-helical molecules'. In: *Physical Review B* 89.20 (May 2014), p. 205434. DOI: 10.1103/PhysRevB.89.205434. (Visited on 05/22/2025) (cited on page 66).

[312] William Bro-Jørgensen, Marc H. Garner, and Gemma C. Solomon. 'Quantification of the Helicality of Helical Molecular Orbitals'. In: *The Journal of Physical Chemistry A* 125.36 (2021), pp. 8107–8115. DOI: 10.1021/acs.jpca.1c05799 (cited on page 67).

[313] Marc H. Garner and Clemence Corminboeuf. 'The fundamental relation between electrohelicity and molecular optical activity'. In: *Physical Chemistry Chemical Physics* 25.22 (2023), pp. 15200–15208. DOI: 10.1039/d3cp01343j (cited on page 67).

[314] Frank Neese. 'Efficient and accurate approximations to the molecular spin-orbit coupling operator and their use in molecular g-tensor calculations'. In: *The Journal of chemical physics* 122.3 (2005), p. 034107 (cited on page 67).

[315] Volodymyr V. Maslyuk et al. 'Enhanced Magnetoresistance in Chiral Molecular Junctions'. In: *The Journal of Physical Chemistry Letters* 9.18 (Sept. 2018), pp. 5453–5459. DOI: 10.1021/acs.jpclett.8b02360. (Visited on 03/19/2025) (cited on page 68).

[316] T. K. Ng. 'Nonlinear transport in mesoscopic systems'. In: *Physical Review Letters* 68.7 (1992), pp. 1018–1021. DOI: 10.1103/physrevlett.68.1018 (cited on page 69).

[317] P. Bokes and R. W. Godby. 'Maximum-entropy theory of steady-state quantum transport'. In: *Physical Review B* 68.12 (2003), p. 125414. DOI: 10.1103/physrevb.68.125414 (cited on page 69).

[318] P. Bokes, H. Mera, and R. W. Godby. 'Current-constraining variational approaches to quantum transport'. In: *Physical Review B* 72.16 (2005), p. 165425. DOI: 10.1103/physrevb.72.165425 (cited on page 69).

[319] Prakash Parida, Swapan K. Pati, and Anna Painelli. 'Negative differential conductance in nanojunctions: A current constrained approach'. In: *Physical Review B* 83.16 (2011), p. 165404. DOI: 10.1103/physrevb.83.165404 (cited on page 69).

[320] Pierre F. Maldague. 'Optical spectrum of a Hubbard chain'. In: *Physical Review B* 16.6 (1977), pp. 2437–2446. DOI: 10.1103/physrevb.16.2437 (cited on page 70).

[321] Matthias Geyer et al. 'Chirality-Induced Spin Selectivity in a Coarse-Grained Tight-Binding Model for Helicene'. In: *The Journal of Physical Chemistry C* 123.44 (Nov. 2019), pp. 27230–27241. DOI: 10.1021/acs.jpcc.9b07764. (Visited on 03/19/2025) (cited on page 70).

[322] Shlomi Matityahu et al. 'Spin-dependent transport through a chiral molecule in the presence of spin-orbit interaction and nonunitary effects'. In: *Physical Review B* 93.7 (2016), p. 075407. DOI: 10.1103/physrevb.93.075407 (cited on page 71).

[323] C. L. Kane and E. J. Mele. In: *Physical Review Letters* 95.14 (2005), p. 146802. DOI: 10.1103/physrevlett.95.146802 (cited on page 72).

[324] C. L. Kane and E. J. Mele. 'Quantum Spin Hall Effect in Graphene'. In: *Physical Review Letters* 95.22 (2005), p. 226801. DOI: 10.1103/physrevlett.95.226801 (cited on page 72).

[325] Qing-feng Sun, X. C. Xie, and Jian Wang. 'Persistent spin current in nanodevices and definition of the spin current'. In: *Physical Review B* 77.3 (2008), p. 035327. DOI: 10.1103/physrevb.77.035327 (cited on page 72).

[326] D. K. Andrea Phan Huu et al. 'Ab initio parametrization of a generalized Hubbard model in a molecule displaying chirality-induced spin selectivity'. en. In: *Communications Materials* 6.1 (May 2025), pp. 1–9. DOI: 10.1038/s43246-025-00821-3. (Visited on 05/29/2025) (cited on pages 77, 80, 82).

[327] Supriyo Datta. 'Electrical resistance: an atomistic view'. In: *Nanotechnology* 15.7 (2004), S433–S451. DOI: 10.1088/0957-4484/15/7/051 (cited on page 77).

[328] Vankayala Kiran et al. 'Helicenes—A New Class of Organic Spin Filter'. In: *Advanced Materials* 28.10 (2016), pp. 1957–1962. DOI: 10.1002/adma.201504725 (cited on page 77).

[329] Chidambar Kulkarni et al. 'Highly Efficient and Tunable Filtering of Electrons' Spin by Supramolecular Chirality of Nanofiber-Based Materials'. In: *Advanced Materials* 32.7 (2020), p. 1904965. DOI: 10.1002/adma.201904965 (cited on page 77).

[330] R. Naaman, Y. Paltiel, and D. H. Waldeck. 'Chiral Molecules and the Spin Selectivity Effect'. In: *The Journal of Physical Chemistry Letters* 11.9 (2020), pp. 3660–3666. DOI: 10.1021/acs.jpclett.0c00474 (cited on page 77).

[331] Amit Kumar Mondal et al. 'Spin Filtering in Supramolecular Polymers Assembled from Achiral Monomers Mediated by Chiral Solvents'. In: *Journal of the American Chemical Society* 143.18 (2021), pp. 7189–7195. DOI: 10.1021/jacs.1c02983 (cited on page 77).

[332] J. Fransson. 'Vibrational origin of exchange splitting and "chiral-induced spin selectivity'. In: *Physical Review B* 102.23 (Dec. 2020), p. 235416. DOI: 10.1103/PhysRevB.102.235416. (Visited on 03/19/2025) (cited on page 77).

[333] R. Smorka, S. L. Rudge, and M. Thoss. 'Influence of nonequilibrium vibrational dynamics on spin selectivity in chiral molecular junctions'. In: *The Journal of Chemical Physics* 162.1 (2025). DOI: 10.1063/5.0235411 (cited on page 77).

[334] Samuel L. Rudge et al. 'The Role of Quantum Vibronic Effects in the Spin Polarization of Charge Transport through Molecular Junctions'. In: *arXiv* (2025), //arxiv.org/pdf/2503.09286v1. DOI: 10.48550/ARXIV.2503.09286 (cited on pages 77, 80, 82).

[335] Thomas P. Fay and David T. Limmer. 'Origin of Chirality Induced Spin Selectivity in Photoinduced Electron Transfer'. In: *Nano Letters* 21.15 (2021), pp. 6696–6702. DOI: 10.1021/acs.nanolett.1c02370 (cited on page 80).

[336] Tapan Kumar Das et al. 'Temperature-Dependent Chiral-Induced Spin Selectivity Effect: Experiments and Theory'. In: *The Journal of Physical Chemistry C* 126.6 (Feb. 2022), pp. 3257–3264. DOI: 10.1021/acs.jpcc.1c10550. (Visited on 03/19/2025) (cited on page 80).

[337] Suraj S. Chandran et al. 'Electron transfer and spin–orbit coupling: Can nuclear motion lead to spin selective rates?' In: *The Journal of Chemical Physics* 156.17 (2022). DOI: 10.1063/5.0086554 (cited on page 80).

[338] D.P. Craig and T. Thirunamachandran. 'A theory of vibrational circular dichroism in terms of vibronic interactions'. In: *Molecular Physics* 35.3 (1978), pp. 825–840. DOI: 10.1080/00268977800100611 (cited on page 81).

[339] Laurence A. Nafie. 'Vibrational optical activity: From discovery and development to future challenges'. In: *Chirality* 32.5 (2020), pp. 667–692. DOI: 10.1002/chir.23191 (cited on page 81).

[340] Shane M. Parker et al. 'Communication: Active-space decomposition for molecular dimers'. In: *The Journal of Chemical Physics* 139.2 (July 2013), p. 021108. DOI: 10.1063/1.4813827. (Visited on 09/01/2025) (cited on page 83).

[341] S. Kivelson et al. 'Missing bond-charge repulsion in the extended Hubbard model: Effects in polyacetylene'. In: *Physical Review Letters* 58.18 (1987), pp. 1899–1902. DOI: 10.1103/physrevlett.58.1899 (cited on page 85).

[342] Anna Painelli and Alberto Girlando. 'Interacting electrons in 1D: Applicability of Hubbard models'. In: *Synthetic Metals* 27.1-2 (1988), A15–A20 (cited on page 85).

[343] Klaus Hunger and Martin U Schmidt. *Industrial organic pigments: production, crystal structures, properties, applications*. John Wiley & Sons, 2019 (cited on page 93).

[344] Ju Mei et al. 'Aggregation-induced emission: together we shine, united we soar!' In: *Chemical reviews* 115.21 (2015), pp. 11718–11940 (cited on page 93).

[345] Hironori Kaji et al. 'Purely organic electroluminescent material realizing 100% conversion from electricity to light'. In: *Nature communications* 6.1 (2015), p. 8476 (cited on page 93).

[346] Xisen Hou et al. 'Tunable solid-state fluorescent materials for supramolecular encryption'. In: *Nature communications* 6.1 (2015), p. 6884 (cited on page 93).

[347] Kousik Kundu et al. 'Hydrocyanines: a class of fluorescent sensors that can image reactive oxygen species in cell culture, tissue, and in vivo'. In: *Angewandte Chemie (International ed. in English)* 48.2 (2009), p. 299 (cited on page 93).

[348] Aijaz A Dar and Asif A Malik. 'Photoluminescent organic crystals and co-crystals'. In: *Journal of Materials Chemistry C* 12.27 (2024), pp. 9888–9913 (cited on page 93).

[349] Johannes Gierschner et al. 'Luminescence in crystalline organic materials: from molecules to molecular solids'. In: *Advanced Optical Materials* 9.13 (2021), p. 2002251 (cited on page 93).

[350] Yuning Hong, Jacky WY Lam, and Ben Zhong Tang. 'Aggregation-induced emission'. In: *Chemical Society Reviews* 40.11 (2011), pp. 5361–5388 (cited on page 93).

[351] Brian W D'Andrade and Stephen R Forrest. 'White organic light-emitting devices for solid-state lighting'. In: *Advanced materials* 16.18 (2004), pp. 1585–1595 (cited on page 93).

[352] Patrice HN Crosby and Anil N Netravali. 'Green thermochromic materials: a brief review'. In: *Advanced Sustainable Systems* 6.9 (2022), p. 2200208 (cited on page 93).

[353] Juan Zhao et al. 'Recent progress in the mechanofluorochromism of distyrylanthracene derivatives with aggregation-induced emission'. In: *Materials Chemistry Frontiers* 2.9 (2018), pp. 1595–1608 (cited on page 93).

[354] Xiaobo Huang et al. 'Effective structural modification of traditional fluorophores to obtain organic mechanofluorochromic molecules'. In: *Journal of Materials Chemistry C* 6.19 (2018), pp. 5075–5096 (cited on page 93).

[355] Aisen Li et al. 'Piezochromic mechanism of organic crystals under hydrostatic pressure'. In: *Materials Chemistry Frontiers* 5.6 (2021), pp. 2588–2606 (cited on page 93).

[356] Bernardo A Nogueira, Chiara Castiglioni, and Rui Fausto. 'Color polymorphism in organic crystals'. In: *Communications Chemistry* 3.1 (2020), pp. 1–12 (cited on page 93).

[357] Gautam R Desiraju. 'Crystal engineering: a holistic view'. In: *Angewandte Chemie International Edition* 46.44 (2007), pp. 8342–8356 (cited on page 94).

[358] Massimiliano Cavallini et al. 'Lithographic alignment of discotic liquid crystals: a new time–temperature integrating framework'. In: *Advanced materials* 21.46 (2009), pp. 4688–4691 (cited on page 94).

[359] Denis Gentili et al. 'A time-temperature integrator based on fluorescent and polymorphic compounds'. In: *Scientific reports* 3.1 (2013), pp. 1–7 (cited on page 94).

[360] Denis Gentili et al. 'Polymorphism as an additional functionality of materials for technological applications at surfaces and interfaces'. In: *Chemical Society Reviews* 48.9 (2019), pp. 2502–2517 (cited on page 94).

[361] Zhenghuan Lin et al. 'Polymorphism-dependent fluorescence of bisthienylmaleimide with different responses to mechanical crushing and grinding pressure'. In: *CrystEngComm* 16.48 (2014), pp. 11018–11026 (cited on page 94).

[362] Ludwig Gattermann. 'Ueber einige Derivate des m-Nitro-p-Toluidins'. In: *Berichte der deutschen chemischen Gesellschaft* 18.1 (1885), pp. 1482–1488 (cited on page 94).

[363] GA Stephenson et al. 'Conformational and color polymorphism of 5-methyl-2-[(2-nitrophenyl) amino]-3-thiophenecarbonitrile'. In: *Journal of pharmaceutical sciences* 84.11 (1995), pp. 1385–1386 (cited on page 94).

[364] M Busch and Ernst Pungs. 'Über isomere Verschiedenfarbige Pikrylamine'. In: *Journal für Praktische Chemie* 79.1 (1909), pp. 546–554 (cited on page 94).

[365] Erich F Paulus, Frank JJ Leusen, and Martin U Schmidt. 'Crystal structures of quinacridones'. In: *CrystEngComm* 9.2 (2007), pp. 131–143 (cited on pages 94, 96).

[366] SS Labana and LL Labana. 'Quinacridones'. In: *Chemical Reviews* 67.1 (1967), pp. 1–18 (cited on page 94).

[367] C Binant, B Guineau, and A Lautié. 'The application of electronic and vibrational spectroscopic techniques to the identification of quinacridone pigments in vehicle paint systems'. In: *Journal of the Society of Dyers and Colourists* 106.5-6 (1990), pp. 187–191 (cited on page 94).

[368] Peter Erk et al. 'The innovative momentum of crystal engineering'. In: *CrystEngComm* 6 (2004), pp. 474–483 (cited on pages 94, 95, 106).

[369] *Quinacridone Pigments Market Size is projected to reach USD 539 million by 2030, growing at a CAGR of 6.1%: Straits Research*. Accessed: 2022-08-09. URL: https://www.globenewswire.com/en/news-release/2022/08/09/2494931/0/en/Quinacridone-Pigments-Market-Size-is-projected-to-reach-USD-539-million-by-2030-growing-at-a-CAGR-of-6-1-Straits-Research.html (cited on page 94).

[370] Chenguang Wang, Zuolun Zhang, and Yue Wang. 'Quinacridone-based π-conjugated electronic materials'. In: *Journal of Materials Chemistry C* 4.42 (2016), pp. 9918–9936 (cited on page 94).

[371] Hui Li et al. 'Donor–acceptor copolymers containing quinacridone and benzothiadiazole for thin film transistors'. In: *Journal of Materials Chemistry C* 1.10 (2013), pp. 2021–2027 (cited on page 94).

[372] Tianlei Zhou et al. 'Nitrile-Substituted QA Derivatives: New Acceptor Materials for Solution-Processable Organic Bulk Heterojunction Solar Cells'. In: *Advanced Energy Materials* 1.3 (2011), pp. 431–439 (cited on page 94).

[373] Hong-Ze Gao. 'Theoretical study on charge transport of quinacridone polymorphs'. In: *International Journal of Quantum Chemistry* 112.3 (2012), pp. 740–746 (cited on page 94).

[374] Daniel Lüftner et al. 'Experimental and theoretical electronic structure of quinacridone'. In: *Physical Review B* 90.7 (2014), p. 075204 (cited on page 94).

[375] Christian Winkler, Florian Mayer, and Egbert Zojer. 'Analyzing the Electronic Coupling in Molecular Crystals—The Instructive Case of α-Quinacridone'. In: *Advanced Theory and Simulations* 2.5 (2019), p. 1800204 (cited on page 94).

[376] Christian Winkler et al. 'Understanding the correlation between electronic coupling and energetic stability of molecular crystal polymorphs: the instructive case of quinacridone'. In: *Chemistry of Materials* 31.17 (2019), pp. 7054–7069 (cited on page 94).

[377] Oliver Kühn. 'Frenkel exciton dynamics: A theoretical perspective'. In: *Handbook of Organic Materials for Electronic and Photonic Devices* (2019), pp. 259–279 (cited on page 94).

[378] H Yamagata et al. 'The nature of singlet excitons in oligoacene molecular crystals'. In: *The Journal of chemical physics* 134.20 (2011) (cited on pages 94, 106).

[379] Nicholas J. Hestand et al. 'Confirmation of the Origins of Panchromatic Spectra in Squaraine Thin Films Targeted for Organic Photovoltaic Devices'. In: *The Journal of Physical Chemistry C* 119.33 (Aug. 2015), pp. 18964–18974. DOI: 10.1021/acs.jpcc.5b05095 (cited on pages 94, 106).

[380] Samuele Giannini et al. 'On the role of charge transfer excitations in non-fullerene acceptors for organic photovoltaics'. In: *Materials Today* 80 (2024), pp. 308–326 (cited on pages 94, 111).

[381] Nicholas J Hestand and Frank C Spano. 'Expanded theory of H-and J-molecular aggregates: the effects of vibronic coupling and intermolecular charge transfer'. In: *Chemical reviews* 118.15 (2018), pp. 7069–7163 (cited on pages 94, 106).

[382] Davide Giavazzi et al. 'Optical spectra of complex aggregates and crystals: Vibronic band structure and Davydov splitting'. In: *The Journal of Chemical Physics* 162.17 (May 2025). DOI: 10.1063/5.0263317 (cited on page 94).

[383] Painelli, A. and Terenziani, F. 'Optical Spectra of Push-Pull Chromophores in Solution: A Simple Model'. In: *The Journal of Physical Chemistry A* 104.47 (2000), pp. 11041–11048 (cited on page 94).

[384] Luca Grisanti et al. 'Essential State Models for Solvatochromism in Donor-Acceptor Molecules: The Role of the Bridge'. In: *The Journal of Physical Chemistry B* 113.14 (2009), pp. 4718–4725 (cited on page 94).

[385] Francesca Terenziani et al. 'Essential-state model for polymethine dyes: Symmetry breaking and optical spectra'. In: *The Journal of Physical Chemistry Letters* 1.12 (2010), pp. 1800–1804 (cited on page 94).

[386] D'Avino, G. and Terenziani, F. and Painelli, A. 'Aggregates of Quadrupolar Dyes: Giant Two-Photon Absorption from Biexciton States'. In: *ChemPhysChem* 8 (2007), pp. 2433–2444 (cited on page 94).

[387] Gabriele D'Avino et al. 'Bistability in Fc-PTM crystals: The role of intermolecular electrostatic interactions'. In: *Journal of the American Chemical Society* 130.36 (2008), pp. 12064–12072 (cited on page 94).

[388] Somananda Sanyal et al. 'Superlinear amplification of the first hyperpolarizability of linear aggregates of DANS molecules'. In: *Phys. Chem. Chem. Phys.* 19 (36 2017), pp. 24979–24984. DOI: 10.1039/C7CP04732K (cited on page 94).

[389] S. Sanyal et al. 'Aggregates of quadrupolar dyes for two-photon absorption: the role of intermolecular interactions'. In: *Phys. Chem. Chem. Phys.* 18 (40 2016), pp. 28198–28208. DOI: 10.1039/C6CP05153G (cited on page 94).

[390] Brunella Bardi et al. 'Multistimuli-Responsive Materials from Benzothiadiazole-Based Charge-Transfer Chromophores: Interdependence of Optical Properties and Aggregation'. In: *ChemPhotoChem* 2.12 (2018), pp. 1027–1037 (cited on page 94).

[391] David Bialas et al. 'Essential States Model for Merocyanine Dye Stacks: Bridging Electronic and Optical Absorption Properties'. In: *The Journal of Physical Chemistry C* 123.30 (July 2019), pp. 18654–18664. DOI: 10.1021/acs.jpcc.9b04430 (cited on page 94).

[392] Mattia Anzola and Anna Painelli. 'Aggregates of polar dyes: Beyond the exciton model'. In: *Physical Chemistry Chemical Physics* 23.14 (2021), pp. 8282–8291 (cited on pages 94, 125).

[393] Daniel Timmer et al. 'Charge Delocalization and Vibronic Couplings in Quadrupolar Squaraine Dyes'. In: *Journal of the American Chemical Society* 144.41 (2022), pp. 19150–19162. DOI: 10.1021/jacs.2c08682 (cited on page 94).

[394] Thomas Körzdörfer and Jean-Luc Brédas. 'Organic Electronic Materials: Recent Advances in the DFT Description of the Ground and Excited States Using Tuned Range-Separated Hybrid Functionals'. In: *Accounts of Chemical Research* 47.11 (2014). PMID: 24784485, pp. 3284–3291. DOI: 10.1021/ar500021t (cited on page 95).

[395] Lars Goerigk and Stefan Grimme. 'Double-hybrid density functionals'. In: *WIREs Computational Molecular Science* 4.6 (2014), pp. 576–600. DOI: https://doi.org/10.1002/wcms.1193 (cited on page 95).

[396] Takao Tsuneda and Kimihiko Hirao. 'Long-range correction for density functional theory'. In: *WIREs Computational Molecular Science* 4.4 (2014), pp. 375–390. DOI: https://doi.org/10.1002/wcms.1178 (cited on page 95).

[397] Mihails Arhangelskis et al. 'Time-dependent density-functional theory for modeling solid-state fluorescence emission of organic multicomponent crystals'. In: *The Journal of Physical Chemistry A* 122.37 (2018), pp. 7514–7521 (cited on page 95).

[398] Joseph CA Prentice and Arash A Mostofi. 'Accurate and efficient computation of optical absorption spectra of molecular crystals: The case of the polymorphs of ROY'. In: *Journal of Chemical Theory and Computation* 17.8 (2021), pp. 5214–5224 (cited on page 95).

[399] Xibo Feng, Axel D Becke, and Erin R Johnson. 'Theoretical investigation of polymorph-and coformer-dependent photoluminescence in molecular crystals'. In: *CrystEngComm* 23.24 (2021), pp. 4264–4271 (cited on page 95).

[400] Davide Presti et al. 'Understanding aggregation-induced emission in molecular crystals: insights from theory'. In: *The Journal of Physical Chemistry C* 121.10 (2017), pp. 5747–5752 (cited on page 95).

[401] Michele Turelli et al. 'Organic compounds for solid state luminescence enhancement/aggregation induced emission: a theoretical perspective'. In: *Physical Chemistry Chemical Physics* 25.27 (2023), pp. 17769–17786 (cited on page 95).

[402] Miguel Rivera, Michael Dommett, and Rachel Crespo-Otero. 'ONIOM (QM: QM) electrostatic embedding schemes for photochemistry in molecular crystals'. In: *Journal of Chemical Theory and Computation* 15.4 (2019), pp. 2504–2516 (cited on page 95).

[403] Amir Sidat et al. 'Performance of point charge embedding schemes for excited states in molecular organic crystals'. In: *The Journal of Chemical Physics* 159.24 (2023) (cited on page 95).

[404] A Muñoz-Losa et al. 'Quantum mechanical methods applied to excitation energy transfer: A comparative analysis on excitation energies and electronic couplings'. In: *The Journal of chemical physics* 129.3 (2008) (cited on page 95).

[405] Chao-Ping Hsu. 'The electronic couplings in electron transfer and excitation energy transfer'. In: *Accounts of Chemical Research* 42.4 (2009), pp. 509–518 (cited on page 95).

[406] Luca Grisanti et al. 'Roles of local and nonlocal electron-phonon couplings in triplet exciton diffusion in the anthracene crystal'. In: *Physical Review B* 88.3 (2013), p. 035450 (cited on page 95).

[407] Per-Arno Plötz, Thomas Niehaus, and Oliver Kühn. 'A new efficient method for calculation of Frenkel exciton parameters in molecular aggregates'. In: *The Journal of Chemical Physics* 140.17 (2014), p. 174101 (cited on page 95).

[408] Tommaso Salzillo et al. 'Spectroscopic identification of quinacridone polymorphs for organic electronics'. In: *CrystEngComm* 21.24 (2019), pp. 3702–3708 (cited on pages 95, 106).

[409] Kristian Berland and Per Hyldgaard. 'Exchange functional that tests the robustness of the plasmon description of the van der Waals density functional'. In: *Physical Review B* 89.3 (2014), p. 035412 (cited on page 97).

[410] Asim Najibi and Lars Goerigk. 'The nonlocal kernel in van der Waals density functionals as an additive correction: An extensive analysis with special emphasis on the B97M-V and ωB97M-V approaches'. In: *Journal of Chemical Theory and Computation* 14.11 (2018), pp. 5725–5738 (cited on page 97).

[411] 'Balanced basis sets of split valence, triple zeta valence and quadruple zeta valence quality for H to Rn: Design and assessment of accuracy'. In: 7 () (cited on page 97).

[412] Frank Neese. 'The ORCA program system'. In: *Wiley Interdisciplinary Reviews: Computational Molecular Science* 2.1 (2012), pp. 73–78 (cited on pages 97, 98).

[413] Narbe Mardirossian and Martin Head-Gordon. 'ωB97X-V: A 10-parameter, range-separated hybrid, generalized gradient approximation density functional with nonlocal correlation, designed by a survival-of-the-fittest strategy'. In: *Physical Chemistry Chemical Physics* 16.21 (2014), pp. 9904–9924 (cited on page 98).

[414] Yihan Shao et al. 'Benchmarking the performance of time-dependent density functional theory methods on biochromophores'. In: *Journal of chemical theory and computation* 16.1 (2019), pp. 587–600 (cited on page 98).

[415] Jiashu Liang et al. 'Revisiting the performance of time-dependent density functional theory for electronic excitations: Assessment of 43 popular and recently developed functionals from rungs one to four'. In: *Journal of chemical theory and computation* 18.6 (2022), pp. 3460–3473 (cited on page 98).

[416] Xia Wu, Xiaoyu Xie, and Alessandro Troisi. 'Calibration of several first excited state properties for organic molecules through systematic comparison of TDDFT with experimental spectra'. In: *Journal of Materials Chemistry C* 12.46 (2024), pp. 18886–18892 (cited on page 98).

[417] So Hirata and Martin Head-Gordon. 'Time-dependent density functional theory within the Tamm–Dancoff approximation'. In: *Chemical Physics Letters* 314.3 (Dec. 1999), pp. 291–299. DOI: 10.1016/S0009-2614(99)01149-5. (Visited on 07/31/2025) (cited on page 98).

[418] Felix Plasser and Hans Lischka. 'Analysis of excitonic and charge transfer interactions from quantum chemical calculations'. In: *Journal of chemical theory and computation* 8.8 (2012), pp. 2777–2789 (cited on page 98).

[419] Felix Plasser, Michael Wormit, and Andreas Dreuw. 'New tools for the systematic analysis and visualization of electronic excitations. I. Formalism'. In: *The Journal of chemical physics* 141.2 (2014), p. 024106 (cited on page 98).

[420] Felix Plasser et al. 'New tools for the systematic analysis and visualization of electronic excitations. II. Applications'. In: *The Journal of chemical physics* 141.2 (2014), p. 024107 (cited on page 98).

[421] Felix Plasser. 'TheoDORE: A toolbox for a detailed and automated analysis of electronic excited state computations'. In: *The Journal of Chemical Physics* 152.8 (2020), p. 084108 (cited on pages 98, 100, 112, 113, 115–118, 121, 123, 124).

[422] Pauli Virtanen et al. 'SciPy 1.0: Fundamental Algorithms for Scientific Computing in Python'. In: *Nature Methods* 17 (2020), pp. 261–272. DOI: 10.1038/s41592-019-0686-2 (cited on page 100).

[423] Robert C. Weast. *Handbook of Chemistry and Physics [64th. Edition, 1983-1984]*. CRC Press, 1984 (cited on page 101).

[424] Jin Mizuguchi and Takatoshi Senju. 'Solution and solid-state spectra of quinacridone derivatives as viewed from the intermolecular hydrogen bond'. In: *The Journal of Physical Chemistry B* 110.39 (2006), pp. 19154–19161 (cited on pages 101, 102, 104).

[425] Frank Wennmohs Frank Neese et al. *ORCA - An ab initio, DFT and semiempirical SCF-MO package - Version 5.0.2*. 2022 (cited on page 101).

[426] A Girlando et al. 'Direct evidence of overdamped Peierls-coupled modes in the temperature-induced phase transition in tetrathiafulvalene-chloranil'. In: *Physical Review B* 78.4 (2008), p. 045103 (cited on page 102).

[427] Alberto Girlando et al. 'Peierls and Holstein carrier-phonon coupling in crystalline rubrene'. In: *Physical Review B* 82.3 (2010), p. 035208 (cited on page 102).

[428] Christopher J Bardeen. 'Excitonic processes in molecular crystalline materials'. In: *MRS bulletin* 38.1 (2013), pp. 65–71 (cited on page 106).

[429] Christopher J Bardeen. 'The structure and dynamics of molecular excitons'. In: *Annual review of physical chemistry* 65 (2014), pp. 127–148 (cited on page 106).

[430] Sang Kyu Park et al. 'Stimuli-Responsive Reversible Fluorescence Switching in a Crystalline Donor–Acceptor Mixture Film: Mixed Stack Charge-Transfer Emission versus Segregated Stack Monomer Emission'. In: *Angewandte Chemie International Edition* 55.1 (Nov. 2015), pp. 203–207. DOI: 10.1002/anie.201508210 (cited on page 106).

[431] Leander Ernst et al. 'Photoinduced stepwise charge hopping in -stacked perylene bisimide donor–bridge–acceptor arrays'. In: *Nature Chemistry* 17.5 (Mar. 2025), pp. 767–776. DOI: 10.1038/s41557-025-01770-7 (cited on page 106).

[432] Pierluigi Cudazzo et al. 'Frenkel versus charge-transfer exciton dispersion in molecular crystals'. In: *Phys. Rev. B* 88 (19 Nov. 2013), p. 195152. DOI: 10.1103/PhysRevB.88.195152 (cited on page 106).

[433] Frederik Unger et al. 'Optical Absorption Properties in Pentacene/Tetracene Solid Solutions'. In: *The Journal of Physical Chemistry A* 128.4 (2024), pp. 747–760 (cited on page 106).

[434] Michael Kasha. 'Characterization of electronic transitions in complex molecules'. In: *Discuss. Faraday Soc.* 9 (0 1950), pp. 14–19. DOI: 10.1039/DF9500900014 (cited on page 107).

[435] Benoıt Champagne, Vincent Liégeois, and Freddy Zutterman. 'Pigment violet 19—a test case to define a simple method to simulate the vibronic structure of absorption spectra of organic pigments and dyes in solution'. In: *Photochemical & Photobiological Sciences* 14.2 (2015), pp. 444–456 (cited on page 108).

[436] Mauricio Rodriguez-Mayorga et al. 'From many-body ab initio to effective excitonic models: a versatile mapping approach including environmental embedding effects'. In: *Journal of Chemical Theory and Computation* 20.19 (2024), pp. 8675–8688 (cited on page 110).

[437] Anna S Bondarenko et al. 'Multiscale modeling of molecular structure and optical properties of complex supramolecular aggregates'. In: *Chemical Science* 11.42 (2020), pp. 11514–11524 (cited on page 111).

[438] Benedikt Zerulla et al. 'A multi-scale approach for modeling the optical response of molecular materials inside cavities'. In: *Advanced Materials* 34.21 (2022), p. 2200350 (cited on page 111).

[439] Vladimir M Agranovich. *Excitations in organic solids*. Vol. 142. OUP Oxford, 2009 (cited on page 125).

Ringraziamenti

Alla fine di questo percorso non posso fare a meno di stupirmi nel valutare quanto ho studiato e imparato. Il progetto a me assegnato non era facile né chiaro, e sono sicuro di aver lavorato in maniera imperfetta e migliorabile, senza riuscire a fare forse quanto si sarebbe aspettato. D'altro canto, un progetto così complesso mi ha costretto a studiare matematica, fisica, chimica, informatica e tanto altro, imparando cose sparse che ora fanno parte del mio bagaglio culturale e per le quali non smetterò mai di ringraziare questi tre difficili anni. Sono stati anni complessi, ma non posso che essere felice del percorso, e se dovessi tornare indietro a tre anni fa rifarei quasi tutte le scelte davanti alle quali mi sono trovato. Quindi il primo grazie va al me di tre anni fa per aver avuto il coraggio di lanciarsi in questa avventura. Ma ora andiamo ai ringraziamenti veri.

Come prima cosa è d'obbligo ringraziare Anna per aver supervisionato il mio dottorato con occhio attento e preciso, e soprattutto per avermi sgridato costantemente per la mia incapacità di spiegarmi, sia in inglese che in italiano. Dopo di lei, ringrazio Andrea Phan e Francesco Di Maiolo per aver co-supervisionato questa tesi e avermi guidato nella scoperta del mondo accademico. Ringrazio Andrea Landi, che ha iniziato e concluso con me questo percorso ed è stata una grande fonte di riflessione per la diversità di idee ed esperienze. Ringrazio Francesco Bertocchi, Marco e Matteo Bedogni con cui ho passato la maggior parte delle pause pranzo e pause caffe nell'ultimo anno, in particolare Francesco che considero davvero uno dei ricercatori più in gamba e spiritosi che abbia mai incontrato, e che ha aiutato molto nel plasmare le mie scelte future. Ringrazio Davide per avermi insegnato che durante il dottorato lo stress te lo metti addosso soprattutto tu, e quindi sta a te decidere la maggior parte della tensione che vuoi sentire. Infine ringrazio tutti gli altri membri del gruppo con cui ho condiviso cene, chiacchiere, esperienze divulgative e soprattutto le tante lamentele da pausa caffè: Cristina, Andrea Lapini, Matteo Masino, Francesca, Ilaria, Andrea DD, Alessandro, Ottavia, e tutti i tesisti che negli anni sono passato nella nostra ala.

Ringrazio le mie sorelle Linda, Sofia e Serena, e mio fratello Raffaele, a cui faccio pesare il mio amore per la scienza da quando sono nati - specialmente Linda e Sofia che subiscono da più di vent'anni. Ringrazio i miei genitori che si stupiscono di più del mio saper (circa) parlare in inglese che del mio lavoro scientifico e che hanno permesso questi anni di studio. Ringrazio i miei nonni, che fino all'ultimo hanno voluto condividere i miei successi, insuccessi e dubbi. In ultimo, fra i parenti, ringrazio i miei cugini Maria e Matteo con cui ho condiviso chiacchierate su modelli, equazioni, teoremi e parecchi viaggi in treno. A proposito, NON ringrazio Trenitalia per aver cambiato i vagoni bici sostituendoli con cubicoli che mi costringono ad aggiustare la bici una volta al mese almeno.

Ringrazio Davide per non capire nulla di scienze e prestarsi a farsi cogliere in fallo per il puro piacere mio di correggerlo. Ringrazio Gianluca Visag(h)li per aver condiviso il suo percorso con me e avermi fatto partecipe di tutti i suoi successi. Ringrazio gli amici con cui ho condiviso multiple birre parlando di università, in particolare Marco, Martina, Emma e Phoenix.

Ringrazio Giacomo e Samuel, e il gruppo Telegram dalle 4 ore giornaliere di audio con cui condividiamo i dettagli più inutili delle nostre vite dalla triennale. Nonostante la distanza, sono le uniche persone che sento giornalmente da 4 anni e a cui ho sempre qualcosa da dire e da chiedere, nonché le persone con cui parlo più spesso di scienza e problemi. Possa la vita regalarci un forno, un pianoforte, uno spettro Raman sensato, bar aperti ad orario colazione e tanti chilometri di distanza dall'Olanda. Spero la domanda "When shall we three meet again?" trovi presto risposta.

Infine ringrazio Giorgia, mia migliore amica da quattordici anni, fidanzata da quattro e ormai quasi moglie. Il suo costante supporto è stato fondamentale: nel sopportare la mia eterna stanchezza, nel commentare le mie lamentele sullo stato della scienza, nell'ascoltare senza possibilità di capire spiegazioni su modelli e calcoli, nell'imparare i nomi di tutte le persone che ho incontrato nel corso del dottorato, nel ricordarmi che sono un pò intelligente anche quando sembro molto stupido. Sento che questa tesi sia molto anche tua, e sapendo che, da orso quale sono, non gioirò troppo di questo traguardo pensando già alla prossima bandierina da raggiungere, ti auguro di festeggiare per me e brindare alla fine di questo percorso come preambolo di un nuovo cammino tutto da scoprire.